DESIGN AND OPTIMIZATION OF EFFICIENT PEROVSKITE BASED TANDEM SOLAR CELL

By

Mashrife Jaman Radib
Student ID : 1802007

Abrar Adib
Student ID : 1802019

A thesis submitted in partial fulfilment of the requirements for the degree of BACHELOR of SCIENCE in EEE

Department of Electrical and Electronic Engineering

CHITTAGONG UNIVERSITY OF ENGINEERING AND TECHNOLOGY

MAY 2024

Declaration

I hereby certify that none of the content in this Thesis has ever before been submitted for academic credit at this or any other school. To the best of my knowledge, the Thesis does not contain any content that has been written by someone else or published somewhere before, except where proper credit is given. Furthermore, the Thesis complies with the CUET guidelines on PLAGIARISM and ACADEMIC INTEGRITY.

--- ---

Mashrife Jaman Radib **Abrar Adib**

Student ID: 1802007 **Student ID: 1802019**

Department of Electrical and Electronic Engineering

Chittagong University of Engineering & Technology (CUET)

Dedication

To my beloved Parents

Approval by the Supervisor

This is to certify that Mashrife Jaman Radib and Abrar Adib have conducted this work under my direct supervision and that they have complied with all applicable academic requirements set forth by the Chittagong University of Engineering and Technology. As such, they are eligible to submit the following thesis in support of their application for the degree of BACHELOR of SCIENCE in the Department of Electrical and Electronic Engineering.

Mrinmoy Dey
Associate Professor
Department of Electrical and Electronic Engineering
Chittagong University of Engineering & Technology

Acknowledgement

First and foremost, we owe it to the Almighty, ALLAH, to convey our thankfulness for his blessings being bestowed upon us. Then we would love to thank our dearest parents for all of their supports during the process. Finally, we would like to extend our thanks to our supervisor, Mrinmoy Dey for allowing us to be a part of his research experience. We also want to express our profound gratitude to him for his constant guidelines, inspirations and unwavering support throughout our Thesis. His passion for study and teaching have peaked our interests to advance our understanding of science and extend our knowledge in the field of solar energy.

Abstract

A growing interest in energy to reduce human influence towards the environment have led to significant advancements in the sector of renewable energy in recent years. The rise in overall energy consumption can be featured to several factors like population growth, technological advancements, improving daily environments, growing urbanization, and globalization. Regarding the sources of modern power generation, solar cells are seen as a suitable alternative for fossil fuels. The third generation solar structures based on perovskite materials are turning into more common because of their low marginal cost as well as higher efficiency. Tandem structure allows them to collect wider spectrum of sunlight and exceed the overall performance of the single junction solar cells. In this thesis work, various Methylammonium based potential perovskite materials were investigated for the top sub-cell of tandem solar cell. Methylammonium Tin Bromide ($MASnBr_3$) is introduced as the tandem top cell and several bottom cells based on Silicon (c-Si), Germanium Telluride (GeTe), Copper Indium Diselenide ($CuInSe_2$) were designed. The tandem structure consisting of $MASnBr_3$ top cell and $CuInSe_2$ bottom cell has showed the best device performance with PCE of 41.68% (V_{oc}= 1.71 volts, J_{sc}= 30.55 mA/cm^2, FF= 80.07%). Superior efficiency was achieved because of the lower bandgap of the bottom cell and higher bandgap of the top cell material. The cell also showed good thermal stability with a temperature coefficient of -0.095%/^{o}C which makes our designed solar cell equally stable and efficient. The designed and proposed perovskite-based tandem solar cells can be further investigated for further performace improvements.

Table of Contents

Declaration ii

Dedication iii

Approval by the Supervisor iv

Acknowledgement v

Abstract vi

Nomenclature xvii

CHAPTER 1 : INTRODUCTION 1

1.1 Motivation 1

1.1.1 Emissions of Greenhouse Gases 4

1.1.2 Renewable Energy Sources 5

1.1.3 Status and Possibilities of Hydroelectric Power 8

1.1.4 Status and Possibilities of Biomass Energy 8

1.1.5 Status and Possibilities of Wind Energy 9

1.1.6 Status and Possibilities of Geothermal Energy 10

1.1.7 Solar Energy 11

1.2 Cells, Significance, Scope and Definitions 13

CHAPTER 2 : LITERATURE REVIEW 15

2.1 A Concise Look at the Evolution of Solar Cell Technology 15

2.1.1 The Sun's Spectrum 15

2.1.2 Concentrated Solar Power and Photovoltaic Solar 17

2.2 Global Expansion of PV 17

2.2.1 Different Generations of Solar Cells 17

2.3 Single Junction Solar Cells 21

2.4 Tandem Solar Cells 21

2.5 Best Researched Cell Efficiency 23

2.6 What is Perovskite 24

2.7 Why Perovskite Solar Cell 26

2.8 Evolution of Perovskite Solar Cell 27

2.9 Present Situation with Perovskite Solar Cells 28

2.10 Perovskite Solar Cells 29

2.11 $CH_3NH_3SnBr_3$ material overview 29

2.11.1 Crystal structure of $CH_3NH_3SnBr_3$ 30

2.11.2 Properties of $CH_3NH_3SnBr_3$ 31

2.1.1.3 Related Works on $CH_3NH_3SnBr_3$Thin Film Solar Cell 35

2.12 $CH_3NH_3SnI_3$ material overview 36

2.12.1 Properties of $CH_3NH_3SnI_3$ 38

2.1.2 Related Works on $CH_3NH_3SnI_3$ Thin Film Solar Cell 41

2.13 Perovskite Based Tandem 43

2.13.1 Related work on Perovskite-Si Tandem solar cell 44

2.13.2 Related work on $MASnBr_3$ based Tandem solar cell 45

2.13.3 Optimized High Current Tandem Solar Cells 46

2.14 Deposition Technique of Perovskite Solar Cell 46

2.14.1 Deposition Technique of $MASnBr_3$ Perovskite 47

2.14.2 Deposition Technique of Si Tandem Cell 48

2.14.3 Deposition Technique of GeTe Tandem Cell 49

2.14.4 Deposition Technique of $CuInSe_2$ Tandem Cell 50

2.14.5 Deposition Technique of Si Single Junction Cell 50

2.14.6 Deposition Technique of GeTe Single Junction Cell 51

2.14.7 Deposition Technique of $CuInSe_2$ Single Junction Cell 52

CHAPTER 3: DEVICE PHYSICS 54

3.1 The Basic Semiconductor Concept 54

3.1.1 Effect of Photovoltaic 54

3.1.2 Absorbance and Absorption Coefficient 55
3.1.3 Density of states (DOS) 56
3.1.4 Fermi Function 56
3.1.5 Energy Bandgap 57
3.2 Types of Semiconductor 59
3.2.1 Intrinsic Semiconductor 59
3.2.2 Extrinsic Semiconductor 60
3.3 p-n Junction 61
3.3.1 p-n Homojunction 61
3.3.2 p-n Heterojunction 62
3.3.3 Multi-Junction 62
3.3.4 Metal Semiconductor Junction 64
3.4 Solar Cell Equation 65
3.4.1 Analysis of Diffusion Length 67
3.4.2 Surface Recombination Analysis 67
3.4.3 Work Function 69
3.4.4 Loss Mechanism 69
3.4.5 Fermi Level 71
3.4.6 Intrinsic Carrier Density 71
3.5 Basic Structure of Solar cells 72
3.5.1 Equivalent Circuit of Solar Cells 73
3.5.2 Light Absorption in Solar Cells 74
3.6 Characteristics Parameters 75
3.6.1 Short-Circuit Current 75
3.6.2 Open circuit voltage 76
3.6.3 Fill factor 77
3.6.4 Conversion efficiency 78
CHAPTER 4 : RESEARCH METHODOLOGY 80
4.1 Introduction 80
4.2 Designing of Cells 80

4.3 Simulation Softwares 80
4.3.1 AMPS-1D 81
4.3.2 PC1D 81
4.3.3 wxAMPS 82
4.4 SCAPS-1D 83
4.4.1 SCAPS Parameters 83
4.4.2 Action Panel Interface 84
4.4.3 Interface of Problem Statement 86
4.4.4 Device Structure Panel 86
4.4.5 Output Parameter 87
CHAPTER 5 : DESIGN AND SIMULATION 89
5.1 Introduction 89
5.2 Optimization of $MASnBr_3$ Top Cell 89
5.2.1 Material Parameters for the used ETL Layers in the Top Cell 89
5.2.2 Comparison of the Simulation Results of Different ETL layers 90
5.2.3 TiO_2 Window Layer Thickness Optimization : 91
5.2.4 TiO_2 Window Layer Doping Concentration Optimization : 92
5.2.5 Material Parameters for the used HTL Layers in the Top Cell 93
5.2.6 Comparison of the Simulation Results of HTL layers 94
5.2.7 Cu_2O HTL Layer Thickness Optimization 95
5.2.8 Cu_2O HTL Layer Doping Concentration Optimization 96
5.2.9 Structure of Perovskite Top Cell 97
5.2.10 $MASnBr_3$ Absorber layer Thickness Optimization : 99
5.2.11 $MASnBr_3$ Absorber Layer Doping Optimization 100
5.2.12 $MASnBr_3$ Absorber layer Defect Density Optimization : 101

5.2.13 Effect of Temperature Variation : 102
5.2.14 JV Curve of $MASnBr_3$ Top Cell 103
5.2.15 QE Curve of $MASnBr_3$ Top Cell 104
5.2.16 Effect of Series Resistance (R_s) on $MASnBr_3$ Top Cell 105
5.2.17 Effect of Shunt Resistance (R_{sh}) on $MASnBr_3$ Top Cell 106
5.3 Optimization of c-Si Bottom Cell 107
5.3.1 Structure of c-Si Bottom Cell 107
5.3.2 Thickness Optimization of c-Si (n) Layer 108
5.3.3 Thickness Optimization of c-Si (p) Absorber Layer 109
5.3.4 Carrier Density Optimization of c-Si (p) Absorber Layer 110
5.3.5 JV curve of c-Si Bottom Cell 111
5.3.6 QE curve of c-Si Bottom Cell 112
5.3.7 Thermal Stability of c-Si Bottom Cell 113
5.3.8 $MASnBr_3$/c-Si Tandem Cell : 114
5.4 Optimization of GeTe Bottom Cell 116
5.4.1 Structure of GeTe Bottom Cell 116
5.4.2 Thickness Optimization of GeTe Absorber Layer 117
5.4.3 Carrier Density Optimization of GeTe Absorber Layer 118
5.4.4 JV curve of GeTe Bottom Cell 119
5.4.5 QE curve of GeTe Bottom Cell 121
5.4.6 Thermal Stability of GeTe Bottom Cell 122
5.4.7 $MASnBr_3$/GeTe Tandem Cell 123
5.5 Optimization of $CuInSe_2$ Bottom Cell 125
5.5.1 Structure of $CuInSe_2$ Bottom Cell 125
5.5.2 Thickness Optimization of $CuInSe_2$ Absorber Layer 126

5.5.3 Carrier Density Optimization of $CuInSe_2$ Absorber Layer 127

5.5.4 JV curve of $CuInSe_2$ bottom Cell 128

5.5.5 QE curve of $CuInSe_2$ bottom Cell 130

5.5.6 Thermal Stability of $CuInSe_2$ Bottom Cell :..... 131

5.5.7 $MASnBr_3$/$CuInSe_2$ Tandem Cell 132

5.6 Results and Analysis 134

5.6.1 Comparison between the designed solar cells performance 134

5.6.2 $MASnBr_3$ Cell Performance With and Without BSF Layer 135

5.6.3 Comparison between thermal stability of the designed solar cells..... 137

5.6.3.1 Thermal Stability of $CH_3NH_3SnBr_3$ /Si Tandem Cell..... 137

5.6.3.2 Thermal Stability of $CH_3NH_3SnBr_3$ /GeTe Tandem Cell 138

5.6.3.3 Thermal Stability of $CH_3NH_3SnBr_3$ /$CuInSe_2$ Tandem Cell..... 139

5.7 Comparison between this work and previously published works 140

CHAPTER 6 : CONCLUSION..... 141

6.1 Summary 141

6.2 Key Findings 142

6.3 Limitations and Future Recommendations 143

References..... 144

Appendices..... 155

List of Figures

Figure 1-1 : Global Electricity Production from Solar Cell. 2
Figure 1-2 : Breakdown of Renewable Energy in Total Final Energy Consumption. 3
Figure 1-3: Worldwide Energy Production Capacity by Renewable Sources in 2021. 3
Figure 1-4: (a) Bangladesh's current power production mix. (b) The country's current capacity to generate energy from renewable sources. 4
Figure 1-5 : Emission of Greenhouse Gases. 5
Figure 1-6:Renewable Energy Sources. 6
Figure 1-7 : Renewable Electricity Generation by Energy Source. 6
Figure 1-8 : Worldwide Power Generation. 7
Figure 1-9 : Estimated Renewable Share. 8
Figure 1-10 : Total International Installed Wind Energy Capacity (GW). 10
Figure 1-11 : Status and Possibilities of Geothermal Energy. 11
Figure 1-12 : Schematic of Solar Energy. 12
Figure 1-13 : Working of Solar Panels. 13
Figure 2-1 : Spectrum of Solar Radiation. 16
Figure 2-2 : Classification of Solar Cell. 17
Figure 2-3 : First Generation Solar Cell. 18
Figure 2-4 : A detailed brief of Second Generation Solar Cell. 19
Figure 2-5 : Second Generation Solar Cell. 20
Figure 2-6 : Third Generation Solar Cell. 20
Figure 2-7 : Basic Structure of Tandem Solar Cell 22
Figure 2-8 : The dielectric function's imaginary portion ($\epsilon 2$) for the cubic $CH_3NH_3SnI_3$ perovskite at different temperatures 40
Figure 2-9 : Wave vector, TDOS and PDOS of $CH_3NH_3SnI_3$ 41
Figure 2-10 : (a) The solar device's compatibility with the energy range. (b) Lead-free $CH_3NH_3SnI_3$ solar device. 42

Figure 3-1 : Effect of Photovoltaic on Solar Panel. 55
Figure 3-2 : Photon absorption in a direct bandgap semiconductor. 56
Figure 3-3 : Detailed overview of Fermi-Dirac Function. 57
Figure 3-4 : Energy Band Diagram. 58
Figure 3-5 : Schematic of Intrinsic Semiconductor. 59
Figure 3-6 : Schematic of Extrinsic Semiconductor. 60
Figure 3-7 : Band Diagram of p-n Homojunction. 61
Figure 3-8 : Band Diagram of p-n Heterojunction. 62
Figure 3-9 : Multi-Junction Solar Cell 63
Figure 3-10 : Band Diagram of Metal Semiconductor Junction. 64
Figure 3-11 : Circuit Diagram of Solar Cell. 66
Figure 3-12 : I-V curve of Solar Cell. 66
Figure 3-13 : Surface Recombination Analysis. 68
Figure 3-14 : Optical losses in Solar Cell. 70
Figure 3-15 : Equivalent Circuit of a Solar Cell. 74
Figure 3-16 : Short Circuit Current vs Open Circuit Voltage. 76
Figure 3-17 : Open Circuit Voltage vs Short Circuit Current. 77
Figure 3-18 : Fill Factor. 78
Figure 4-1 : SCAPS−1D Simulator Startup Panel Interface 85
Figure 4-2 Layer Properties Panel 87
Figure 5-1: TiO_2 Window Layer Thickness Optimization 91
Figure 5-2 : TiO_2 Window Layer Carrier Density (N_D) Optimization 92
Figure 5-3 : Cu_2O BSF Layer Thickness Optimization 95
Figure 5-4 : Cu_2O BSF Layer Thickness Optimization 96
Figure 5-5 : Structure of Perovskite Top Cell 97
Figure 5-6 : $MASnBr_3$ Absorber layer Thickness Optimization 99
Figure 5-7 : $MASnBr_3$ Absorber Layer Doping Concentration 100
Figure 5-8 : $MASnBr_3$ Absorber layer Defect Density Optimization 101
Figure 5-9 : Effect of Temperature Variation 102
Figure 5-10 : JV curve of $MASnBr_3$ Top Cell 103
Figure 5-11 : Effect of Series Resistance (Rs) on $MASnBr_3$ Top Cell 105

Figure 5-12 : Effect of Shunt Resistance (Rsh) on $MASnBr_3$ Top Cell 106
Figure 5-13 : Structure of c-Si Bottom Cell..... …..100
Figure 5-14 : Thickness Optimization of c-Si (n) Layer..... 108
Figure 5-15 : Thickness Optimization of c-Si (p) Layer..... 109
Figure 5-16 : Carrier Density Optimization of c-Si (p) Layer 110
Figure 5-17 : JV curve of c-Si Bottom Cell..... 111
Figure 5-18 : Thermal Stability of c-Si Bottom Cell 113
Figure 5-19 : Structure of $MASnBr_3$/c-Si Tandem Cell 107
Figure 5-20 : JV curve of $MASnBr_3$/c-Si Tandem Cell..... 115
Figure 5-21 : Structure of GeTe Bottom Cell 109
Figure 5-22 : Thickness Optimization of GeTe Absorber Layer..... 117
Figure 5-23 : Carrier Density Optimization of GeTe Absorber Layer 118
Figure 5-24 : JV curve of GeTe Bottom Cell 120
Figure 5-25 : Thermal Stability of GeTe Bottom Cell..... 122
Figure 5-26 : Structure of $MASnBr_3$/GeTe Tandem Cell..... 116
Figure 5-27 : JV curve of $MASnBr_3$/GeTe Tandem Cell 124
Figure 5-28 : Structure of $CuInSe_2$ Bottom Cell..... 118
Figure 5-29 : Thickness Optimization of $CuInSe_2$ Absorber Layer 126
Figure 5-30 : Carrier Density Optimization of $CuInSe_2$ Absorber Layer..... 127
Figure 5-31 : JV curve of $CuInSe_2$ Bottom Cell..... 129
Figure 5-32 : Thermal Stability of $CuInSe_2$ Bottom Cell 131
Figure 5-33 : Structure of $MASnBr_3$/$CuInSe_2$ Tandem Cell 125
Figure 5-34 : JV curve of $MASnBr_3$/$CuInSe_2$ Tandem Cell..... 133
Figure 6-1 : Thermal Stability of $CH_3NH_3SnBr_3$ /Si Tandem Cell..... 137
Figure 6-2 : Thermal Stability of $CH_3NH_3SnBr_3$ /GeTe Tandem Cell..... 138
Figure 6-3 : Thermal Stability of $CH_3NH_3SnBr_3$ /$CuInSe_2$ Tandem Cell 139

List of Tables

Table 5-1 : Input parameters for various ETL layers 82
Table 5-2 : Simulation results for various ETL layers 83
Table 5-3 : Input parameters for various HTL layers 86
Table 5-4 : Simulation results for various HTL layers 87
Table 5-5 : Input parameters for various layers of $MASnBr_3$ top cell 90
Table 5-6 : Input parameters for various layers of c-Si bottom cell 99
Table 5-7 : Input parameters for various layers of GeTe bottom cell 107
Table 5-8 : Input parameters for various layers of $CuInSe_2$ bottom cell 114
Table 6-1 : Comparative study between designed solar cells performance 139
Table 6-2 : Summary of the Thermal Stability of the designed solar cells 125
Table 6-1 : Comparative study between designed solar cells performance 139
Table 6-3 : Comparative study between this work and previously published works 139

Nomenclature

List of Symbols and Abbreviations

Symbols

E_g	Band Gap Energy(eV)
E_F	Fermi Level Energy(eV)
α	Absorption Co-efficient (nm^{-1}, cm^{-1})
μ	Mobility of carrier (cm^2 /V-s)
λ	Wavelength of the Photon (nm)
ρ	Density of Charge (C/cm^3)
Φ_b	Height of barrier (eV)
μ_n	Mobility of Electron (cm^2 /V-s)
μ_p	Mobility of Hole (cm^2 /V-s)
χ	Electron Affinity(eV)
σ_n	Cross-section of a Localized State for Capturing an Electron (cm^2)
σ_p	Cross-section of a Localized State for Capturing a Hole (cm^2)
V_{bi}	Built-in Potential (eV)
J_{SC}	Short Circuit Current Density (mA/cm^2)
V_{OC}	Open Circuit Voltage (V)
N_A	Acceptor Carrier Concentration (cm^{-3})
N_V	Donor Carrier Concentration (cm^{-3})
E_c	Energy of the Conduction-band Edge
E_v	Energy of the Valence-band Edge

Acronyms and Abbreviations

I-V	Current-Voltage Characteristics
FF	Fill Factor
ETL	Electron Transport Layer
HTL	Hole Transport Layer
ITO	Indium Tin Oxide
PCE	Power Conversion Efficiency
GeTe	Germanium Telluride
BSF	Back Surface Field
c-Si	Crystalline Silicon
TCO	Transparent Conductive Oxide
GHG	Greenhouse Gases
TiO_2	Titanium Dioxide
AZO	Aluminium-Doped Zinc Oxide
SCAPS	Solar Cell Capacitance Simulator
AMPS	Analysis of Microelectronic and Photonic Structure
AM	Air Mass

CHAPTER 1 : INTRODUCTION

In the current energy landscape, solar cells play a critical role by providing clean, renewable electricity that outperforms fossil fuels in several important aspects. They offer an environmentally beneficial substitute for scarce fossil fuels by sustainably harvesting sunlight, producing no pollutants or greenhouse gasses while in use. In addition to improving energy security and minimizing the impact on the environment, this also lessens reliance on unstable fossil fuel sources. Furthermore, by increasing employment and becoming more cost-competitive, the solar business boosts the economy. Continuous research in solar cell technology encourages innovation by increasing affordability and efficiency which also supports global development efforts by providing electricity access in distant locations. In general, solar cells are essential to the progress made towards a future with more resilient and sustainable energy sources.

1.1 Motivation

Solar cells, sometimes referred as photovoltaic cells, are vital for their role in producing renewable energy, diversifying energy sources, permitting off-grid applications, enabling decentralized production, integrating into urban infrastructure, creating jobs, propelling technological advancements, improving the environment and advancing equitable access to and use of energy. In conclusion, solar cells are essential for promoting economic growth, environmental preservation, energy security and sustainable development in the contemporary world.

There are several strong arguments in favor of using solar cells as a renewable energy source rather than their non-renewable alternative. Primarily, solar energy represents environmental sustainability since it is a clean, environmentally friendly power source that reduces the damaging emissions of pollutants and greenhouse gases linked to conventional fossil fuels. Utilizing the sun's abundant and boundless energy, solar power offers an almost endless source of renewable energy.

Additionally, because of ongoing technology advancements and business economies of scale, solar power has increased dramatically. Solar photovoltaic (PV) systems expenditures has significantly decreased as a result of these developments, boosting the accessibility and affordability of solar energy for a wide range of applications, from large-scale utility installations to residential rooftops.

Moreover, one characteristic that distinguishes solar energy and emphasizes its adaptability and versatility in a range of environments and deployment scales is its scalability. Solar PV systems offer flexibility and customization to satisfy a range of energy needs. They can be designed as independent installations or seamlessly incorporated into the infrastructure that already exists.

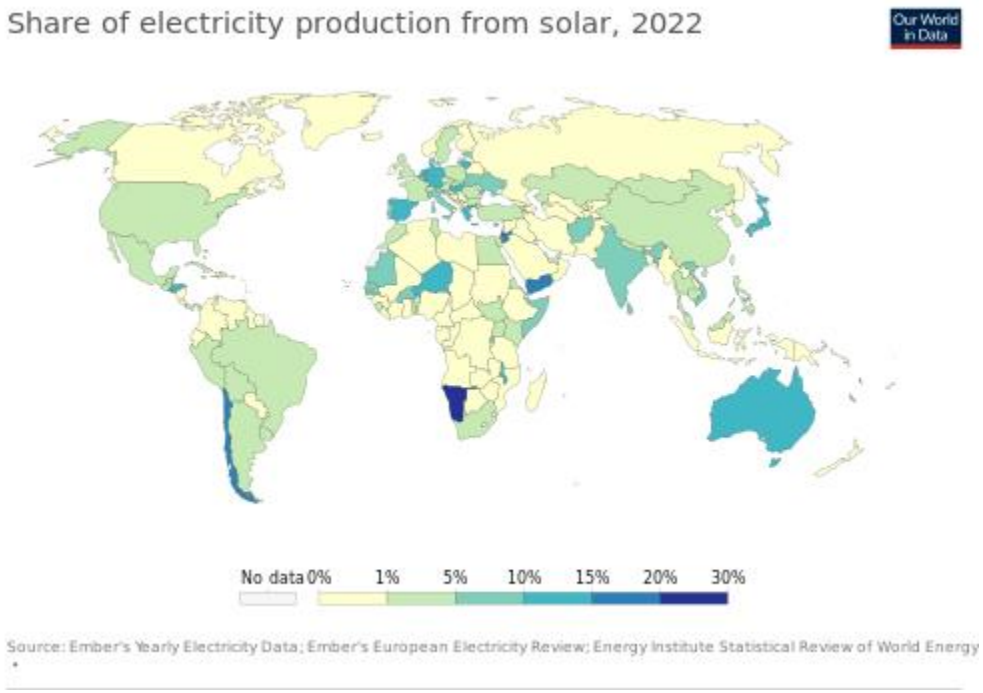

Figure 1-1 : Global Electricity Production from Solar Cell [1].

Apart from its affordability and expandability, solar energy also has low maintenance needs and low running expenses, which makes it a hassle-free and financially feasible energy option. Solar PV systems may work effectively even in distant or off-grid settings, offering energy independence and security. This adds to the appeal of solar power.

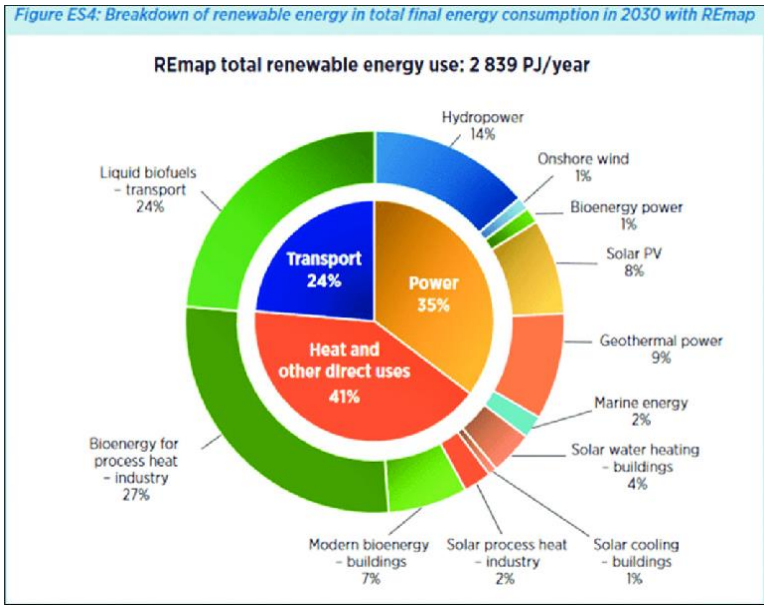

Figure 1-2 : Breakdown of Renewable Energy [2].

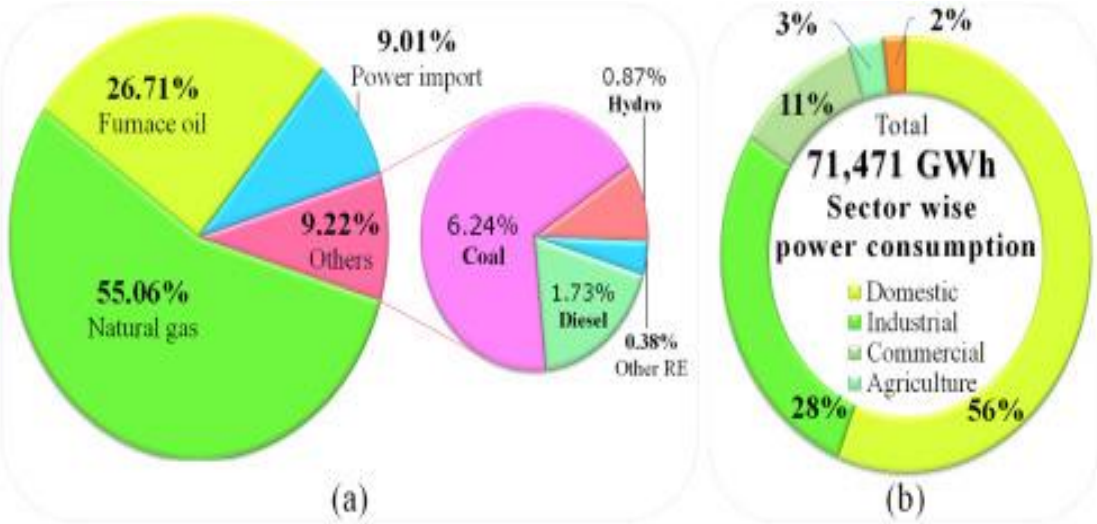

Figure 1-3: Worldwide Production of energy Capacity by Renewable Sources in 2021 [3].

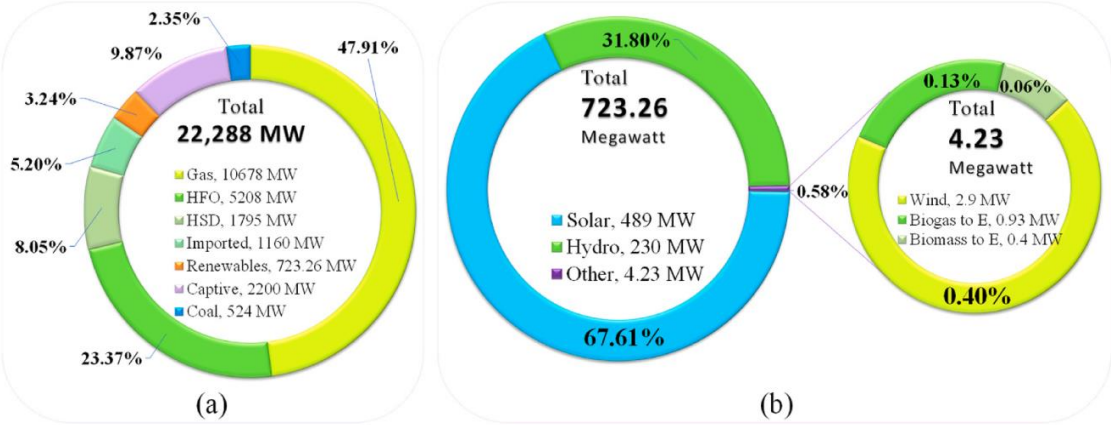

Figure 1-4: (a) Bangladesh's current power production mix. (b) The country's current capacity to generate energy from renewable sources [3].

Ultimately, solar energy represents a robust and sustainable substitute for traditional fossil fuels in the production of electricity, providing a route towards more sustainable, greener and cleaner future in energy. The promise of solar energy as a revolutionary force in the global energy landscape is becoming more and more clear as solar technology advances, opening the door to a more sustainable and brighter future.

1.1.1 Emissions of Greenhouse Gases

Earth's atmosphere includes greenhouse gases, which are one of the main drivers of environmental degradation and warming worldwide. The major greenhouse gases released by human activities are a mixture including (CO_2), (CH_4), (N_2O) and gases that contain fluorine. In order to provide energy, fuel for transportation, industry and deforestation, fossil fuels must be burned. This produces CO_2. Landfills, agriculture, livestock digestion and the extraction of fossil fuels are among the causes of methane emissions. Both industrial and agricultural processes release nitrous oxide into the atmosphere.

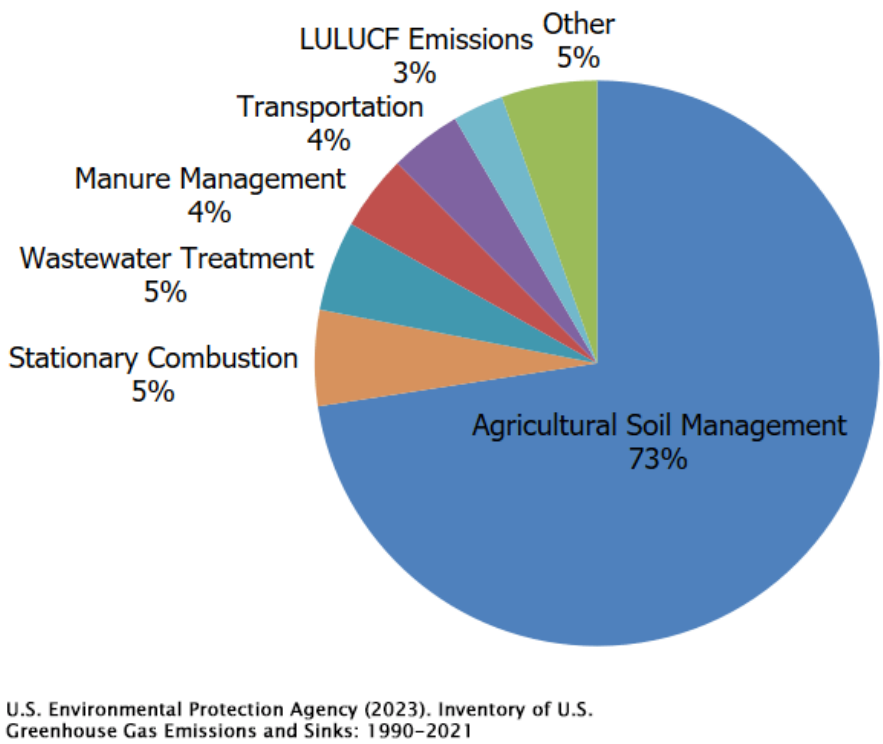

Figure 1-5 : Emission of Greenhouse Gases [4].

Furthermore, the usage of fluorinated gases in a range consisting industrial applications raises the emissions of greenhouse gases. The burning of fuels, factory production, deforestation and agriculture are some of the human activities that cause these gases to be emitted into the atmosphere. As a result, they retain solar radiation, raising global temperature and causing climate change. To minimize the impacts of it and its negative consequences on the environment, ecosystems and human societies, it is essential to minimize greenhouse gas emissions.

1.1.2 Renewable Energy Sources

Longer-term sustainability and frequent renewal are possible with these sources. The following energy sources are considered sustainable: wind, solar, tidal, biomass, nuclear, geothermal and wave. The globe is going to anticipate a new standard of carbon emission , in that way carbon will be useful to develop new products in the industries, because renewable energies are less polluting.

Both they and the items they produce will be assessed based on the amount of carbon emissions. [1]

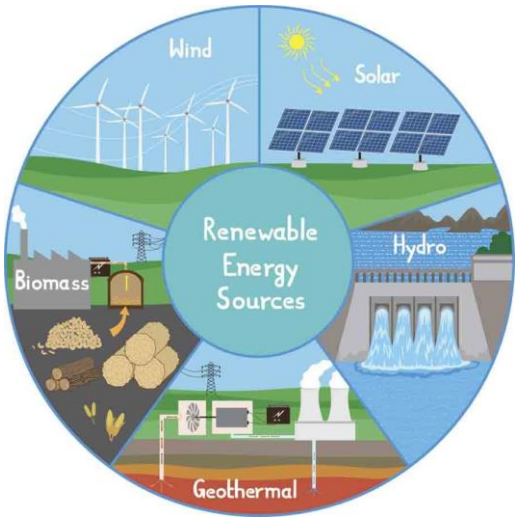

Figure 1-6:Renewable Energy Sources [5].

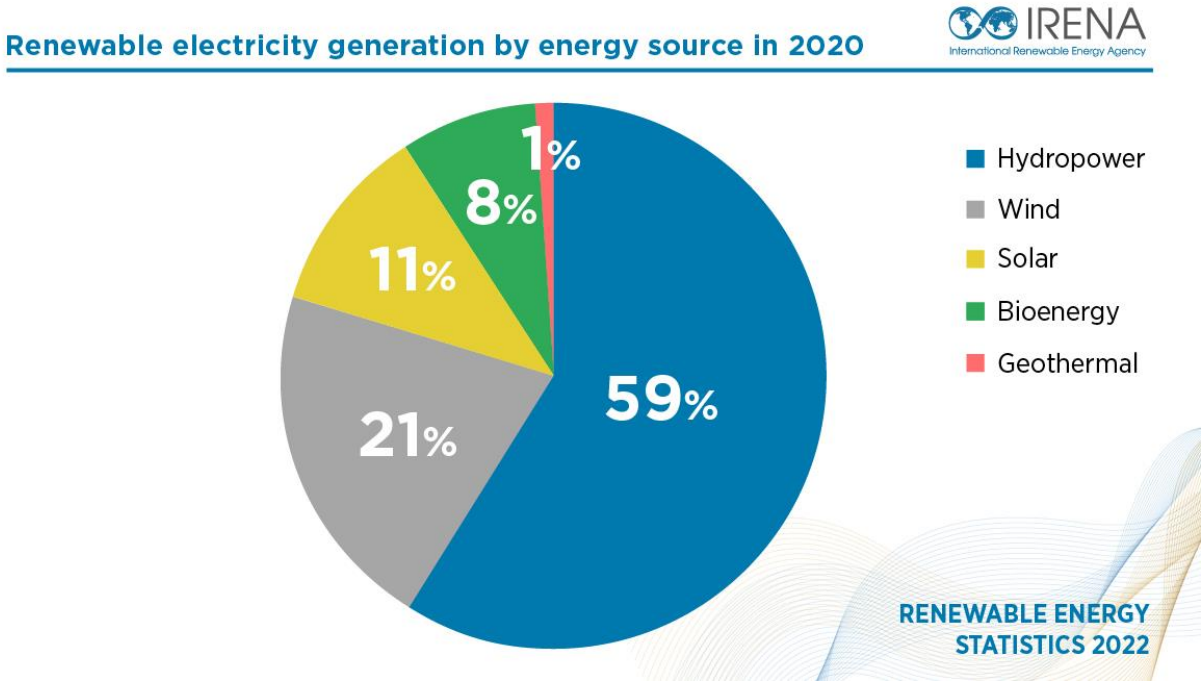

Figure 1-7 : Renewable Electricity Generation by Energy Source [6].

Reducing global warming is mostly dependent on utilizing renewable energies to satisfy the required demand for electricity. In the heating and transportation sectors, the substitution of

electricity produced from renewable sources for fossil fuels, particularly natural gas and oil, can also aid in lowering carbon dioxide emissions. The current structure must be modified to make the use of energy for the growing coupling of sectors economically appealing in order to facilitate this development. Still, for many years to come, traditional energy sources will be crucial. Thus, it's critical to keep raising energy efficiency and advancing CO_2 utilization and carbon capture and storage technology in addition to growing renewable energy sources.[2]

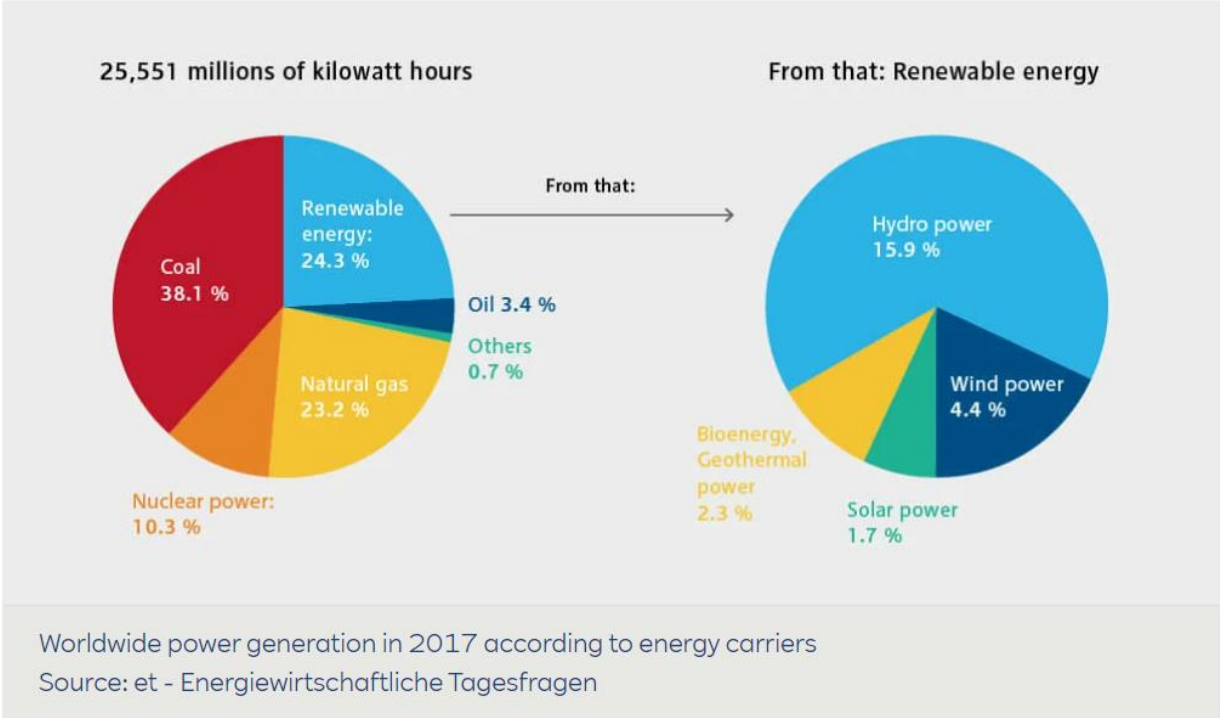

Figure 1-8 : Worldwide Power Generation [7].

The cumulative effect of all the expansion and financial outlays in renewable energy is beginning to show. According to the graph below, renewable energies account for almost 26% of the world's electricity production and more than one-third of installed capacity worldwide.

However, with hydropower accounting for about 16 percent, over half of the energy comes from renewable sources. Wind and solar, which are commonly associated with renewables, account for only 8% of the total. Renewables have a long way to go, even in the power sector.[3]

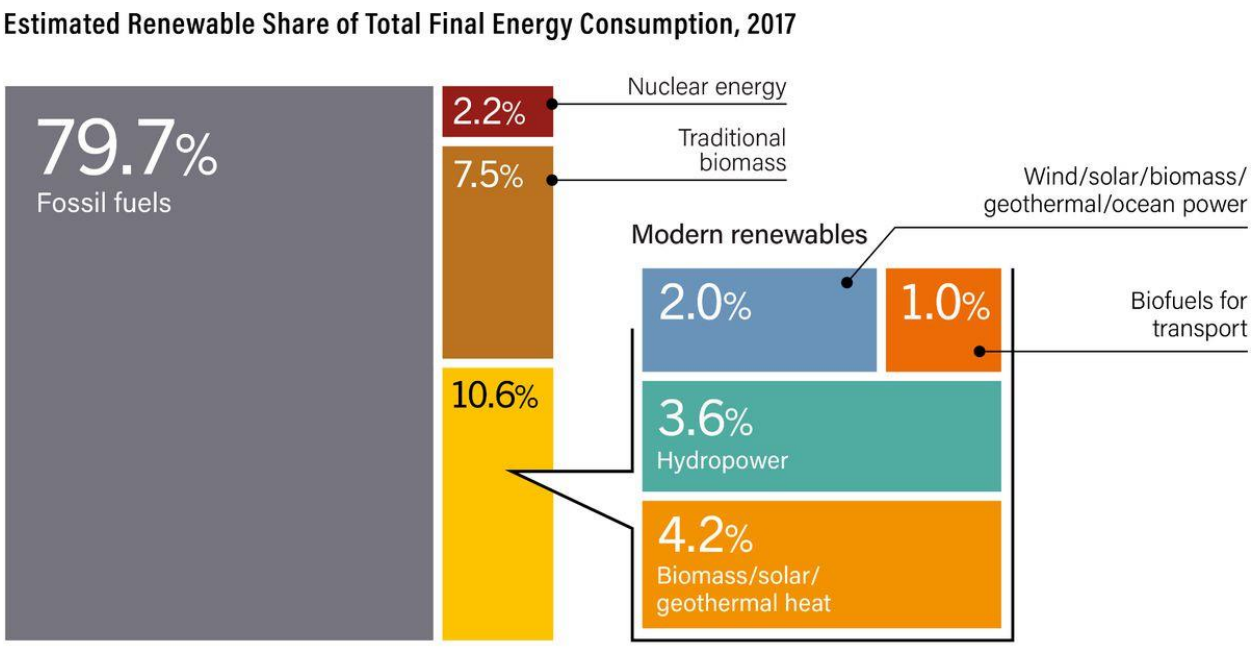

Figure 1-9 : Estimated Renewable Share [8].

1.1.3 Status and Possibilities of Hydroelectric Power

The environmental problems are connected to use of the fossil fuels that generate electricity have made energy planners look more and more for sustainable alternatives [1]. Hydropower has gained attention as a long-standing energy source that is used globally, particularly in isolated areas [4]. Bangladesh has a large number of rivers, yet it mostly depends on fossil fuels to supply its energy demands [5]. The potential for hydropower worldwide is also covered. Bangladesh's best bet for sustainable energy is small-scale hydropower, according to economic and environmental evaluations. Approximately 232 rivers in Bangladesh have the potential to generate small-scale hydropower at suitable flow rates, improving the security of electricity in isolated regions [4].

1.1.4 Status and Possibilities of Biomass Energy

International commodities markets are quickly emerging for the markets for biomass used in industry for energy purposes. It is challenging to determine the volumes of biomass that are traded internationally for energy purposes for a number of reasons, including difficulties with the summary of relevant statistics. Although there are distinct market overviews for ethanol and

pellets, there are no thorough statistics and summaries that combine different biomass streams [6]. Most industrial heat derived from biomass is generated through combustion, while commercially accessible gasification systems are also utilized. Combined heat consisting of power production predominantly relies on the steam cycles. Biomass exhibits versatility in meeting the diverse temperature requirements of various industries [7]. Exploring additional, more efficient and alternative applications for biomass is imperative. Industries producing solid biomass byproducts commonly employ biomass-fired systems. However, challenges include significant initial investment, competition with fossil fuels and limitations in feedstock availability. Despite Europe’s near-balance between solid biomass production and consumption, resource pressure continues to mount [8]. As such, it is imperative that sustainability be taken into account and that resources be closely observed. [6]

1.1.5 Status and Possibilities of Wind Energy

Wind energy has a substantial and quickly changing worldwide status and potential. Nowadays, wind energy is a pretty popular renewable energy sources, that contributes significantly to global production of electricity [9]. To diversify their energy sources, lower their greenhouse gas emissions and improve energy security, nations all over the world are investing in onshore and offshore wind projects. Technological developments have reduced prices and increased wind energy's competitiveness versus fossil fuels. Examples of these developments include enhanced turbine efficiency and design [10]. Furthermore, because wind farms are so adaptable, they may be installed in a variety of locations, including coastal and urban areas.

Wind energy will keep on playing a comprehensive role in tackling the effects of climate change and fulfilling global energy demands with further innovation, supportive policies, and investments [11].

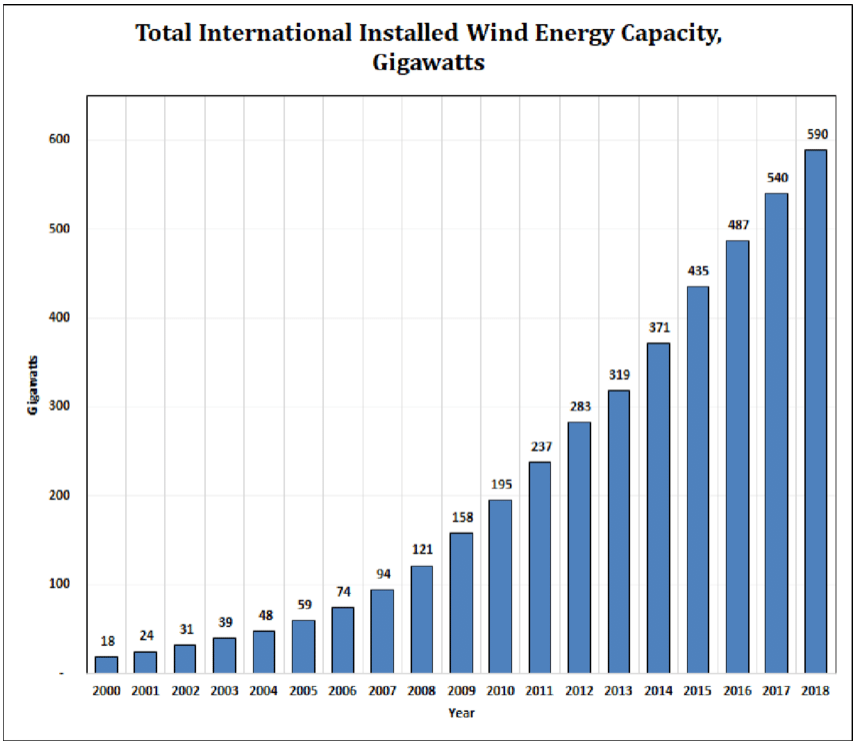

Figure 1-10 : Total International Installed Wind Energy Capacity (GW) [14].

1.1.6 Status and Possibilities of Geothermal Energy

The globe consumes around 400 EJ of primary energy annually, with fossil fuels accounting for 80% of this total. Renewables account for 14% of primary energy, including traditional biomass (10%), major hydropower facilities (>10MW) (2%), "new renewables" (2%) [12]. Nuclear sources currently contributes around 6% to the global energy mix. The World Energy Council predicts a substantial increase in global primary energy consumption by 2050, ranging from 50% to 275%, depending on various scenarios. Renewable sources are being expected to contribute between 20% and 40% in primary energy by 2050, and this contribution could rise to 30% to 80% by 2100. Remarkably, renewables have a technical potential of 7600 EJ/year, that is better than sufficient to meet world's future energy requirements [13].

Geothermal fields in most countries exhibit low to medium enthalpy, with temperatures ranging from less than 100°C to 150°C. However, Turkey, Iran, and Yemen stand out with high enthalpy geothermal fields exceeding 150°C [14]. CO_2-circulated technologies are recommended for

effectively utilizing low to medium enthalpy based geothermal resources in the MECs (Middle Eastern countries) in residential, agricultural, and manufacturing processes [12]. For nations that are lacking mineral reserves, leveraging geothermal energy can be a very promising solution to satisfy their energy requirements while simultaneously reducing climate change impact as well as air pollution impacts [14].

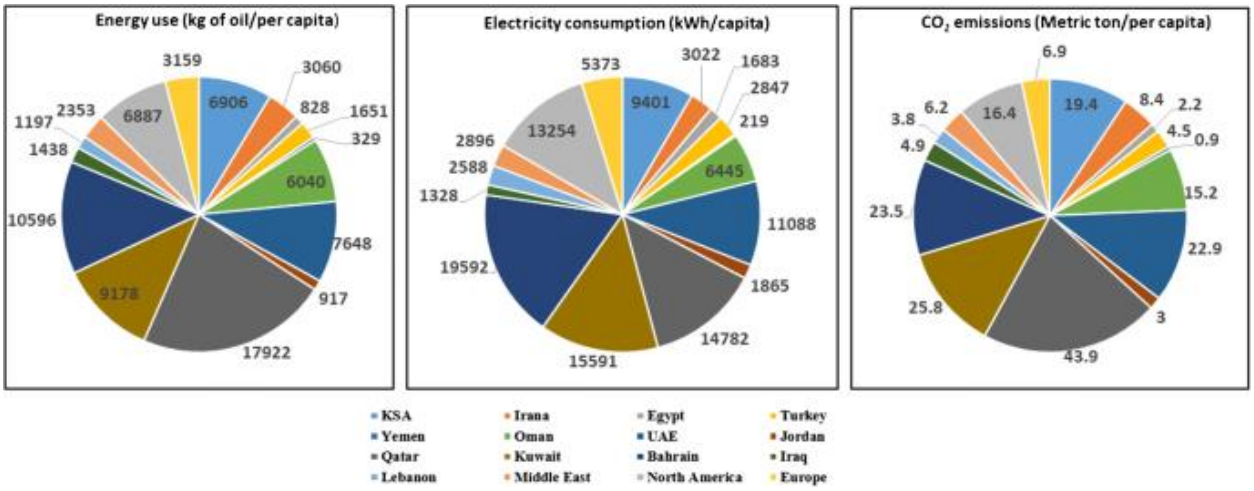

Figure 1-11 : Status and Possibilities of Geothermal Energy [18].

1.1.7 Solar Energy

Heat, electricity and chemical processes can all be triggered by solar energy, which is produced by the sun's radiation. Our present and future energy needs are greatly outweighed by the solar energy which reaches earth. It is possible to meet world's energy requirements if this plentiful but widely distributed resource is properly utilized. Comparing solar energy to finite fossil fuels like coal, oil, natural gas as well as its endless supply and eco-friendliness, makes solar energy a more appealing renewable energy option in the twenty-first century. [15]

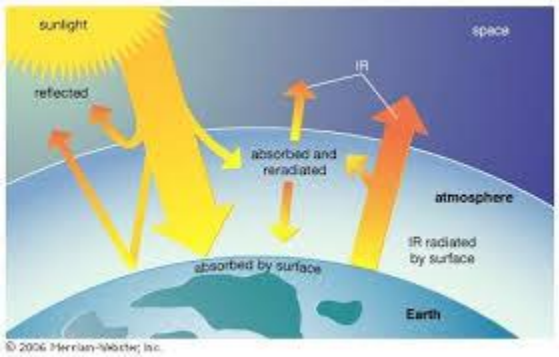

Figure 1-12 : Schematic of Solar Energy [19].

Even though it is plentiful, the intensity of sunlight at the Earth's surface is quite modest. Nonetheless, it continues to be a powerful energy source because of the vast radial radiation from the far-off Sun. Up to 54% of incoming sunlight can be absorbed or scattered by clouds and the Earth's atmosphere, with only a small amount of additional light being lost. Around half of sunlight which goes to Earth is visible light, with the remaining half being made up primarily of infrared radiation with traces of ultraviolet and other electromagnetic radiation. [16]

The fact that our planet receives sun energy that is considered as equivalent to over 200,000 times that is more than world's daily capacity of electricity generation means that solar energy inherits outstanding potential. Yet, the high costs connected with solar energy's generation, conversion and storage continue to prevent solar energy from being widely used, even with its inherent affordability. Both electrical as well as thermal energy can be produced from solar energy, but the former is easier to do. [17]

The process of turning solar energy into useful power is how solar power works. For human use, the sun produces two forms of energy: heat and electricity. The main source for both of these energy sources is solar power, whether it is found on large "solar farms" or rooftops of homes. [18]

Silicon and other semiconductor materials are commonly used in solar panels. After that, these panels are placed inside a metal frame and have glass covering them. Photons, which are little energy packets from sunlight, interact with semiconductor materials to liberate electrons and produce an electric charge. Direct current (DC) generated by the photovoltaic (PV) effect is the

electric current that is detected by the wiring inside solar panels. AC electricity is subsequently produced by an inverter from DC electricity. Standard wall outlets use an electrical current known as AC [19].

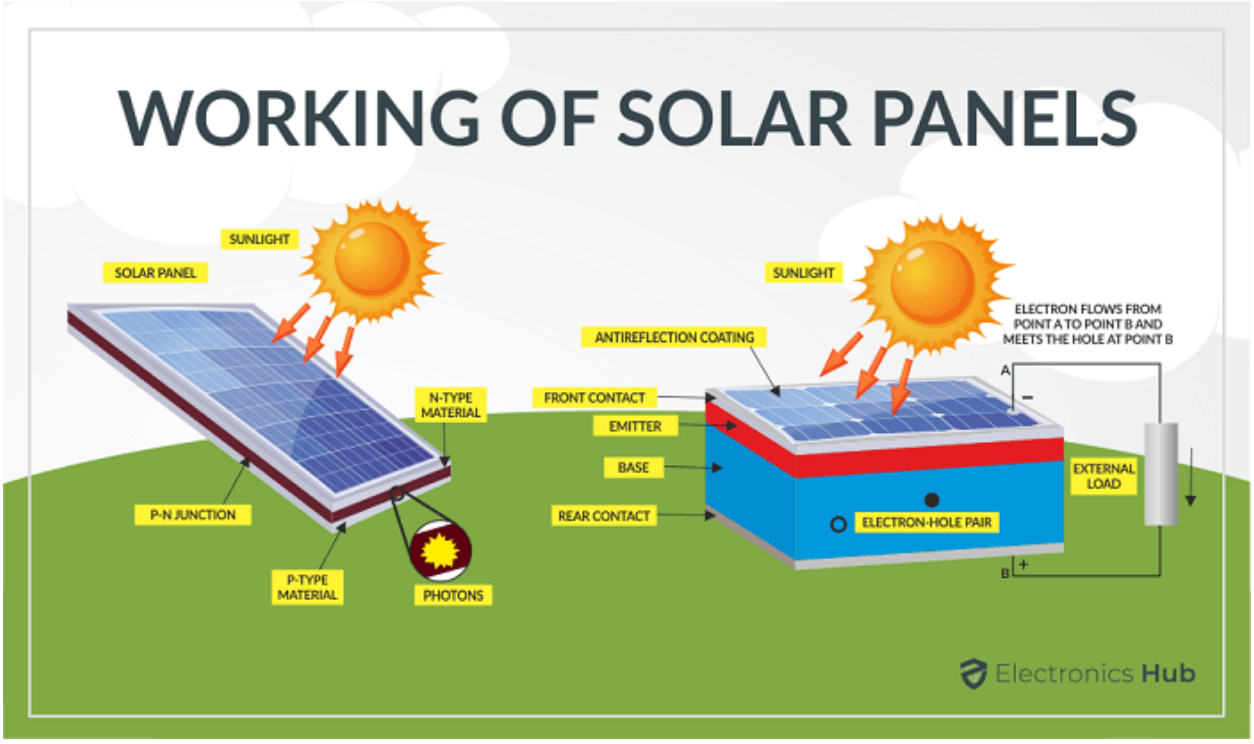

Figure 1-13 : Working of Solar Panels [22].

1.2 Cells, Significance, Scope and Definitions

In the solar related power device, the solar cell is the smallest part. For a solar panel, several sun cells are combined. Photovoltaic systems primarily rely on solar cells as its power producing element. [20] Large-area semiconductor diodes are what solar cells are in actuality. Electric current is produced from light energy, or photon energy, thanks to photovoltaic effect. Photovoltaic cells that are another name for solar cells. They produce electricity by converting light energy [21].

Climate change, a issue is largely attributed to human actions over the past two centuries, especially the use of fossil fuels, for energy generation. Many countries are now turning to sources,

like wind power to address this challenge [22]. Since the 1950s, technological developments have significantly increased the cost and efficiency of solar panels, making them a competitive option for producing clean energy. The field of solar photovoltaics (PV) has experienced significant growth, with installation numbers rising worldwide and costs falling [23].

Solar panels use silicon semiconductors of p type as well as n type. P type layer of silicon is made by introducing materials like boron or materials like gallium which consist one electron in its energy level than (Si). As a result boron doped silicon begins to create electron vacancies known as "holes." In contrast n type silicon is formed by incorporating elements like phosphorus, which have an extra one electron, within their level compared to (Si) [24]. Silicon that has been doped with phosphorus establishes bonds with nearby silicon atoms, but the extra electron is free to roam throughout the silicon lattice [25].

Electrons accelerates from n-doped layer, towards the holes of p-doped layer at the junction of these two layers, in a cell because of how p type as well as n type silicon layers are positioned.[26] An internal electric field forms, around the junction due to the build up of positively charged molecules on one part and negatively charged molecules, on the region creates the depletion zone [27].

The action of sunlight causes holes in silicon of the photovoltaic solar cell by releasing electrons. In case this occurs inside electric field, electrons will accelerate towards n-doped layer also holes towards the p-doped layer. Following that, the electrons exit the depletion zone and create an electrical current that eventually converts to electricity when they come into touch with a metallic wire [28].

CHAPTER 2 : LITERATURE REVIEW

2.1 A Concise Look at the Evolution of Solar Cell Technology

Nowadays, most solar cells which are sold in the market are made of silicon, either mono-crystalline or multi-crystalline, and have an efficiency of roughly 10% to 16%. Although efficiencies of over 20% have been shown in lab tests, these technologies are still more expensive than other power generation methods, hence attempts to lower production costs are required. When weighed against thin-film silicon-based devices, amorphous silicon-based devices are more cost-effective to manufacture. Their efficiency is still lower, usually less than 10%, which could restrict the amount of money that can be saved [29]. The goal of hybrid technologies, such as the HIT cell, is to retain high efficiency while reducing production costs. These III-V compounds are good for space applications and concentrator systems, but they are costly and contain components that could be hazardous or rare [30].

Thin-film solar cells, like the ones that use CdTe and also $CuGaInSe_2$, offer significant cost savings over crystalline silicon technology. Future advances in solar technology may include the use of organic materials, nanotechnology and tandem/multijunction devices to maximize solar spectrum usage. Furthermore, the solar business demonstrates its dedication to environmental sustainability by emphasizing recycling, lowering greenhouse gas emissions and limiting environmental effect [29].

2.1.1 The Sun's Spectrum

The solar spectrum encompasses the electromagnetic energy emitted by sun, spanning wavelengths from ultraviolet (UV) to infrared (IR) . Photons of different energies and wavelengths make up its constituents, which determine its intensity and form. UV, visible and infrared (IR) are the three primary sections into which the spectrum is usually divided. Photon energies in UV light, which have wavelengths less than 400 nm, range from 3 to 5 electron volts (eV). Photons having energy between (1.8 and 3) eV are found in the visible spectrum, which spans (400 to 700) nm.

By comparison, photon energies in the infrared region range from around 0.35 eV to 1.8 eV and wavelengths longer than 1000 nm are included in this region [31].

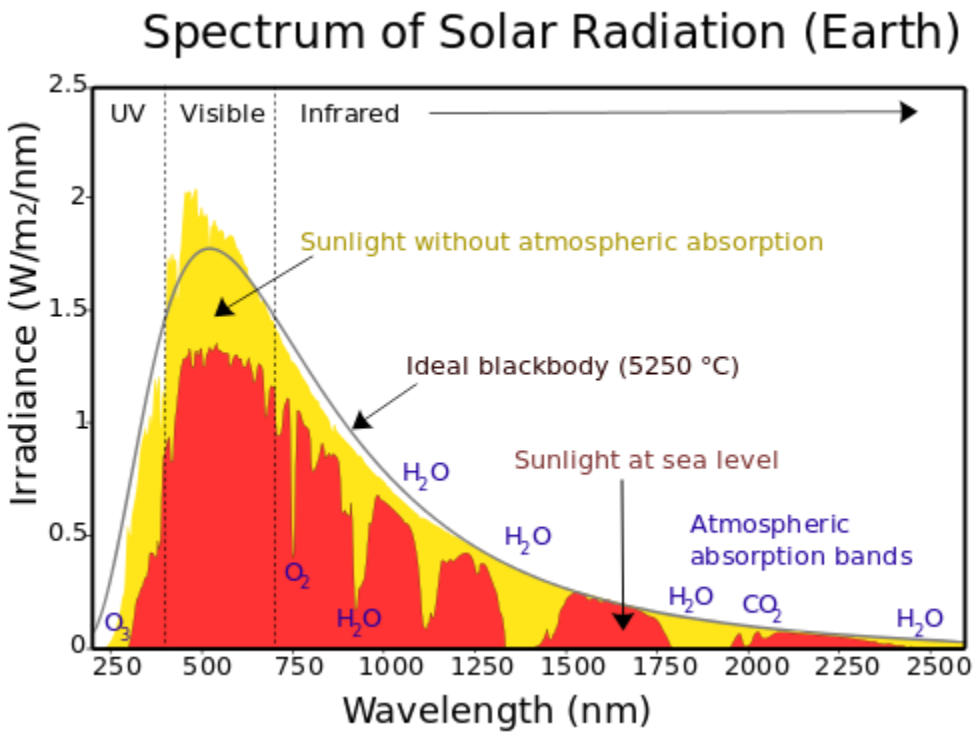

Figure 2-1 : Spectrum of Solar Radiation [36].

Factors such as the Earth-Sun distance, sunlight angle, air pollution levels and weather patterns affect how intense the solar spectrum is when it reaches Earth. The form and intensity of the spectrum significantly affect solar cells, that are made to turn solar radiation into electrical power. To optimize the effectiveness and efficiency of solar cells, scientists and engineers must possess a comprehensive grasp of solar spectrum. As a result, it's crucial to take into account when designing and implementing solar cells [31].

2.1.2 Concentrated Solar Power and Photovoltaic Solar

Theoretically within the most abundant energy supply on earth surface, solar energy represents a substantial alternative to fossil fuels. There are two different ways to convert this energy into electricity: thermodynamic cycles along with photovoltaic conversion. Solar thermal technological advances, often referred to as thermodynamic solar technologies, have gained significant traction and are considered extremely promising alternatives. They function at both medium and high temperatures, typically 500°C and roughly 1000°C [32].

2.2 Global Expansion of PV

2.2.1 Different Generations of Solar Cells

Solar cells come in first, second, and third generations, all of which are named by the semiconducting substance used in them [33].

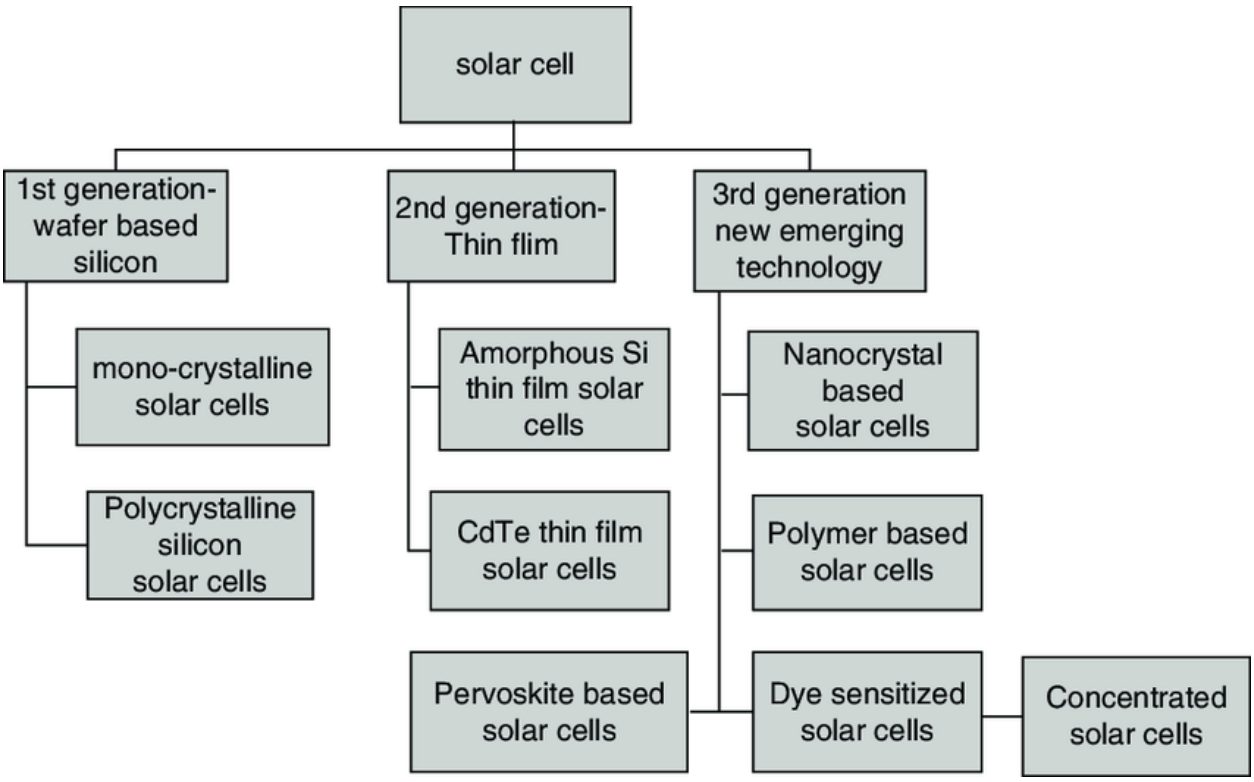

Figure 2-2 : Classification of Solar Cell [39].

2.2.2.1 First-Generation Solar Cells or Crystalline Silicon Cells

Crystalline silicon (c-Si) encompasses various silicon crystal types, including polycrystalline silicon (poly-Si) (composed of multiple small crystals) and monocrystalline silicons. It serves as the primary semiconductor materials in the photovoltaic technology, particularly for creating solar cells. Additionally, monocrystalline silicon is used in electronics for manufacturing microchips. The silicon used for microchips has significantly lower impurity levels compared to that required for solar cells. The production process involves chemical process of purification to create ultra-pure polysilicon, which is followed by the recrystallization to create monocrystalline silicon. Solar cells which are made from crystalline silicons are considered to as conventional or first-generation cells. The photovoltaic systems that these cells are incorporated into allow for the solar electricity to be harvested from sunlight. Crystalline silicon, which is usually found in its monocrystalline form and has fewer imperfections than needed for the creation of solar cells, is used to create microchips in electronics [34].

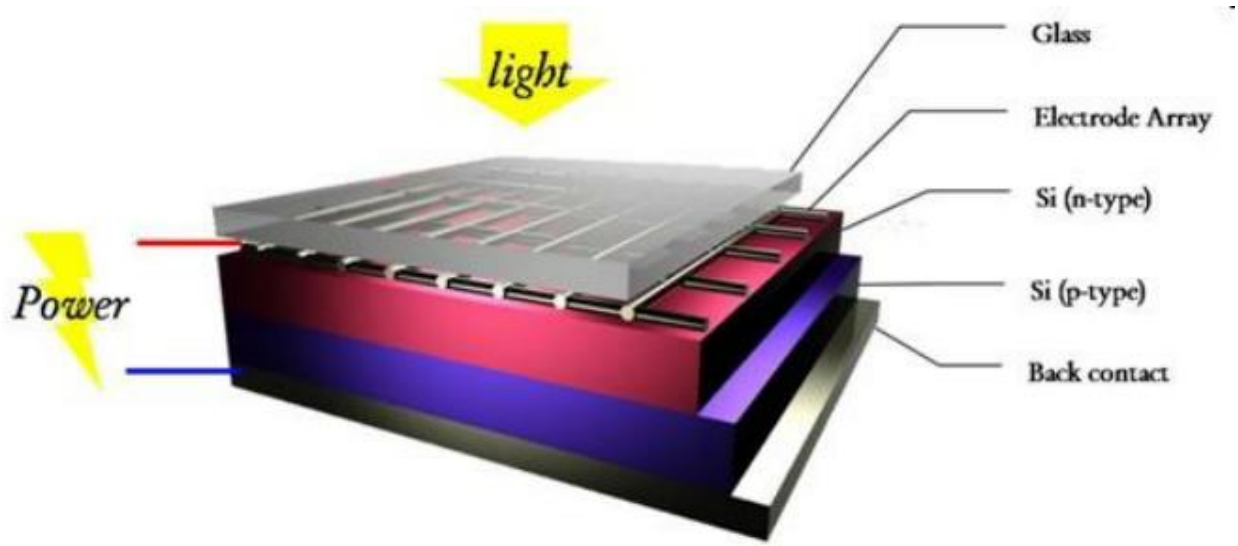

Figure 2-3 : First Generation Solar Cell [41].

Chemical purification is used in the production process to produce hyper-pure polysilicon, which is further refined through recrystallization to produce silicon suitable for semiconductors. Wafers are created by further processing the ensuing cylindrical boules [33].

2.2.2.2 Second-Generation Solar Cells or Thin Film Solar Cells

Type	Efficiency	Advantages	Disadvantages
a-Si	• 4%–8% for modules placed on the market • Small cells in lab can reach 12% [14]	a-Si solar cells are the cheapest on the market	• The layers are much thinner and there is less material to absorb solar radiation compared to sc-Si and mc-Si hence, the efficiencies of thin-film solar modules are lower than crystalline ones • Degradation in their power output (in the range 15%–35%) when exposed to the sun [11]
GaAs	• 29% record efficiency in laboratory [15] • The band gap is 1.43 eV	High efficiency and less thickness than silicon ones	High cost
CdTe	• 10%–15% • (21% record efficiency) [15] • The band gap is 1.45 eV	CdTe cells can exploit a broader wavelength spectrum than Si cells, close to the natural one. Low costs, as cadmium is abundant and generated as a by-product of important industrial materials like zinc	Cadmium by itself is one of the most toxic materials known, and cadmium telluride has some toxic properties
CIGS	• 20% • (under certain conditions) • The band gap is 1.68 eV	• Process is less energy intensive than manufacturing of the crystalline silicon solar cell • Good resistance to heat	• Less efficient than Si solar cells • CIGS cells use toxic chemicals • Currently very expensive to produce

Figure 2-4 : A detailed brief of Second Generation Solar Cell [42].

The second emergence is considered to as thin-film solar entities. Those cells are produced by applying one or multiple thin levels of the photovoltaic material into a substrate made of glass, plastic, metal etc. Some of the commercially available materials consisting cadmium telluride (CdTe), copper indium gallium diselenide (CIGS) as well as amorphous thin-film silicon [35].

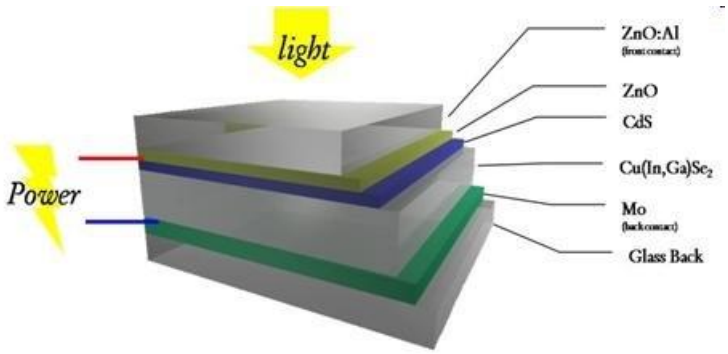

Figure 2-5 : Second Generation Solar Cell [44].

In 1970s, American scientists began developing solar cells named as thin film [25]. These panels provide a practical way to collect solar energy and can be used for a number of things, including lighting street lamps, traffic signals, parking lots and woodland areas. Solar cells named as thin film are significantly more cost-effective compared to traditional silicon wafer cells [33].

2.2.2.3 Third-Generation Solar Cells

New developments in solar cell technology combine the benefits of crystalline or thin-film solar cells to increase usability and efficiency. Several junctions with various semiconducting materials, such as amorphous silicon, organic polymers, or perovskite crystals, are frequently used in these technologies [33]. Third-generation systems usually use gallium arsenide or amorphous silicon multi-layer cells [36]. One theoretical advancement is frequency conversion, which improves power generation by transforming unusable light frequencies into ones that may be used [33].

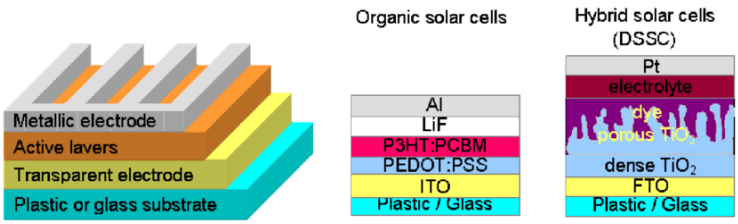

Figure 2-6 : Third Generation Solar Cell [36], [37].

Furthermore, these technologies are refined by methods like multiple-carrier ejection and hot-carrier effects. In contrast to first-generation manufacturing processes that favor high-quality, single-crystal PV devices, albeit with energy- and time-intensive procedures to attain near-limit efficiencies for single-bandgap devices, this makes it easier to install photovoltaic systems widely [37].

2.3 Single Junction Solar Cells

A single layer made from semiconductor material like silicon, is utilized to create a single junction solar entity. Through a mechanism called photovoltaic effect, photovoltaic cell can turn sunlight into usable electricity. Single junction solar cells are commonly available and quite easy to fabricate. They are employed globally in many different applications and are a significant element of renewable sector. The p-n junction connection which is a part of single-junction photovoltaic cell facilitates the current flow that happens when sunlight strikes a semiconducting substance [38].

While single junction photovoltaic cells can receive light throughout a broad spectrum, they are particularly effective at converting light within a certain wavelength range. Because of this, depending to the particular material, they can usually convert 15% to 20% of the energy in sunshine into electricity [39].

2.4 Tandem Solar Cells

A stack of various solar cells at top one another is what tandem cells are in essence. This arrangement will allow us to harness more solar energy. To maximize solar energy absorption, we may place a solar cell that performs exceptionally well at absorbing blue light adjacent to one that performs similarly well at absorbing green and red light. Let say red, blue, and green light are combined to create all the colors that are needed on TV and computer screens, if you look at how they are made. A white light can be created by utilizing all three of them. In the other hand, we

need to gather all three of the colors-blue, red, and green-if we wish to gather all of the visible white light [40].

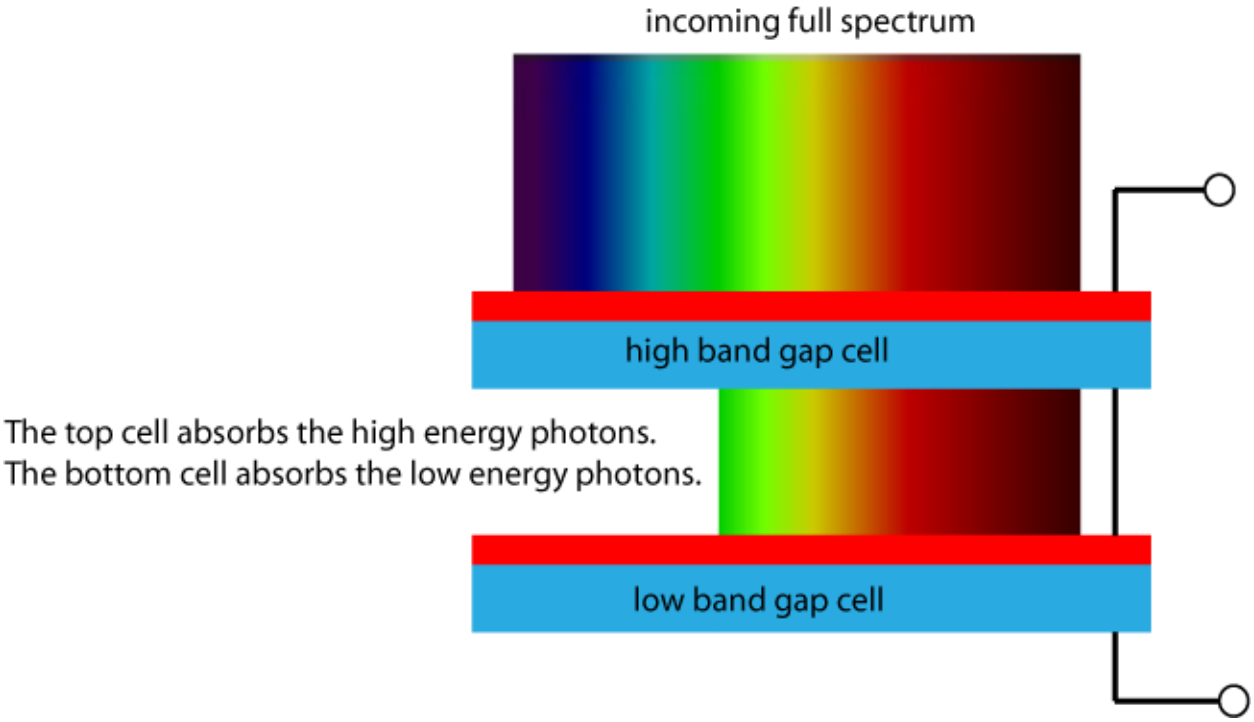

Figure 2-7 : Basic Structure of Tandem Solar Cell [40] .

The "Shockley-Queisser limit" refers to the highest efficiency that certain solar cell types, referred to as "single-junction cells" (silicon, for example), can ever achieve. Upon closer inspection, we can observe that photons, or individual light particles, possess a spectrum of wavelengths and consequently, energy. It is for this reason that rainbows can occasionally be seen when it rains: the water divides the sunlight into its various colors and each color has a unique wavelength. Infrared and ultraviolet light are two further portions of the solar spectrum that are invisible to the human eye [40].

When the cells are being stacked one into as on top to the other, it matters which way they go. The semiconductor material that absorbs blue light has a broader band gap that is more than green or red light due to its higher energy. Also semiconductor material having smaller band gap is better at absorbing red light. Blue light can also be absorbed by this substance, but doing so is energy-consuming. It is a waste of time and effort, similar to building a bridge over a minor brook that

you could easily step over. In order to eliminate this energy and maximize the benefits of sunlight, light must first reach the blue light absorber. The green and red light, on the other hand, will not have sufficient energy to cross this band gap and will instead pass along to the next layer. Here, the red light can continue through to a third layer while the green light which has the next-highest energy can be absorbed. You may maximize the benefits of the sun by doing this [40].

Tandem arrangements, which consist of two or more cells, are made so that the succeeding cells can absorb most of the solar radiation. These kinds of arrangements are thought to be the most sought-after solutions for producing solar electricity at a lower cost by boosting efficiency over the single junction cells' theoretical limitations. Modern single junction silicon solar cells, which lead the market today, have been developed over the course of more than 60 years and as a result, their efficiency at the laboratory size is approximately 25% [41].

2.5 Best Researched Cell Efficiency

The greatest verified conversion efficiencies regarding the research cells across a wide range of Photovoltaic technologies are displayed in an updated version of NREL's Best Research-Cell Efficiency Chart. With the interactive interface of this latest version, users may create personalized charts that highlight particular technologies or historical periods and access research data spanning several decades. Depending on the information that is now available in NREL's records, users can now examine details like efficiency along with current, voltage output, and fill factor. The chart is noteworthy because it shows a record-high researched cell efficiency of 47.1% . This is a contrast to the constant efficiency improvement observed in silicon solar cells during the 1980s and emphasizes current improvements in new technologies like perovskite solar cells [42].

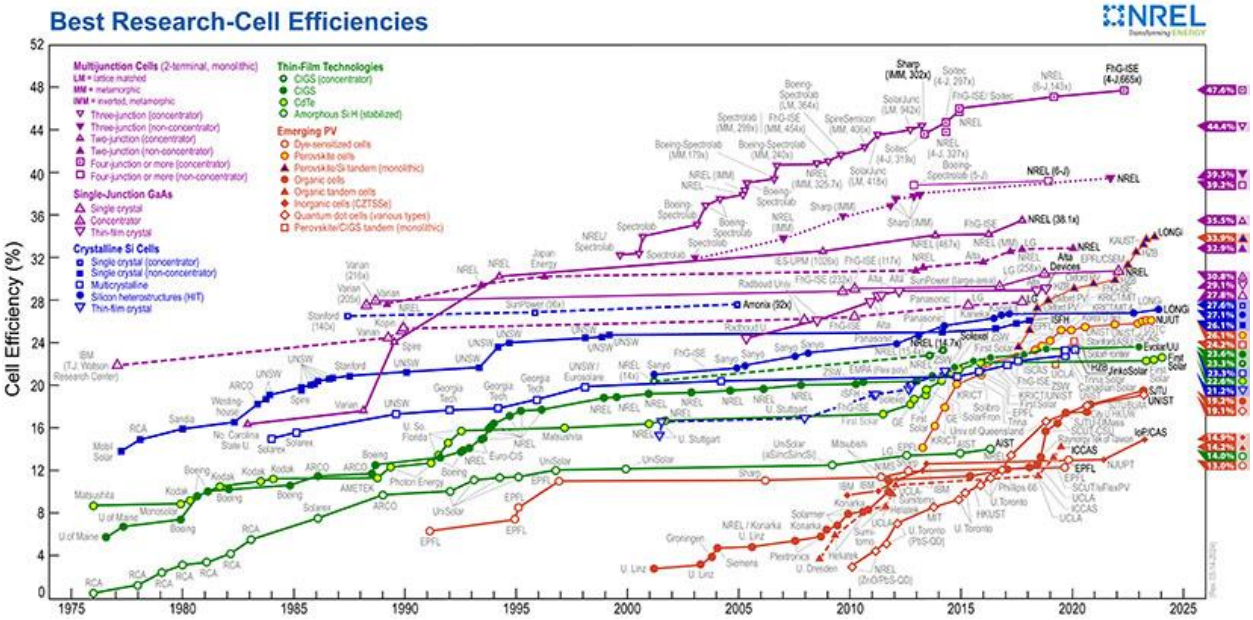

Figure 2-8 : Best researched cell efficiency [42].

2.6 What is Perovskite

Perovskite, with the chemical formula $CaTiO_3$, is named after Lev Perovski, a Russian mineralogist. In 1839, the mineral Gulf Rose was given this name. While the concepts of perovskite along with perovskite structure are frequently used synonymously, a perovskite formation is any unique material that reflects almost same crystallographic structure like perovskite (the generic form), usually represented as ABX3. Genuine perovskite, on the other hand, is a mineral made of calcium, titanium, and oxygen in the form of $CaTiO_3$.

Figure 2-9 : Perovskite structure [43]

Depending on the individual atoms or molecules that make up its structure, perovskite materials can have a wide variety of intriguing features. These include phenomena such as "huge magnetoresistance," which is useful in microelectronics because it causes the material's resistance to electricity to change when exposed to a magnetic field. Furthermore, some perovskites exhibit superconductivity, which allows for the transfer of electricity without any resistance. Perovskite materials exhibit a multitude of fascinating traits beyond these; they include high thermopower, energy ordering, ferroelectricity and linked fundamental, magnetic, and transport properties. As such, the field of perovskites offers chemists, physicists and material scientists a wealth of exciting opportunities for investigation and inquiry [43].

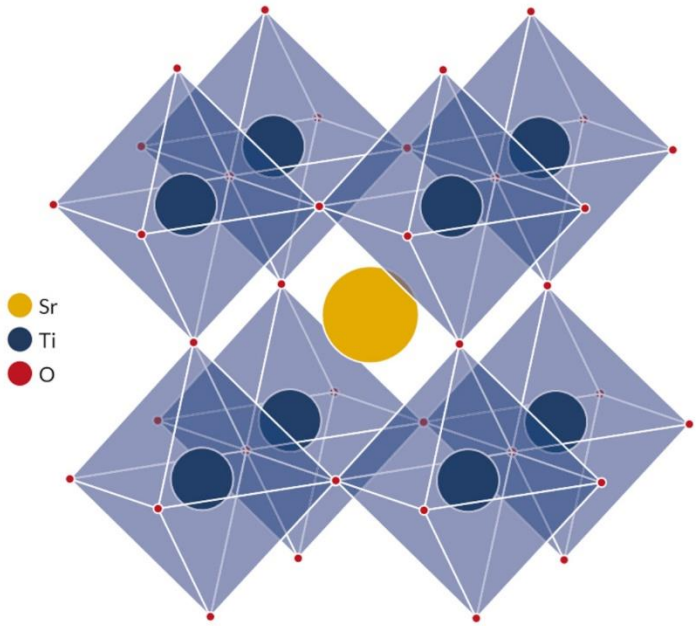

Figure 2-10 : Crystal structure of Perovskite [43].

A perovskite structure can be simplest described as a cubic unit cell with a purple core, green and blue midpoints for oxygen atoms, gray corners for titanium atoms, and purple center points for calcium atoms. (Further back layers are indicated by darker hues). The arrangement of the perovskite structure can be understood in terms of large positively ionized molecular or molecular type as a proton situated at the cube's core. Next, smaller, negatively ionized atom X occupies the cube's faces (anion), whereas molecules B, which are mostly positively ionized cations, occupy cube's corners [43].

2.7 Why Perovskite Solar Cell

Perovskite solar power has a wide bandgap. Due to intense competition in the industry where system prices are dependent on efficiency, which makes it feasible to merge them with lower bandgap photovoltaic technology, that will boost efficiency. Perovskite solar cells also have other benefits including flexibility, thin-film, adaptability, lightweight and low processing costs.

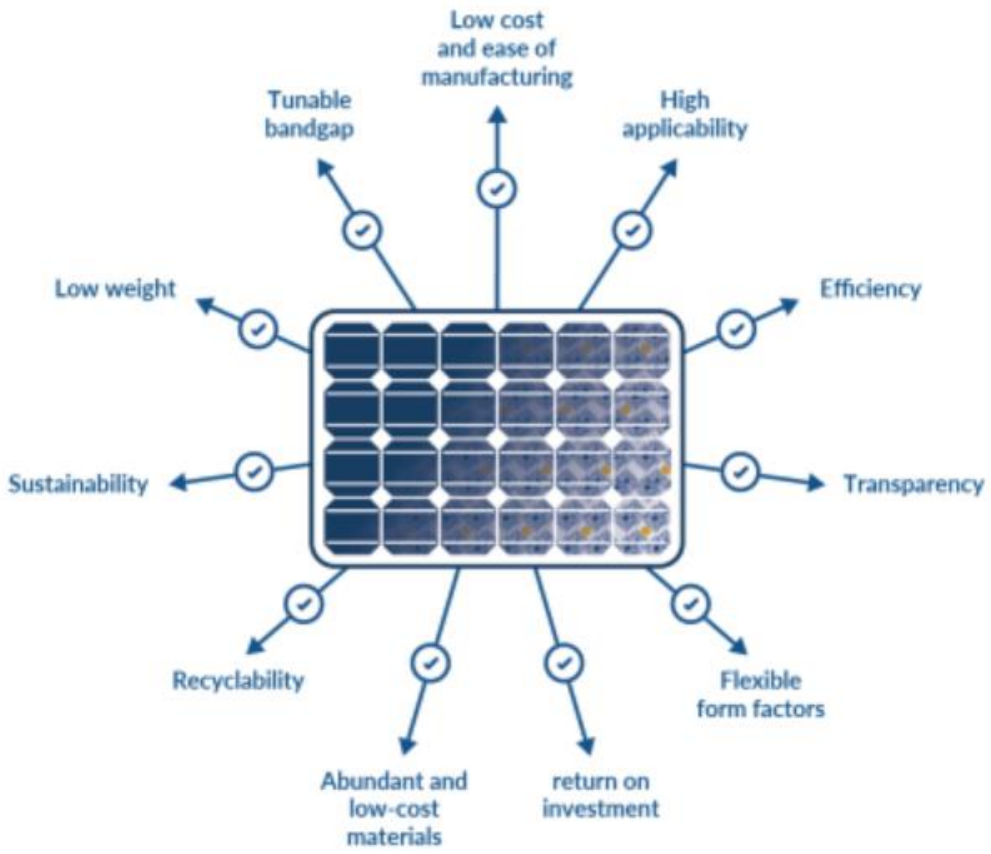

Figure 2-11 : Perovskite and its multiple uses [43].

The first perovskite was merely a dye in a basic DSSC variation, but over time, the device structure has changed to potentially become a new planar architecture system. With regard to photovoltaic applications, perovskites are superior to silicon because they can convert more sunshine into electricity by reacting to a broad limit of visible light. However, before perovskite solar cells can become commercially successful, they have to surpass many challenges. These include worries regarding the cells' longevity, instability and lack of stability in moisture-laden conditions, in addition to the potential for lead leakage a very hazardous element into the surrounding environment. The technology is still a ways off from being commercially viable [43].

2.8 Evolution of Perovskite Solar Cell

Recently metal-halide hybrid perovskites that have been instrumental in driving the growth of the sustainable energy sector while also showcasing its enormous potential to satisfy the demands of

both the expanding energy consumption and the expanding social development needs. Because of their special qualities, which include excellent absorption capacity, rapid photogeneration of liberated carriers, extended carrier propagation dimensions, simple fabrication and low manufacturing costs, perovskite based solar cells have developed extraordinarily. Power conversion rates up to the marketable grade were rapidly achieved by PSCs. The process of creating hybrid perovskites has shown how important an influence base metal cations have on the crystal structure and intrinsic characteristics of these materials. Because of this, the correlated doping method has been able to take on a unique role in the history of PSC growth during the last ten years [44].

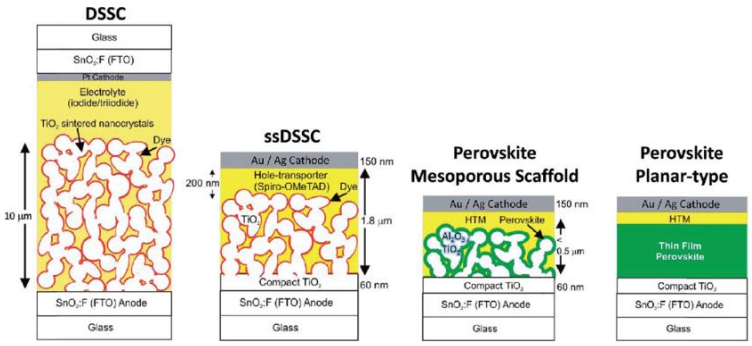

Figure 2-12 : Perovskite Solar Cell Development [44].

2.9 Present Situation with Perovskite Solar Cells

Because of the perovskite structure's abundance of chances for compositional and physical property optimization, as well as its chemical adaptability, products made from these substances have a broad range of possible uses [45].

Scientists are currently becoming more and more excited about optical methods related to using perovskites for next-generation computing and internet of things (IoT) advancements. We will witness significantly better internet speeds by utilizing light instead of energy to carry data [46].

2.10 Perovskite Solar Cells

The top 10 scientific achievements of 2013 is the composite solar cell made of organic-inorganic metallic perovskite ($CH_3NH_3PbX_3$) materials that has drawn interest from all across the world [47]. Perovskite materials have the advantages of having an excellent suppression factor, strong charge accessibility, extended carrier lifespan and a lengthy carrier transport location, which enable them to be used as both a layer for absorbing light and an electron/hole transport layer [48]. Fact is that perovskite related solar entities have increased in photo conversion efficiency from 3.7% in 2009 to 21.1% in 2016 indicates that they are the best alternative for next batch of the entities in order to substitute silicon related solar entities in the future [49]. Lately, perovskite solar entities have demonstrated performance for small-area devices that exceeds 15% sunlight-to-electricity efficiency of conversion. The fundamental properties of metal-organic halide-based composite organic-inorganic perovskites, also known as active absorber layers $(NH_4)PbI_3$ as well as $(CH_3NH_3)PbI_3$, are poorly understood [50]. With power conversion performance like efficiency of 20%, the most effective family of the solar-cell materials consists of zinc blende and chalcopyrite, which are derivatives of the tetrahedral diamond structure [51]. Promising light emission characteristics of hybrid perovskites point to their possible application in the low-cost also light-emitting elements as well as lasers. Optimizing these devices needs a deeper comprehension of light-to-electricity conversion. The mobility and recombination mechanisms of the carriers in the hybrid perovskites are covered in detail in this overview [52].

2.11 $CH_3NH_3SnBr_3$ material overview

The study of viable substitutes for large and expensive silicon-based solar cells is centered on perovskites [53]. In the recent years, lead related perovskite solar entities have set record performance benchmarks [54].

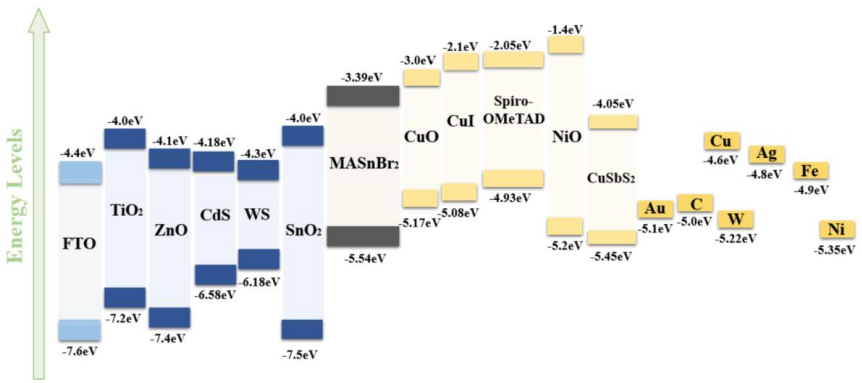

Figure 2-13 : Material overview of $CH_3NH_3SnBr_3$ [53].

On the other hand, these are unstable and may eventually be harmful to your health. As a result, efforts to equal and ultimately surpass the achievements of lead perovskite equivalents have been made in parallel while searching for ideally inorganic perovskite solar cells [53].

2.11.1 Crystal structure of $CH_3NH_3SnBr_3$

The atoms of tin (Sn) and bromine (Br) encircling each other in a cubic lattice form the crystal structure of $CH_3NH_3SnBr_3$. The coordination of six bromine atoms with each tin atom results in an octahedral shape. Furthermore, the methylammonium (CH_3NH_3) cations are found in the lattice's interstitial gaps [55].

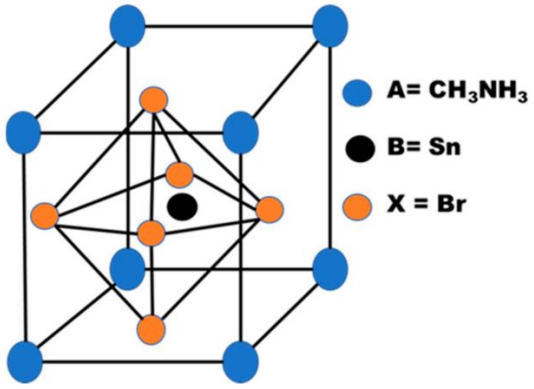

Figure 2-14 : Crystal structure of $CH_3NH_3SnBr_3$ [55].

The distinct characteristics of $CH_3NH_3S_nBr_3$ stem from this configuration, which makes it appealing for a number of optoelectronic uses [53].

2.11.2 Properties of $CH_3NH_3SnBr_3$

(a) Material Characteristics

Methylammonium tin bromide, or $CH_3NH_3S_nBr_3$, is a material with the optoelectronic qualities, perovskite crystal structure, and semiconducting nature. The electromagnetic spectrum's visible range is absorbed by $CH_3NH_3S_nBr_3$, which has a straight bandgap that makes it appropriate for optoelectronic uses [53]. Photovoltaic and other electrical devices benefit from its low recombination rates and great charge carrier mobility [54]. To further add to its special qualities, the inorganic perovskite lattice contains organic cations like methylammonium in its crystal structure [55].

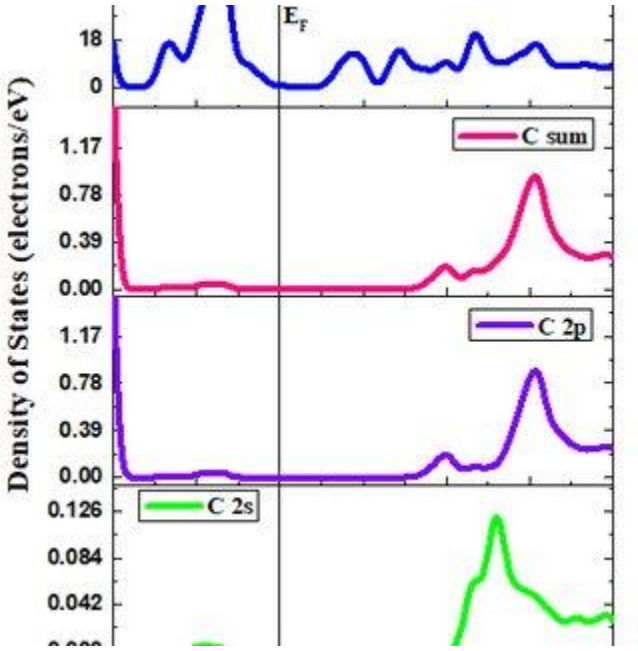

Figure 2-15 : Density of States (DOS) of $MASnBr_3$ [55].

These qualities make $CH_3NH_3SnBr_3$ a material that holds great promise for the use in semiconductor devices like LEDs and solar cells.

(b) Mechanical property

Although Methylammonium Tin Bromide, or $CH_3NH_3SnBr_3$, has attracted a lot of interest for its optoelectronic qualities, its mechanical characteristics still needs to be investigated. However, comparisons with other perovskite materials are possible [56]. In this regard, compounds such as $CH_3NH_3PbI_3$ have demonstrated softness and ductility properties in addition to relatively low hardness and Young's modulus values [47]. These findings imply that $CH_3NH_3SnBr_3$ and its other perovskite equivalents might exhibit comparable mechanical characteristics. For the purpose of better understanding its structural integrity and possible uses in a variety of disciplines, more research into its mechanical properties is necessary [57].

(c) Optical property

Due to its straight bandgap in the visible spectrum, methylammonium tin bromide ($MASnBr_3$) demonstrates potential for optoelectronic applications, particularly in solar cells. This property allows for efficient light absorption that is perfect for solar energy conversion [58].

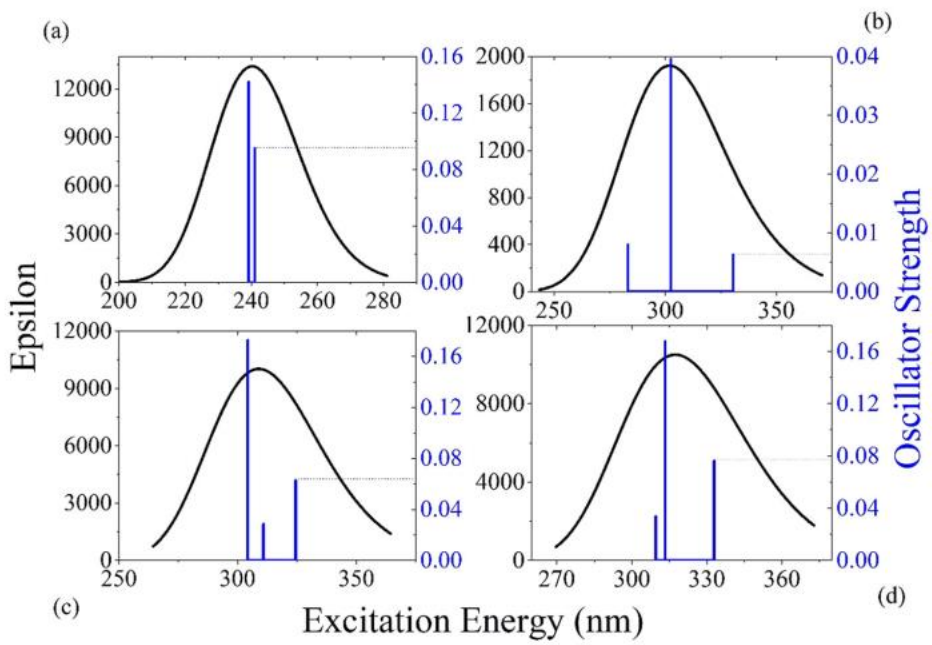

Figure 2-16 : Optical properties (ellipson, oscillator strength) regarding MASnBr3 [58].

By combining mathematical functions with molecular orbitals (MOs), the volume of states (DOS) including the range of spectrum was produced. Sn(5p), Br(4s), as well as Br(4p) orbitals make up the LUMO, whereas Sn(5s), Sn(5p), along with Br(4p) orbitals make up the HOMO. The animosity that exists between a bonded and lone couple is probably what causes the HOMO to be seen to be more delocalized than the LUMO. From 1 to 4, it is seen that the HOMO-LUMO gap shrinks as "n" grows. After modeling the ($CH_3NH_3SnBr_3$) n cluster ($n \rightarrow \infty$), The wavelength, optical gap, and HOMO–LUMO gap that correspond to the intake band maxima were found to be, respectively, 346.03 nm (3.5830 eV), 3.091 eV and 3.622 eV. The estimated HOMO–LUMO gap of $CH_3NH_3SnBr_3$ from DOS was 2.19 eV [59].

The material exhibits good optical transparency and a low exciton binding energy, which makes it appropriate for use in transparent conductive coatings and other optoelectronic devices. The optical characteristics of $MASnBr_3$ underscore its potential to augment the efficacy of solar cells and other photovoltaic apparatuses. However, additional investigation is imperative to fully maximize its pragmatic implementation [58].

(d) Electronic Property

Methylammonium tin bromide, or $CH_3NH_3SnBr_3$, exhibits distinct optoelectronic characteristics and semiconducting behavior that define its electrical characteristics. Being a perovskite, $CH_3NH_3SnBr_3$ has an absorption that reaches into the visible portion relates to the electromagnetic spectrum as well as a direct bandgap that makes it excellent for solar applications [53].

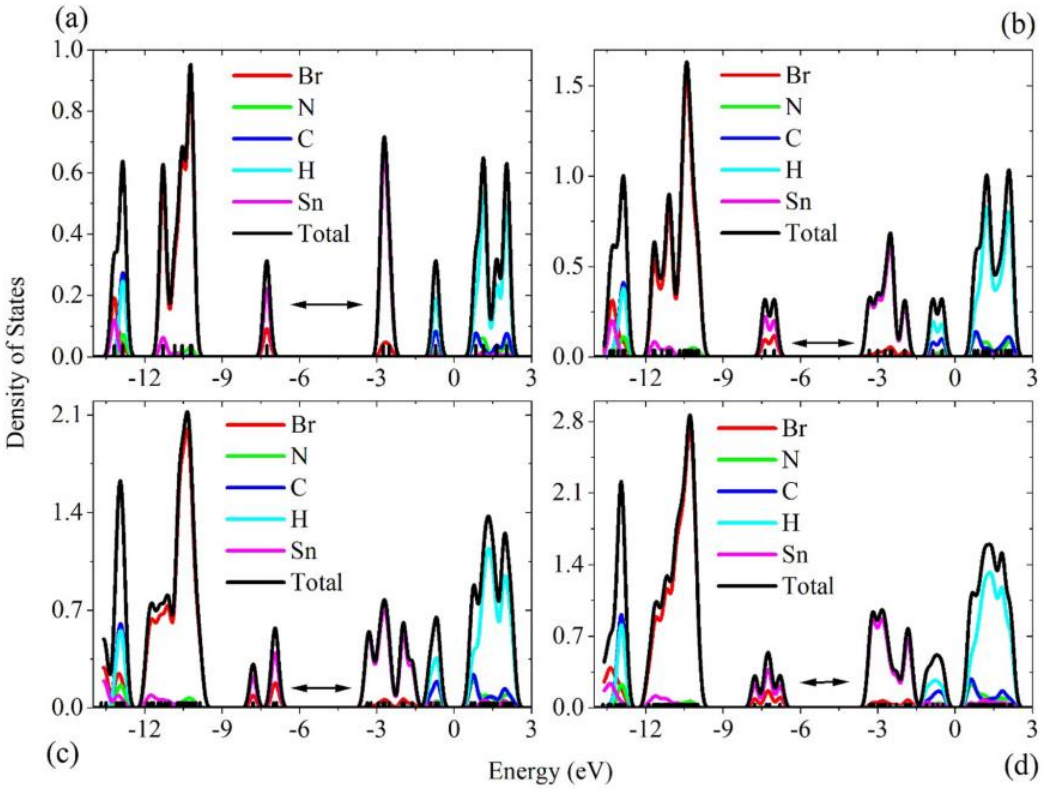

Figure 2-17 : Zone population of MASnBr3 [59].

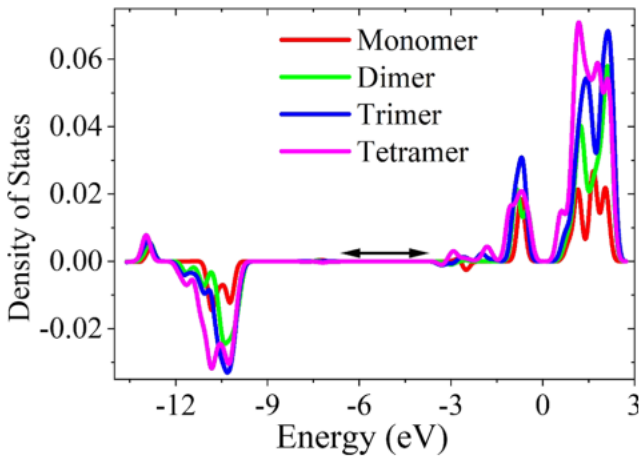

Figure 2-18 : Zone population vs Energy [59].

It shows promise for application of solar entities and other semiconductor devices because of its high charge carrier mobility and low recombination rates. Furthermore, variables like temperature,

pressure, and doping can alter its electrical structure, opening up possibilities for adjusting its characteristics for certain uses [59].

2.1.1.3 Related Works on $CH_3NH_3SnBr_3$Thin Film Solar Cell

The study of viable substitutes for large and expensive silicon-based solar cells is centered on perovskites. Recent years have seen record-breaking efficiency levels achieved by lead-based composite perovskite photovoltaic entity. Long-term health hazards may arise from these, though, as they have stability issues [51]. As a result, efforts to correspond with and ultimately exceed the accomplishments of lead perovskite equivalents have been made in parallel while searching for ideally inorganic perovskite photovoltaic entity. This work reports on a system improvement method driven by modeling to create very efficient Pb-free n-i-p Methylammonium Tin Bromide ($MASnBr_3$) perovskite photovoltaic cells. It has been investigated how different hole as well as electron conveyance layers affect the performance parameters of $MASnBr_3$ structures [53].

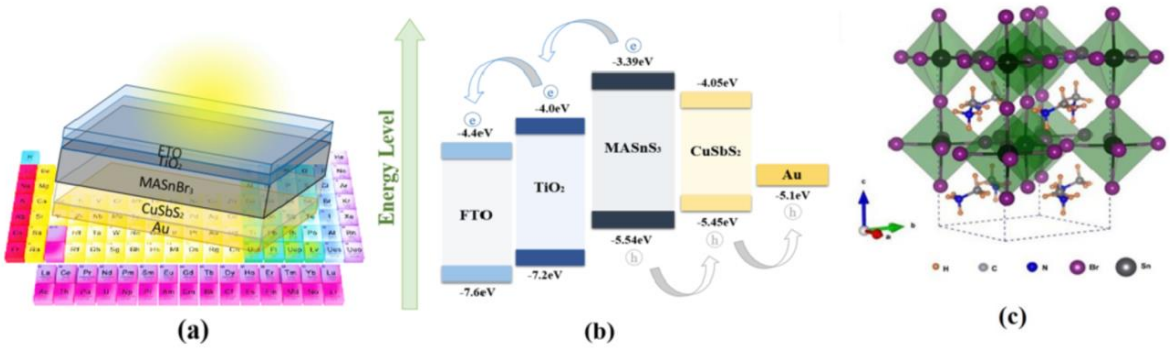

Figure 2-19 : (a) Early Mechanism (b) Arrangement of energy bands (c) $MASnBr_3$ structure [53].

The $MASnBr_3$ perovskite solar cell was investigated in the current work using a variety of HTLs (Cu_2O, $CuSbS_2$, NiO, CuI and Spiro-OMeTAD) and ETLs (SnO_2, WS_2, TiO_2, ZnO, CdS). The thickness as well as carrier concentration of the HTLs along with ETLs the concentration of recipient and supplier doping charges in the absorber layer, the defect density related to the perovskite layer, the interface defect density between the ETL/PEPV layer and the HTL/PEPV layer, the back contact activity operation and series as well as shunt resistance and all of the

parameters have been optimized. The PCE is 34.52%, the FF was 88.30% and the optimal structural performance was attained at a different temperature [53].

The PSC performance using NiO (200 nm) as the HTL and various ETLs.

PSC Structure	V_{oc} (V)	J_{sc} (mA/cm^2)	FF (%)	PCE (%)
FTO/TiO_2/$MASnBr_3$/NiO/Au	1.0218	35.2611	82.23	29.63
FTO/ZnO/$MASnBr_3$/ NiO /Au	1.0235	35.2586	82.41	29.74
FTO/CdS/$MASnBr_3$/ NiO /Au	1.0223	35.2420	82.30	29.65
FTO/WS_2/$MASnBr_3$/ NiO /Au	1.0235	35.2262	81.72	29.46
FTO/SnO_2/$MASnBr_3$/ NiO /Au	1.0242	35.2548	82.44	29.77

This work focuses on lead-free perovskite photovoltaic entity that use the $MASnBr_3$ perovskite layer and are examined using SCAPS 1D software. Different materials are used in place of different back contact metals as electron moving section and hole moving section. The analysis shows that efficiency of cell is highly dependent on factors such back contact metals, HTLs, ETLs and perovskite layer characteristics. For the best possible device performance, the characteristics of the perovskite component must be adjusted and the back metal contacts must be carefully chosen. A specific arrangement of cells comprising glass/FTO/SnO_2/$MASnBr_3$/NiO/Au, is linked to the highest efficiency and produces promising values for V_{oc}, J_{sc}, FF and PCE, according to simulation studies. Additionally, the thickness related to the perovskite layer greatly manipulates device efficiency; the most effective configuration has a typical thickness of 500 nm. Additionally, the work demonstrates that even though temperature-dependent IV parameters rapidly decline, device stability may be achieved at 300 K [53].

2.12 $CH_3NH_3SnI_3$ material overview

Perovskites based on lead have garnered significant interest as possible contenders for the upcoming generation of solar cells. However, concerns about environmental contamination and human toxicity significantly impede the commercial use of lead-based perovskites. Therefore, it is imperative to identify suitable alternatives for lead-based perovskites [60].

A solar entity capacitance simulator was being analyzed to simulate photoexcited lead-free photovoltaic entity. To study the output parameters under AM 1.5G light, it was modeled. The primary focus of simulation efforts is on the absorber layer's width, acceptor volume, and defect count which relates to the photovoltaic performance of the solar device. Furthermore, an investigation was conducted into the effects of different metal contact work functions [61].

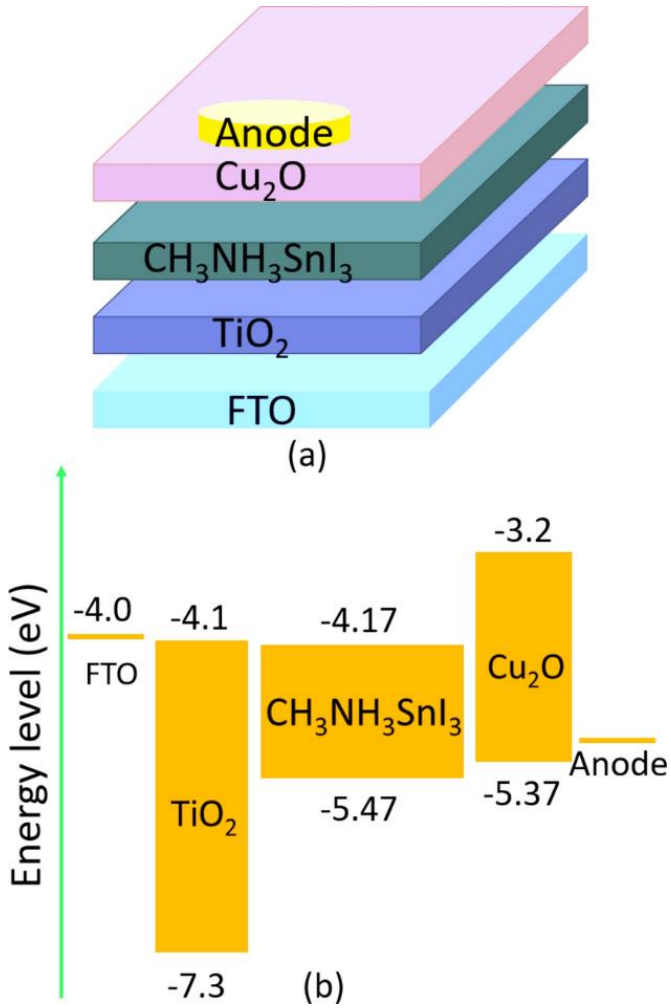

Figure 2-20 : (a) initial device structure , (b) configured energy bands [61].

(a) Crystal Structure of $CH_3NH_3SnI_3$

In an aerobic environment, $CH_3NH_3SnI_3$ crystals were formed using the cooling crystallization method, reaching a maximum size of 10 mm × 6 mm × 6 mm. $CH_3NH_3SnI_3$ crystal formed is in cubic phase, have a lattice constants consisting a = b = c = 6.2480 Å, according to an XRD study of the crystal powder. An analysis of the oxidation mechanism of $CH_3NH_3SnI_3$ was conducted and the results of XRD and also EDX indicate that chemical characteristics of the crystal are not stable in air. $CH_3NH_3SnI_3$ crystal produced has high crystallinity, according to HRTEM [62].

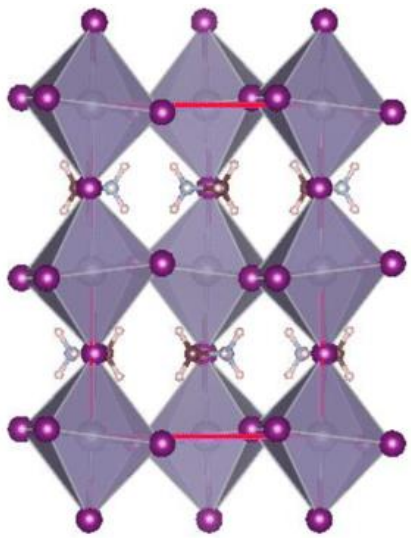

Figure 2-21 : Crystal structure of $MASnI_3$ [63].

2.12.1 Properties of $CH_3NH_3SnI_3$

Material Characteristics

Methylammmonium Tin Tri-iodide ($CH_3NH_3SnI_3$) is one kind of without lead perovskite semiconductor substance that has gained popularity for photonic applications. $CH_3NH_3SnI_3$ small crystals are grown on D-shaped fiber as a saturated absorber in order to provide mode-locked pulses for ber lasers. With an elevated nonlinear photonic fluctuation magnitude of 15.2% and a particularly low saturated absorption intensity which is 76.4 MW cm^{-2}, the saturated absorber

device is impressive. By incorporating the $CH_3NH_3SnI_3$ saturable absorber, ytterbium-doped (Yb-doped) optic laser was able to produce steady mode-locking flashes with a range of 1.77 ns, a maximum power output which exhibits at 28.19 mW, a 3 dB range of roughly 8.09 nm and a center wavelength of 1064 nm. The output device pulses have a 5.6% power consumption and remarkable durability over time, which are typical features of dissipative solution [63].

(a) Mechanical Property

Relaxing a structure until all atomic forces are zero does not guarantee that it will stay stable when other forces act on it. By looking at the elastic constants of $CH_3NH_3SnI_3$ to determine its mechanical stability. Given a strained reference density given as V ref, the entire energy E that relates to the crystal at a volume V can be found using the formula under isotropic pressure P [64].

$$E(V,\epsilon) = E(V^{\mathrm{ref}}, \epsilon = 0) + V^{\mathrm{ref}} \sum_{ij} \sigma_{ij}\epsilon_{ij} + \frac{V^{\mathrm{ref}}}{2} \sum_{ij} C_{ij}(V^{\mathrm{ref}})\epsilon_i\epsilon_j + O(\epsilon^3),$$

[64]

(b) Optical Property

The optical properties of $CH_3NH_3SnI_3$ were investigated by computing real part (ε1) as well as imaginary (ε2) part of dielectric operation, refractive index, intake factor, transparency and loss function versus energy using the DFT technique in the GGA approximation. The hypothetical component of the insulating operation, that describes the capture motion of $CH_3NH_3SnI_3$, was calculated electronically. Additionally, the real component like dielectric function is used to extract the hypothetical part, which expresses the electronic polarizability of the system, using the Kramers-Kronig relations [65].

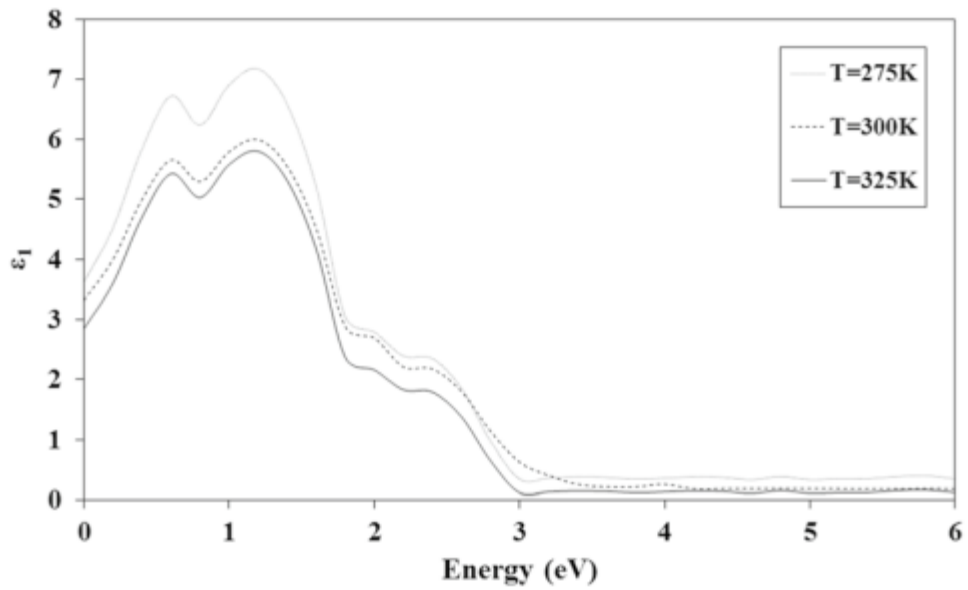

Figure 2-22 : The dielectric function's real component (ϵ1) for the cubic $MASnI_3$ perovskite at different temperatures [66]

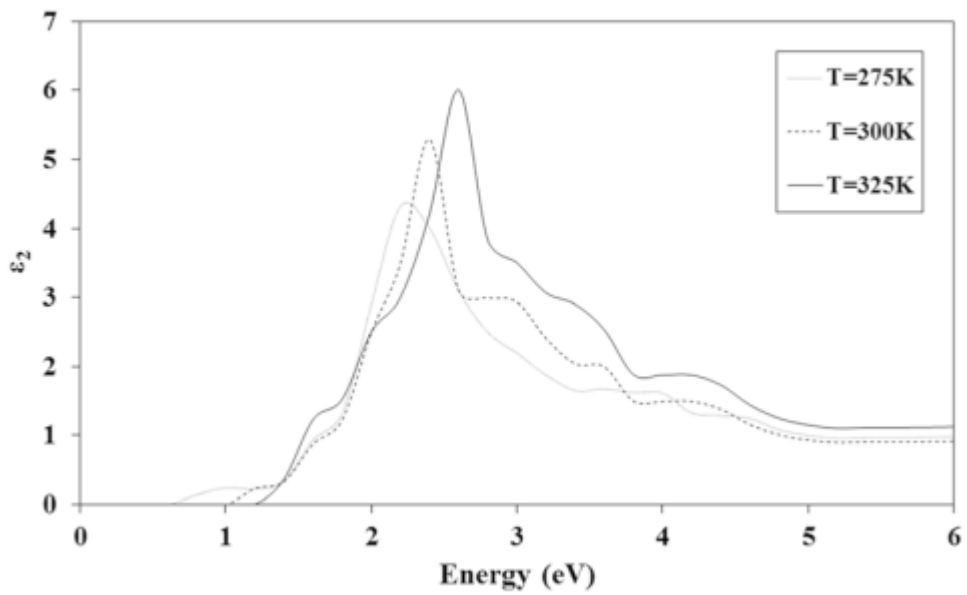

Figure 2-8 : The dielectric function's imaginary portion (ϵ2) for the cubic $MASnI_3$ perovskite at different temperatures [66]

(c) Electronic Property

The orthorhombic phase's computed band-structure is displayed in Figure 2-9. The horizontal dashed line indicates the so-called Fermi level, which has been moved to zero. As possible it can be observed in the Figure 2-9, Because the valence band being maximum (VBM) also conduction band being minimum (CBM) are almost situated at gamma point within Brillouin zone, the substance under examination exhibits an immediate band gap of semiconductor nature at this point [64].

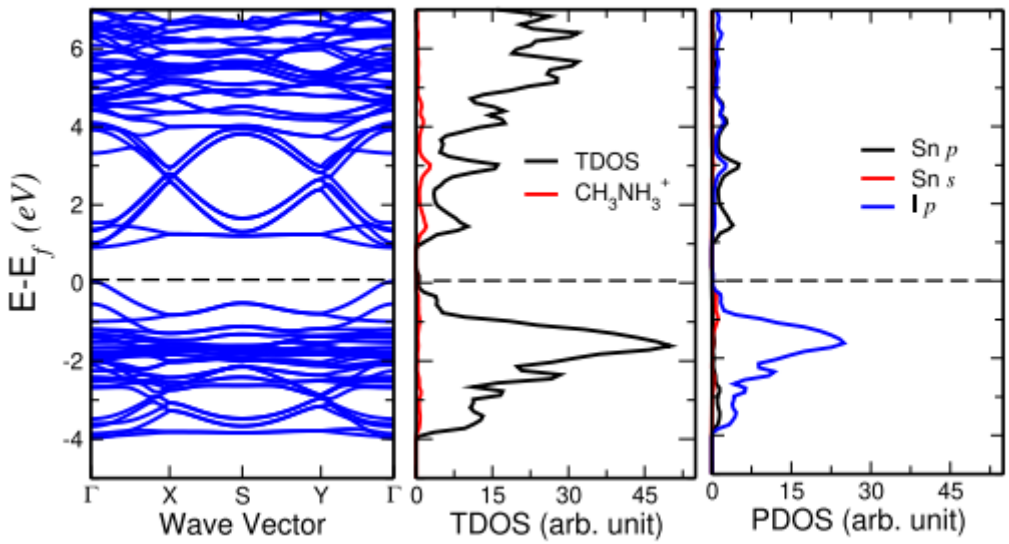

Figure 2-9 : Wave vector, TDOS and PDOS of $MASnI_3$

DFT calculated the middle-class cation projected density of states (PDOS), Sn and I atomic orbital PDOS and band allignment (left), overall volume of units and $CH_3NH_3^+$ of the orthorhombic perovskite $CH_3NH_3SnI_3$ at 0.7 GPa [64].

2.1.2 Related Works on $CH_3NH_3SnI_3$ Thin Film Solar Cell

A novel photovoltaic cell architecture is the subject to this analysis, in which the light-absorbing layer is $CH_3NH_3SnI_3$ and the electron-grabbing layer is CdS. Physical parameters such as the

extent of the layer that is in use, defect density and quantity of low acceptors were numerically changed to improve the device. The proposed solar cell architecture demonstrated a system with an efficient J_{sc} of 33.41 mA/cm^2, V_{oc} of 0.879 V, FF of 85.24% and PCE of 25.01%. The device's composition deteriorates considerably and the solar cell's ability to convert energy is reduced at temperatures above 300 K, according to temperature analysis. Furthermore, a back contact with higher work function, such Platinum, makes an ohmic contact at HTL/anode interaction, enhancing the cell's functionality [66].

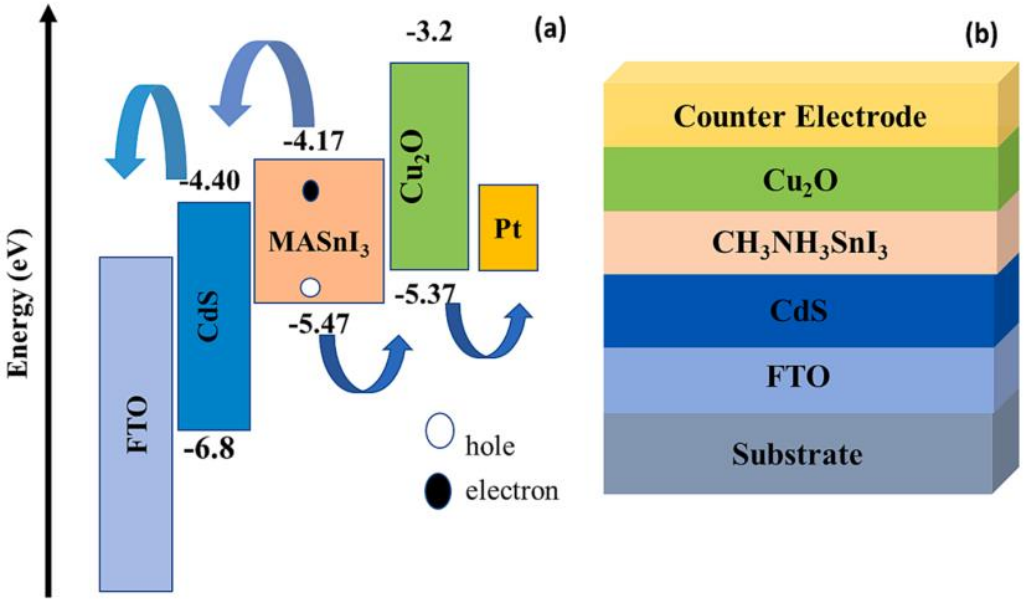

Figure 2-10 : (a) The solar device's compatibility with the energy range. (b) Lead-free $MASnI_3$ solar device [67].

This study explores the use of lead-free, ecologically friendly $CH_3NH_3SnI_3$ perovskite as a light-harvesting material. Using SCAPS 1D, a numerical modeling of the apparatus structure FTO/CdS/$CH_3NH_3SnI_3$/Cu_2O/anode was performed. With the optimization of intrinsic layer physical parameters like shallow acceptor density, defect density and thickness, an extremely effective method with J_{sc} of 33.41 mA/cm^2, V_{oc} of 0.879 V, FF of 85.24%, and PCE of 25.01% was attained. The consequence of temperature is also looked at and it was found that higher temperatures increase the opposite saturated current and restrict photovoltaic entity efficiency.

Increased defect density accelerates recombination, which lowers performance. Additionally, the performance of various metal electrodes were observed. It was found that while Au, Cu and Pd anodes form the Schottky junctions at their interface, limiting the amount of hole transfer, Pt anodes form ohmic contact on anode/Cu_2O link obstacle allowing the hole to transport into the anode. The findings indicate that for rear metal electrodes, metals with work functions greater than Cu_2O (5.37 eV) are advised [66].

2.13 Perovskite Based Tandem

The main energy source used up until now has been fossil fuels. But forecasts indicate that in the ensuing decades, energy from green sources; especially photovoltaic cells will overtake fossil fuels as the primary energy source. Monocrystalline and multi-crystalline solar cells based on silicon crystals currently dominate the photovoltaics market. The standard conversion effectiveness of perovskite photovoltaics is about 26%, however studies suggest that this might reach 30%. In the meantime, crystalline silicon-based single-junction photovoltaic cells attain a conversion efficiency that is roughly 25%. The majority of the incoming AM1.5 light are absorbed by these single-junction cells. In order to get around this restriction, scientists suggest building tandem cells, which are made up of a number of sub-cells that can each absorb various amounts of incident light because of their individual energy gaps and absorbing surfaces [67].

Tandem solar entities, or multi-junction solar entities, reflect a possible alternative to single-junction solar cells, overcoming their limitations. These TSCs are made up of many light absorbers with different range intervals. Their capacity to catch light over broad range of wavelength gives them a distinct advantage. Perovskite photovoltaic cells (PSCs) are a promising challenger in the market because of their easily adjustable band gaps, remarkable 25.2% power conversion efficiency (PCE) and simple manufacturing method. Perovskite TSCs have generated a lot of attention in both scientific research circles and commercial companies since their original discovery in 2014, which has led to considerable advancements in thin-film perovskite photovoltaic technology [68].

Although single-junction photovoltaic cells may eventually be surpassed by all-perovskite tandem solar entities, the latter's certified performance has always lagged. A thick structure of mixed Sn-Pb narrow-bandgap cell is necessary for tandem solar cells to achieve large sunlight densities. One major obstacle, nevertheless, is the short carrier diffusion length in Sn-Pb perovskites [69].
A scientific investigation presented an efficient design for a perovskite photovoltaic cell (PSC) that substituted electron carrying substances or hole movement elements over the conventional ones. This new method uses cuprous oxide (Cu_2O) for the hole transport layer (HTL) and zinc oxysulfide (ZnOS) for the electron transport layer (ETL). Doping the perovskite layer suggests that an n-p PSC lacking a layer for electron transportation may be able to outperform the traditional n-i-p construction, providing better stability and performance metrics by lowering quantities of layers as well as interfaces. This novel arrangement has the potential to progress solar cell technology [70].

Scientific attempts to address present issues and improve the performance of multijunction (tandem) PSCs have escalated in response to the notable results in these systems. Photons that have energy lower than the perovskite bandgap may be harvested thanks to the $MoTe_2$ layer, which has a bandgap of about 1 eV. Hole transport degradation of absorbing area causes stacking absorbers with varying bandgaps has caused the open circuit voltage to drop. Thus, we saw an imrovement in efficiency from 18.52% to 20.32% and a rise in open circuit voltage of up to 0.1 eV. Achieving a high performance is possible because the energy band-structure of the $MoTe_2$ and graphene oxide layers is precisely aligned with the band edges of the adjacent layers [71].

2.13.1 Related work on Perovskite-Si Tandem solar cell

The design and simulation of a tandem solar cell employing silicon and $MAPbI_3$-xClx as absorber is shown in this study. The bottom cell's silicon layer is 2 μm thick, which enables it to absorb as much of the spectrum that the perovskite sub-cell transmits. Using a suggested approach, the $MAPbI_3$-xClx layer's thickness is optimized. The result metrics indicate that 205 nm was the ideal layer thickness for the $MAPbI_3$-xClx. The suggested tandem cell exhibits a efficiency of 33.09%

with a V_{oc} of 1.9 V also short circuit current density of 19.95 mA/cm^2, according to the simulation results [67].

In this study, a two-subcell multi-junction solar cell designed and optimized with SCAPS-1D is described. Transparent conductive oxide, perovskite and CuO make up the top ($MAPbI_3$-x Clx) sub-cell (PSC). The bottom cell is made up of levels consisting of zinc oxide (ZnO) and cadmium sulfide (CdS), sandwiched between a silicon (Si) absorber layer and a TCO that is severely manipulated to perform the role of the layer of electron transport which acts like primary role as a transparent layer [67].

The developed tandem cell is offered with a useful thickness range and a high power conversion efficiency. Perovskite and silicon were used as absorbers in a multi-junction solar cell that was shown. To do betterment in the thickness of the perovskite entity, an optimization algorithm is proposed. As an alternative to silicon, the consequences demonstrate that electron transport-layer that is free perovskite is a suitable top sub-cell. The suggested tandem solar cell has shown an photo-conversion efficiency of 33.09% [67].

2.13.2 Related work on $MASnBr_3$ based Tandem solar cell

An $MASnBr_3$-based perovskite photovoltaic cell makes up the top sub-cell of the suggested tandem cell, while crystalline silicon makes up the bottom entity. Evaluating the tandem entity configuration's performance potential is the goal of this research. According to simulation studies, the tandem cell can outperform individual cells with a PCE of 42.7%. A thorough discussion is held on the material's interferes on the PCE of perovskite solar cell's hole moving layers and electron carrying layers. The research indicates the optimum materials for HTL and ETL are $CuSbS_2$ and AZO, respectively. The dominance of multiple factors on the tandem solar cell's behaviours which is the perovskite layer's thickness, bandgap, defect density and HTL and ETL thickness. An Efficiency (eta) of 30.88% is obtained from the independent top cell (FF=84.87%, J_{sc}= 32.02 mA/cm^2, V_{oc}= 1.13 V). Efficiency (eta) of 21.80% is obtained from the independent bottom cell (FF=85.24%, J_{sc}=20.30 mA/cm^2, V_{oc}=0.74V). The efficiency of a TSC using $MASnBr_3$ on c-Si is 42.70% (FF=85.24%, J_{sc}=15.48 mA/cm^2, V_{oc}=1.87 V).

It is established that AZO and $CuSbS_2$, the appropriate substances to ETL and HTL, respectively, are used. Subsequently, the consequences of absorber layer thickness, absorber layer defect density, absorber layer's band-gap, thickness of AZO and $CuSbS_2$ thickness on PSC performance are investigated. The PSC is configured as glass substrate/FTO/AZO/$MASnBr_3$/$CuSbS_2$ /Au. The most effective thicknesses were found to be 100 nm for AZO and 400 nm for $CuSbS_2$. By using this PSC which is used for the top sub-cell and c-Si which is used for the bottom sub-cell, we have also mimicked the tandem structure. The efficiency has increased from 30.88% in a single construction to higher value at 42.7% in tandem, as we have shown [72].

2.13.3 Optimized High Current Tandem Solar Cells

2T tandem cells convert energy with high photo-conversion efficiency. The operating current density is one of their primary drawbacks since 2T tandem solar cells are comparable to electrically linked series sub-cells. The current flowing in top sub-cell will rise as well as the current flowing in bottom sub-cell will fall as the thickness of the top absorber layer increases. Overall performance is limited because the tandem cell must function at its value due to sub-cell along with the minimal current. Multi-junction cells are a better option than single-junction cells in the quest to produce solar cells with a high efficiency because they can absorb a wider spectrum. It is possible to collect a larger spectrum and with a higher photo-conversion performance means efficiency by increasing the number of connections. However, this simultaneously raises the cell's cost and complexity. High efficiency is achieved by using only two-junction photovoltaic cells. This is accomplished by resolving a primary issue with two-terminal tandem photovoltaic cells, which is that the tandem cell is forced to run at its own current density by the sub-cell with a lower current (near the bottom) [73].

2.14 Deposition Technique of Perovskite Solar Cell

The deposition techniques utilized in fabricating perovskite photovoltaic cells are pivotal in achieving optimal efficiency and performance. Among the primary methods employed are solution processing, vapor deposition, and hybrid approaches. Solution processing encompasses techniques

like spin coating, wherein a perovskite precursor solution is uniformly spread onto a substrate and then spun at high speeds to create a thin, even film. Widely favored for its simplicity and cost-effectiveness, this method is popular in research and industrial applications alike [74].

On the other hand, vapor deposition techniques, including thermal evaporation and chemical vapor deposition (CVD), offer meticulous control over film thickness and composition, critical for producing high-performance devices. These methods enable precise manipulation of deposition conditions, ensuring the desired film quality and properties [75].

Hybrid techniques, such as sequential deposition and vapor-assisted solution processing, integrate the advantages of both solution and vapor methods. By combining these approaches, researchers can achieve superior film quality, enhanced device performance, and improved scalability. While each technique presents its unique advantages and challenges, their judicious selection is paramount in enhancing the efficiency and commercial viability of perovskite solar entities in the renewable energy landscape [76].

2.14.1 Deposition Technique of $MASnBr_3$ Perovskite

The selection of deposition technique for MASnBr3 perovskite solar entities depends on factors such as the expected film quality, scalability, and cost. Solution-based methods like spin coating and blade coating are popular in research settings due to their simplicity and effectiveness. Vapor-based and hybrid techniques offer potential for producing high-quality films, while printing techniques hold promise for scalable production. Optimization of these deposition methods is crucial to achieving high-efficiency MASnBr3 perovskite solar entities [77].

The deposition technique for MASnBr3 perovskite is a meticulous process aimed at producing thin films of superior quality suitable for solar cell applications. It typically commences with the meticulous preparation of a precursor solution comprising essential chemical constituents like methylammonium bromide (MABr) and tin bromide (SnBr2). This solution is delicately deposited onto a substrate through various methods like spin coating, doctor blading, or slot-die coating, with spin coating being particularly favored for its ability to yield uniform films efficiently [78].

Subsequently, the deposited precursor film undergoes annealing at elevated temperatures to enhance the crystallization process of perovskite structure, a pivotal step for achieving the desired

crystalline phase and optimizing the film's optoelectronic properties. Further enhancement of film quality and device performance can be achieved through additional post-treatment techniques like antisolvent washing or surface passivation. It is imperative to exercise meticulous control over deposition parameters and subsequent processing steps to ensure the fabrication of MASnBr3 perovskite films with the ideal morphology, crystallinity, and electronic properties necessary for efficient solar cell operation [79].

2.14.2 Deposition Technique of Si Tandem Cell

The deposition techniques for Si tandem solar cells involve a combination of advanced methods tailored to each layer's specific requirements. The selection of technique relies on the material properties, desired film quality, and scalability. Continuous advancements in these techniques are crucial for improving the efficiency also commercial viability of tandem solar cells [80].

The deposition techniques for silicon (Si) tandem solar cells, which combine multiple layers of semiconductor materials to improve overall efficiency, are varied and tailored to the specific materials used in the tandem structure. Here, I outline some of the key deposition techniques for the layers within Si tandem photovoltaic cells, focusing on both the silicon bottom cell and the top cell materials, which are often perovskites or other high-bandgap materials [81].

The deposition technique for Si tandem solar cells involves a series of intricate steps to fabricate high-efficiency photovoltaic devices. Initially, a substrate, typically made of glass or silicon, is prepared and cleaned thoroughly to ensure optimal adhesion and uniformity of the subsequent layers. The deposition of the bottom cell begins with the deposition of a textured silicon wafer, which serves as the foundation for subsequent layers. This textured silicon wafer is often coated with an anti-reflective layer to minimize light reflection and enhance light absorption. Subsequently, layers of doped silicon, including the p-type as well as n-type levels, are deposited utilizing techniques such as chemical vapor deposition (CVD) or plasma-enhanced chemical vapor deposition (PECVD). These layers are precisely controlled to achieve the desired doping concentrations and thicknesses, crucial for optimizing carrier transport and collection within the cell [82].

Following the deposition of the bottom cell, the fabrication process proceeds with the deposition of intermediate layers, such as tunnel junctions or interlayers, to facilitate efficient current matching and electrical coupling within top and bottom entities. Finally, the top cell is deposited using similar techniques, followed by the integration of transparent conductive oxide (TCO) layers and metal contacts to complete the tandem structure. Each deposition step is meticulously controlled to ensure uniformity, quality, and compatibility between the different cell layers, ultimately leading to the fabrication process of better-performance Si tandem solar cells [83].

2.14.3 Deposition Technique of GeTe Tandem Cell

The deposition techniques for GeTe tandem solar cells encompass a range of advanced methods tailored to the specific requirements of each layer in the tandem structure. These techniques include MBE, sputtering, thermal evaporation, CVD, ALD, PLD, spin coating, and inkjet printing. Each technique offers unique advantages in terms of film quality, uniformity, and scalability, contributing to the overall efficiency and commercial viability of GeTe tandem solar cells. Continuous advancements in these deposition methods are significant for optimizing the performance as well as production of high-efficiency tandem solar cells [84].

The deposition technique for GeTe tandem solar cells involves a sophisticated process tailored to achieve high-efficiency photovoltaic devices. Initially, a substrate, typically made of glass or silicon, is meticulously cleaned to ensure optimal adhesion and uniformity of subsequent layers. The bottom cell deposition starts with the deposition of a textured germanium telluride (GeTe) layer, serving as the foundation for subsequent layers. This GeTe layer is often deposited using techniques like molecular beam epitaxy (MBE) or sputtering to effectively control its thickness and crystallinity [85].

Doping of the GeTe layer may also be performed during deposition activity to attain the desired electrical properties. Following the GeTe layer deposition, additional layers such as tunnel junctions or interlayers may be deposited to facilitate efficient current matching and electrical coupling between the top and bottom cells. The fabrication process proceeds with the deposition of the top cell using similar techniques, followed by the integration of transparent conductive oxide (TCO) layers and metal contacts to complete the tandem structure. Each deposition step is carefully

controlled to ensure uniformity, quality, and compatibility between the different cell layers, ultimately leading to the fabrication of high-performance GeTe tandem solar entities [86].

2.14.4 Deposition Technique of $CuInSe_2$ Tandem Cell

The deposition techniques for $CuInSe_2$ tandem solar cells encompass a variety of methods tailored to achieve high-quality, efficient, and scalable photovoltaic devices. Techniques such as co-evaporation, sputtering, electrodeposition, spray pyrolysis, CBD, PLD, and hybrid methods each offer unique advantages for the precise control of film properties and the fabrication of multi-junction structures. Continuous advancements in these deposition techniques are significant for optimizing the performance as well as commercial viability of $CuInSe_2$ tandem solar cells [87].

The deposition technique for $CuInSe_2$ (CIS) tandem solar cells involves a series of meticulous steps to create efficient photovoltaic devices. Initially, a substrate, typically glass or molybdenum-coated glass, is prepared and cleaned thoroughly to ensure proper adhesion and uniformity of subsequent layers. The bottom cell deposition commences with the deposition of a CIS absorber layer, often using techniques like co-evaporation or sputtering, to achieve the desired thickness and composition. This step is crucial as it determines light absorption properties of the bottom cell. Following the CIS layer deposition, additional layers such as buffer layers (e.g., CdS, Zn(O,S)) and window layers (e.g., ZnO) may be deposited to enhance carrier transport and light absorption. The fabrication process proceeds with the deposition of the top cell, typically composed of materials like amorphous silicon (a-Si) or cadmium telluride (CdTe), using similar deposition techniques. Finally, transparent conductive oxide (TCO) layers along with metal contacts are deposited to complete the tandem structure. Each deposition step is carefully controlled to ensure optimal layer thickness, composition, and interface quality, ultimately leading to the fabrication of better-performance CIS tandem solar entities [88].

2.14.5 Deposition Technique of Si Single Junction Cell

The deposition techniques for silicon single-junction solar cells are well-established and involve a series of carefully controlled steps to produce high-efficiency devices. From the initial crystal

growth of silicon wafers to the deposition of anti-reflective coatings and metal contacts, each step is important for evaluating the performance and reliability of the final solar cell. Advances in these techniques continue to drive improvements in efficiency and cost-effectiveness, maintaining silicon's dominant position in the photovoltaic market [89].

The deposition technique for silicon (Si) single-junction solar cells involves several intricate steps aimed at fabricating efficient photovoltaic devices. Initially, a Si wafer substrate is prepared, cleaned meticulously, and then subjected to various surface treatments to optimize its electrical properties and surface passivation [90].

Next, a thin layer of intrinsic amorphous silicon (a-Si) or hydrogenated amorphous silicon (a-Si) is deposited onto the substrate using process such as plasma-enhanced chemical vapor deposition (PECVD) or sputtering. This intrinsic layer serves as the absorber material, where photon absorption and electron-hole pair generation occur. Following the deposition technique regarding intrinsic layer, additional doped layers of p-type as well as n-type silicon are deposited sequentially to create a p-n junction, crucial for charge separation and the generation of an electric field. These doped layers are typically deposited using PECVD or thermal diffusion techniques, ensuring precise control over doping concentration and layer thickness [91].

Finally, transparent conductive oxide (TCO) layers and metal contacts are attached onto the cell surface to facilitate electron collection and current flow. Each deposition step is meticulously optimized to achieve the desired material properties and device performance, resulting in the fabrication for high and better efficiency Si single-junction solar cells [92].

2.14.6 Deposition Technique of GeTe Single Junction Cell

The deposition techniques for GeTe single-junction solar cells involve various sophisticated methods that ensure high-quality film formation, precise control over material properties, and scalability for potential industrial applications. Each technique has its own advantages and is chosen based on specific requirements such as film quality, thickness control, and application scale. Advances in these techniques continue to push the boundaries of efficiency and performance for GeTe-based photovoltaic devices [93].

The deposition technique for germanium telluride (GeTe) single-junction solar cells involves a series of steps to create a high-quality thin film suitable for photovoltaic applications. Initially, a germanium (Ge) substrate or an appropriate substrate coated with a germanium layer is prepared and cleaned thoroughly to eliminate any impurities. Deposition of the GeTe thin film is typically taken using physical vapor deposition (PVD) techniques such as thermal evaporation or sputtering. During deposition, GeTe material is evaporated or sputtered onto the substrate surface under controlled vacuum conditions, allowing for precise control over film thickness and composition. Subsequent annealing processes may be employed to evaluate the crystallinity and electrical properties of the GeTe film. Post-deposition treatments such as annealing in a controlled atmosphere or surface passivation techniques may also be utilized to further enhance the film quality and device performance. Careful optimization of deposition parameters and post-processing steps is essential to fabricate GeTe thin films with the desired structural and optoelectronic properties for efficient solar cell operation [94].

2.14.7 Deposition Technique of $CuInSe_2$ Single Junction Cell

The deposition techniques for $CuInSe_2$ single-junction solar cells are varied, each with its own set of advantages and applications. Co-evaporation and sputtering are the most commonly used methods due to their ability to produce high-quality films. Electrodeposition, chemical bath deposition, spray pyrolysis, and MOCVD offer alternative methods that can be cost-effective and scalable. Advances in these techniques continue to enhance the efficiency and performance of CuInSe2 solar cells, making them a viable option for commercial and industrial solar energy applications [95].

The deposition technique for copper indium selenide ($CuInSe_2$) single-junction solar cells involves a series of steps to produce a high-quality thin film suitable for photovoltaic applications. Initially, a substrate such as glass or molybdenum-coated glass is prepared and cleaned to remove any contaminants. The deposition of the $CuInSe_2$ thin film is typically achieved using methods such as co-evaporation or sputtering. In co-evaporation, high-purity copper, indium, and selenium sources are simultaneously evaporated onto the substrate surface in a controlled vacuum environment. This

enables for exact control to the stoichiometry and composition of the $CuInSe_2$ film. Alternatively, sputtering involves bombarding a $CuInSe_2$ target with high-energy ions to dislodge material from the final target surface, which then deposits onto the substrate. Following deposition, the film may undergo annealing processes to promote crystallization and enhance the structural and optoelectronic properties. Post-deposition following treatments like sulfurization or selenium vapor annealing may also be employed to further enhance film quality and device performance. Optimization of deposition parameters and post-processing steps is critical for fabricating CuInSe2 thin films with the desired morphology and electrical characteristics for efficient solar cell operation [96].

CHAPTER 3: DEVICE PHYSICS

3.1 The Basic Semiconductor Concept

Semiconductor solar cells are essentially quite straightforward apparatuses. Semiconductors are able to absorb light and transfer some of the energy related to absorbed photons to electrons as well as holes, which are the carriers of electrical current. The carriers are separated and gathered using a semiconductor diode that preferentially conducts the electrical current produced in that direction. As a result, all that makes up a solar entity is a precisely engineered semiconductor diode which is capable of efficiently absorbing solar light energy and converting it into electrical energy [97].

3.1.1 Effect of Photovoltaic

The photovoltaic impact is a phenomenon that happens when sunlight interacts with a solar cell. Within the cell, this action produces either voltage or electric current. In essence, solar panels use this phenomenon to convert solar radiation into the electrical energy. Then, Edmond Becquerel noted firstly photovoltaic effect some time in 1839 and then Edmond saw that a wet cell's voltage increased when its silver plates were exposed to sunshine. The foundation for our comprehension of solar energy conversion was established by this crucial observation [98].

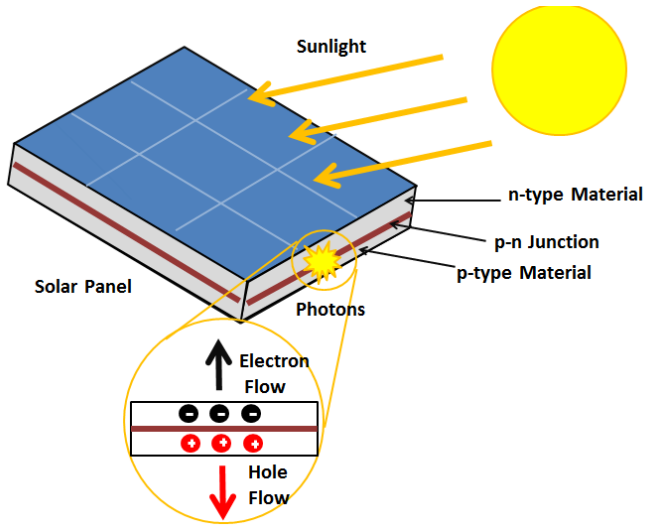

Figure 3-1 : Effect of Photovoltaic on Solar Panel [98].

The interaction between two variation of semiconductors, p-doped and n-doped entity, to produce p-n formation drives the photovoltaic effect in solar cells. Photons of light enter the solar cell and impart energy to semiconductor electrons, pushing them into a higher energy state. As a result, electron-hole pair is formed, also because of electric field which is at junction space, the liberated electrons can now flow through the material. The electrons present in the cell tend to flow towards the negative side rather than the positive side, creating an electric current [98].

3.1.2 Absorbance and Absorption Coefficient

Absorbance is defined as "the log of the proportion of incident to outgoing radiant intensity across an object (excluding the impact on cell barriers)". In contrast, for materials that scattered light, "The inverse logarithm of one less absorptance, calculated on an identical sample" is the definition of absorbance. Absorption is the actual process of collecting photons; however, absorbance is not just used to measure absorption; it can also measure other physical processes caused by the absorption, like reflection, scattering, also attenuation (of transmitted radiant power) [99].

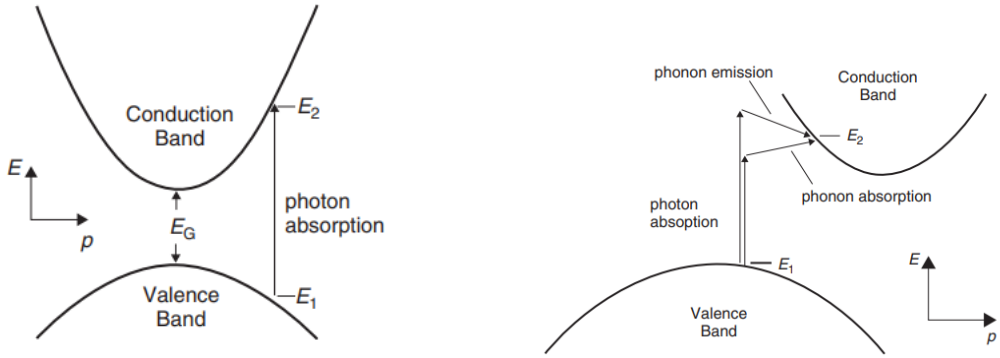

Figure 3-2 : Photon absorption in a direct and indirect bandgap semiconductor [99].

3.1.3 Density of states (DOS)

One important property commonly used in quantum processes of condensed matter field is the Density of States (DOS). The energy levels of phonons, photons or electrons in a crystal are described by this parameter. Understanding the behavior of quantum particles in condensed matter systems depends critically on these energy levels. The electronic DOS measures the energy levels at which electrons in a quantum mechanical system are "packed."

A system's density of state (DOS), often known as the amount of permitted modes or states/unit energy range, is a crucial instrument for assessing its features. It quantifies the several states that an electron can be in at a specific energy level. Important properties of conductive materials, like particular heat, paramagnetic susceptibility and other transporting occurrences, are controlled by this function. Through DOS computations, important information can be extracted by examining the general distribution of states as a function related to the energy as well as the distance between bands of energy in semiconductors [100].

3.1.4 Fermi Function

The Fermi distribution function:

$$f(E) = 1/[1 + \exp((\frac{E-E_F}{KT})] \quad \ldots\ldots\ldots\ldots\ldots\ldots(3.1)$$

here E_F is regarded as Fermi energy, T is the absolute temperature and E is regarded asthe electron energy. In terms of physics, it means that: f(E) is the likelihood where an electron in an instance of being energetic at energy E. Accordingly, f(E) represents the likelihood that an electron is in this condition and 1 - f(E) represents the likelihood that it is empty .The formula shows that for each given energy state at E, the probability of occupancy depends on both the temperature T and the value of Fermi energy E_F [101].

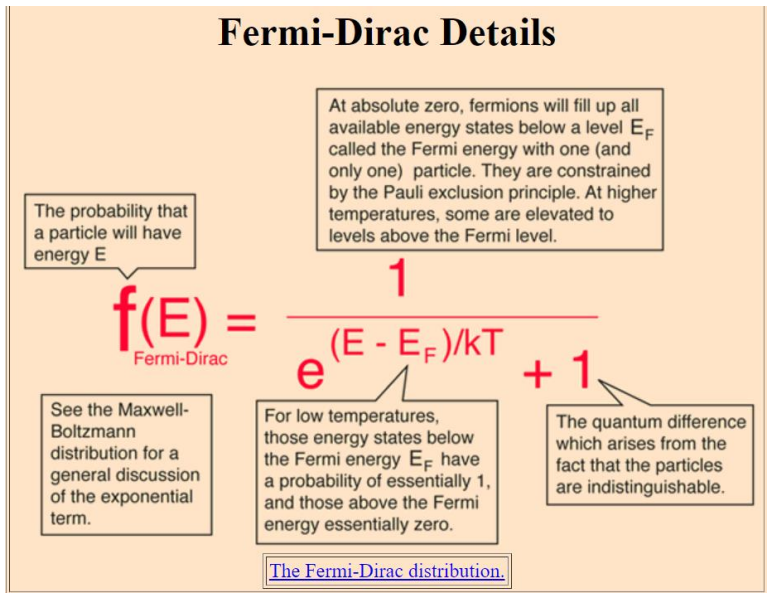

Figure 3-3 : Detailed overview of Fermi-Dirac Function [102].

Therefore, an understanding of Fermi energy seems essential to utilize the electrical as well as thermal instances of solids. The Fermi function indicates the existence of some electrons above Fermi level at higher temperatures. Fermi level performs a significant role towards band theory, especially in doped semiconductors because impurities change the Fermi energy level and change the band gaps of certain semiconductors [102].

3.1.5 Energy Bandgap

The behavior of electrons is very different from that of atoms that are separated in the domain of solid materials. Even while each individual atom has a certain amount of electron energy, when these atoms combine to create solids, the circumstances alter. The electrons in the highest orbit have different energies depending on how close their surrounding atoms are. The neighboring atomic nucleus attracts the electrons in the outermost orbit when two isolated charges get close to one another. As a result, the electron energies are no longer constant; rather, they vary, possibly rising above or falling below their starting points. Electrons have different energies inside the same orbit. The term "energy band" refers to the collection of these various energy levels. Nonetheless, the presence of nearby atoms has no effect on the energy of the electrons in the inner orbit [80].

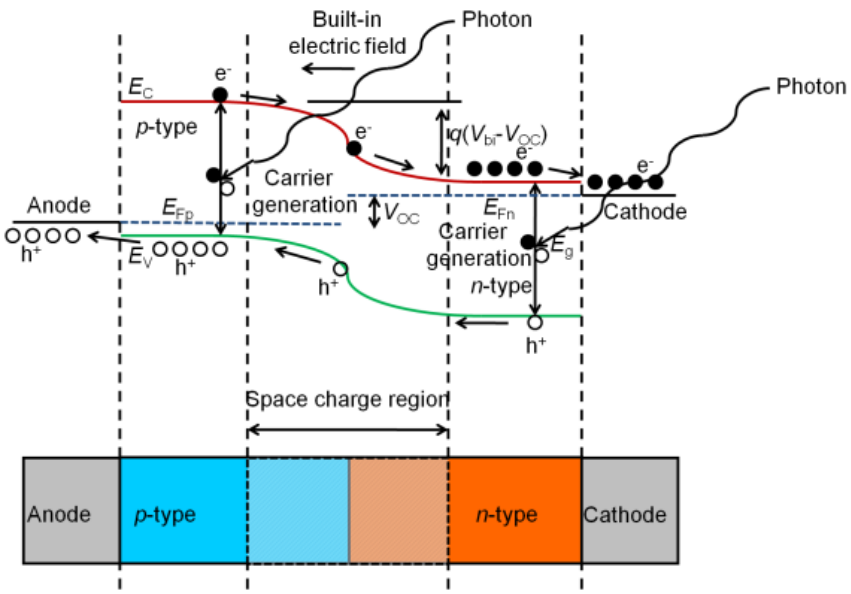

Figure 3-4 : Energy Band Diagram [103].

Solar entities energy band allignment diagram displays the electron's various energies. The diagram of a general silicon semiconductor solar cell consisting of two bands: valence, conduction and an energy gap. Sunlight photons stimulate electrons in valence band in order to move towards conduction band, that in turn form EHPs. The charge carriers are divided by the intrinsic electric field that is at p-n junction, producing a voltage. Through the use of an external circuit, electrons go from n-type zone to p-type zone, creating electricity. Visualizing this process is important for comprehending how solar cells work and how efficient they are.

3.2 Types of Semiconductor

There are two categories into which semiconductors can be divided:

- Intrinsic Semiconductor
- Extrinsic Semiconductor

3.2.1 Intrinsic Semiconductor

An undoped semiconductor, or intrinsic semiconductor, is one that has been painstakingly created to attain extraordinary purity. There is only one elemental species in it. Leading examples of intrinsic semiconductors include germanium (Ge) and silicon (Si). These substances are tetravalent, which means that every atom in them has four valence electrons. These electrons are covalently bound to the atoms at zero degree Celsius, which provides the basis for the atoms special characteristics [104].

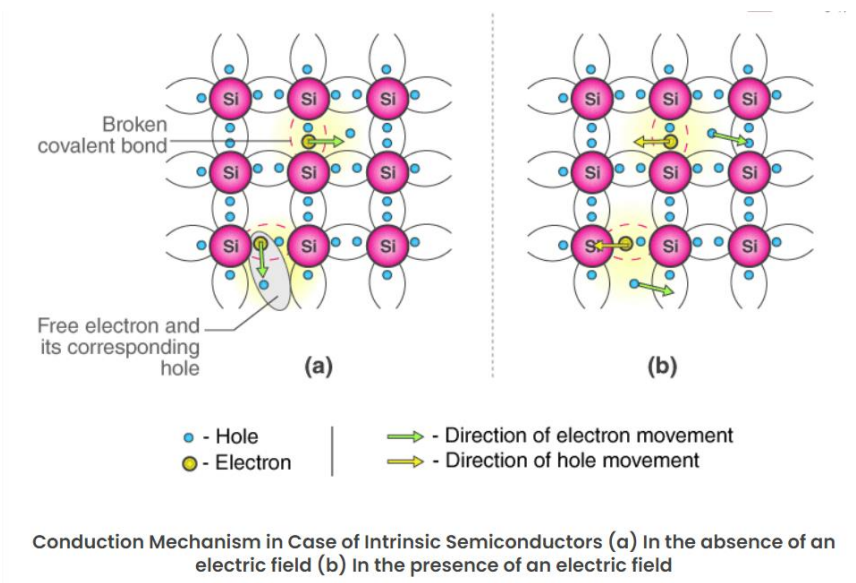

Figure 3-5 : Schematic of Intrinsic Semiconductor [104].

Certain electrons within the lattice receive sufficient energy to escape their bound states when the temperature increases. These freed electrons travel through the substance on a movable basis. Hole formation occurs simultaneously in the first electron locations. These free electrons and holes are necessary for semiconductors to carry electricity. Crucially, there are exactly as many positive charge bearers (holes) as negative charge bearers (electrons). Reduced conductivity, however, can result from ionizing a handful of atoms in the lattice due to an excess of thermal energy [104].

3.2.2 Extrinsic Semiconductor

Here intentional insertion of contaminants into an inherent semiconductor, known as doping, substantially boosts its conductivity. We can manipulate the electrical characteristics of an unprocessed semiconductor material (like silicon or germanium) by deliberately introducing impurity atoms that are either electron-rich or electron-deficient in comparison. Typically, a dopant atom replaces just one atom out of every 107 in a doped semiconductor [104].

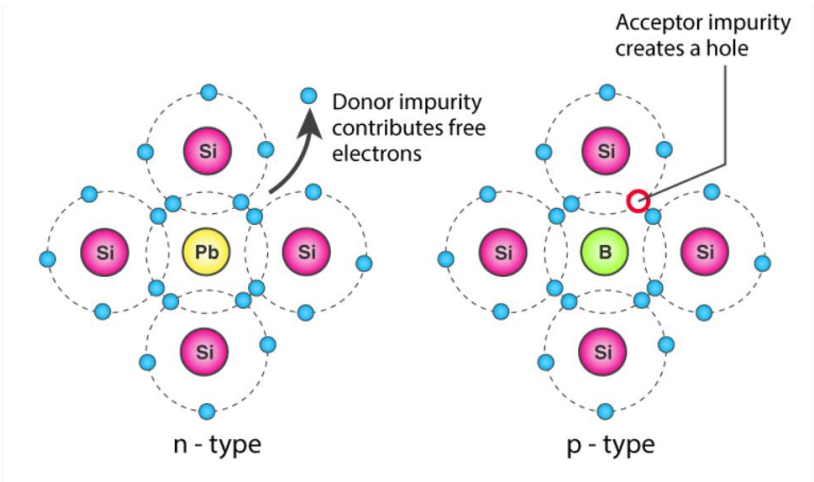

Figure 3-6 : Schematic of Extrinsic Semiconductor [104].

3.3 p-n Junction

A photovoltaic entity is a device consisting two layers: one p-type silicon and one n-type silicon. Because there are greater number of positively charged holes (vacancies) in that p-type layer owing to a shortage of valence electrons, there are more electrons within n-type layer than there are in the others. Near the point where the two layers overlap, the electrons from the n-doped region of the junction travel towards the holes within p-doped region. Thus, electrons fill in the holes surrounding the connection and generate an area known as the depletion zone [105].

3.3.1 p-n Homojunction

When a p-type semiconductor and another n-type semiconductor regions composed of the similar material come together to form a junction, it's known as a p-n homojunction. This structure's p-type area has an enormous amount of holes which are positively charged, while the n region has surplus of electrons that are negatively charged. The diffusion of charge carriers from one region to the other causes an electric field to arise at the junction when these regions come into contact. When the cell is lighted, this electric field aids in separating the photogenerated EHPs, which results in the production of electrical current [106].

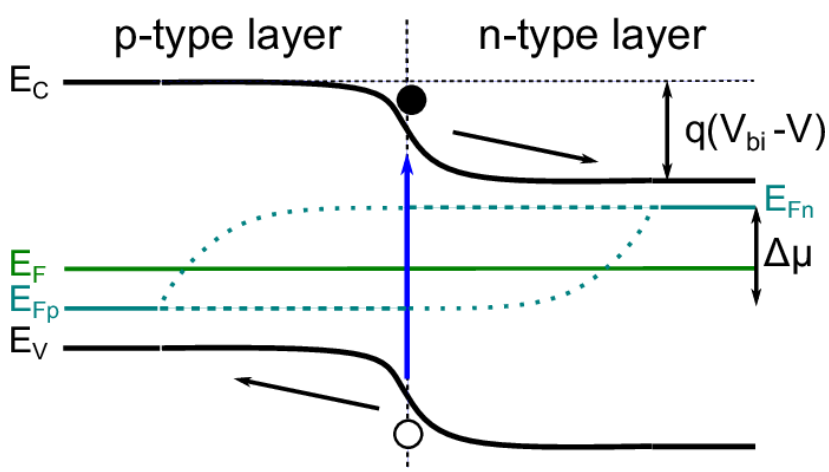

Figure 3-7 : Band Diagram of p-n Homojunction [106].

3.3.2 p-n Heterojunction

Semiconductor area consisting of a p-type along with n-type created a contact area made of different materials is referred to as a p-n heterojunction in a solar cell. In this configuration, one substance has more positively charged "holes" (p-type), whereas the other substance has more negatively charged electrons (n-type). These areas, when in touch with one another, generate an electric field to the interface because of the mismatch in energy levels between the two materials. In order to produce electricity when the cell is illuminated, this electric field helps to separate photogenerated electron-hole pairs. In comparison to homojunctions, heterojunctions provide advantages including improved charge carrier separation and reduced recombination losses [107].

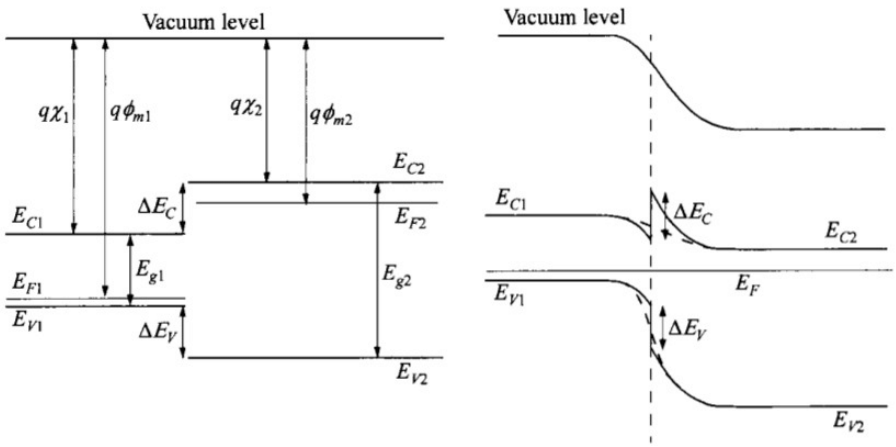

Figure 3-8 : Band Diagram of p-n Heterojunction [107].

3.3.3 Multi-Junction

Multijunction solar cells made of III–V semiconductors are being evaluated globally for possible incorporation into CPV systems with the goal of increasing energy output for utility companies. These cells have an impressive efficiency rate they have been above 40% since 2006 which dramatically reduces the total cost of CPV systems. The majority of concentrator systems in use today favor III-V multijunction cells due to their exceptional performance. However, careful considerations like epitaxial growth to guarantee compatibility of lattice properties among various material systems and the use of low-resistance metal contacts so that it can reach optimal

performance are essential for the effective design of multijunction cells. Optimizing the front metal grid pattern is also necessary to minimize losses from resistance in the semiconductor sheet and gridlines, thus maximizing absorption of light [108].

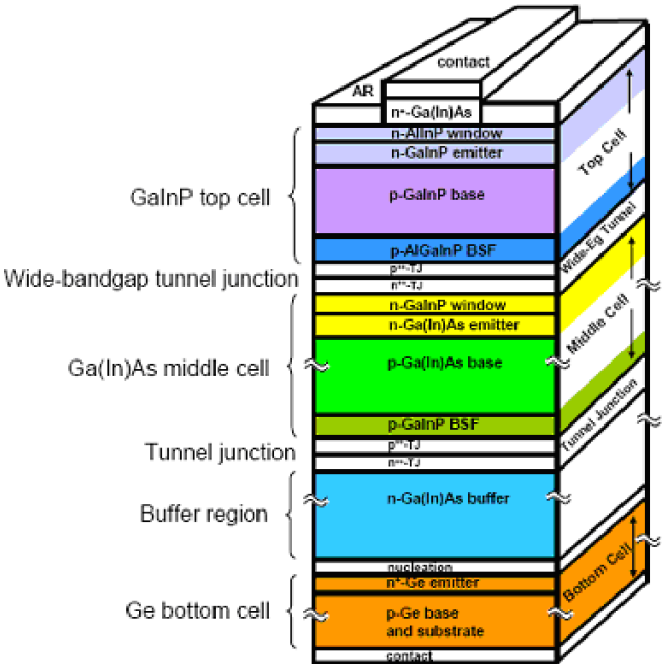

Figure 3-9 : Multi-Junction Solar Cell [108]

The creation of multijunction solar cells, which combine several cells with different bandgap energies, has the ability to greatly enhances efficiency and reach a theoretical maximum of 86.8%. The best options for this purpose are III–V compound semiconductors, which are well-known for having direct bandgaps that guarantee significant absorption and wide spectral coverage. With an astounding 39% efficiency, multijunction solar cells successfully have become the most efficient photovoltaic devices thanks to this clever technique [109].

Various heteroepitaxial and mechanically stacked technologies combined have increased the possibilities for designing novel III-V multijunction photovoltaic cells on the silicon substrates. Elements of III-V on Si multijunction solar cells may be able to achieve efficiencies of over 40% under concentrated sunlight, according to recent advancements in both integration approaches, pointing to a promising future for this technology [110].

3.3.4 Metal Semiconductor Junction

Charge carriers created by sun absorption can be removed from a metal-semiconductor junction, which is the contact involving a metal contact and semiconductor material. As a result of the metal and semiconductor's different work functions, this junction creates an intrinsic potential barrier that aids in keeping the charge carriers apart. To increase the performance of photovoltaic cells, properties of this junction, such as the height of the Schottky barrier, are essential. Electronic and optoelectronic devices rely heavily on metal-semiconductor junctions. The Schottky-Mott rule, which is based on energy level alignment, ideally predicts the height of Schottky barrier that characterizes them. At normal metal-semiconductor ohmic contacts, Fermi-level pinning is often seen [111].

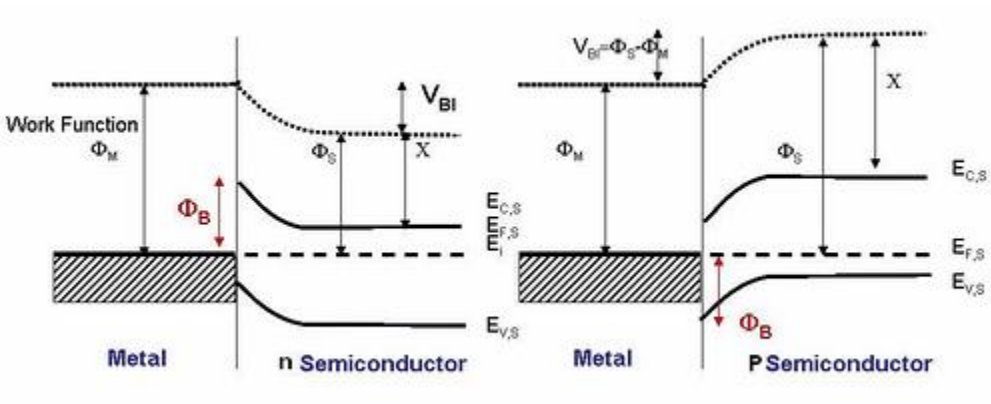

Figure 3-10 : Band Diagram of Metal Semiconductor Junction [111].

Van der Waals metal-semiconductor junctions present an attractive approach to the design of interfaces with almost no chemical disturbance and Fermi-level pinning. Despite using direct chemical bonding, completely level metal films can be laminated into two-dimensional (2D) semiconductor to create these junctions. Work function related to the metal controls the height of the Schottky barrier, a crucial parameter in these junctions. It is possible to carefully control this barrier height to get close to the Schottky-Mott limit. High-performance transistors with superior electron and hole mobilities can be created by transferring metallic films (like silver, platinum) with matching work functions to the conduction along with valence band boundaries of materials like molybdenum sulfide. Moreover, better open-circuit voltage photodiodes can be produced

using unequal interface combinations with different work functions. In conclusion, this novel strategy creates intriguing new opportunities associated with the construction of effective electronic devices based on the metal-semiconductor interfaces and 2D materials [112].

This study confirms the theoretical boundary of metal-semiconductor contacts and offers a non-destructive metal integration method applicable in optoelectronics and high-performance electronics[112].

3.3.5 p-n Junction Diode Equation

The current and voltage in ideal diode are given by the equation as below:

$$I = I_0 \left[\exp\left(\frac{qV}{KT}\right) - 1\right] \ldots\ldots\ldots\ldots\ldots\ldots (3.2)$$

$$V_0 = \frac{KT}{q} \ln\left(\frac{N_A N_B}{{n_i}^2}\right) \ldots\ldots\ldots\ldots\ldots\ldots\ldots\ldots (3.3)$$

Where n_i is regarded as intrinsic carrier density and I_0 is saturation current [113].

3.4 Solar Cell Equation

In the dark, solar cell acts like normal p-n junctions. The solar current is-

$$I = I_0[\exp(\frac{qV}{KT}) - 1] \ldots\ldots\ldots\ldots\ldots\ldots (3.4)$$

In the presence of light, a photovoltaic unit can be compared to current source joined in series with one diode. The illumination current I_L runs in the different like opposite direction with respect to diode current I_D.

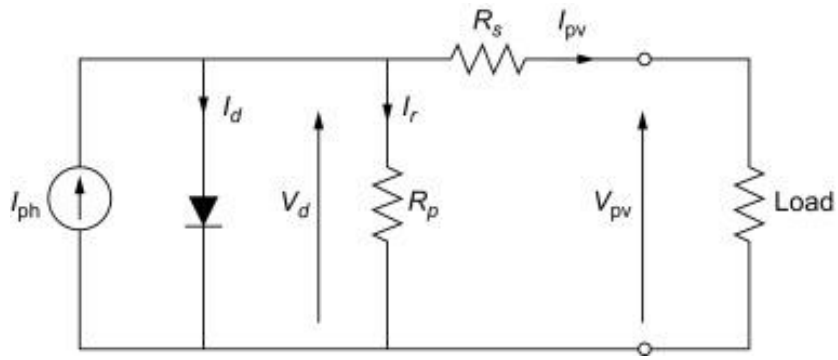

Figure 3-11 : Circuit Diagram of Solar Cell [113].

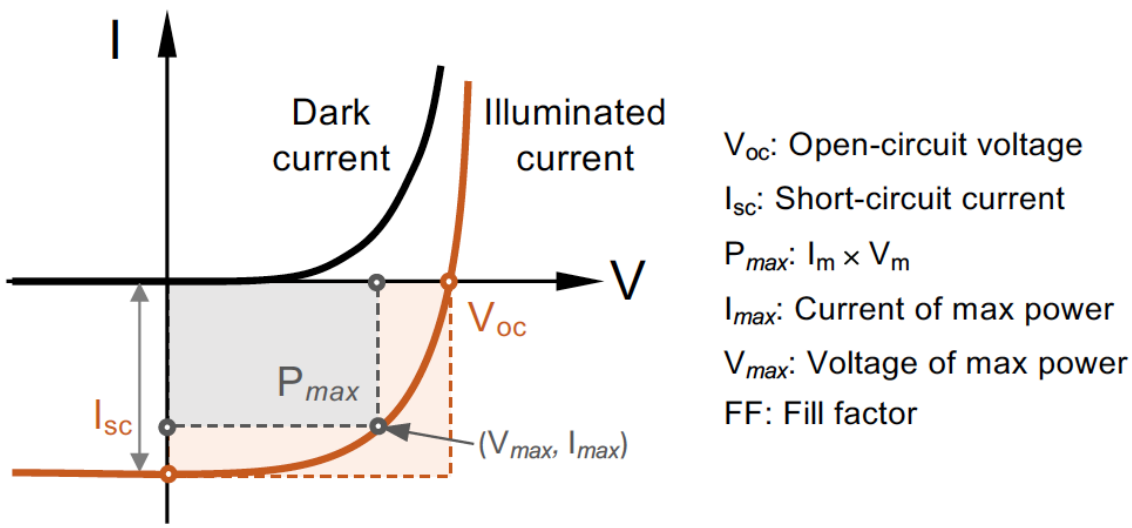

Figure 3-12 : I-V curve of Solar Cell [114].

And the equation are-

$$I = I_0 \left[\exp\left(\frac{qV}{KT}\right) - 1\right] - I_D \ldots\ldots\ldots\ldots\ldots\ldots\ldots(3.5)$$

$$J = J_0[\exp(\frac{qV}{nKT}) - 1] - J_{sc} \ldots\ldots\ldots\ldots\ldots\ldots\ldots(3.6)$$

$$V_{0c} = \frac{nKT}{q}[\ln\left(\frac{I_{sc}}{I_s}\right) + 1] \ldots\ldots\ldots\ldots\ldots\ldots\ldots(3.7)$$

Here J_0 and J_{sc} are the saturation and short circuit current density respectively.

3.4.1 Analysis of Diffusion Length

The average distance that the associated charge travels within a semiconductor determines diffusion length (L_d) including electrons or holes in that semiconductor. Shorter diffusion lengths are a result of increased recombination rates in heavily doped semiconductor materials. When choosing semiconductor materials, higher diffusion lengths-which are a key factor to take into account indicate materials with longer lifespans. "Diffusion" refers to the charge carriers movement as a function of a concentration gradient. Drift is the term for movement brought on by an electric field. If a transient external excitation causes the number of minority carriers to increase over what it would be in an equilibrium situation. The increased minority carriers will eventually return to that equilibrium carrier concentration as a result of and through the process of recombination. The typical requirement of time that charge carrier can sustain in the excited state when EHPs are created before the carrier recombines is known as the minority charge carrier lifespan of a material, and it is represented by the symbol. It is denoted by –

$$D = \mu \left(\frac{KT}{q} \right) \quad \text{.....(3.8)}$$

$$L_D = (D\tau)^{1/2} \quad \text{.....(3.9)}$$

$$L_n = (D_n \tau_n)^{1/2} \quad \text{.....(3.10)}$$

$$L_p = (D_p \tau_p)^{1/2} \quad \text{.....(3.11)}$$

3.4.2 Surface Recombination Analysis

Examining the processes which take place at the surface of semiconductor materials specifically the attachment of charge carriers is the aim of surface recombination studies. Understanding and maximizing the characteristics of semiconductor devices, such photovoltaic cells and photodetectors, depends on this approach. To reduce the loss of charge carriers at semiconductor surface, methods such as time-resolving photoluminescence as well as transient absorption method as spectroscopy are used to assess variables such surface passivation, interface states and surface shape. The goal of improving surface recombination processes is to increase semiconductor device functionality and efficiency for a variety of applications. Surface recombination affects reductions in I_{sc} as well as V_{oc} , which is a critical factor in solar performance of solar entities. Understanding the fundamentals of solar cell operation requires precise calculation of recombination losses. A comprehensive impedance model is offered, connecting electronic kinetics at the interfaces with capacitive and resistive processes. It has been found that carrier collecting losses, which affect photocurrent, are 1%. Moreover, a decrease of 0.3 V compared to the general radiative range is attached to the reduction in surface hole concentration and photovoltaic loss [114].

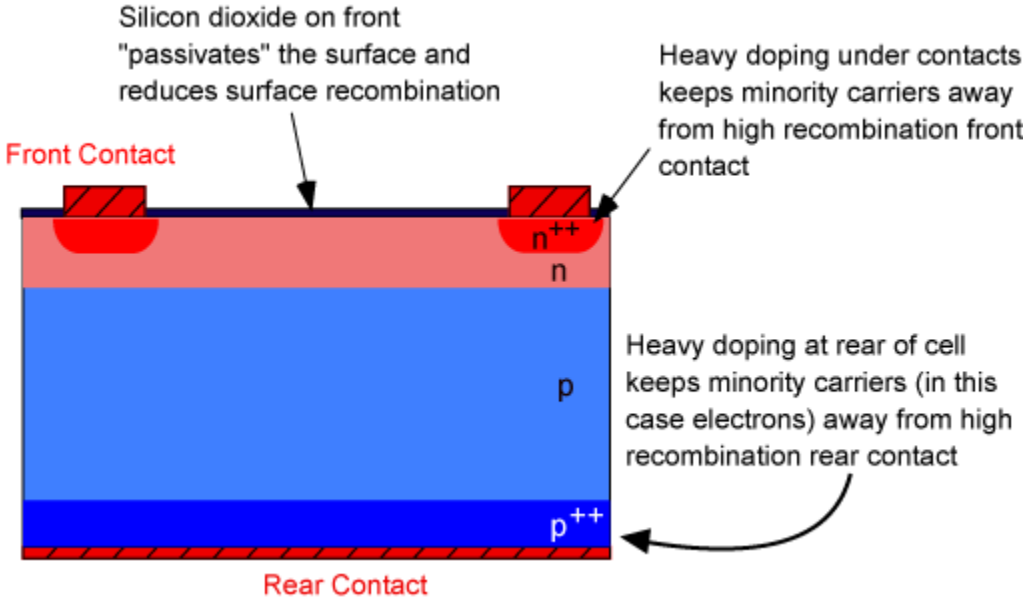

Figure 3-13 : Surface Recombination Analysis [114].

In solar cells, surface recombination is important because it affects the I_{sc} and V_{oc}. Particularly high recombination rate occurs at a solar cell's top surface, where carrier synthesis is strongest, and this has a harmful circumstances towards short-circuit current. A "passivating" layer is put to

the top surface to lessen the amount of hanging silicon bonds in order to lessen this. Considering its lack of imperfection states, a thermally produced silicon dioxide layer is frequently utilized for surface passivation in the electronics industry. Other dielectric layers, like Silicon Nitride, are also used in commercial solar cells. Nevertheless, the treating coating cannot be placed to areas where there is an ohmic metal contact because it is typically an insulator. Instead, surface recombination is reduced by increasing doping beneath the top contacts. The contact zones have no impact on carrier collection, despite the fact that severe doping typically minimizes diffusion length. When a more-recombination surface is near towards the junction area, the most effective course of action for lowering recombination is to maximize doping [115].

3.4.3 Work Function

Electrons are present in the valence bands upto the Fermi energy level (E_F). The term "work function" refers to the energy differential coupling regarding Fermi levels and vacuum levels. We call this energy requirement for removing an electron from a metal the work function. The state of a surface when it is being used has a big impact on its work function. The development of surface processes or surface pollution can have a significant impact on the work's execution.

3.4.4 Loss Mechanism

There are several types of losses that lead to lower solar cell efficiency, including optical, recombination, transmission losses and so on. Here is a brief summary of these losses.

3.4.4.1 Optical Losses

When light is reflected, absorbed or transmitted without becoming electrically charged, solar cells experience optical losses. The efficiency along with power output of the cell are impacted by these losses. Optimizing material composition, enhancing cell design and applying anti-reflective coatings are some methods to lower optical losses. Enhancing solar cell performance and optimizing the production of renewable energy requires addressing these losses. The short-circuit

current is mostly impacted by optical losses, which reduce solar cell power. The light that was bounced off the front surface or didn't get absorbed, leading to the absence of an electron-hole pair, is known as optical losses. Since visible light (350–780 nm) contains sufficient energy to produce electron–hole groups, all the visible light should be absorbed by semiconductor solar cells [116].

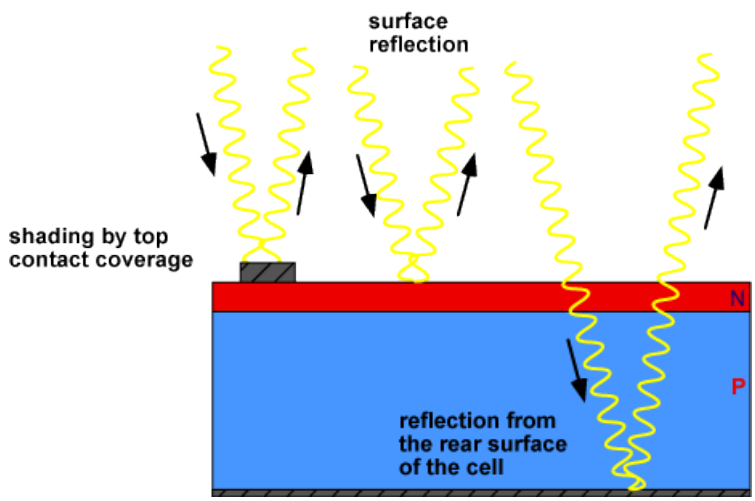

Figure 3-14 : Optical losses in Solar Cell [116].

3.4.4.2 Recombination Losses

Current gathering (short-circuit current) also forward bias injection current (open-circuit voltage) are all affected concurrently by recombination losses. The majority of the time, the criterion used to classify recombination is in area of cell where it occurs. Surface recombination and bulk recombination are the two forms of recombination that happen most commonly. Another possible spot for recombination to occur is the depletion region.

3.4.4.3 Losses Due to Spectral Mismatch

'Spectral mismatch' describes the inaccuracy that results from a discrepancy between the test and standard spectrums. The absorber layer of solar cells is often composed of a semiconductor material whose complex refractive index and band gap energy (E_g) characterize its special optical

features. Electron-hole pairs are theoretically formed only by photons whose energy exceeds band gap allignment energy of the absorber. Since holes and electrons normally occupy the energy levels present at the lower portion of the conduction band and top of the valence band, respectively, the surplus energy from photons are liberated as heat into semiconductor lattice during the thermalization procedure. It is not possible for photons to form electron-hole pairs when their energies are lower than the semiconductor absorber's band gap. Consequently, these photons aren't included in the conversion process. The two major losses present in the conversion process are the losses of the photons along with energy lower than bandgap as well as the losses of the photons consisting energy higher than bandgap.

3.4.5 Fermi Level

The upper bound of level of the electron energy at zero temperature is illustrated by the Fermi level, according to Fermi-Dirac statistics. Electrons follow Pauli exclusion principle and occupy the smallest energy phenomena at absolute zero, forming a "Fermi sea" of electron energy condition. The greatest energy level that electrons can occupy at this temperature is represented by the Fermi level, which is the sea's surface. The majority of common processes involve energies well below the Fermi energy of metals, restricting interactions to a shallow depth described as "ripples on the Fermi sea " [116].

3.4.6 Intrinsic Carrier Density

Conductivity is impacted by temperature and band gap concentration of intrinsic carriers, which include holes and electrons and contribute to conduction in materials. A thorough understanding of intrinsic carrier concentration is necessary to maximize the effectiveness of photovoltaic units. Free carriers develop within valence band as well as conduction band of semiconductors when a carrier accumulates thermal energy and moves from valence band towards conduction band. This is similar to making a jump over an energy gap. The density of these carriers is indicated by the intrinsic carrier concentration, or (n_i). Now let us think about intrinsic materials: genuine semiconductors that do not undergo any impurity-induced alteration. Stated differently, their

carrier concentrations have not been altered by "contamination." Intrinsic carrier density of an intrinsic material is determined by the amout of p-type holes within valence band and electrons present within conduction band. The temperature and band gap of the material are two crucial factors that affect the carrier population. Wider band gaps are associated with lower intrinsic carrier concentrations in materials since it is difficult for carriers to heatly cross such a large gap. Contrarily, increasing the temperature causes more electrons to enter into conduction band, which increases the intrinsic carrier concentration. It's interesting to note that solar cell efficiency is significantly affected by this innate carrier concentration. Thus, these carriers are vital whether we're using sunshine or delving into the intriguing world of semiconductors [117].

3.5 Basic Structure of Solar cells

Usually, a thin-film photovoltaic cell consist of many layers that are placed on a substrate. These layers usually consist of a back contact layer, a transparent conductive oxide (TCO) layer and an absorber layer and a window layer. This design makes it possible so that sunlight can be absorbed and electricity can be produced inside of a lightweight, thin device.

(a) Substrate: When building devices that use TFSC, both a substrate structure and a superstrate structure are viable options. A substrate's interface is transparent and the contact is made by applying a conductive oxide layer on the substrate. When it comes to substrate layout, the substrate is composed of metal or a metal plating on a polymer or glass substrate that also acts as the contact.

(b)Transparent conducting oxide (TCO): "Transparent conducting oxides" are n-type mismatched semiconductors that exhibit remarkable degrees of transparency and efficient electricity conductivity throughout the visible spectrum. As a result, this specific layer has less resistance connection, which allows the absorber layer to receive the majority of the light.

(c) Window layer: In a heterojunction, this layer's main job is to create a junction associated with absorber layer and also making sure that the absorber layer and junction region may receive the maximum amount of light possible. Photocurrent does not originate from the window layer by itself. Maintaining a minimum series resistance requires the window layer's bandgap to have the

maximum theoretical value and the lowest thickness feasible. As a result, resistive loss will be minimized and the maximum optical throughput will be achievable.

(d) Buffer layer: In thermofluidic solar cells (TFSCs), the p-n junction is produced by the combination of two distinct material types: the buffer and absorber layers. These materials differ from one another in terms of bandgap and/or band edge position. Similar to other types of solar cells, TFSCs also require this p-n junction in order to achieve an elevated level of effectiveness.

(e) Absorber layer: The semiconducting material that makes up the absorber layer is commonly thought of as the "heart" of all TFSC. Being the layer that takes in the greatest amount of photons, which leads to electrons migrating into the conduction band and creating photocurrent, this specefic layer is considered as the "photoactive layer".

(f) BSF: Reducing the quantity of carrier recombination at the backside contact surface is intended to enhance the effectiveness of photovoltaic units. Using BSF makes this possible. If a BSF with a high doping concentration was positioned, carriers may be kept from recombining within absorber layer along with the rear contact in the middle.

3.5.1 Equivalent Circuit of Solar Cells

A theoretical circuit diagram that depicts a device's electrical properties is presented through equivalent similar circuit model. It is noteworthy that the components depicted in the model are absent from the actual devices. Rather, these models aid in the visualization and simplification of computations concerning the activity of the cell. These models are very helpful in explaining certain events, comprehending basic device physics and designing more effective devices [118].

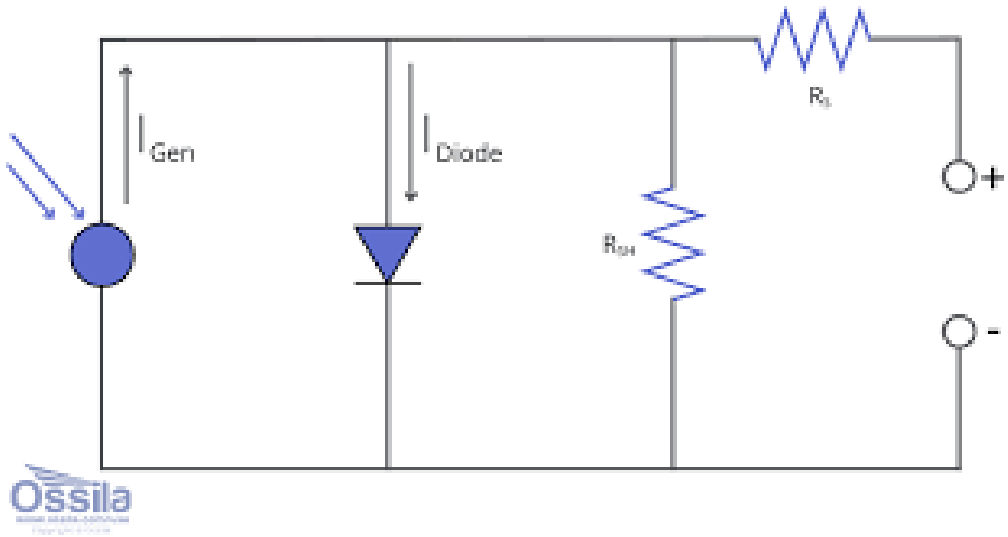

Figure 3-15 : Equivalent Circuit of a Solar Cell [118].

3.5.2 Light Absorption in Solar Cells

In the solar cell, light absorption happens when photons from the sunlight are collected by the semiconductor material, creating pairs of electrons and holes. The photovoltaic effect, in which energized electrons produce an electric current, depends on this absorption criteria. Efficiency of a photovoltaic cell is relied on its capacity to absorb visible and near-infrared solar radiation and transform it into electrical energy that will be utilised. To improve overall performance and efficiency, solar cell design and optimization prioritize maximum light absorption.

The absorption in the visible and UV bands is found to be dominated by the perovskite layer, whilst the IR bands are dominated by the electrode layer. To produce significant optical absorption within IR band, that hasn't been explored yet, we suggest using a closely-spaced named plasmonic nanoparticle material array to optically boost the photon collection in the perovskite layer. The idea is to generate hot spots in active layers using plasmonics, that through nonlinear absorption mechanisms and light-flow-circulating processes, can greatly boost the localized area as light absorption within perovskite material. Under ideal circumstances, a 58.2% IR-band absorption augmentation has been reported in the study [119].

3.6 Characteristics Parameters

The major component of photovoltaic energy systems is solar cell, often regarded as photovoltaic cell. Using the photovoltaic effect to directly convert light into electrical energy. When exposed to light, it functions as a semiconductor device and produces electricity. While its current capacity is correlated with both exposed surface area and incident light intensity, the voltage between its terminals stays constant at about 0.5 volts. It has positive and negative terminals with a semiconductor p-n junction positioned between them, just as other battery cells. Some photons from the sun are collected by a solar cell, which excites the electrons and produces electron-hole pairs. Electrostatic forces cause these pairs, often referred to as light-generated electrons as well as holes, to move in towards opposite directions in p-n junction area of the specefic cell. To facilitate the flow of current when linked to an external circuit, this produces a potential difference across the cell. A solar cell's performance and efficiency and consequently its rating, are based on a number of factors that dictate how well the cell transforms light into electricity. Picking a solar cell for a given project requires an understanding of these factors [120].

3.6.1 Short-Circuit Current

Shorting the cell's terminals while it is in the best possible condition to produce the highest output allows one to measure a solar cell's maximum current. The reason for using the term "optimized condition" is that, for a exact evaluated unit quantity, the rate at which a solar cell produces current also depends on the light's level and angle of incidence. Peak current density should be indicated instead of maximum current since the dimension of the cell accessible to light affects current production as well. One can get the highest possible current density as well as short circuit current intensity grade of a cell by dividing its highest or short circuit current to the exposed space called surface area.

$$J_{sc} = \frac{I_{sc}}{A} \quad \text{.....(3.12)}$$

here A is regarded solar entities area, J_{sc} is the maximum current density, and I_{sc} is short circuit current [120].

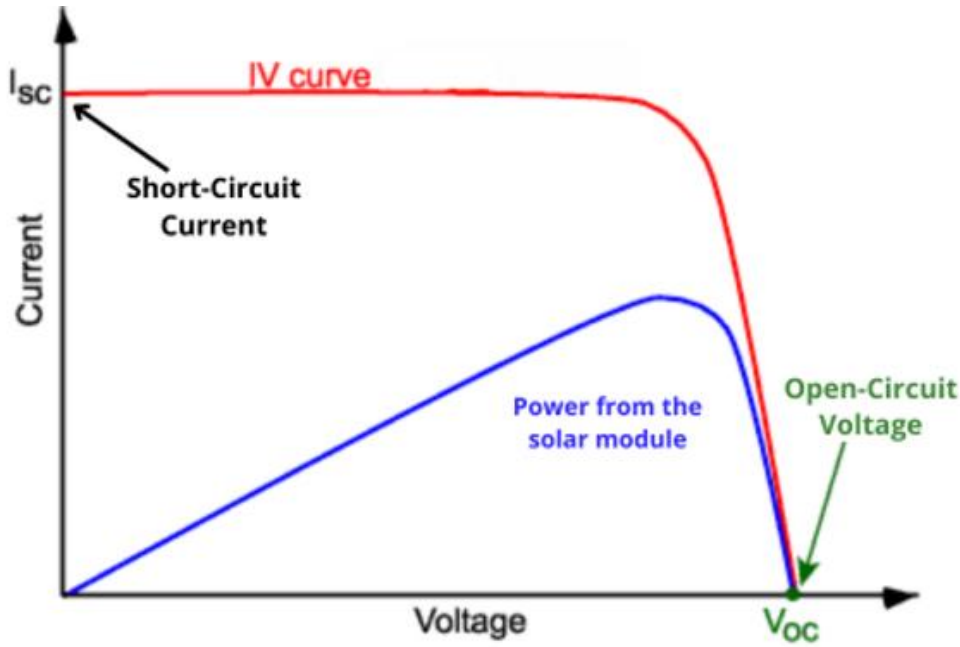

Figure 3-16 : Short Circuit Current vs Open Circuit Voltage [119].

3.6.2 Open circuit voltage

"Open circuit voltage," or V_{oc} for short, is the peak voltage which can be captured from a photovoltaic cell when zero current is running through it. When light creates current at the solar cell junction, bias is formed by that current and the open circuit voltage on the solar cell is roughly equal to the amount of forward bias. Setting total current to zero, one can establish a V_{oc} equation which can be written as-

$$V_{0c} = \frac{nKT}{q}\left[\ln\left(\frac{I_L}{I_0}\right) + 1\right] \ldots\ldots\ldots\ldots\ldots\ldots(3.13)$$

In this case, the Boltzmann constant is K, the saturation current is I_o and the photogenerated current is I_L [98].

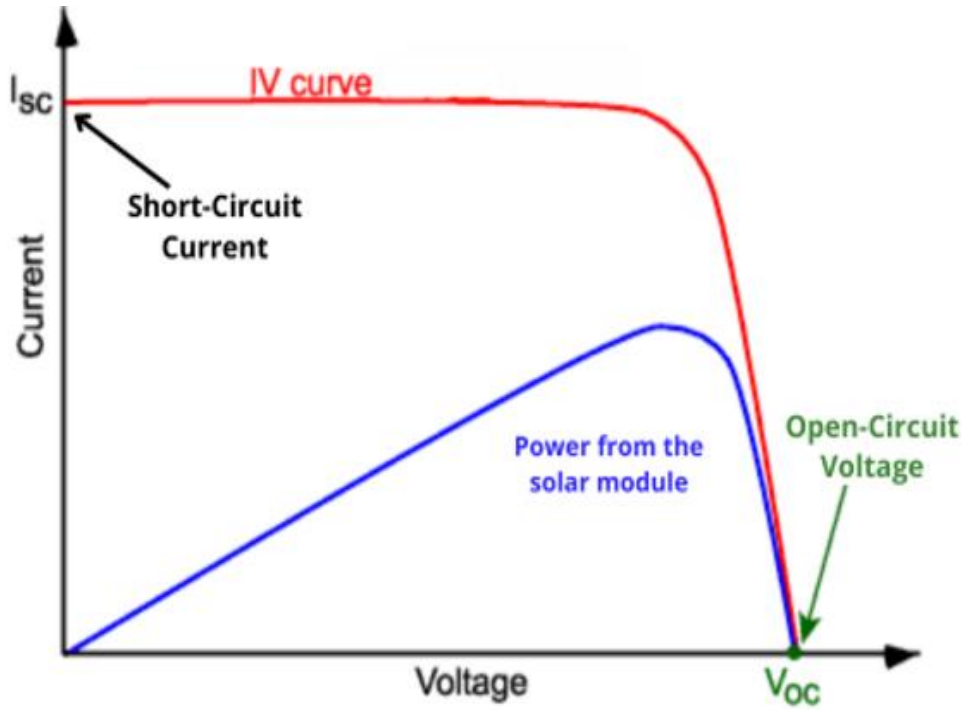

Figure 3-17 : Open Circuit Voltage vs Short Circuit Current [120].

3.6.3 Fill factor

The peak current along with voltage from a photovoltaic unit are known as the short-circuit current as well as the open-circuit voltage, respectively. The solar cell's power is 0 at each of these operational positions, though. Together with V_{oc} and I_{sc}, the "fill factor," or simply "FF," is a indicator that helps to understand the peak power that a solar cell can produce. The FF can be regarded as the following: the ratio related to solar cell's maximum power with the product of V_{oc} and I_{sc} can be written such that-

$$\text{FF} = \frac{V_{MP} I_{MP}}{V_{oc}\, I_{SC}} \quad \text{.....(3.14)}$$

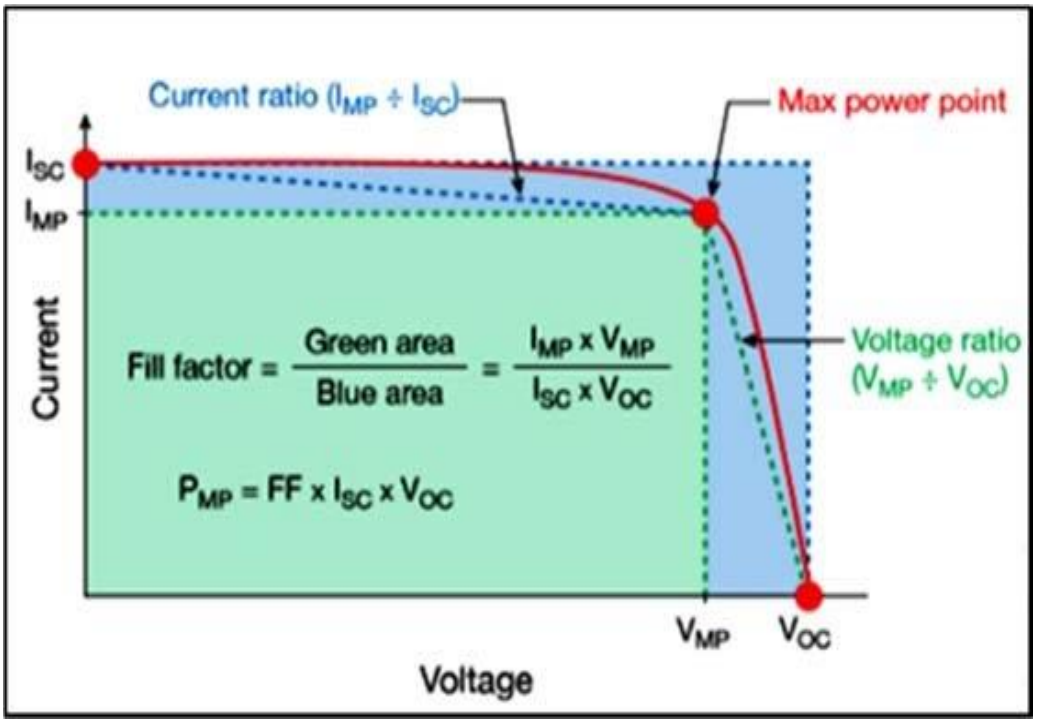

Figure 3-18 : Fill Factor [121].

Graphically, the area covering the greatest rectangle that will be adjusted in the IV curve is represented by the FF, which also demonstrates as a gauge to the solar cell's "squareness". Below is an example of the FF [122].

3.6.4 Conversion efficiency

With increased dependability, solar energy is swiftly rising to the top of the list of renewable energy sources that are frequently utilized in commercial and residential setting. A solar cell's efficiency guarantees that the installed hardware will be used to its fullest potential. Performance is regarded as ratio towards a solar cell's output with its input of solar radiation. One helpful parameter for evaluating the performance of various solar cell types is efficiency. The temperature of the environment and the spectrum and intensity of the incident sunlight have a big influence on how efficient solar cells are [123].

The total percentage regarding incident power that photovoltaic cell may transform to electricity is known as its efficiency:

$$\mathbf{P_{max} = V_{oc} I_{sc} FF} \quad \ldots\ldots\ldots\ldots\ldots\ldots\ldots\ldots (3.15)$$

$$\boldsymbol{\eta} \mathbf{= (V_{oc} I_{sc} FF) / P_{in}} \quad \ldots\ldots\ldots\ldots\ldots\ldots\ldots (3.16)$$

The variables V_{oc}, I_{sc}, FF and η represent voltage, current, and efficiency, respectively, in the context of short- and open-circuit operations [123].

CHAPTER 4 : RESEARCH METHODOLOGY

4.1 Introduction

Creating a model using an extensive set of validated parameters is the most important stage before modeling a solar cell. The approach starts with numerical design, then moves on to explore different simulation techniques, aspects of cell design, differentiating features at different levels, and explaining the component layers. A few notable programs for simulating solar cells are ASA (Advanced Semiconductor Analysis), PC1D (Personal Computer One Dimensional), ISE-TCAD (Integrated Systems Engineering), AMPS (Analysis of Microelectronics and Photonic Structures), and SCAPS (Solar Cells Capacitance Simulator). This task was performed with SCAPS-1D. Modeling solar cells is useful because it makes it easier to make forecasts before production starts. Without the use of simulation tools, adjusting cell properties and figuring out ideal sizes can be difficult due to the large number of variables involved.

4.2 Designing of Cells

The initial and most important step before the simulation starts is to set up the cell structure. This includes defining the cell as a whole in its whole using a variety of parameters that come from different levels. These parameter values are modifiable within acceptable limits determined by the properties of the material. Numerous curves, including characteristic curves, energy band diagrams, generation and recombination rates, electric fields and quantum efficiency curves, can be produced after simulation. Characteristic parameters like the open circuit voltage (V_{oc}), short circuit current density (J_{sc}), fill factor (FF) and efficiency can then be determined using the simulation findings.

4.3 Simulation Softwares

A few notable programs for simulating solar cells are **:**

- ASA (Advanced Semiconductor Analysis)**.**

- PC1D (Personal Computer One Dimensional).
- ISE-TCAD (Integrated Systems Engineering).
- AMPS 1D (Analysis of Microelectronics and Photonic Structures).
- SCAPS 1D (Solar Cells Capacitance Simulator).

4.3.1 AMPS-1D

The acronym AMPS stands for Analysis of Microelectronics, a software developed by S. Fonash and his team at Pennsylvania State University for physics device analysis and device design, particularly for photonic structures. It is compatible with Windows 95 and later versions. AMPS allows for concurrent simulation of multiple problems in separate windows. It supports up to 19 layers for a single device, with simulation parameters such as band gap and mobility being temperature-independent. However, factors like wavelength and absorption coefficient need to be inputted manually. Compared to other modeling tools, AMPS is relatively slow in problem-solving. Key features of AMPS-ID include:

- Excellent user interface with adaptability for visualizing programs.
- Comprehensive user manual for guidance.
- Batch processing capability for simulations.
- Ability to simulate recombination of both band-to-band and Shockley-Read-Hole types.
- Mobility gaps are distinct from optical gaps.
- Limitation to a maximum of 400 mesh points and 19 layers.
- Manual input required for all information.
- Only binary files can be read or modified; text files are not supported [124].

4.3.2 PC1D

Basore and his team developed this program, initially crafted by Sandia National Labs and established at UNSW in Australia. While originally intended for crystalline Si cells, it appears unconventional to utilize this program within a thin-film context. The program's standout feature lies in its straightforward user interface, simplifying the setup of new problems. However, a notable drawback is its limitation to only five layers for device simulation, considered a primary

issue with the software. Nonetheless, it enables simulation of standard IV and spectral response, with results conveniently displayed in separate windows, facilitating easy data replication. Key attributes of PCID include:

A clean and user-friendly interface.

- Swift operation.
- Menu system facilitating parameter adjustments.
- Challenges in modeling a-Si solar cells.
- Constraint on the number of layers, limited to a maximum of five.
- Insufficient graded layers for CIGS devices [125].

4.3.3 wxAMPS

To simulate solar cells, the wxAMPS software was developed as an extension of the existing AMPS simulation program. wxAMPS utilizes a cross-platform library to generate wx widgets and a kernel interface, which is an enhanced iteration of the original AMPS code. Within the wxAMPS code, models for drift-diffusion and intra-band tunneling are integrated, with the latter being specifically designed for heterojunction solar cells. Furthermore, the wxAMPS program underwent modifications to merge Newton and Gummel models, in addition to incorporating intra-band tunneling and trap-assisted tunneling. The foundational principles for these enhancements were drawn from the AMPS software. Notably, the wxAMPS system enables file sharing through a database-oriented WIKI platform. Supported materials in wxAMPS include crystalline Si, CdTe, and CdGe thin films. It also allows simulation of tandem structure solar cells utilizing the traps-assisted tunneling model [126]. Key features of wxAMPS encompass:

- wxAMPS serves as an updated rendition of AMPS, a solar cell simulation tool.
- Emphasis is placed on the performance evaluation of heterojunction solar cells.
- It possesses the capability to read and process various file formats, including spectral files and associated data.
- User-friendly interface facilitating ease of operation.
- Analysis can incorporate an arbitrary number of wavelengths.

4.4 SCAPS-1D

For the simulation of photovoltaic cells, SCAPS (Solar Cell Capacitance Simulator) stands out as the most prominent program. Alongside Alex Niemegeers and Marc Burgelman, scholars such as Koen Decock, Stefaan Degrave and Johan Verschraegen have contributed to its development. SCAPS-1D is commonly utilized for one-dimensional photovoltaic (PV) applications. This software accommodates input from seven independent semiconductor layers, incorporating interactions from both the front and back of the cell. Utilizing these equations, SCAPS solves the fundamental semiconductor equations to assess various parameters of a device, including open-circuit voltage, short-circuit current, fill factor, power conversion efficiency and spectral response (QE). The design of the device is guided by two main objectives: firstly, achieving the realization and verification of actual system characteristics, followed by simulating devices based on given parameters to predict their outcomes. The functional or input parameters of the design system are derived from experimental data obtained from a referenced device. Additionally, all values can be computed as a function of temperature, under both illuminated and dark conditions [127].

4.4.1 SCAPS Parameters

Device design starts with input variables or physical parameters, which are used to solve simple semiconductor calculations. Table 4.1 shows the physical parameters that this program uses for numerical analysis, including layer thickness, electron-hole mobility, intrinsic carrier concentration, electron affinity, band difference and defect density in absorber, buffer and window layers. For simulation, a light source with a power density of 100 mW/cm^2 and a wavelength of 1.5AM solar radiation is used. Table 4.2 shows the different ways that solar cells work.

Table 4.1: Physical Parameters for Numerical Modeling

No. Parameters	Abbreviation	Unit
Layer Thickness	W	μm
Bandgap Energy	E_g	eV
Conduction Band Effective Density of States	N_c	cm^{-3}
Valence Band Effective Density of States	Nv	cm^{-3}
Dielectric Permittivity	ε_r	

Table 4.2: Functional Parameters

No. Parameters	Abbreviation	*Unit*
Power Conversion Efficiency	PCE	%
Short Circuit Current	Jsc	mA/cm^2
Open Circuit Voltage	Voc	V
Fill Factor	FF	%

4.4.2 Action Panel Interface

The initialization panel guidance for the SCAPS simulator is illustrated in Fig. 4.1, depicting segmented divisions numbered sequentially from 1 to 6. The startup interface of the SCAPS-1D simulator in Figure 4-1 presents a cell structure that facilitates easy simulation and calculation of parameters based on material properties.

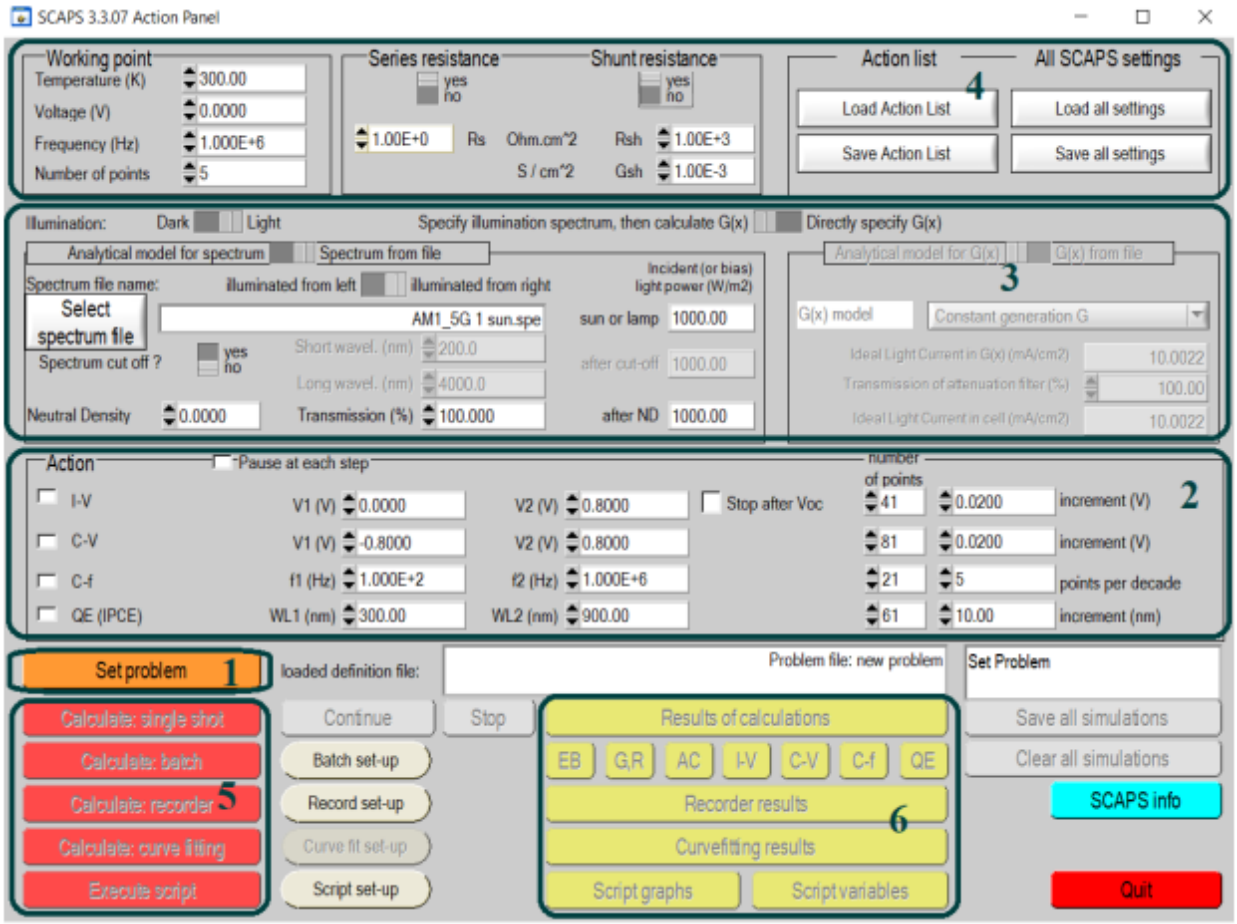

Figure 4-1 : SCAPS−1D Simulator Startup Panel Interface

An overview of these sections is outlined as follows:

(a) Section 1 defines a distinct layer within the unit layout, encompassing both front and back interactions. This program allows simulation of up to seven levels of hierarchical apparatus.

(b) Section 2 discusses configuring a photovoltaic system with defined display, incorporating both back and front contacts. Users have the option to illuminate the device from either the front or back contact side, along with adjusting applied voltage and current.

(c) Section 3 provides essential keys for loading system structure definition files and saving definition files in the library. The Cancel and OK buttons, as well as the Back button, enable users

to navigate back to the initialization screen after exiting or entering the device description interface, respectively.

4.4.3 Interface of Problem Statement

The problem is primarily discussed in terms of detailing the physical attributes of various interface layers. When we click the "Set issue" button, a new interface appears allowing us to identify the diverse physical properties of the layers. Figure 4-2. provides a visual depiction of this interface, also known as the "Device Definition Interface."

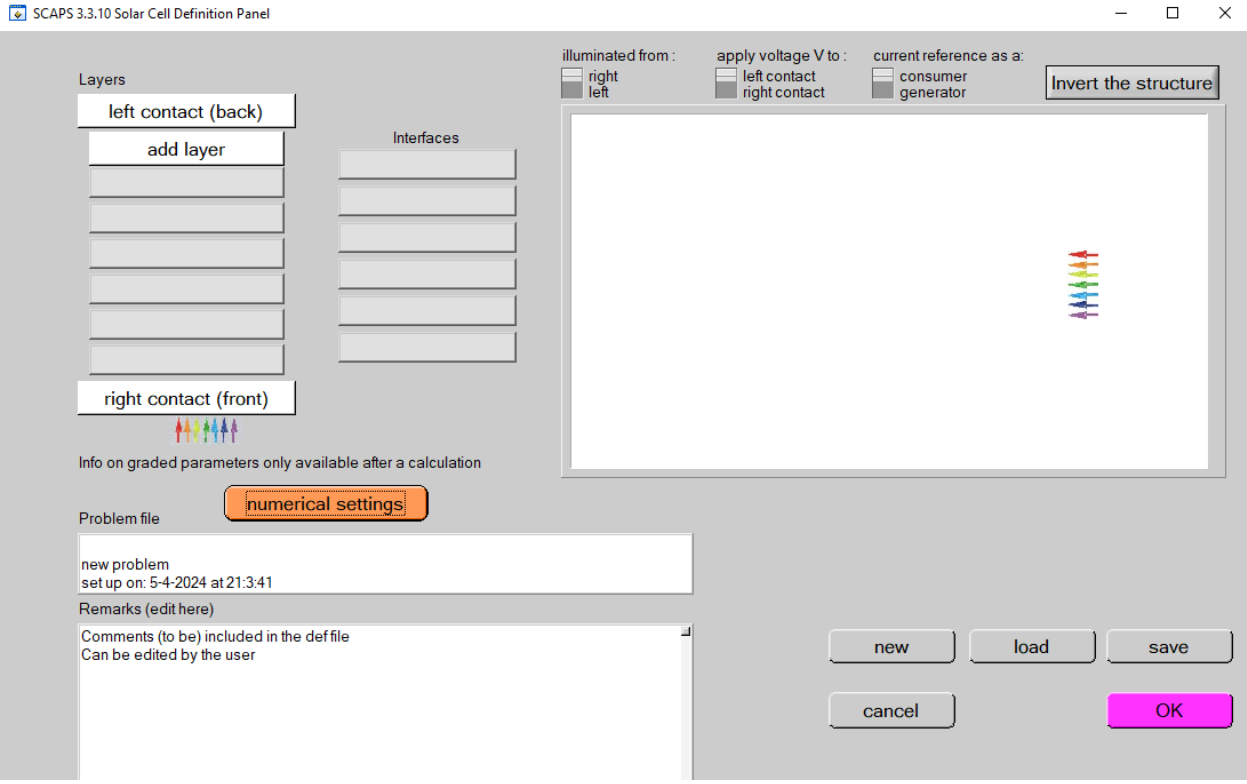

Figure 4-2 Device Definition Interface

4.4.4 Device Structure Panel

To incorporate or define layers within the software utilized for modeling a PV system, you can achieve this by selecting the "add layer" button visible in section 1 of Figure 4-3. A single click with the mouse will activate the program, revealing the properties of the layer. Within the layer

properties interface, users have the option to either establish or introduce new values for the physical parameters of the layer. Figure 4-3 provides a visual representation of the user interface.

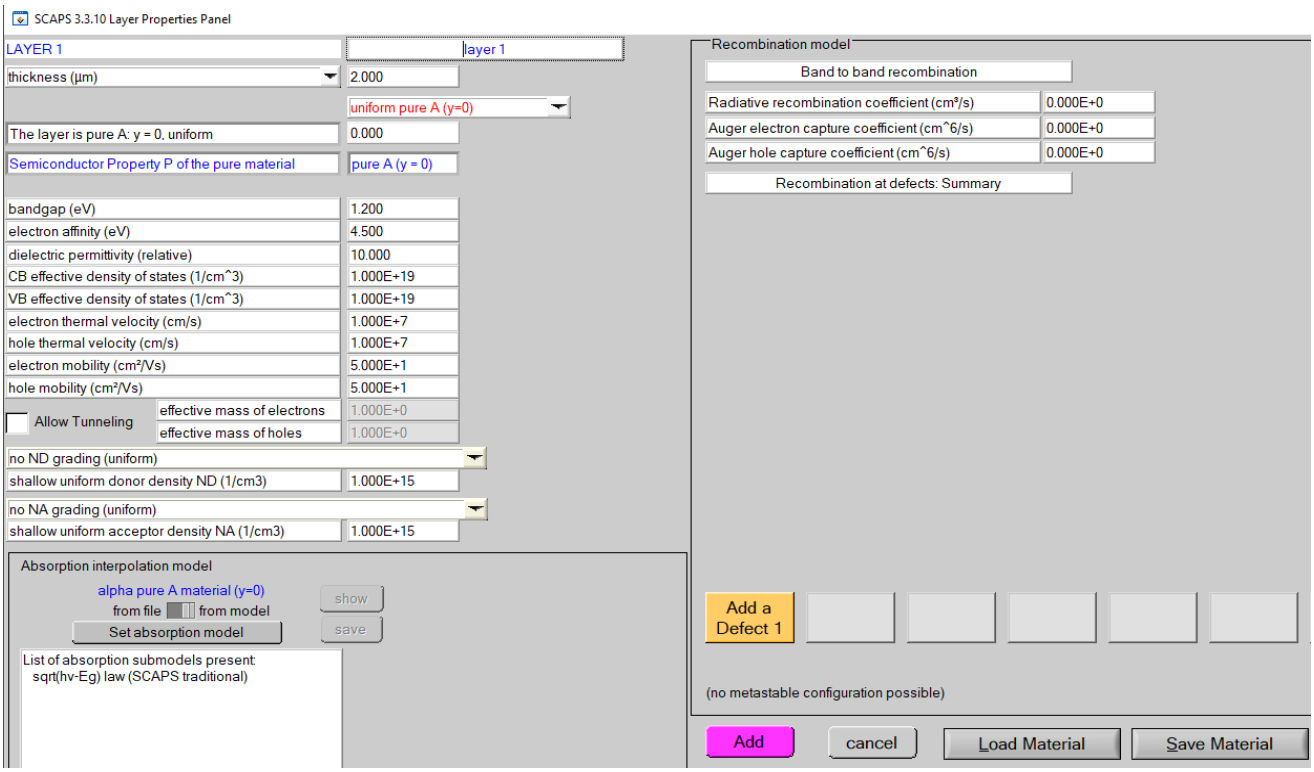

Figure 4-3 Layer Properties Panel

This segment assists in outlining the attributes of a specific material. Following the user's specification of the physical properties at all levels, including those of the absorber layer, buffer layer and window layer, the SCAPS software proceeds with computational modeling or analysis of the defined system structure. Currently, research is underway to examine the influence of various physical variables of the layers on solar system production. These variables encompass doping levels and the widths of the absorption and buffer layers.

4.4.5 Output Parameter

Energy graphs of model cell structures, including band diagrams, carrier densities, current densities and defect densities analysis, are shown in Figure 4-4.

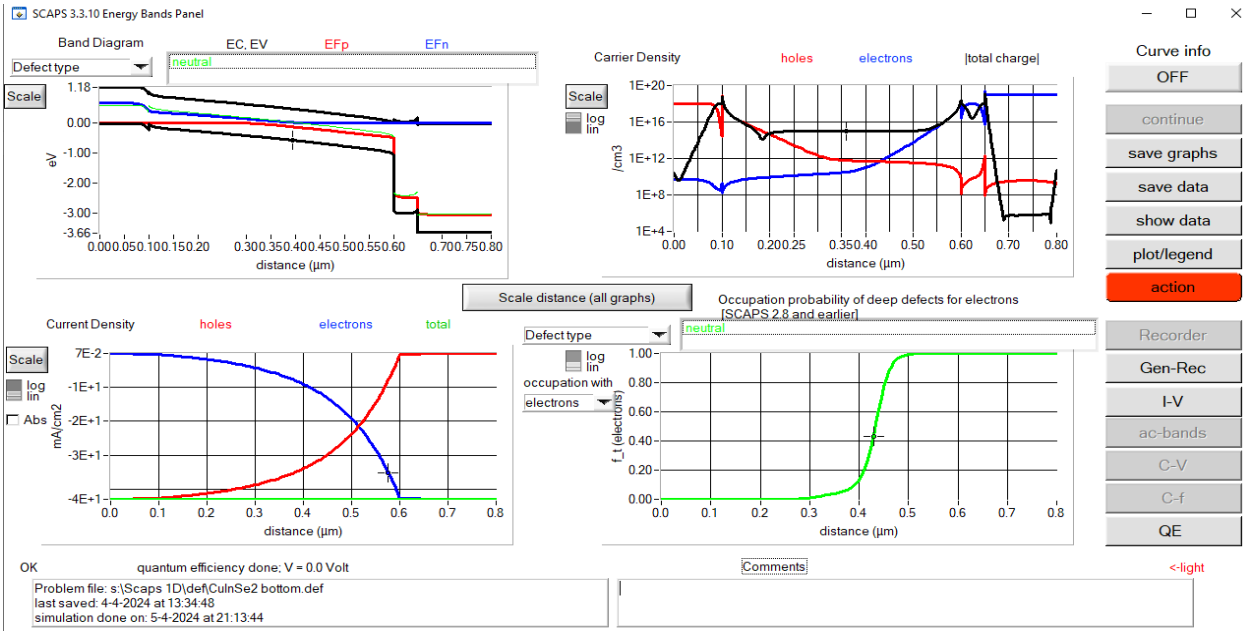

Figure 4-4 Output Panel of Energy Bands

The plots of carrier density and recombination current aid in determining the output parameter of the J-V curve shown in Figure 4-5.

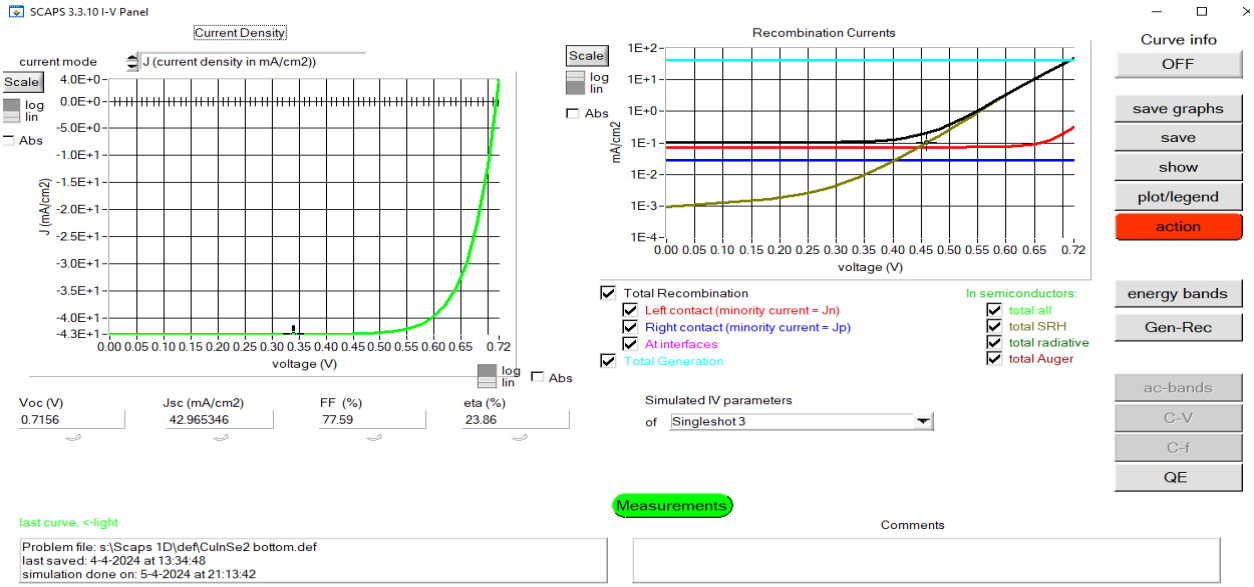

Figure 4-5 Output Panel of J-V Curve

CHAPTER 5 : DESIGN AND SIMULATION

5.1 Introduction

The primary objectives of numerical modeling and simulation in solar cell research involve confirming the accuracy of proposed physical configurations, exploring how the geometry influences solar cell efficiency, and aligning model predictions with real-world observations. The results obtained from various stages are then utilized to pinpoint the most effective Thin Film solar cell for optimal performance, including tasks such as :

- Selecting and refining the window layer.
- Choosing and optimizing the TCO layer.
- Optimizing front and back contacts.
- Analyzing different back surface fields to determine the most suitable option.

5.2 Optimization of $MASnBr_3$ Top Cell

5.2.1 Material Parameters for the used ETL Layers in the Top Cell

We have used four different Electron Transport Layers for our selected top sub-cell which are Titanium Dioxide (TiO_2), Tungsten Disulfide (WS_2), Indium Galium Zinc Oxide (IGZO) and Al doped Zinc Oxide (AZO). The material parameters of these layers are summarized in the following table :

Table 1 : Input parameters for various ETL layers

Parameters	**TiO_2** [105]	**WS_2** [106]	**IGZO** [107]	**AZO** [108]
Thickness, d (μm)	0.150	0.150	0.150	0.150
Electron affinity, x (eV)	4.2	3.95	4.16	4.6

Band gap, E_g (eV)	3.26	2.1	3.05	3.3
Permittivity, $\in r$	10	13.6	10	9
Effective density states at CB, N_c (cm^{-3})	2×10^{17}	2×10^{18}	5×10^{18}	2.2×10^{18}
Effective density states at VB, N_v (cm^{-3})	6×10^{17}	2×10^{18}	5×10^{18}	1.8×10^{19}
Electron mobility, μn (cm^2/V-s)	100	100	15	100
Hole mobility, μp (cm^2/V-s)	25	25	10	25
Donor doping density, N_D (cm^{-3})	1×10^{19}	1×10^{18}	1×10^{18}	1×10^{18}
Acceptor doping density, N_A (cm^{-3})	0	0	0	0
Defect Density, N_t ($1/cm^3$)	1×10^{14}	1×10^{14}	1×10^{14}	1×10^{14}

5.2.2 Comparison of the Simulation Results of Different ETL layers

Table 2 : Simulation results for various ETL layers

Device Structure	**J_{sc} (mA/cm^2)**	**V_{oc} (volts)**	**FF(%)**	**PCE (%)**
ITO/TiO_2/$MASnBr_3$/Au	29.53	1.06	80.37	25.22
ITO/WS_2/$MASnBr_3$/Au	29.64	1.05	79.9	25.13
ITO/IGZO/$MASnBr_3$/Au	29.43	1.06	80.21	25.03
ITO/AZO/$MASnBr_3$/Au	29.40	1.061	79.7	24.85

TiO_2 as the window layer has shown the best performance compared to the other materials. Hence, TiO_2 is selected as the window layer of the top cell. The corresponding values of output parameters are : V_{oc} as 1.06 volts, J_{sc} as 29.53 mA/cm^2, FF as 80.37% and PCE as 25.22%.

5.2.3 TiO_2 Window Layer Thickness Optimization :

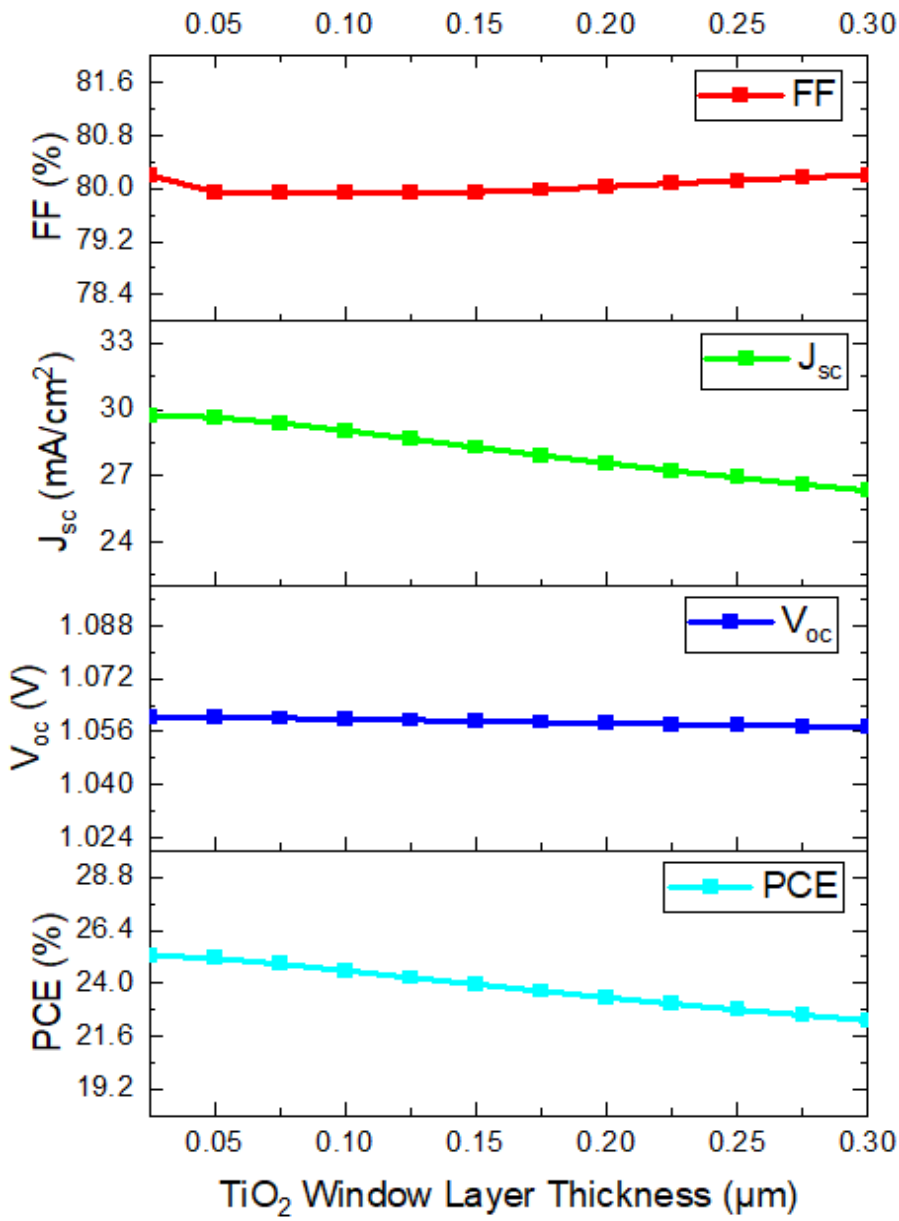

Figure 5-1: TiO_2 Window Layer Thickness Optimization

The thickness of the window layer TiO_2 was varied from 25 nm to 300 nm. V_{oc} remained almost constant throughout the variation which is about 1.06 volts. FF increased slowly in a linear manner while The PCE of the cell gradually decreased due to the lowering of Jsc. For a thickness of about 50 nm, the PCE was found to be about 25.26%.

5.2.4 TiO_2 Window Layer Doping Concentration Optimization :

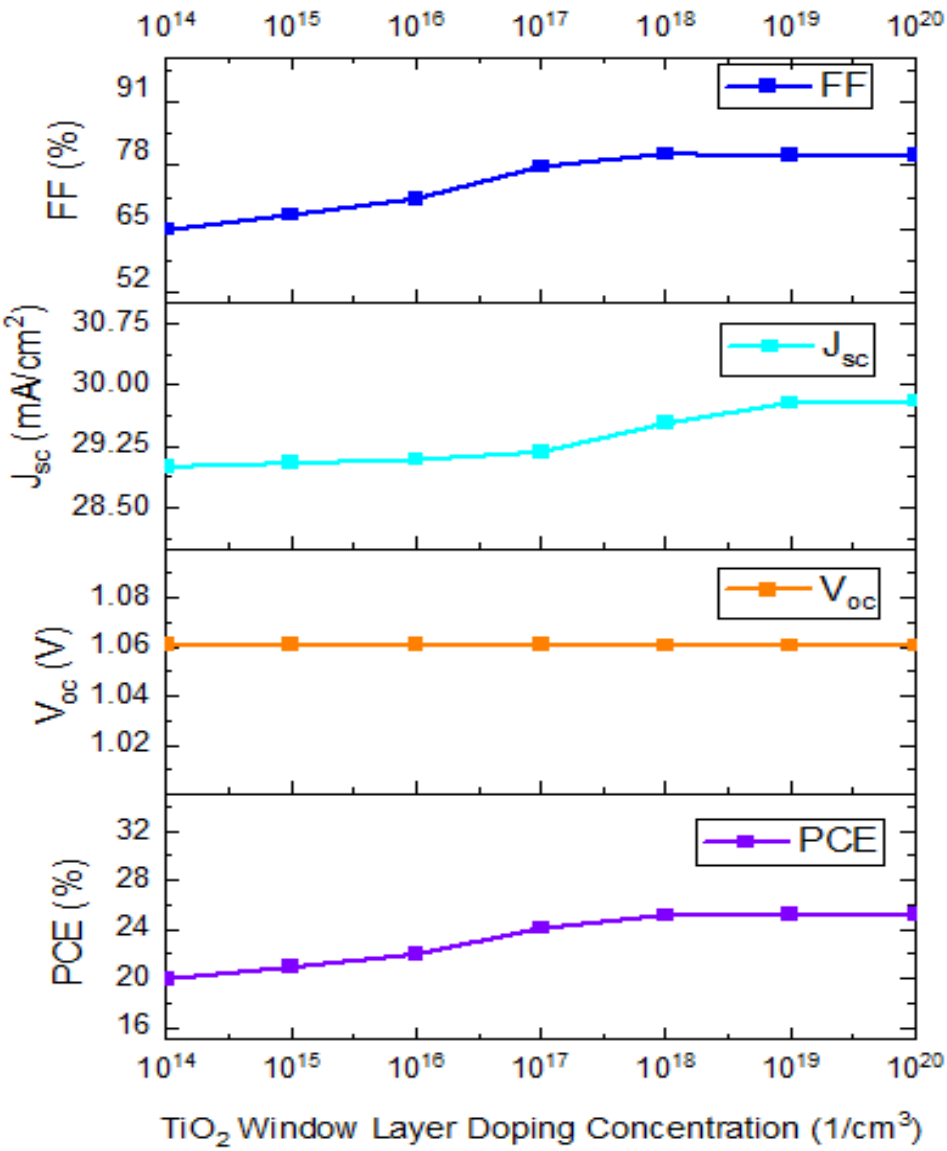

Figure 5-2 : TiO_2 Window Layer Carrier Density (N_D) Optimization

The Carrier Density of the TiO_2 window layer was varied from 10^{14} to 10^{20} in which case also the V_{oc} remained almost constant at 1.06 volts. FF, PCE and J_{sc} first increased linearly and then became saturated after 1×10^{18} doping concentration. For a doping concentration of 1×10^{18}, the value of PCE has shown as 25.26% for TiO_2 as window layer.

5.2.5 Material Parameters for the used HTL Layers in the Top Cell

We have used four different Hole Transport Layers for our selected top sub-cell which are Cu_2O, Spiro-OMeTAD, MoS_2 and $CuSbS_2$. The material parameters of these layers are summarized in the following table :

Table 3 : Input parameters for various HTL layers

Parameters	**Cu_2O** [109]	**Spiro-OMeTAD** [110]	**MoS_2** [111]	**$CuSbS_2$** [112]
Thickness, d (μm)	Variable	Variable	Variable	Variable
Electron affinity, x (eV)	3.2	2.2	3.8	4.2
Band gap, E_g (eV)	2.17	2.9	1.62	1.58
Permittivity, $\in_r$	7.1	3	10.07	8.2
Effective density states at CB, N_c (cm^{-3})	2×10^{17}	2.5×10^{18}	2.8×10^{19}	2×10^{18}
Effective density states at VB, N_v (cm^{-3})	1.1×10^{19}	1.8×10^{19}	1×10^{19}	1×10^{19}
Electron mobility, μ_n (cm^2/V-s)	200	0.0002	12	49
Hole mobility, μ_p (cm^2/V-s)	80	0.0002	2.8	49

Donor doping density, N_D (cm^{-3})	0	0	0	0
Acceptor doping density, N_A (cm^{-3})	1×10^{18}	1×10^{18}	1×10^{17}	1×10^{18}
Defect Density, N_t ($1/cm^3$)	1×10^{14}	1×10^{14}	1×10^{14}	1×10^{14}

5.2.6 Comparison of the Simulation Results of HTL layers

Table 4 : Simulation results for various HTL layers :

Device Structure	**J_{sc} (mA/cm^2)**	**V_{oc} (volts)**	**FF(%)**	**PCE (%)**
ITO/TiO_2/$MASnBr_3$/$CuSbS_2$/Au	30.51	1.046	80.85	25.53
ITO/TiO_2/$MASnBr_3$/Spiro-OMeTAD/Au	30.32	1.045	78.35	25.36
ITO/ TiO_2/$MASnBr_3$/MoS_2/Au	32.10	1.043	77.12	25.80
ITO/ TiO_2/$MASnBr_3$/Cu_2O/Au	30.85	1.048	80.43	26.03

Cu_2O as the HTL layer shows the best performance compared to other materials. Hence, Cu_2O is selected as the HTL layer. The corresponding values of output parameters are : V_{oc} as 1.048 volts, J_{sc} as 30.85 mA/cm^2, FF as 80.43 % and PCE as 26.03 %.

5.2.7 Cu_2O HTL Layer Thickness Optimization

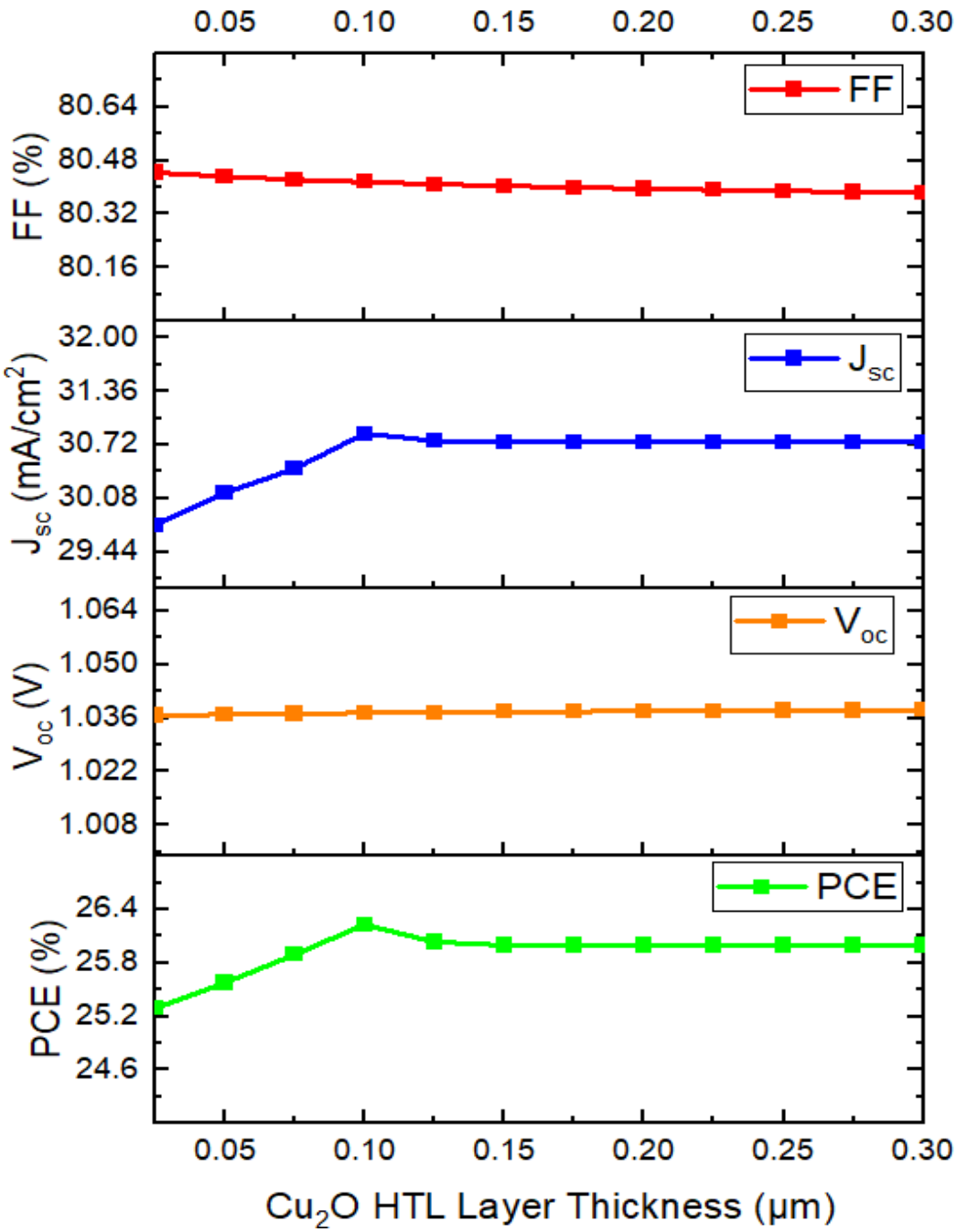

Figure 5-3 : Cu_2O HTL Layer Thickness Optimization

After the insertion of HTL layer, the thickness of the HTL layer Cu_2O was varied from 25 nm to 300 nm. Here, V_{oc} and FF remained almost constant throughout the process. J_{sc} and PCE at first

increased linearly up to 100 nm and slowly became saturated. For a thickness of about 100 nm, the PCE was found to be about 26.23%.

5.2.8 Cu_2O HTL Layer Doping Concentration Optimization

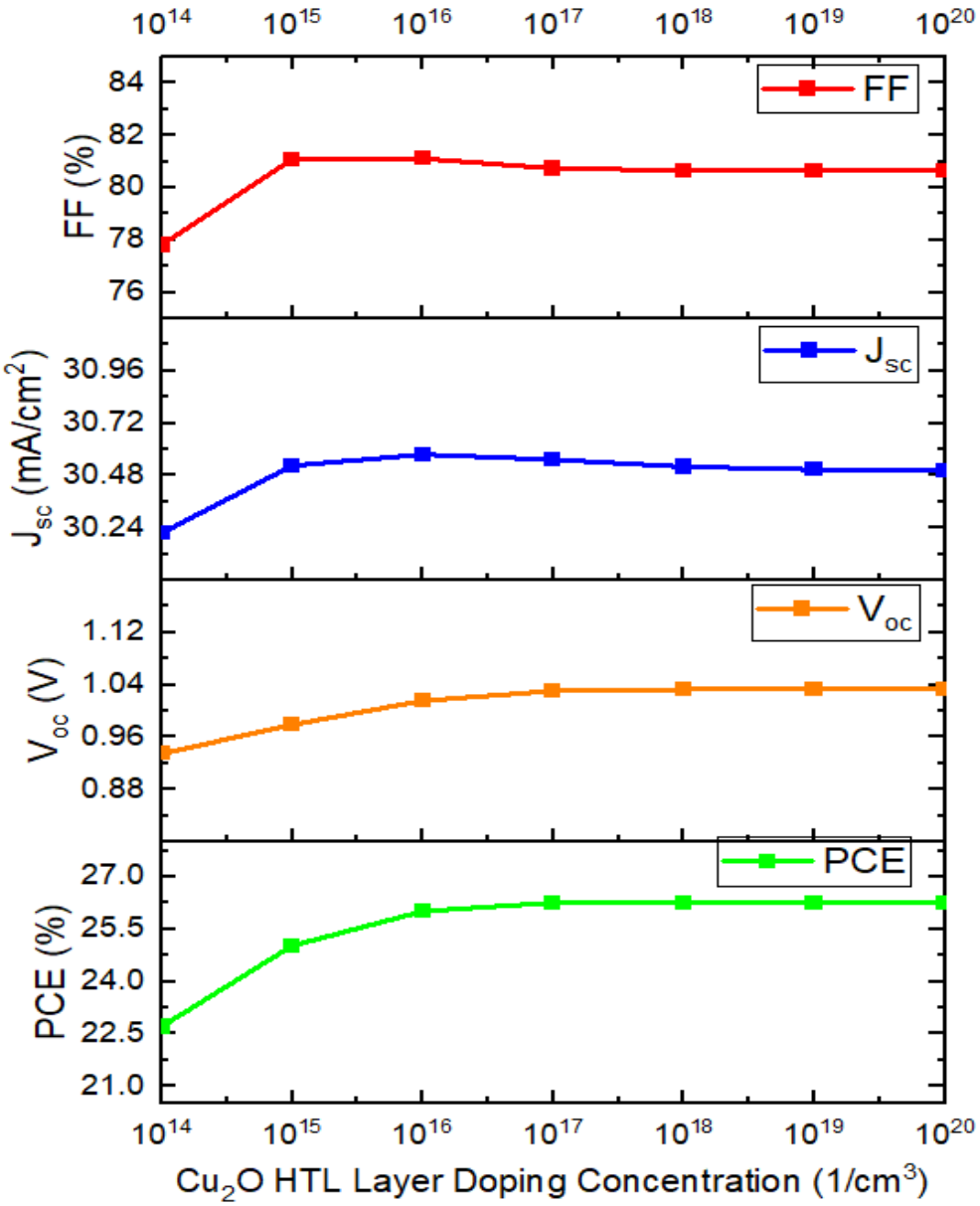

Figure 5-4 : Cu_2O HTL Layer Thickness Optimization

The Carrier Density of the Cu_2O HTL layer was varied from 10^{14} to 10^{20} in which case FF became saturated after doping concentration of 1×10^{15}. Then V_{oc}, J_{sc} and PCE at first linearly increased and finally became saturated. For a doping concentration of 1×10^{17}, the value of PCE has shown as 26.27% for Cu_2O as HTL layer.

5.2.9 Structure of Perovskite Top Cell

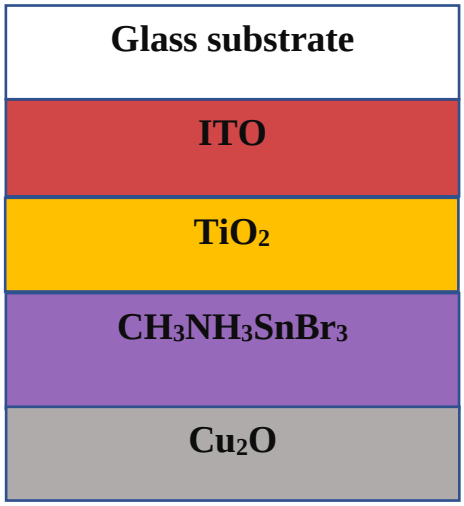

Figure 5-5 : Structure of Perovskite Top

The structure of our proposed top sub-cell has been shown in figure 5-5. We have incorporated Indium Tin Oxide (ITO) as TCO layer, Titanium Dioxide (TiO_2) as window layer, Methyl Ammonium Tin Bromide ($MASnBr_3$) as absorber layer and Cu_2O as HTL layer.

The material parameters of these layers are shown in the following table :

Table 5 : Input parameters for various layers of $MASnBr_3$ top cell

Parameters	**ITO** [113]	**TiO_2** [105]	**$CH_3NH_3SnBr_3$** [114]	**Cu_2O** [112]
Thickness, d (nm)	150	50	500	100

Electron affinity, x (eV)	4.6	4.2	4.17	3.2
Band gap, E_g (eV)	3.5	3.26	1.33	2.17
Permittivity, $\in_r$	8.9	10	10	7.1
Effective density states at CB, N_c (cm^{-3})	2.2×10^{18}	2.2×10^{18}	2.2×10^{18}	2×10^{18}
Effective density state at VB, N_v (cm^{-3})	1.8×10^{19}	1.8×10^{18}	1.8×10^{18}	1×10^{19}
Electron mobility, μ_n (cm^2/V-s)	10	20	1.6	49
Hole mobility, μ_p (cm^2/V-s)	10	10	1.6	49
Donor doping density, N_D (cm^{-3})	1×10^{19}	1×10^{18}	0	0
Acceptor doping density, N_A (cm^{-3})	0	0	1×10^{16}	1×10^{18}
Defect Density, N_t (cm^{-3})	1×10^{14}	1×10^{14}	1×10^{14}	1×10^{14}

5.2.10 $MASnBr_3$ Absorber layer Thickness Optimization :

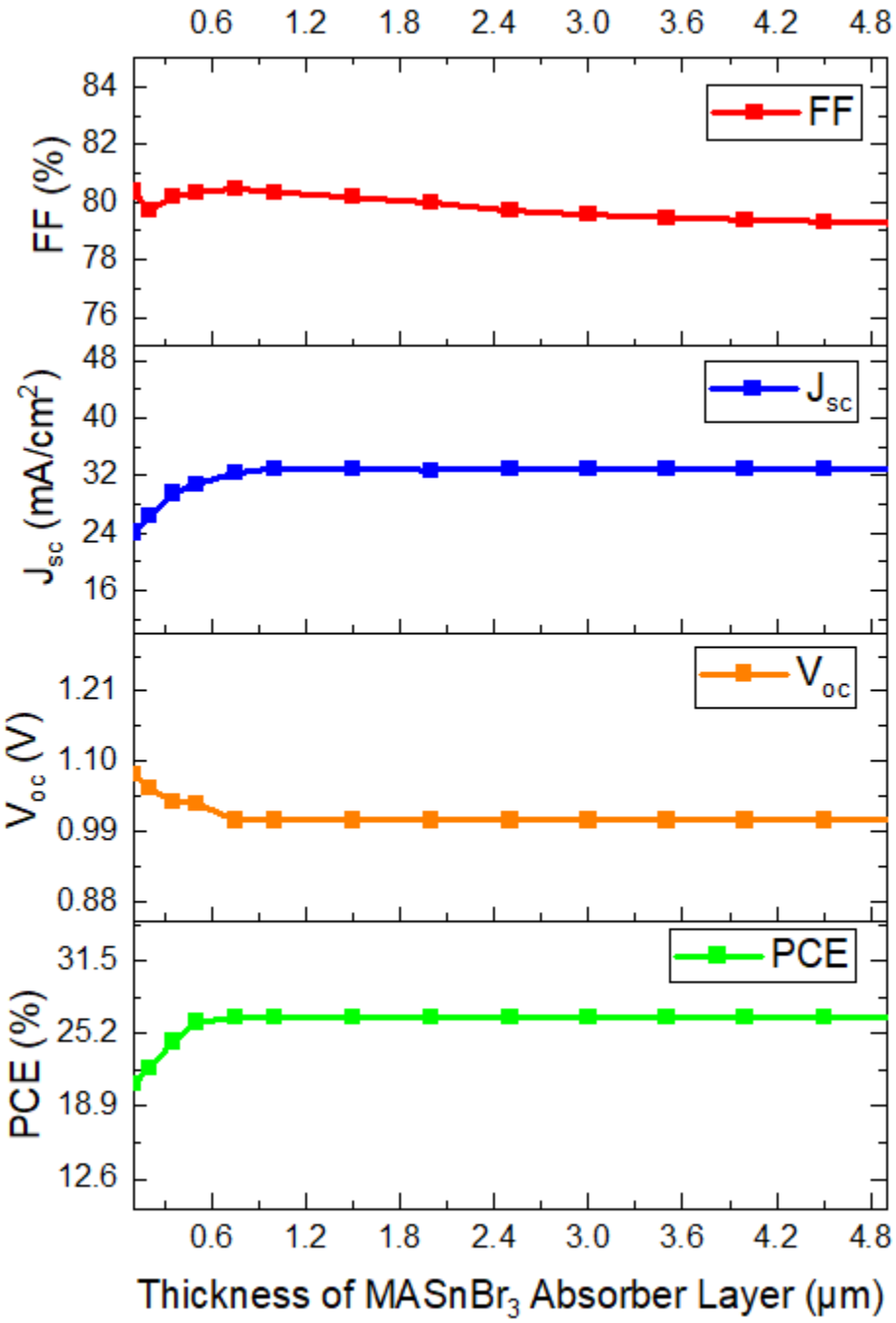

Figure 5-6 : $MASnBr_3$ Absorber layer Thickness Optimization

The thickness of $MASnBr_3$ absorber layer was varied from 100 nm to 5 µm. FF at first increased and then slowly decreased. The value of J_{sc} at first increased up to 1 µm and then it became

constant. As for V_{oc} it first decreased sharply and then became saturated. J_{sc} and PCE at first increased but they also became saturated shortly after 500 nm. As a result 500 nm thickness in chosen for absorber layer for material preservation and PCE was found to be about 26.30%.

5.2.11 $MASnBr_3$ Absorber Layer Doping Optimization

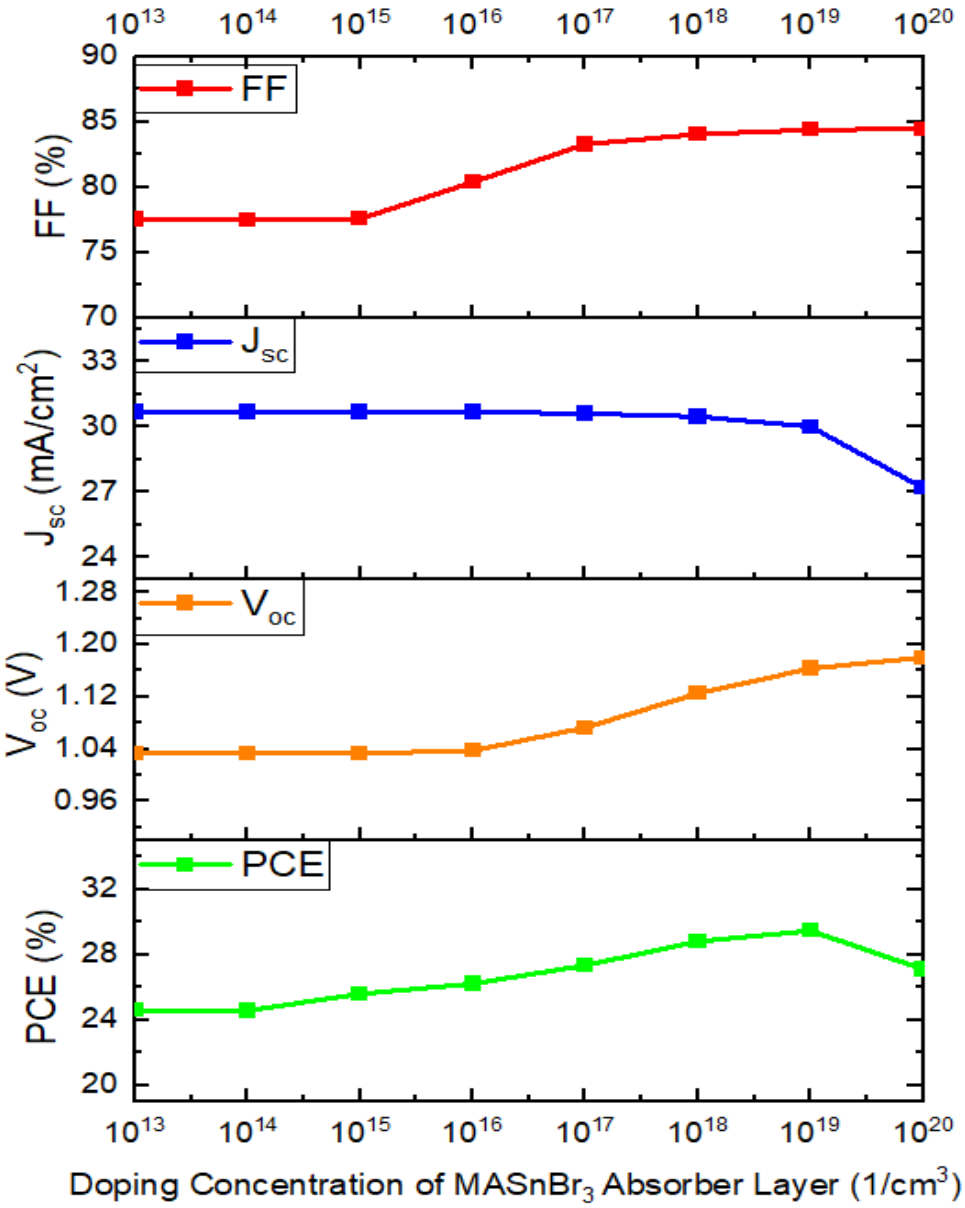

Figure 5-7 : $MASnBr_3$ Absorber Layer Doping Concentration

The Acceptor Carrier Density of the absorber layer was varied from 10^{13} to 10^{20}. Here, J_{sc} remained constant in most of the process but decreased towards the end. The other parameters increased proportionally with the absorber layer thickness but PCE decreased after the doping concentration 1×10^{19} was reached. However, the doping concentration of 1×10^{16} was chosen as the optimum value for the absorber layer.

5.2.12 $MASnBr_3$ Absorber layer Defect Density Optimization :

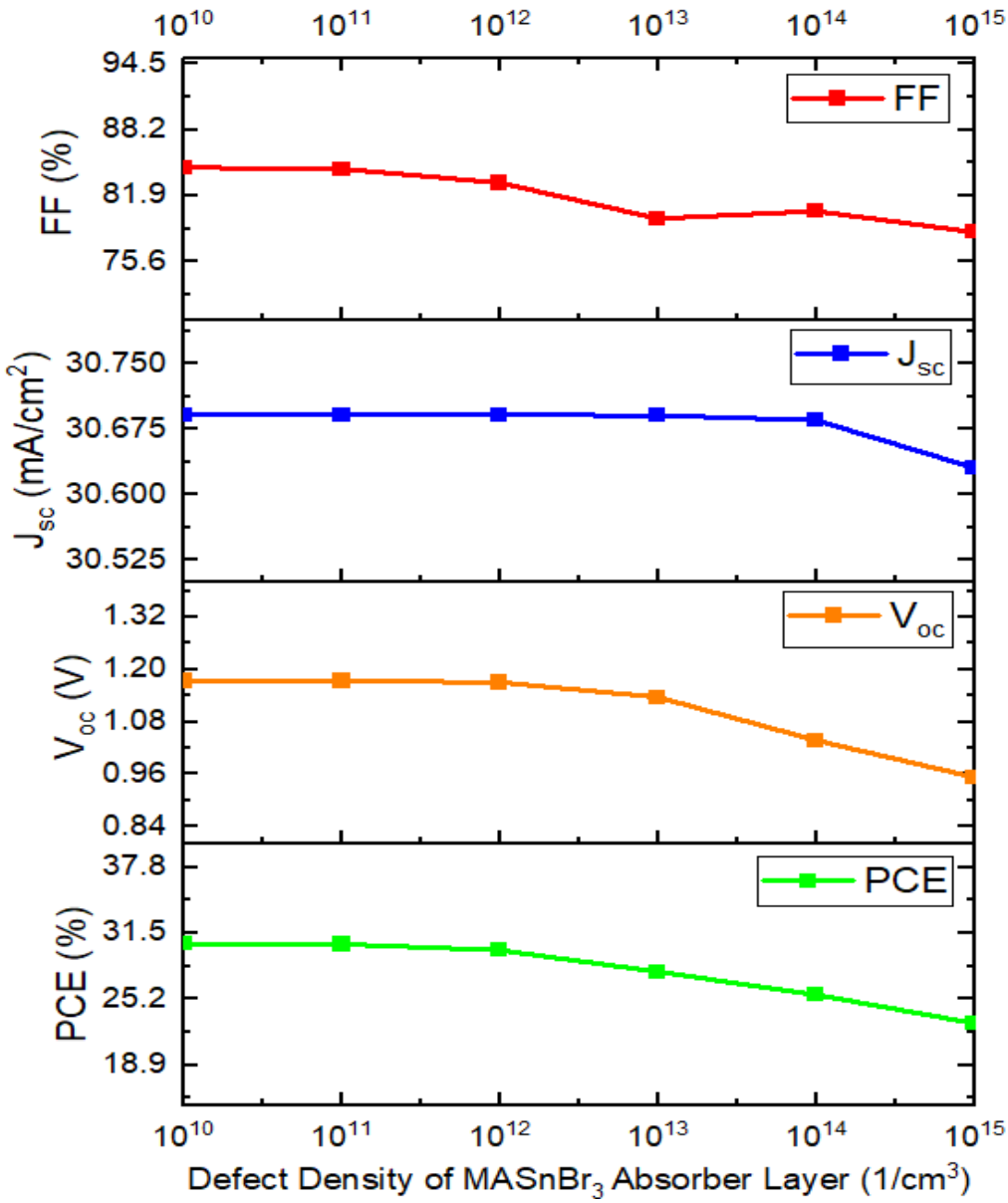

Figure 5-8 : $MASnBr_3$ Absorber layer Defect Density Optimization

The Defect Density of the absorber layer was varied from 10^{10} to 10^{15}. As we can see from the figure, the values of all the parameters decreased in response to the increment of the defect density. The value of 1×10^{13} is chosen as the optimum value of defect density.

5.2.13 Effect of Temperature Variation :

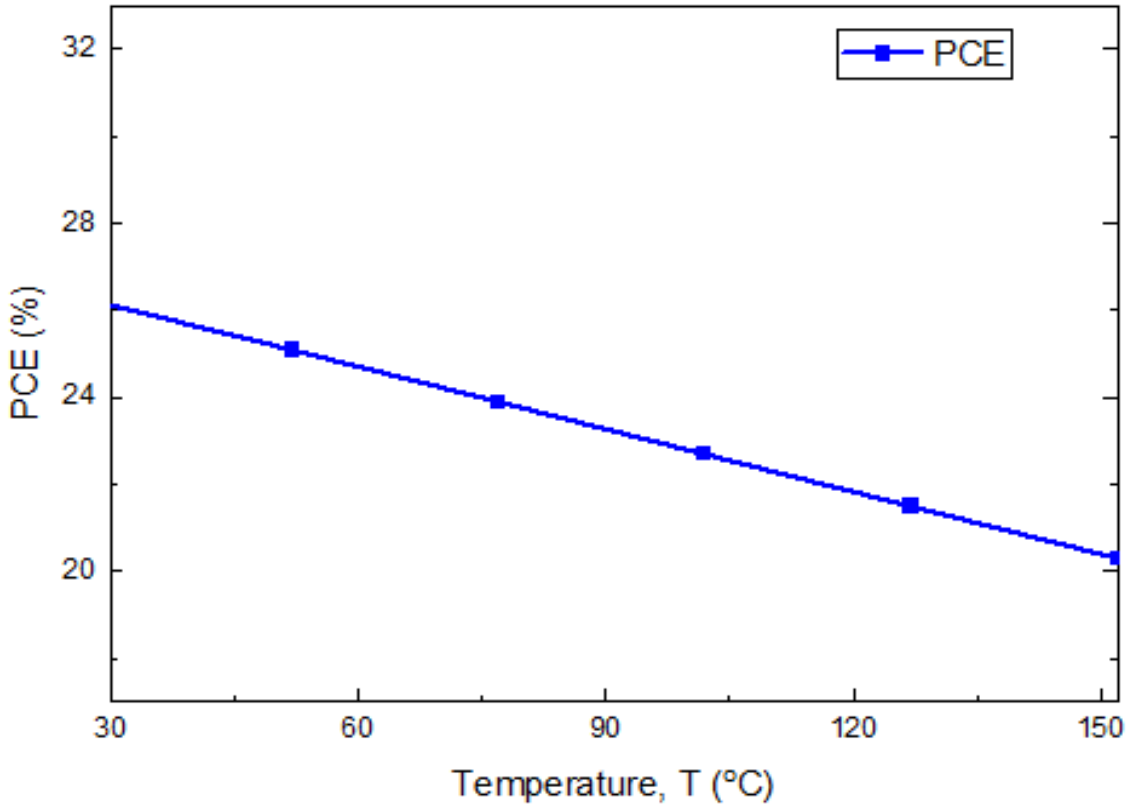

Figure 5-9 : Effect of Temperature Variation

From the figure 5-9, it is evident that PCE went down to 20.28% from 26.30% when temperature was varied from 27°C to 152°C. As a result, the temperature coefficient was calculated to be around -0.048% per °C.

5.2.14 JV Curve of $MASnBr_3$ Top Cell

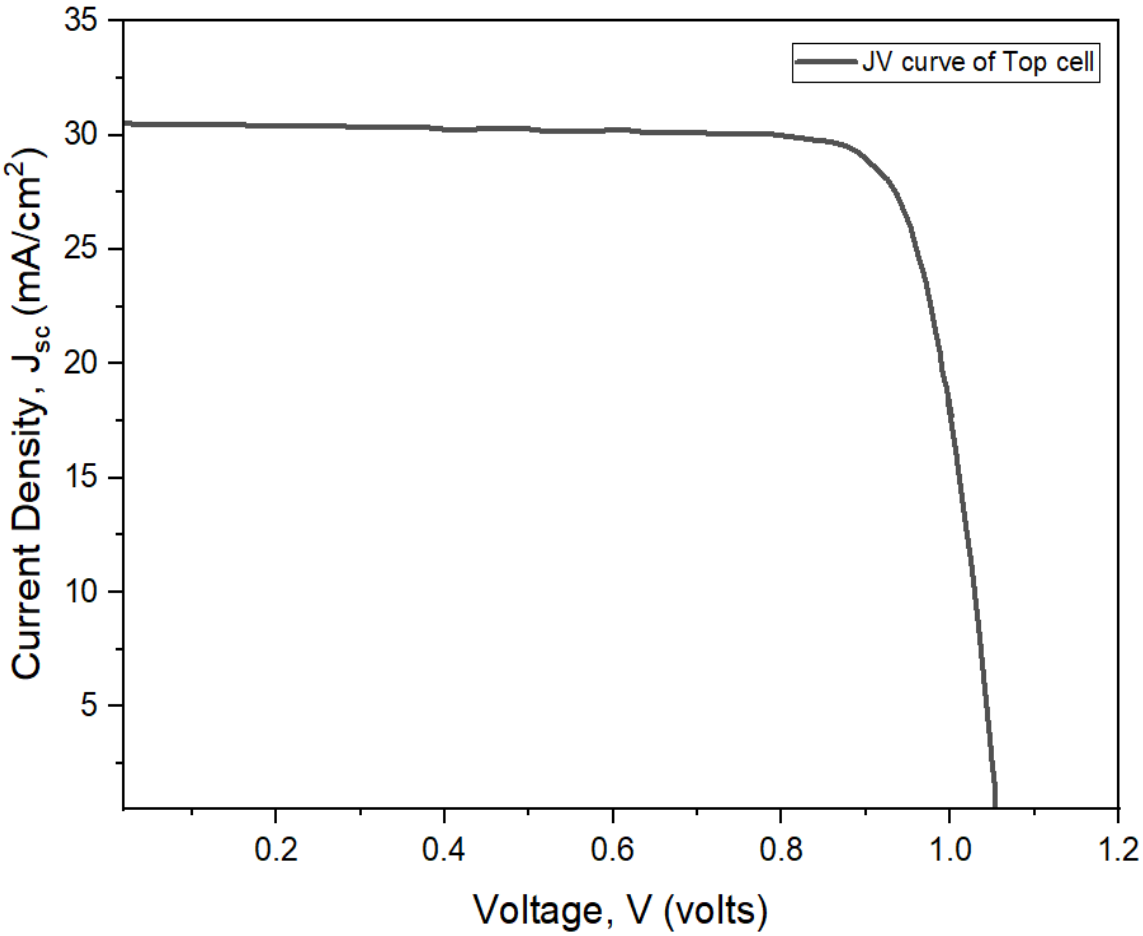

Figure 5-10 : JV curve of $MASnBr_3$ Top Cell

The JV curve relating to the $MASnBr_3$ top cell has been shown in figure 5-10. The JV curve exhibits a short-circuit current density (J_{sc}) of about 30.68 mA/cm^2 and open-circuit voltage (V_{oc}) of 1.04 volts.

The thickness of the absorber layer has been chosen as 500 nm for material preservation and current matching purpose. Our optimized top sub-cell has shown an open-circuit voltage (V_{oc}) of

1.04 volts, short-circuit current density (J_{sc}) of about 30.68 mA/cm^2, Fill Factor of 80.42% and PCE of about 26.30%.

5.2.15 QE Curve of $MASnBr_3$ Top Cell

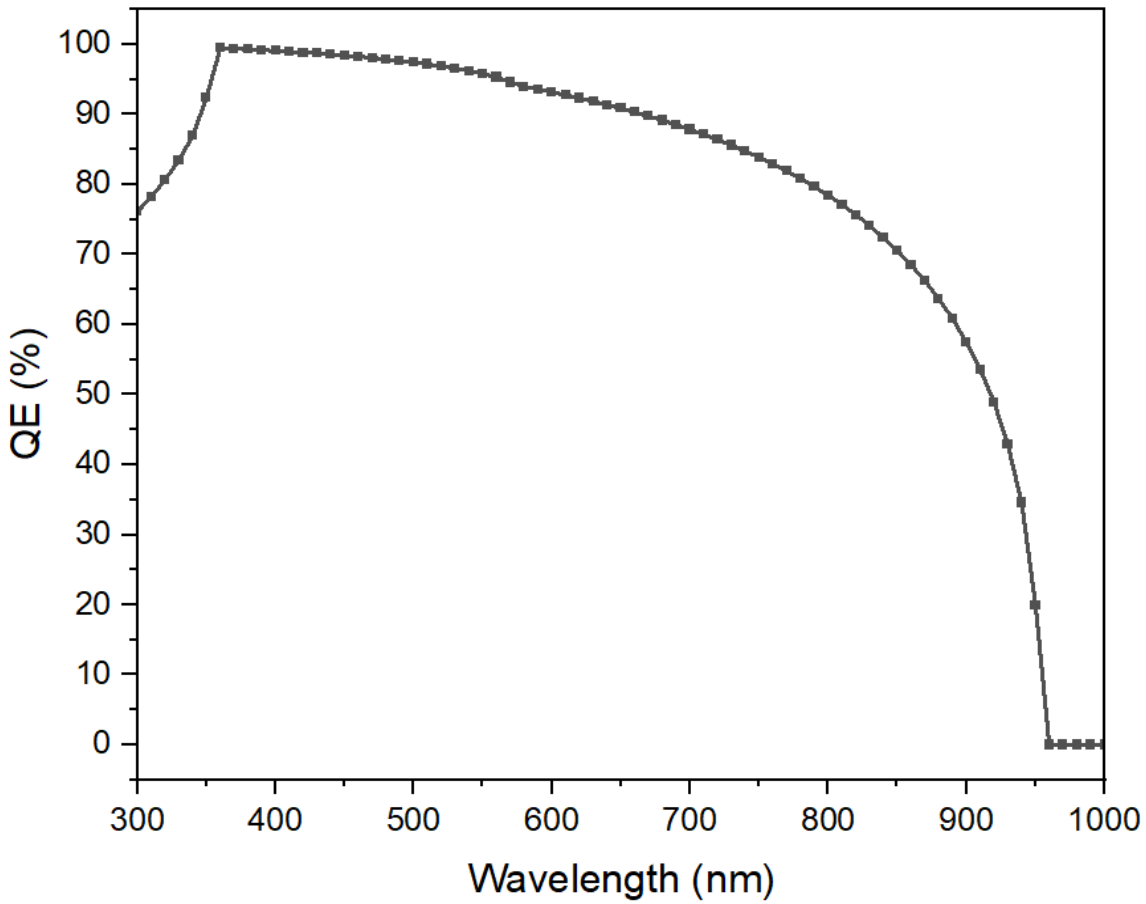

Figure 5-11 : QE vs Wavelength Curve for Top Cell

According to the figure 5-11, the top cell exhibits a quantum efficiency of more than 80% up to 750 nm wavelength. After that, the absorption declines and there was no absorption after 950 nm wavelength. It is notable that it shows an excellent quantum efficiency over visible spectrum of light and thus a decent Power Conversion Efficiency was achieved.

5.2.16 Effect of Series Resistance (R_s) on $MASnBr_3$ Top Cell

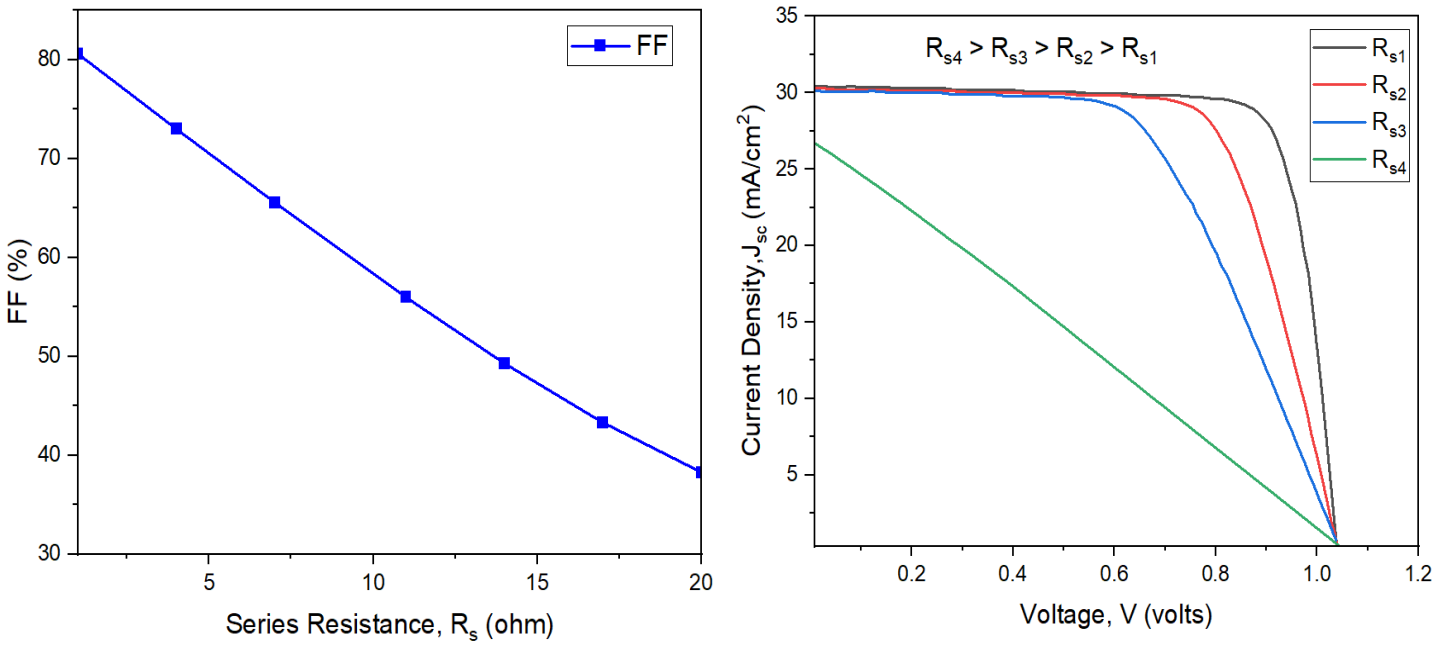

Figure 5-12 : Effect of Series Resistance (Rs) on $MASnBr_3$ Top Cell

In this section, the impact of series resistance, R_s on the top sub-cell has been observed. Increasing series resistance mainly affects the fill factor but excessive value of series resistance can also reduce the short-circuit current density.

From the figure 5-12, it is shown that Fill Factor is reduced from 81% to almost 40% when series resistance is varied from 1 ohm to 20 ohm. Also, JV curves corresponding to the four different levels of series resistance are shown. For maximum series resistance R_{s4}, the short-circuit current density (J_{sc}) has come down considerably as it reduced to around 27 mA/cm^2 from 30 mA/cm^2. Therefore, series resistance mainly affected the fill factor and short-circuit current (J_{sc}) but didn't have much impact on open-circuit voltage (V_{oc}) and PCE.

5.2.17 Effect of Shunt Resistance (R_{sh}) on $MASnBr_3$ Top Cell

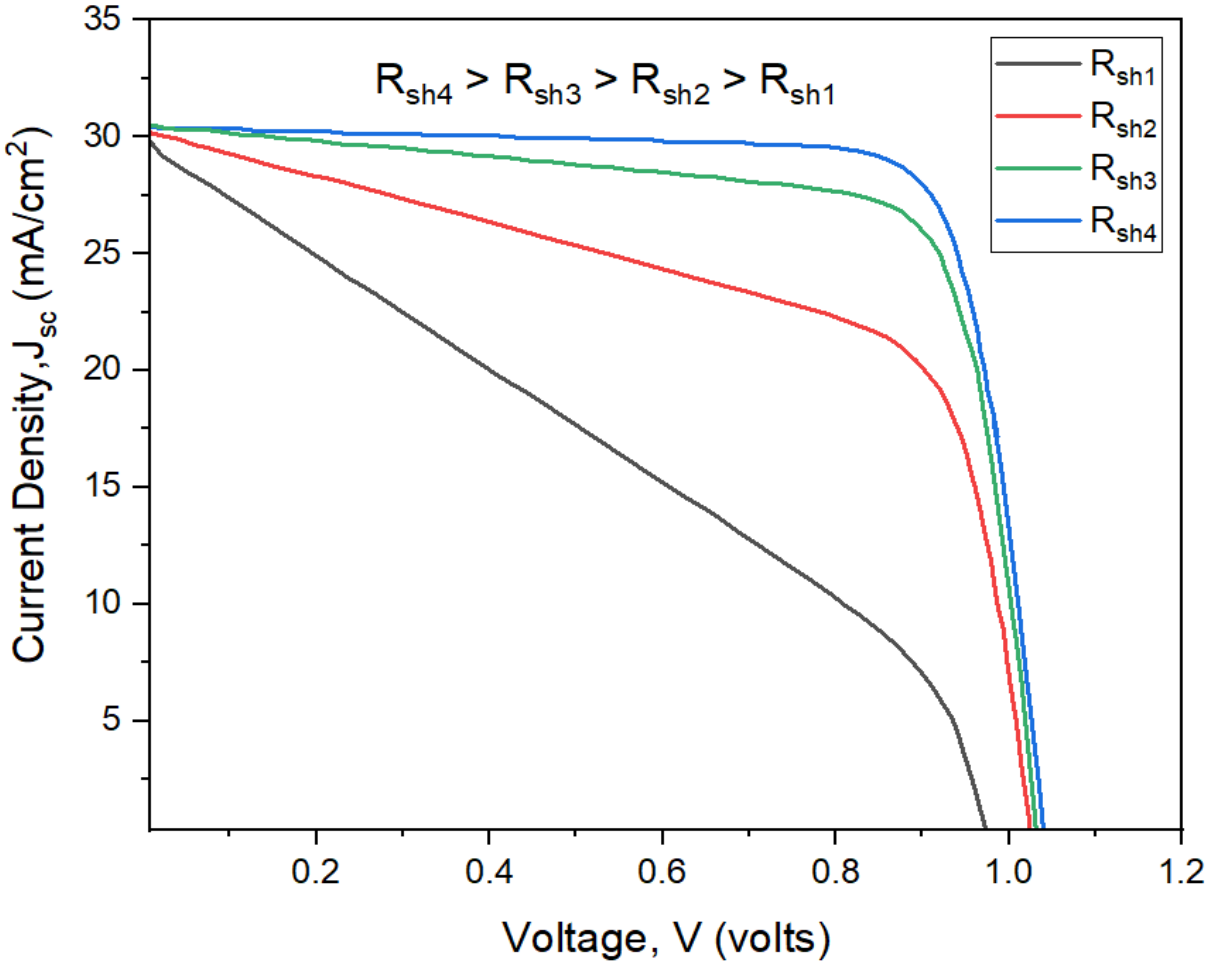

Figure 5-13 : Effect of Shunt Resistance (R_{sh}) on $MASnBr_3$ Top Cell

The main cause of the considerable power losses in solar cells is shunt resistance (R_{sh}). A low shunt resistance opens up a different current channel for the current generated by light. As a result, the voltage produced from the solar cell is lowered because there is less accessible light-generated current in low light, the effects of R_{sh} are especially severe. Consequently, the losses resulting from R_{sh} have a significant impact.

From the figure 5-13, we can see that the open-circuit voltage (V_{oc}) reduces when shunt resistance (R_{sh}) is reduced significantly Although the shunt resistance didn't have much impact on short-circuit current density (J_{sc}).

5.3 Optimization of c-Si Bottom Cell

5.3.1 Structure of c-Si Bottom Cell

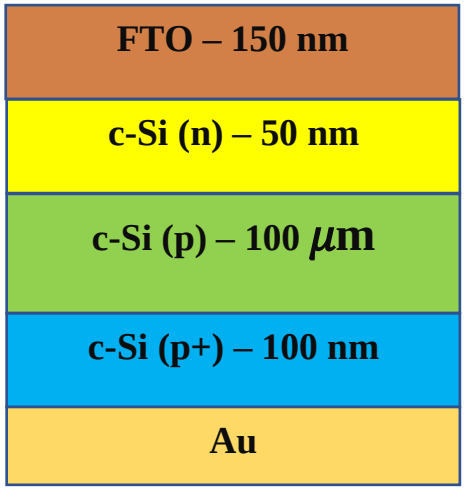

Figure 5-14 : Structure of c-Si Bottom Cell

Table 6 : Input parameters for various layers of c-Si bottom cell

Parameters	**c-Si (n)** [115]	**c-Si (p)** [115]	**c-Si (p+)** [115]	**FTO** [116]
Thickness, d (μm)	0.050	100	0.100	150
Electron affinity, x (eV)	3.9	4.05	3.9	4.4
Band gap, E_g (eV)	1.124	1.124	1.124	3.6
Permittivity, $\in_r$	11.9	11.9	11.9	9
Effective density states at CB, N_c (cm^{-3})	2.8×10^{19}	2.8×10^{19}	2.8×10^{19}	2.2×10^{18}
Effective density states at VB, N_v (cm^{-3})	1.04×10^{19}	1.04×10^{19}	1.04×10^{19}	1.8×10^{19}
Electron mobility, μ_n (cm^2/V-s)	1250	1010	1212	20
Hole mobility, μ_p (cm^2/V-s)	443	443	421	10
Donor doping density, N_D (cm^{-3})	1×10^{18}	0	0	1×10^{18}
Acceptor doping density, N_A (cm^{-3})	0	1×10^{16}	1×10^{18}	0
Defect Density, N_t ($1/cm^3$)	1×10^{14}	1×10^{14}	1×10^{14}	1×10^{14}

5.3.2 Thickness Optimization of c-Si (n) Layer

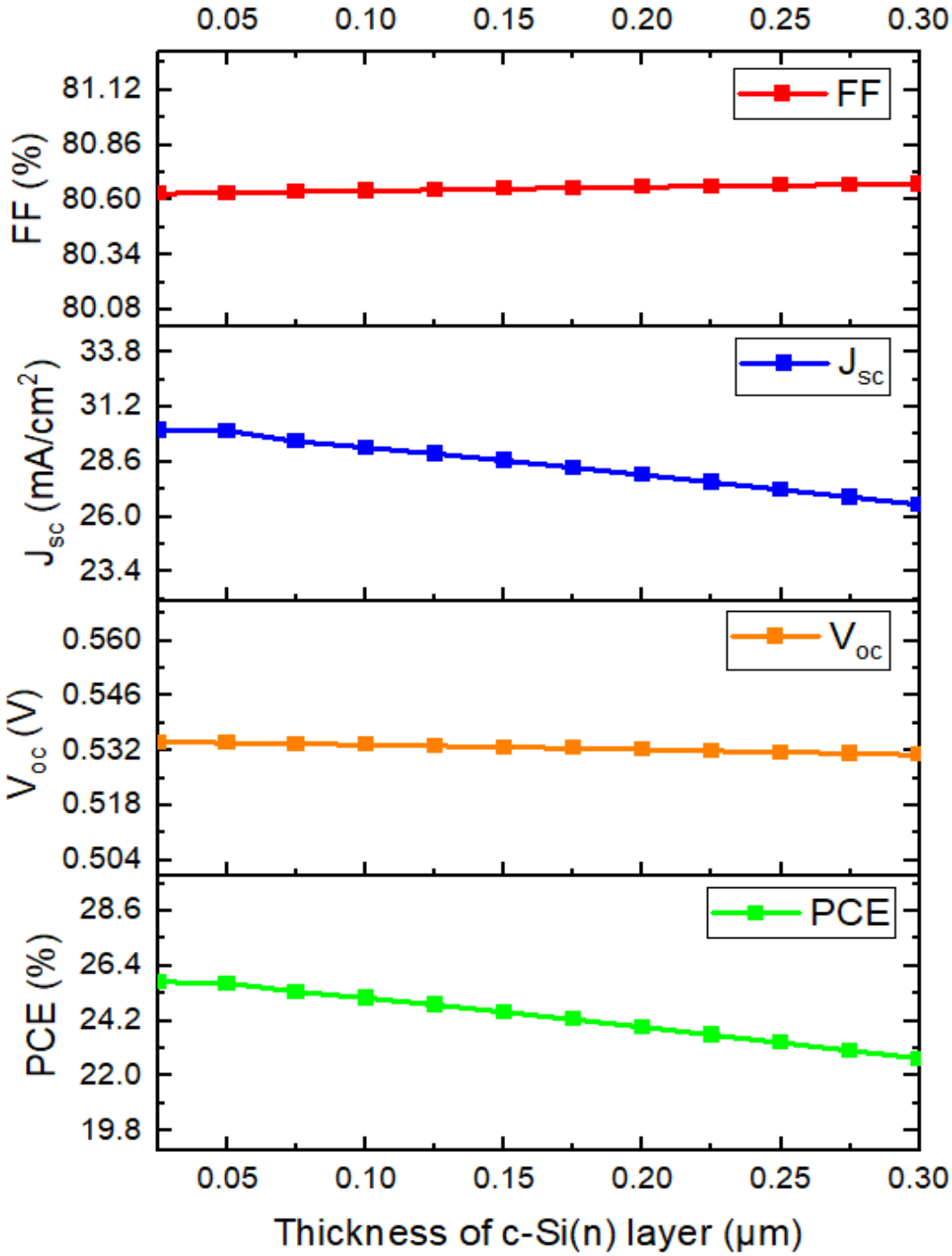

Figure 5-15 : Thickness Optimization of c-Si (n) Layer

The thickness of the c-Si(n) layer was varied from 25 nm to 300 nm. Here, V_{oc} and FF remained almost constant throughout the process. J_{sc} and PCE at first stayed constant up to 50 nm and then they reduced. For a thickness of about 50 nm, the PCE was found to be about 25.12%.

5.3.3 Thickness Optimization of c-Si (p) Absorber Layer

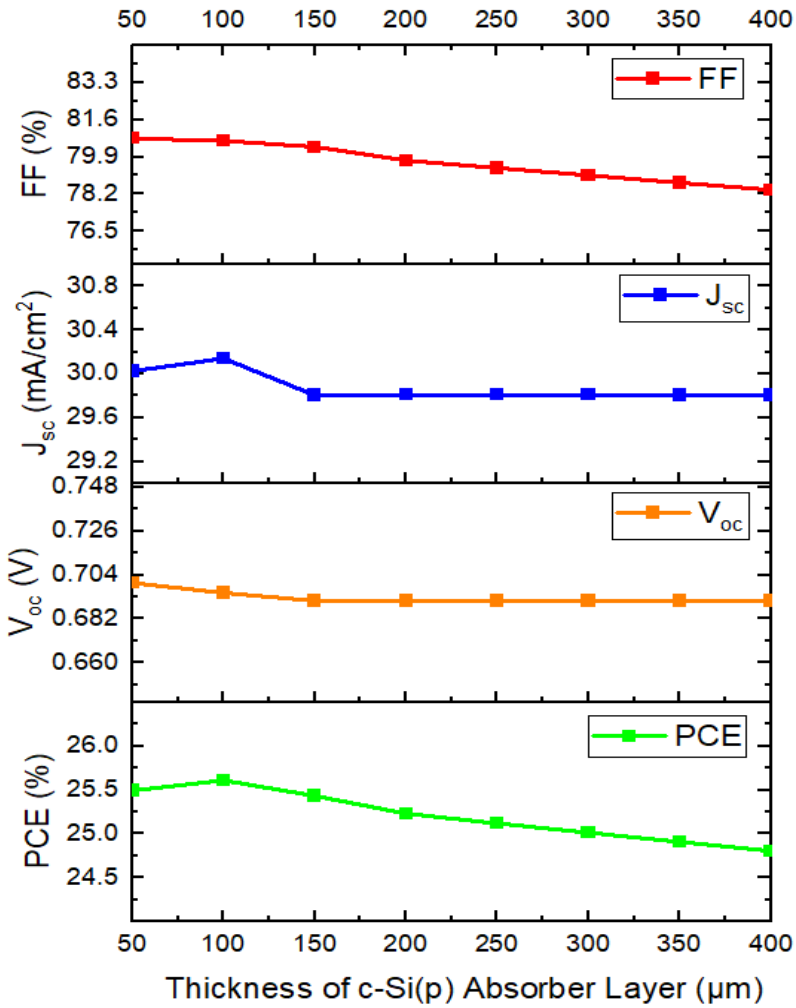

Figure 5-16 : Thickness Optimization of c-Si (p) Layer

The thickness of the c-Si(p) layer was varied from 50 µm to 400 µm. V_{oc} and J_{sc} seems to be constant after the thickness reached 150 µm. Fill factor reduced slowly when the thickness is increased. PCE was maximum at a thickness of 100 µm and afterwards it decreased. At 100 µm thickness, PCE is about 25.61%.

5.3.4 Carrier Density Optimization of c-Si (p) Absorber Layer

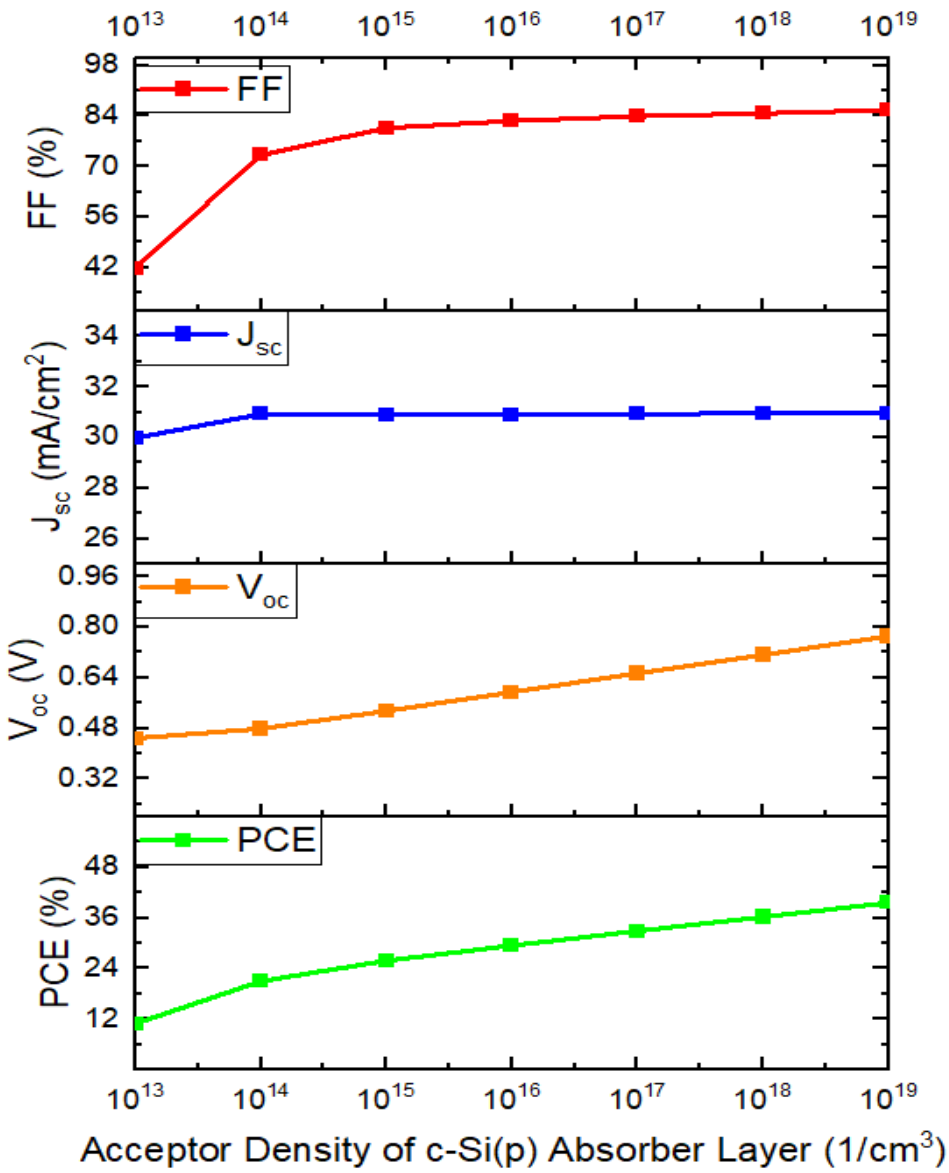

Figure 5-17 : Carrier Density Optimization of c-Si (p) Layer

The Acceptor Carrier Density of the absorber layer was varied from 10^{13} to 10^{19}. Here, J_{sc} remained constant in most of the process. The other parameters increased with the absorber layer thickness but FF became almost saturated towards the end. However, the doping concentration of 1×10^{15} was chosen as the optimum value for the absorber layer.

5.3.5 JV curve of c-Si Bottom Cell

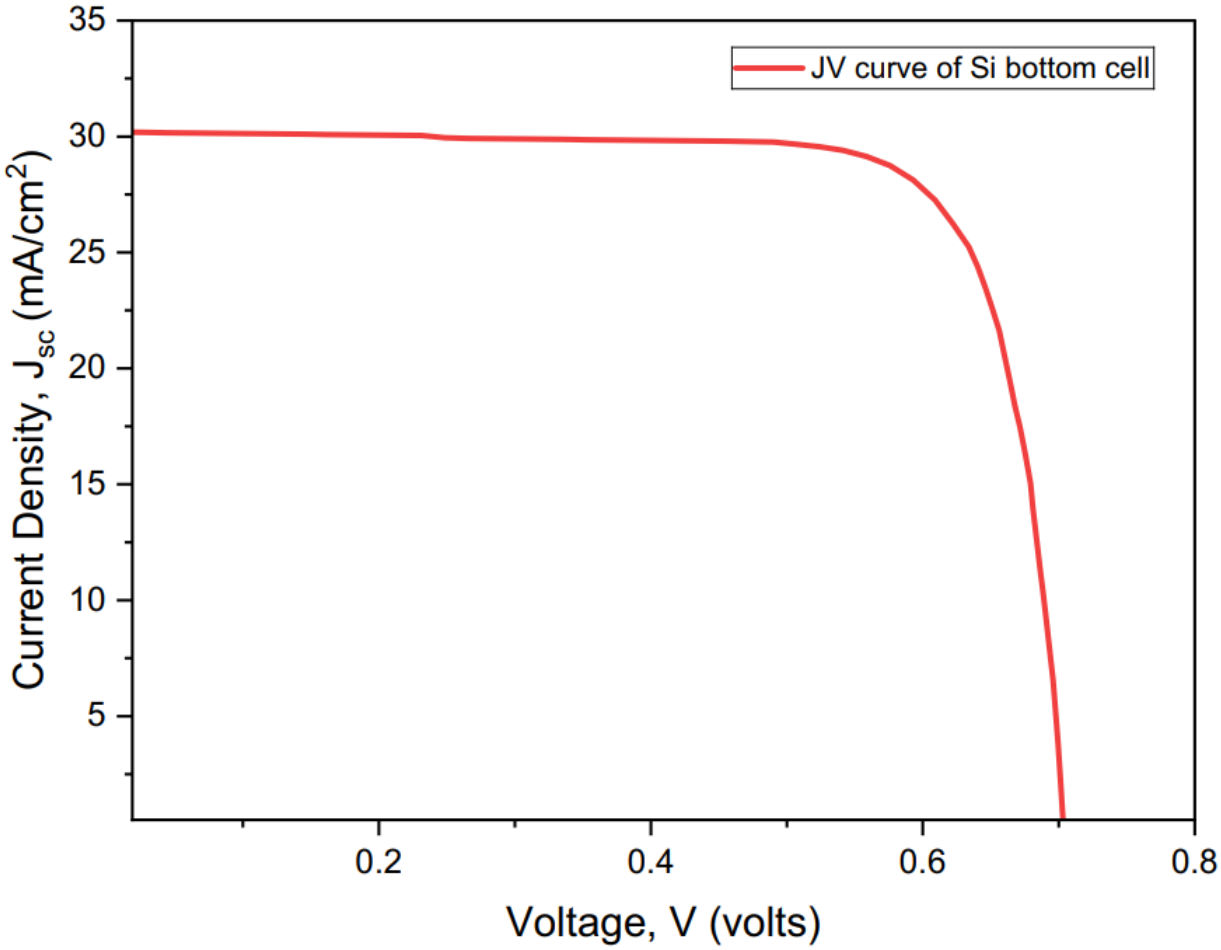

Figure 5-18 : JV curve of c-Si Bottom Cell

The JV curve relating to the Si bottom cell has been shown in figure 5-10. The JV curve exhibits a short-circuit current density (J_{sc}) of about 30.76 mA/cm^2 and open-circuit voltage (V_{oc}) of about 0.71 volts.

The thickness of the Si absorber layer has been chosen as 100 µm current matching purpose. Our optimized Si bottom sub-cell has shown an open-circuit voltage (V_{oc}) of 0.71 volts, short-circuit current density (J_{sc}) of about 30.76 mA/cm^2, Fill Factor of 80.65% and PCE of about 25.85%.

5.3.6 QE curve of c-Si Bottom Cell

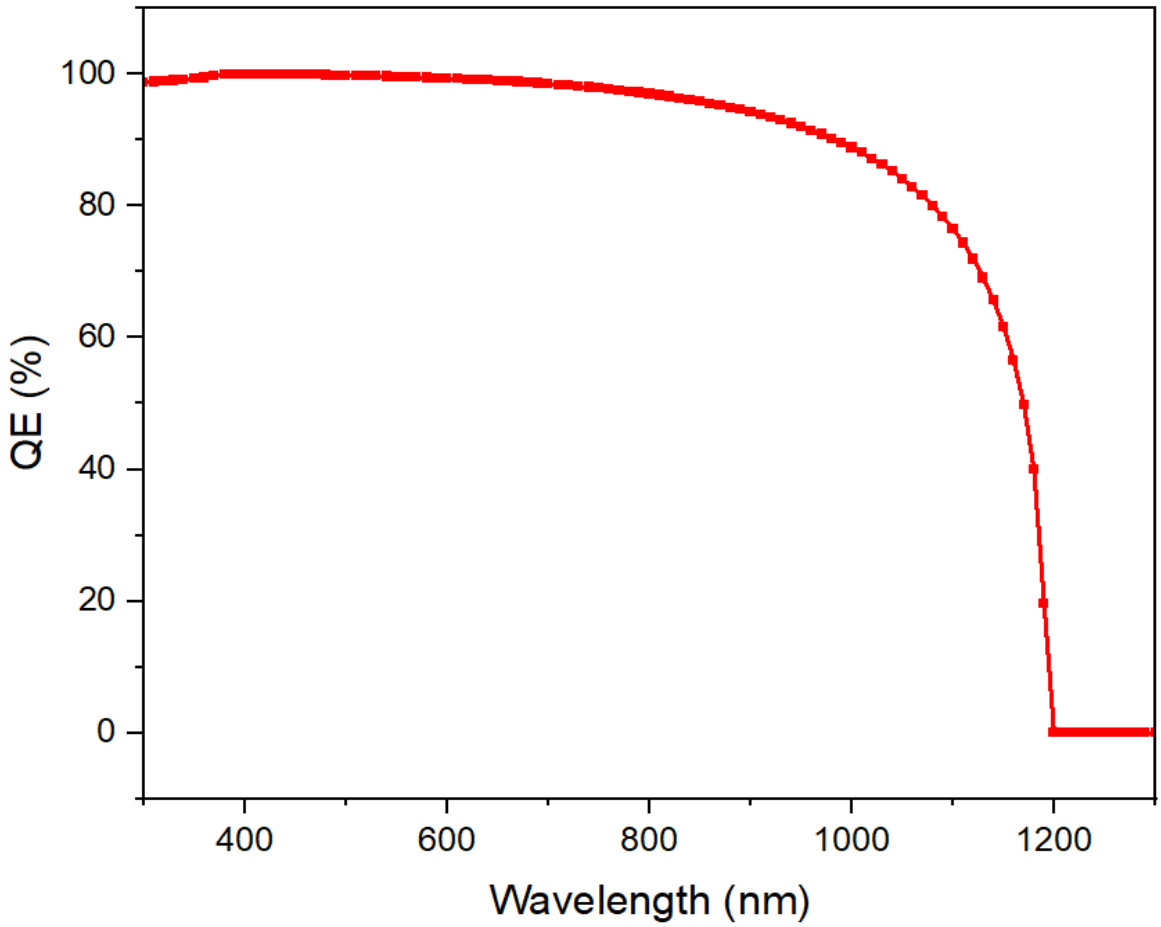

Figure 5-19 : Quantum Efficiency curve for c-Si Bottom Cell

According to the figure 5-19, the c-Si bottom cell exhibits a quantum efficiency of more than 80% up to 1050 nm wavelength. After that, the absorption declines and there was no absorption after 1200 nm wavelength. It is notable that it shows an excellent quantum efficiency over visible as well as infrared spectrum of light and thus a decent Power Conversion Efficiency was achieved.

5.3.7 Thermal Stability of c-Si Bottom Cell

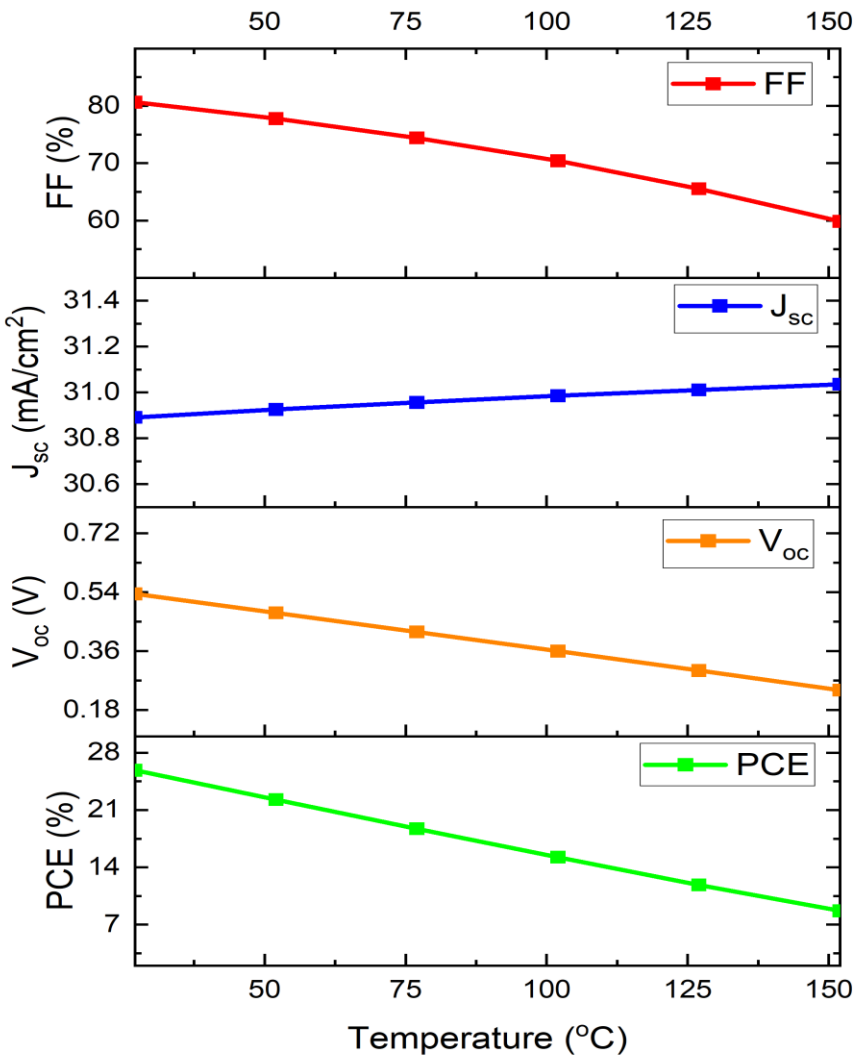

Figure 5-20 : Thermal Stability of c-Si Bottom Cell

Figure 5-20 dictates that PCE went from 25.85% to 8.68% when temperature was varied from 27°C to 152°C. As a result, the temperature coefficient was calculated to be around -0.137% per °C. J_{sc} slightly increased when the temperature is increased due to the reduction of energy band gap and generation of more electron-hole pairs. An increase in interfacial defects, coupled with a

decrease in carrier diffusion length and a rise in series resistance, can account for the decrease in V_{oc} as a function of operating temperature.

5.3.8 MASnBr$_3$/c-Si Tandem Cell :

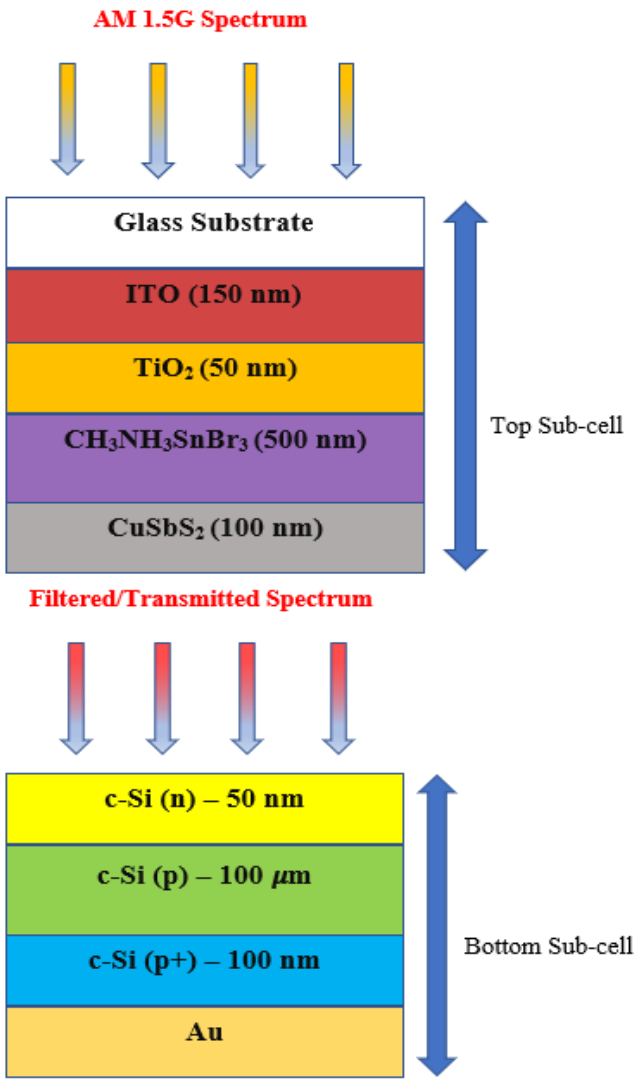

Figure 5-21 : Structure of MASnBr$_3$/c-Si Tandem Cell

Figure 5-21 shows our proposed structure of MASnBr$_3$/c-Si Tandem Cell which consists of MASnBr$_3$ top sub-cell and Si bottom sub-cell. Here, the top cell will absorb mostly AM 1.5G spectrum and the bottom cell will absorb the filtered or transmitted spectrum.

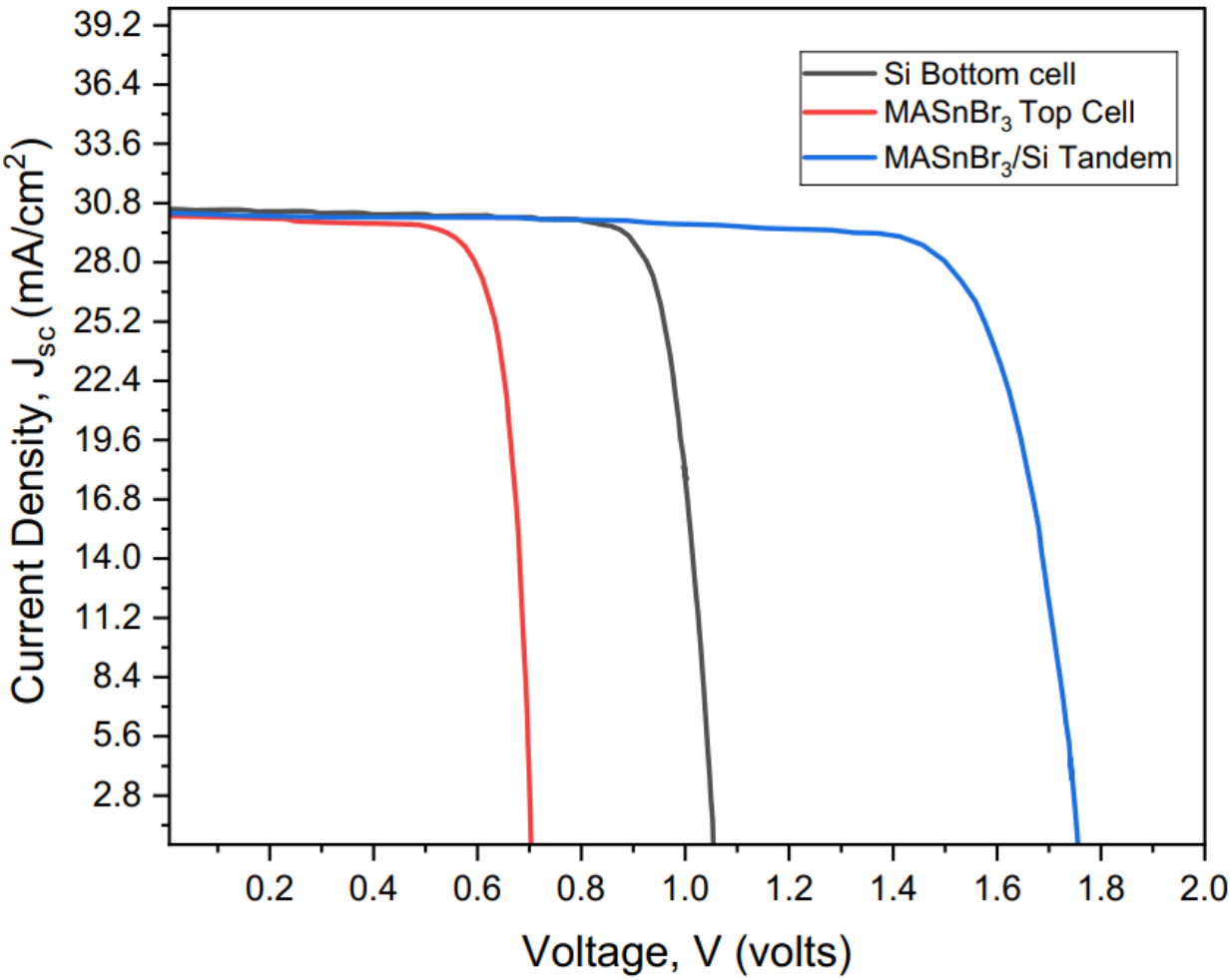

Figure 5-22 : JV curve of $MASnBr_3$/c-Si Tandem Cell

The JV curve relating to the $MASnBr_3$/Si tandem cell has been shown in figure 5-22. The JV curve exhibits a short-circuit current density (J_{sc}) of about 30.75 mA/cm^2 and open-circuit voltage (V_{oc}) of about 1.75 volts which is equal to the sum of open-circuit voltages of top cell and bottom cell. Fill factor and PCE of the tandem cell is 80.43% and 38.86%. Also, the current matching between the top, bottom and tandem cells are also shown in the figure.

5.4 Optimization of GeTe Bottom Cell

5.4.1 Structure of GeTe Bottom Cell

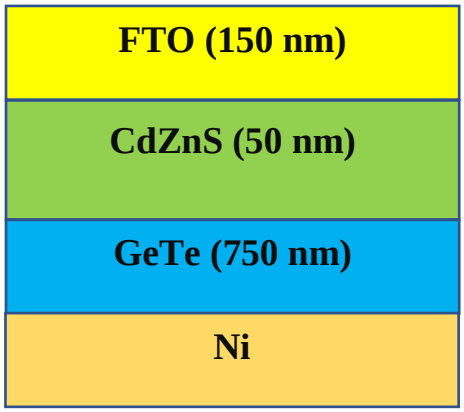

Figure 5-23 : Structure of GeTe Bottom Cell

Table 7 : Input parameters for various layers of GeTe bottom cell

Parameters	**FTO** [116]	**CdZnS** [117]	**GeTe** [118]
Thickness, d (nm)	150	50	750
Electron affinity, x (eV)	4.4	4.44	4.8
Band gap, E_g (eV)	3.6	2.55	0.8
Permittivity, $\in r$	9	9.4	36
Effective density states at CB, N_c (cm^{-3})	2.2×10^{18}	2.1×10^{18}	1×10^{16}
Effective density states at VB, N_v (cm^{-3})	1.8×10^{19}	2.5×10^{16}	1×10^{17}
Electron mobility, μn (cm^2/V-s)	20	95	100
Hole mobility, μp (cm^2/V-s)	10	35	20
Donor doping density, N_D (cm^{-3})	1×10^{18}	1×10^{17}	0
Acceptor doping density, N_A (cm^{-3})	0	0	1×10^{16}
Defect Density, N_t ($1/cm^3$)	1×10^{14}	1×10^{14}	1×10^{14}

5.4.2 Thickness Optimization of GeTe Absorber Layer

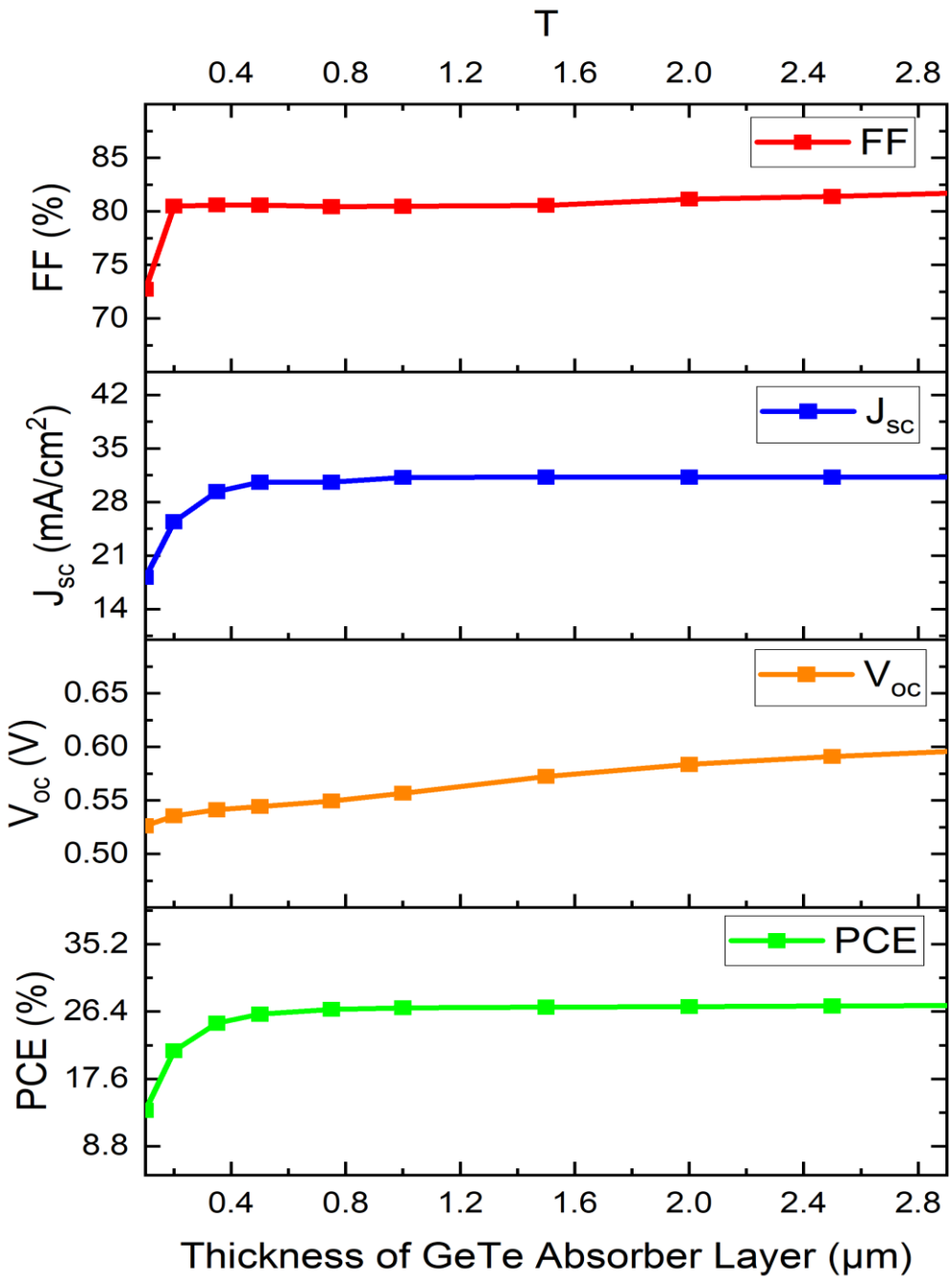

Figure 5-24 : Thickness Optimization of GeTe Absorber Layer

The thickness of the GeTe absorber layer was varied from 100 nm to 3 μm. PCE and J_{sc} seems to be constant after the thickness reached 1 μm. V_{oc} increased slowly when the thickness is increased.

The thickness of 750 nm is chosen as the optimum value for the GeTe absorber layer for material preservation and current matching purpose. At 750 nm thickness, PCE is about 26.70%.

5.4.3 Carrier Density Optimization of GeTe Absorber Layer

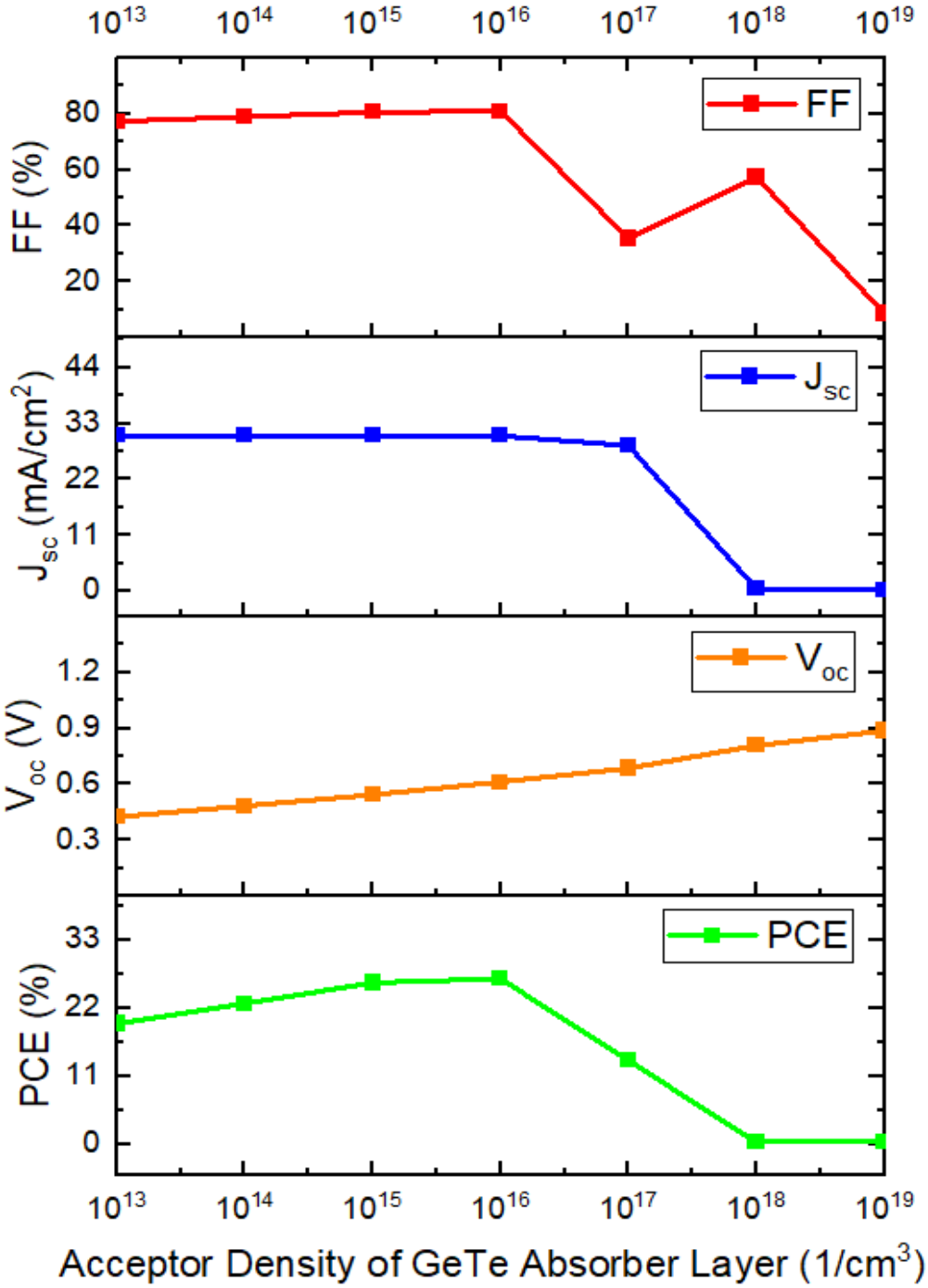

Figure 5-25 : Carrier Density Optimization of GeTe Absorber Layer

The Acceptor Carrier Density of the absorber layer was varied from 10^{13} to 10^{19}. Here, J_{sc} remained constant at first and then sharply declined. V_{oc} proportionally increased with the increase in the carrier density. PCE reaches its maximum value at a doping concentration of 1×10^{16}, after that it went down to a much lower value. So, the doping concentration of 1×10^{15} was chosen as the optimum value for the absorber.

5.4.4 JV curve of GeTe Bottom Cell

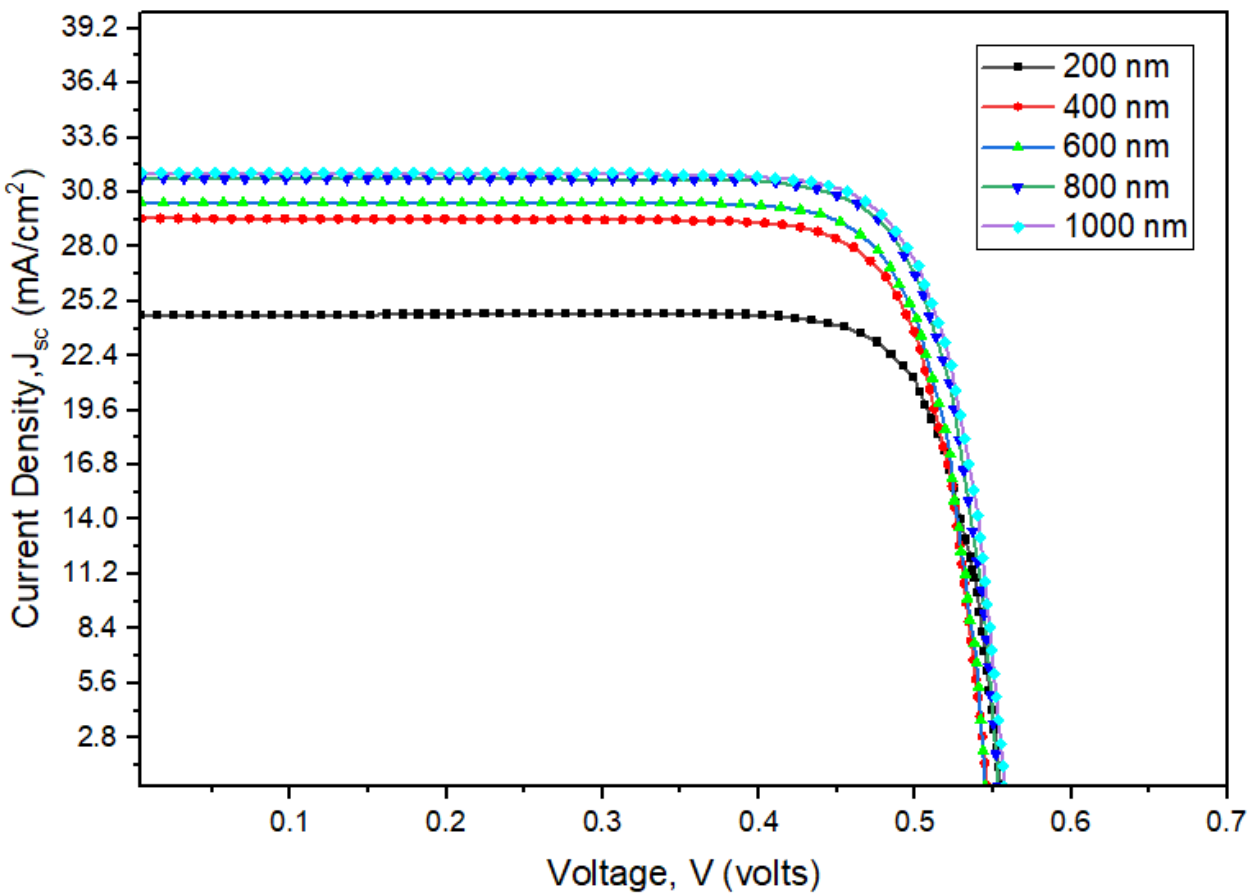

Figure 5-26 : Current Matching Procedure for GeTe Bottom Cell

Figure 5-26 shows the variation of JV curves as the thickness of GeTe absorber layer is varied from 200 nm to 1000 nm. The current density matched with top cell when thickness of the absorber layer is 600 nm.

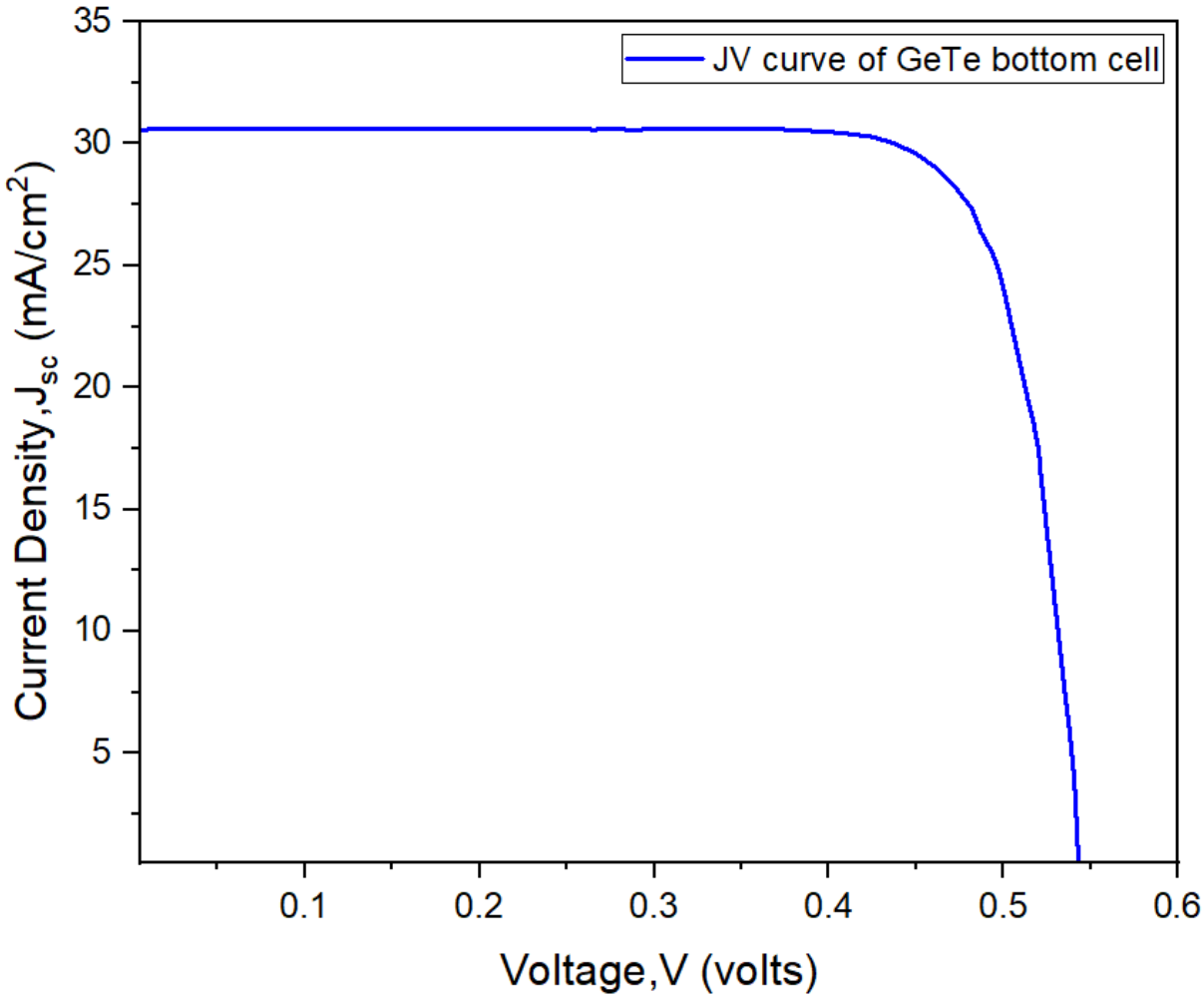

Figure 5-27 : JV curve of GeTe Bottom Cell

The JV curve relating to the GeTe bottom cell has been shown in figure 5-27. The JV curve exhibits a short-circuit current density (J_{sc}) of about 30.60 mA/cm^2 and open-circuit voltage (V_{oc}) of about 0.55 volts.

The thickness of the GeTe absorber layer has been chosen as 750 nm for current matching purpose and material preservation. Our optimized GeTe bottom sub-cell has shown an open-circuit voltage (V_{oc}) of 0.54 volts, short-circuit current density (J_{sc}) of about 30.60 mA/cm^2, Fill Factor of 80.43% and PCE of about 26.70%.

5.4.5 QE curve of GeTe Bottom Cell

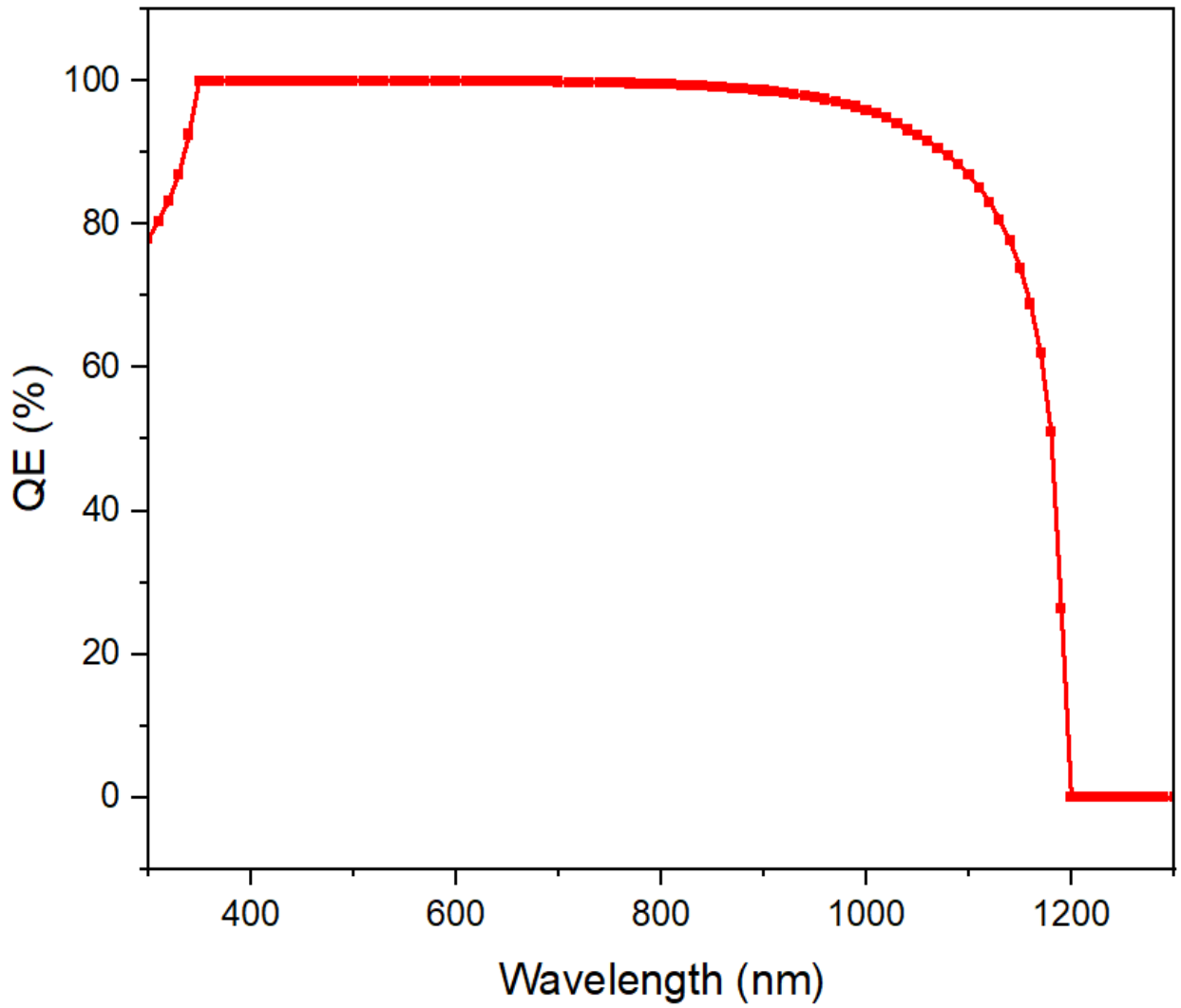

Figure 5-28 : QE vs Wavelength Curve of GeTe Bottom Cell

According to the figure 5-28, the GeTe bottom cell exhibits a quantum efficiency of more than 80% up to 1100 nm wavelength. After that, the absorption declines and there was no absorption after 1200 nm wavelength. It is notable that it shows an excellent quantum efficiency over visible as well as infrared spectrum of light and thus a decent Power Conversion Efficiency was achieved.

5.4.6 Thermal Stability of GeTe Bottom Cell

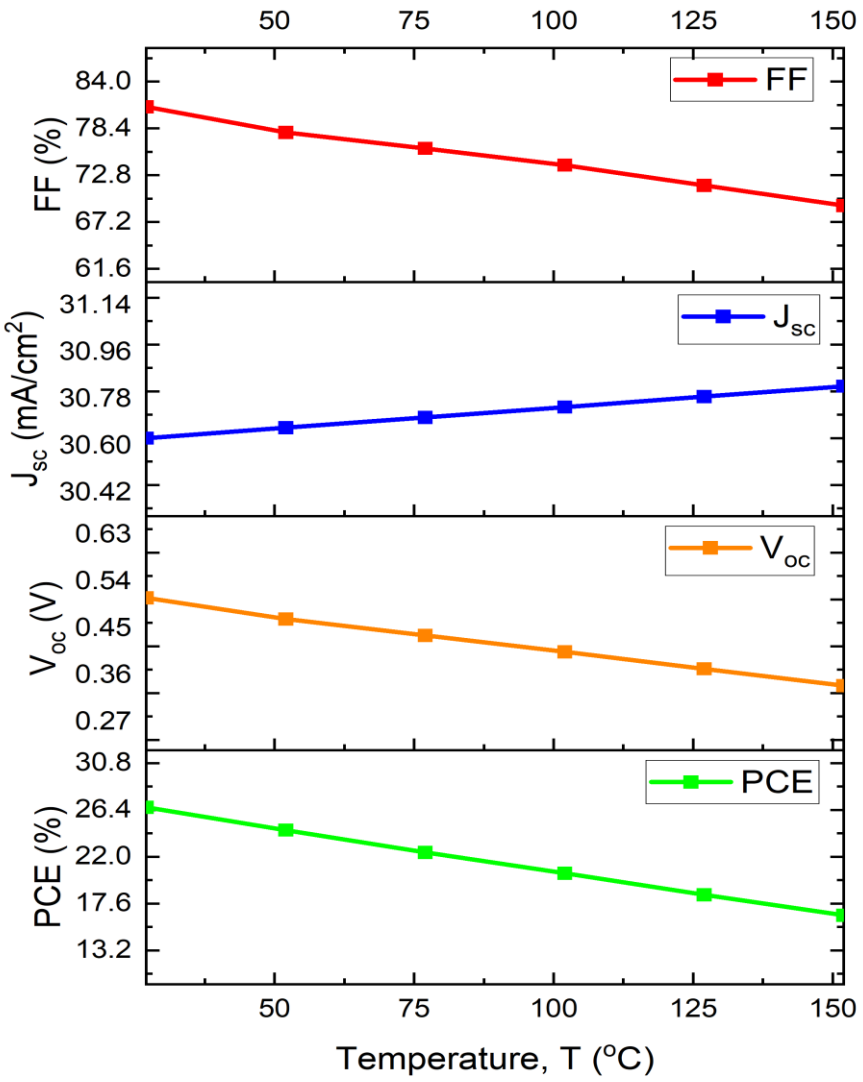

Figure 5-29 : Thermal Stability of GeTe Bottom Cell

Figure 5-29 dictates that PCE went from 26.70% to 16.50% when temperature was varied from 27°C to 152°C. As a result, the temperature coefficient was calculated to be around -0.082% per °C. J_{sc} slightly increased when the temperature is increased due to the reduction of energy band gap and generation of more electron-hole pairs. An increase in interfacial defects, coupled with a decrease in carrier diffusion length and a rise in series resistance, can account for the decrease in V_{oc} as a function of operating temperature.

5.4.7 $MASnBr_3$/GeTe Tandem Cell

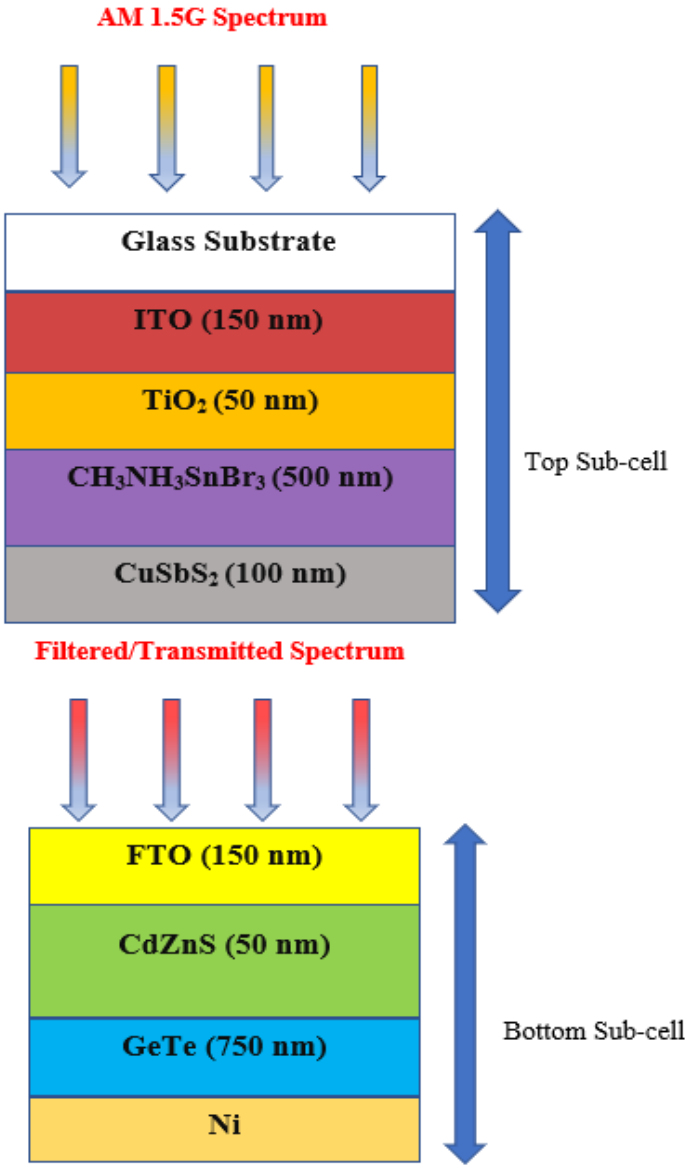

Figure 5-30 : Structure of $MASnBr_3$/GeTe Tandem Cell

Figure 5-30 shows our proposed structure of $MASnBr_3$/GeTe Tandem Cell which consists of $MASnBr_3$ top sub-cell and GeTe bottom sub-cell. Here, the top cell will absorb mostly AM 1.5G spectrum and the bottom cell will absorb the filtered or transmitted spectrum.

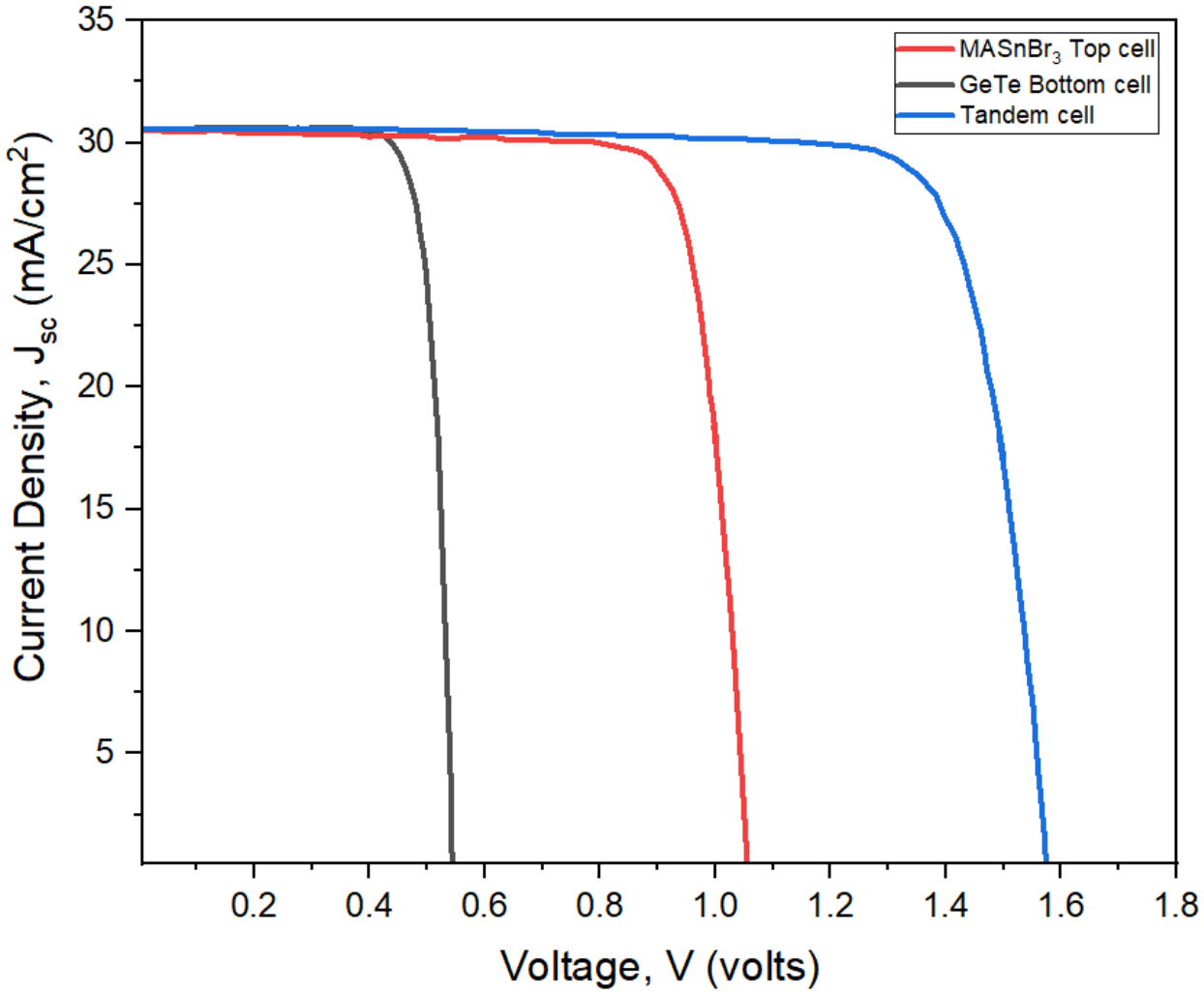

Figure 5-31 : JV curve of $MASnBr_3$/GeTe Tandem Cell

The JV curve relating to the $MASnBr_3$/GeTe tandem cell has been shown in figure 5-31. The JV curve exhibits a short-circuit current density (J_{sc}) of about 30.63 mA/cm^2 and open-circuit voltage (V_{oc}) of about 1.58 volts which is equal to the sum of open-circuit voltages of top cell and bottom cell. Fill factor and PCE of the tandem cell is 81% and 39.20%. Also, the current matching between the top, bottom and tandem cells are also shown in the figure.

5.5 Optimization of $CuInSe_2$ Bottom Cell

5.5.1 Structure of $CuInSe_2$ Bottom Cell

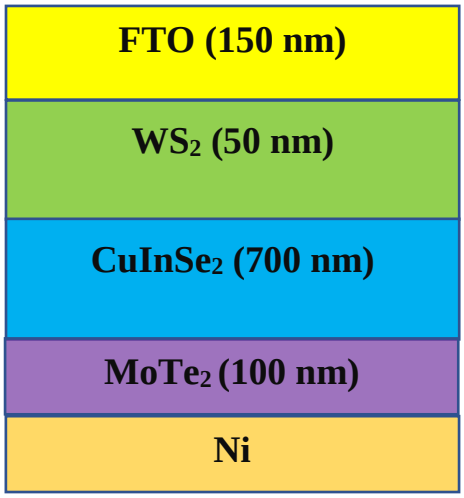

Figure 5-32 : Structure of $CuInSe_2$ Bottom Cell

Table 5.8 : Input parameters for various layers of $CuInSe_2$ bottom cell

Parameters	**FTO** [116]	**WS_2** [119]	**$CuInSe_2$** [120]	**$MoTe_2$** [121]
Thickness, d (nm)	150	50	700	100
Electron affinity, x (eV)	4.4	4.16	4.3	4.35
Band gap, E_g (eV)	3.6	3.05	1.04	1.2
Permittivity, $\in r$	9	10	10	10
Effective density state at CB, N_c (cm^{-3})	2.2×10^{18}	5×10^{18}	2.2×10^{18}	2×10^{18}
Effective density state at VB, N_v (cm^{-3})	1.8×10^{19}	5×10^{18}	1.8×10^{19}	2×10^{18}
Electron mobility, μn (cm^2/V-s)	20	15	100	25
Hole mobility, μp (cm^2/V-s)	10	10	25	100
Donor doping density, N_D (cm^{-3})	1×10^{19}	1×10^{18}	0	0
Acceptor doping density, N_A (cm^{-3})	0	0	1×10^{15}	1×10^{18}
Defect Density, N_t (1/cm^3)	1×10^{14}	1×10^{14}	1×10^{14}	1×10^{14}

5.5.2 Thickness Optimization of $CuInSe_2$ Absorber Layer

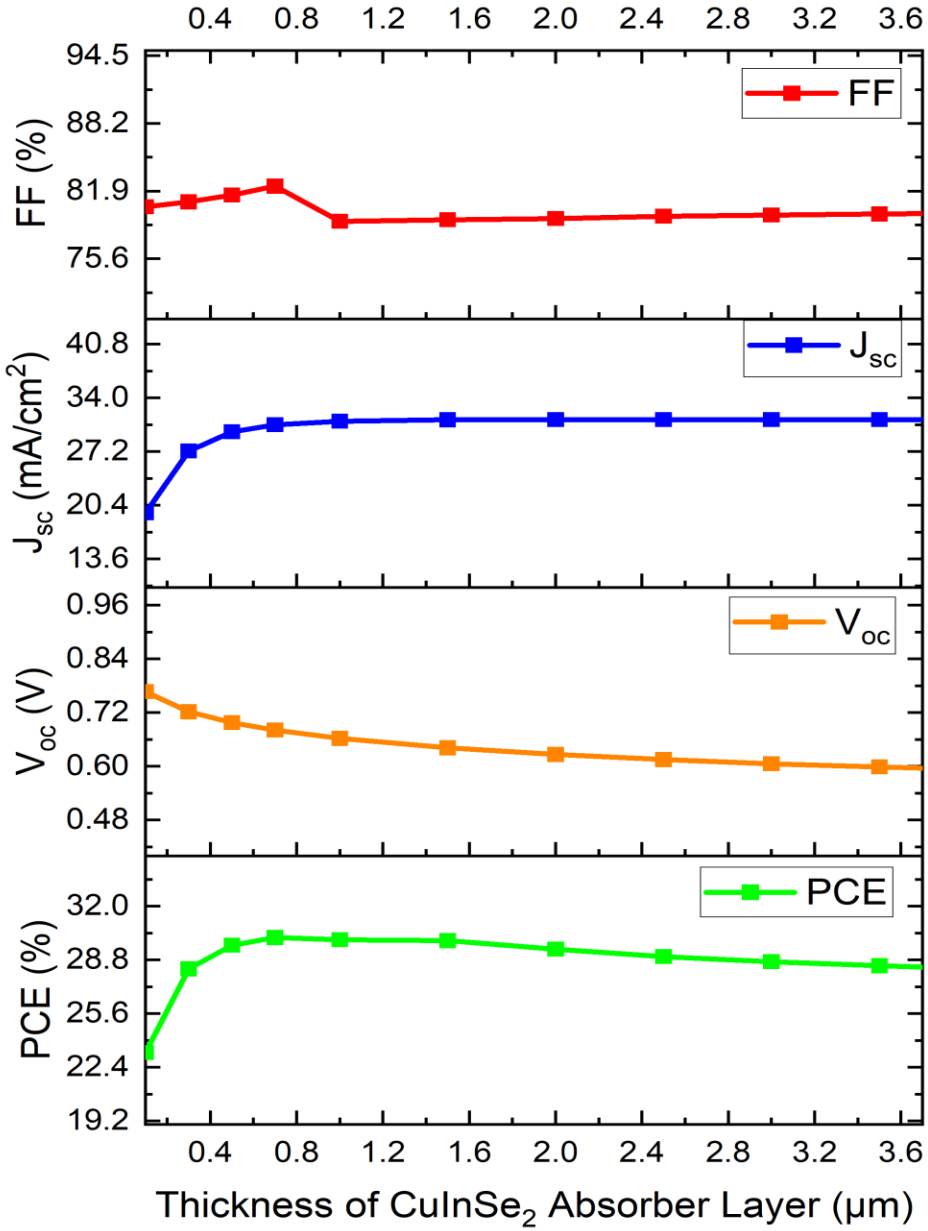

Figure 5-33 : Thickness Optimization of $CuInSe_2$ Absorber Layer

The thickness of the $CuInSe_2$ absorber layer was varied from 100 nm to 4 μm. J_{sc} seems to be constant after the thickness reached 1 μm. V_{oc} decreased slowly when the thickness is increased. FF at first reached maximum level at 700 nm and then shortly after became constant. PCE

increased till 700 nm thickness and then it slowly declined. The thickness of 700 nm is chosen as the optimum value for the GeTe absorber layer for material preservation and current matching purpose. At 700 nm thickness, PCE is about 30.13%.

5.5.3 Carrier Density Optimization of $CuInSe_2$ Absorber Layer

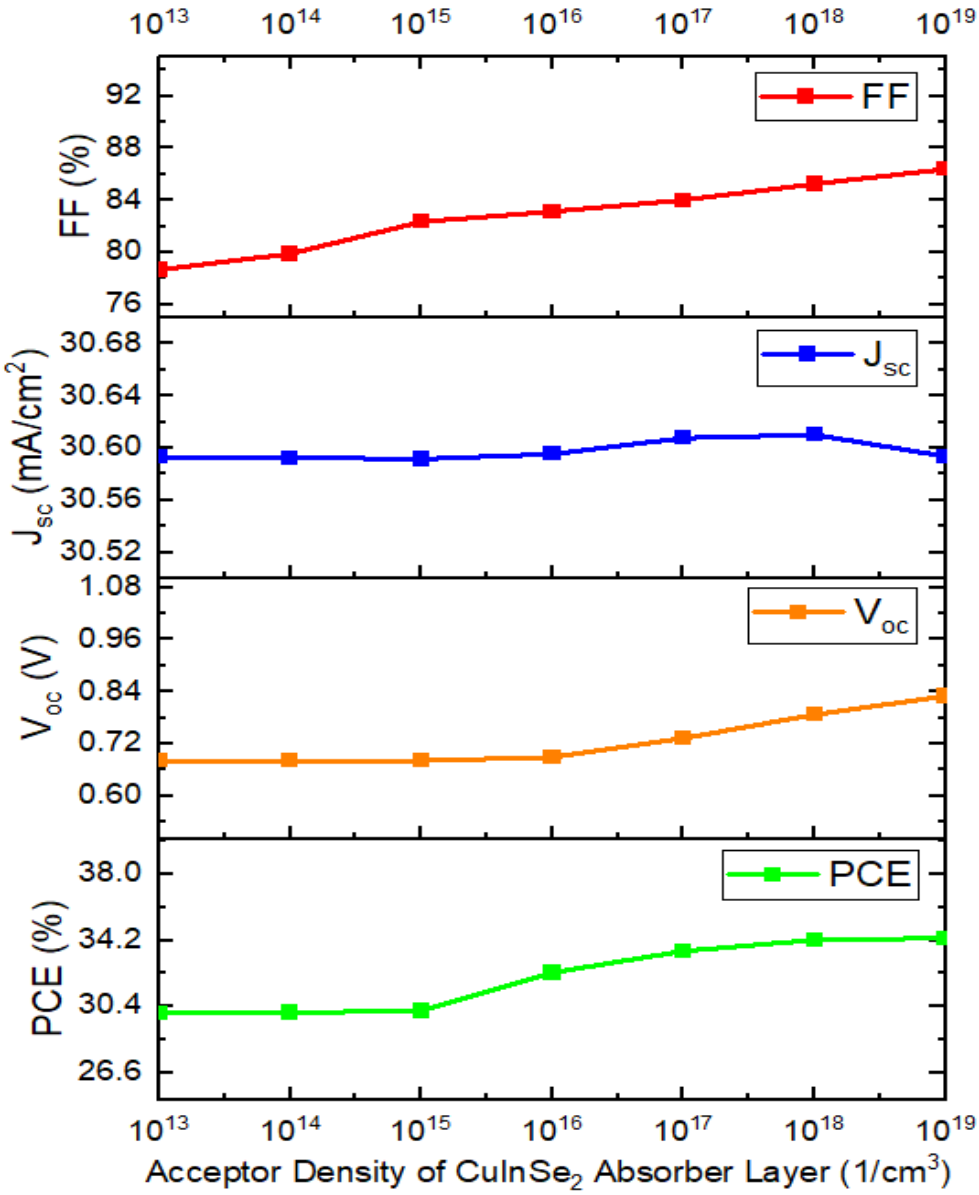

Figure 5-34 : Carrier Density Optimization of $CuInSe_2$ Absorber Layer

The Acceptor Carrier Density of the absorber layer was varied from 10^{13} to 10^{19}. From figure 5-34, we observe that FF increased throughout the process and J_{sc} also didn't deviate much. However,

V_{oc} and PCE seems to be increasing after the concentration 1×10^{15} is reached. The doping concentration of 1×10^{15} is chosen as the optimum value for the absorber layer.

5.5.4 JV curve of $CuInSe_2$ bottom Cell

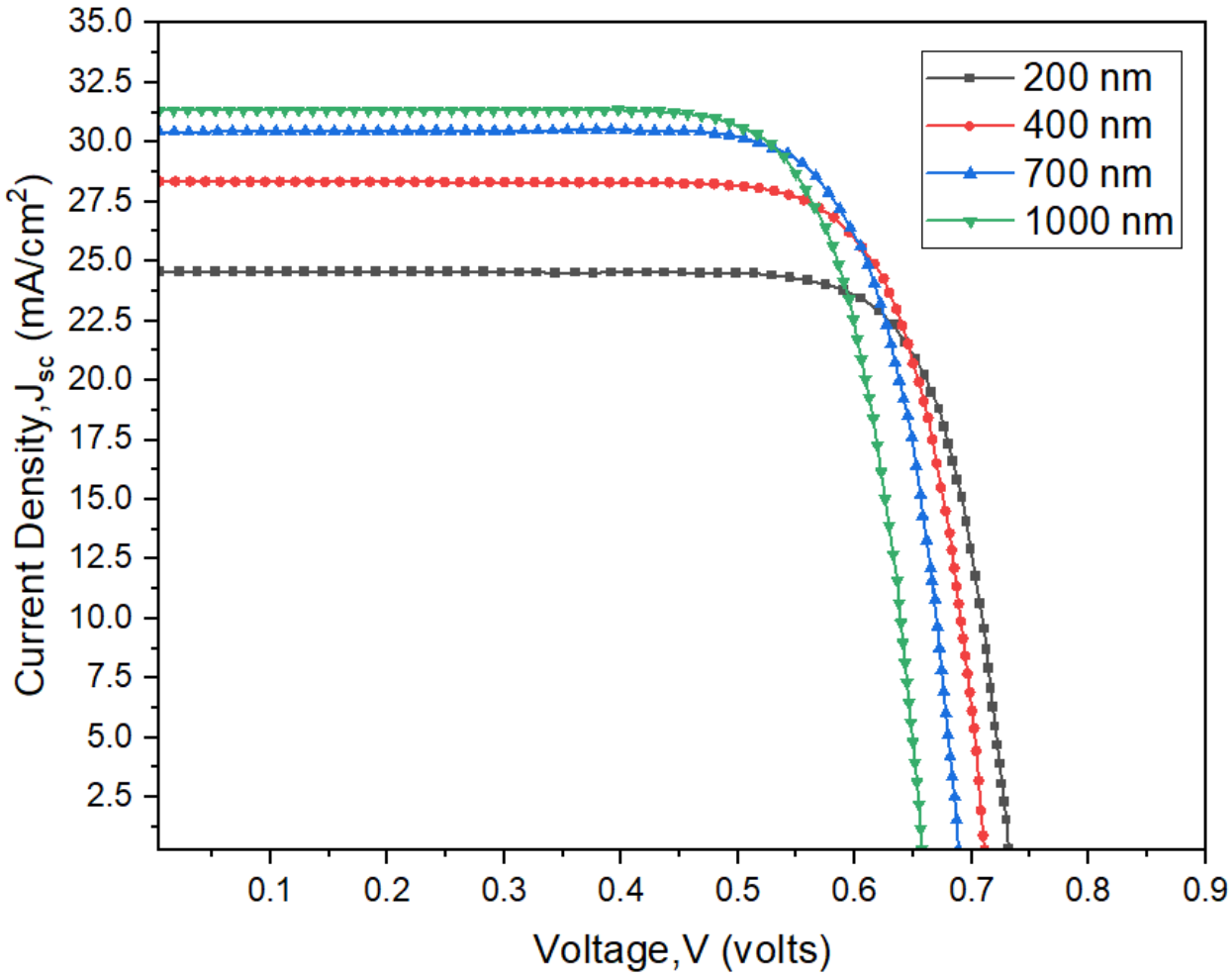

Figure 5-35 : Current Matching Procedure for $CuInSe_2$ Bottom Cell

Figure 5-35 shows the variation of JV curves as the thickness of GeTe absorber layer is varied from 200 nm to 1000 nm. The current density matched with top cell when thickness of the absorber layer is 700 nm.

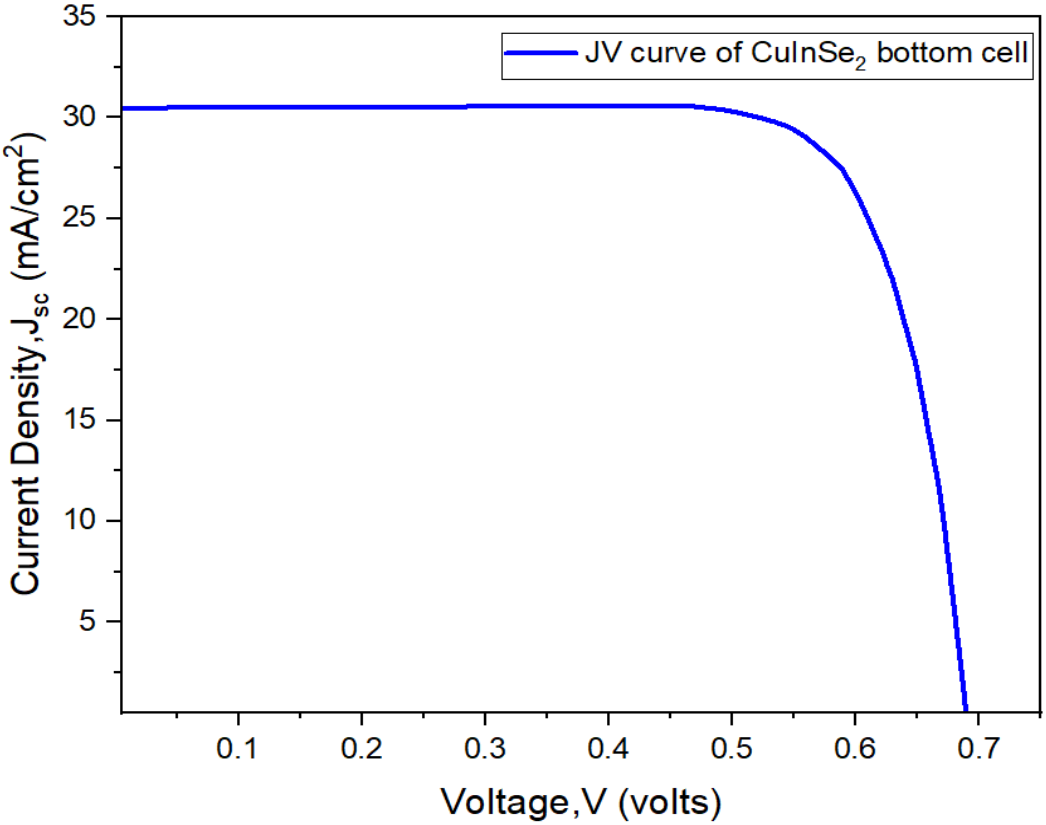

Figure 5-36 : JV curve of $CuInSe_2$ Bottom Cell

The JV curve relating to the $CuInSe_2$ bottom cell has been shown in figure 5-36. The JV curve exhibits a short-circuit current density (J_{sc}) of about 30.58 mA/cm^2 and open-circuit voltage (V_{oc}) of about 0.68 volts.

The thickness of the $CuInSe_2$ absorber layer has been chosen as 700 nm for current matching purpose and material preservation. Our optimized $CuInSe_2$ bottom sub-cell has shown an open-circuit voltage (V_{oc}) of 0.68 volts, short-circuit current density (J_{sc}) of about 30.58 mA/cm^2, Fill Factor of 82.34% and PCE of about 30.13%.

5.5.5 QE curve of $CuInSe_2$ bottom Cell

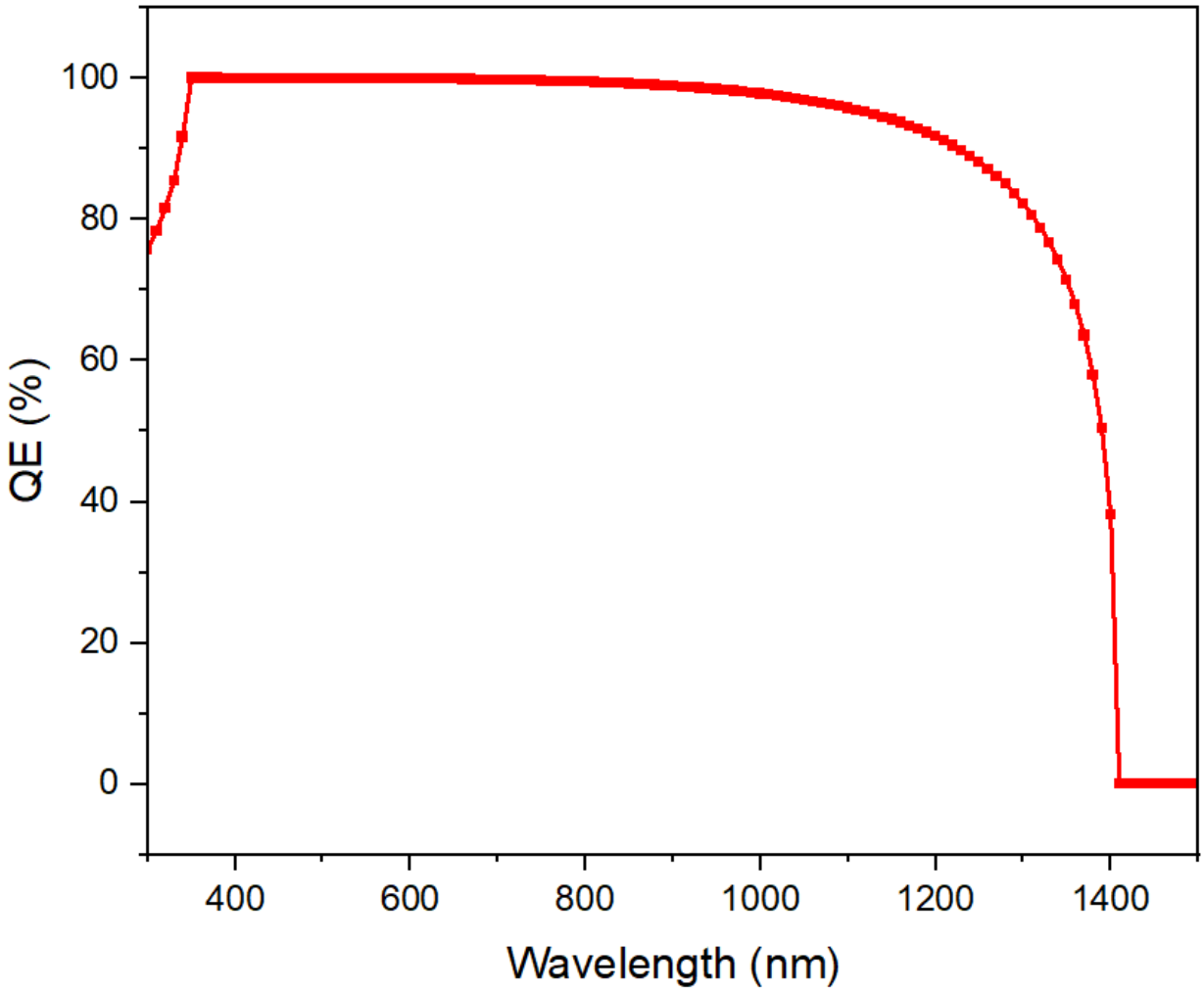

Figure 5-37 : QE vs Wavelength Curve of $CuInSe_2$ Bottom Cell

According to the figure 5-37, the GeTe bottom cell exhibits a quantum efficiency of more than 80% up to 1300 nm wavelength. After that, the absorption declines and there was no absorption after 1400 nm wavelength. It is notable that it shows an excellent quantum efficiency over visible as well as infrared spectrum of light and thus a decent Power Conversion Efficiency was achieved.

5.5.6 Thermal Stability of $CuInSe_2$ Bottom Cell :

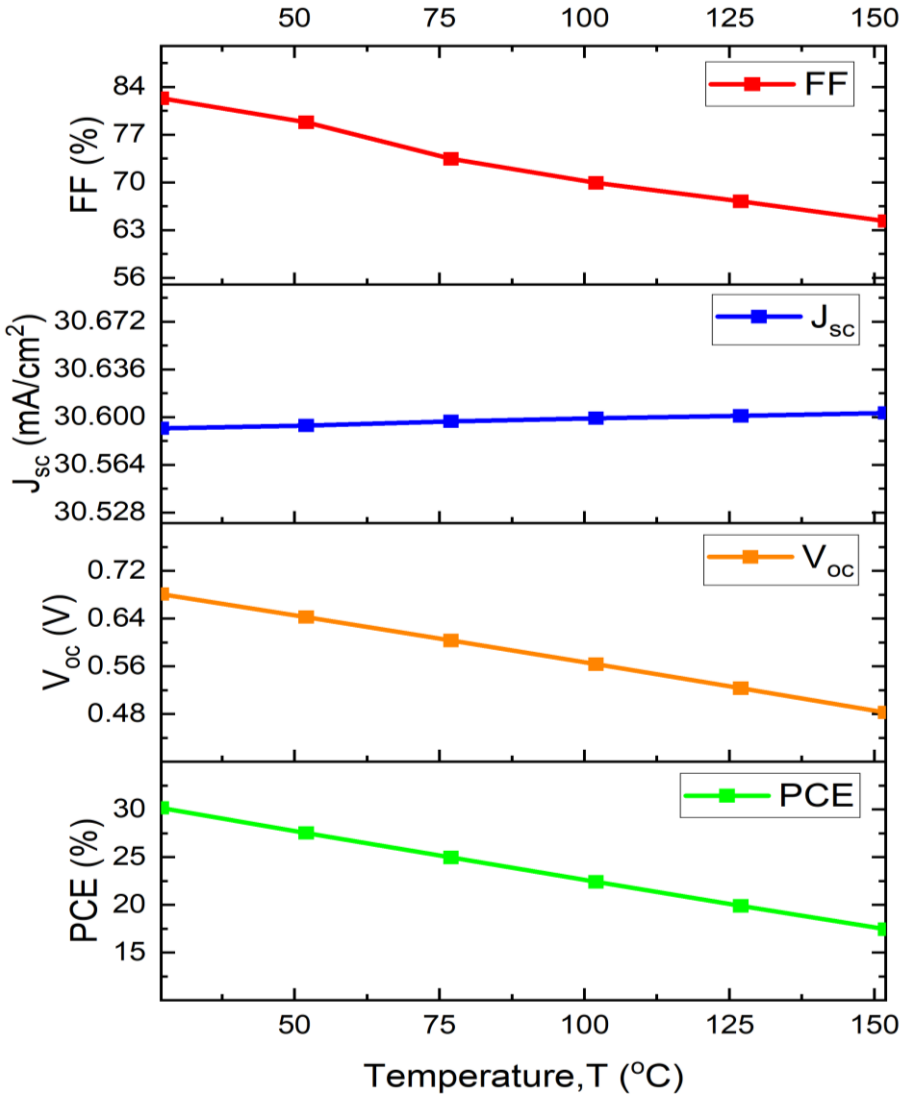

Figure 5-38 : Thermal Stability of $CuInSe_2$ Bottom Cell

Figure 5-38 dictates that PCE went from 30.13% to 17.44% when temperature was varied from 27°C to 152°C. As a result, the temperature coefficient was calculated to be around -0.101% per °C. J_{sc} slightly increased when the temperature is increased due to the reduction of energy band gap and generation of more electron-hole pairs. An increase in interfacial defects, coupled with a decrease in carrier diffusion length and a rise in series resistance, can account for the decrease in V_{oc} as a function of operating temperature.

5.5.7 $MASnBr_3/CuInSe_2$ Tandem Cell

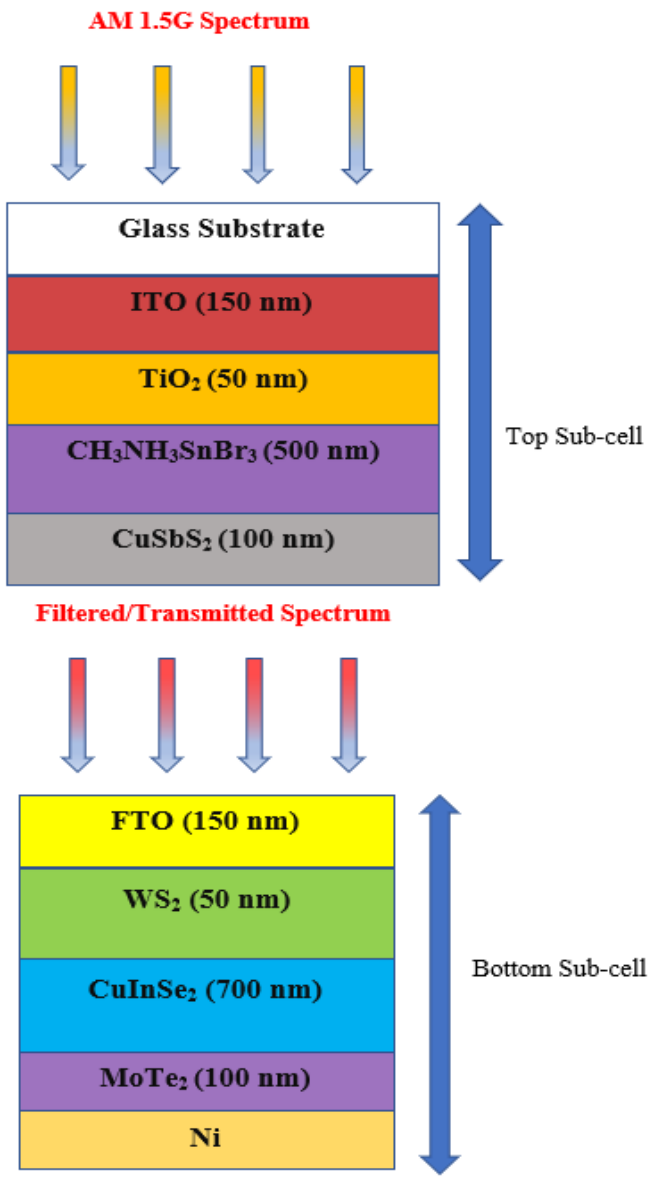

Figure 5-39 : Structure of $MASnBr_3/CuInSe_2$ Tandem Cell

Figure 5-39 shows our proposed structure of $MASnBr_3/CuInSe_2$ Tandem Cell which consists of $MASnBr_3$ top sub-cell and $CuInSe_2$ bottom sub-cell. Here, the top cell will absorb mostly AM 1.5G spectrum and the bottom cell will absorb the filtered or transmitted spectrum.

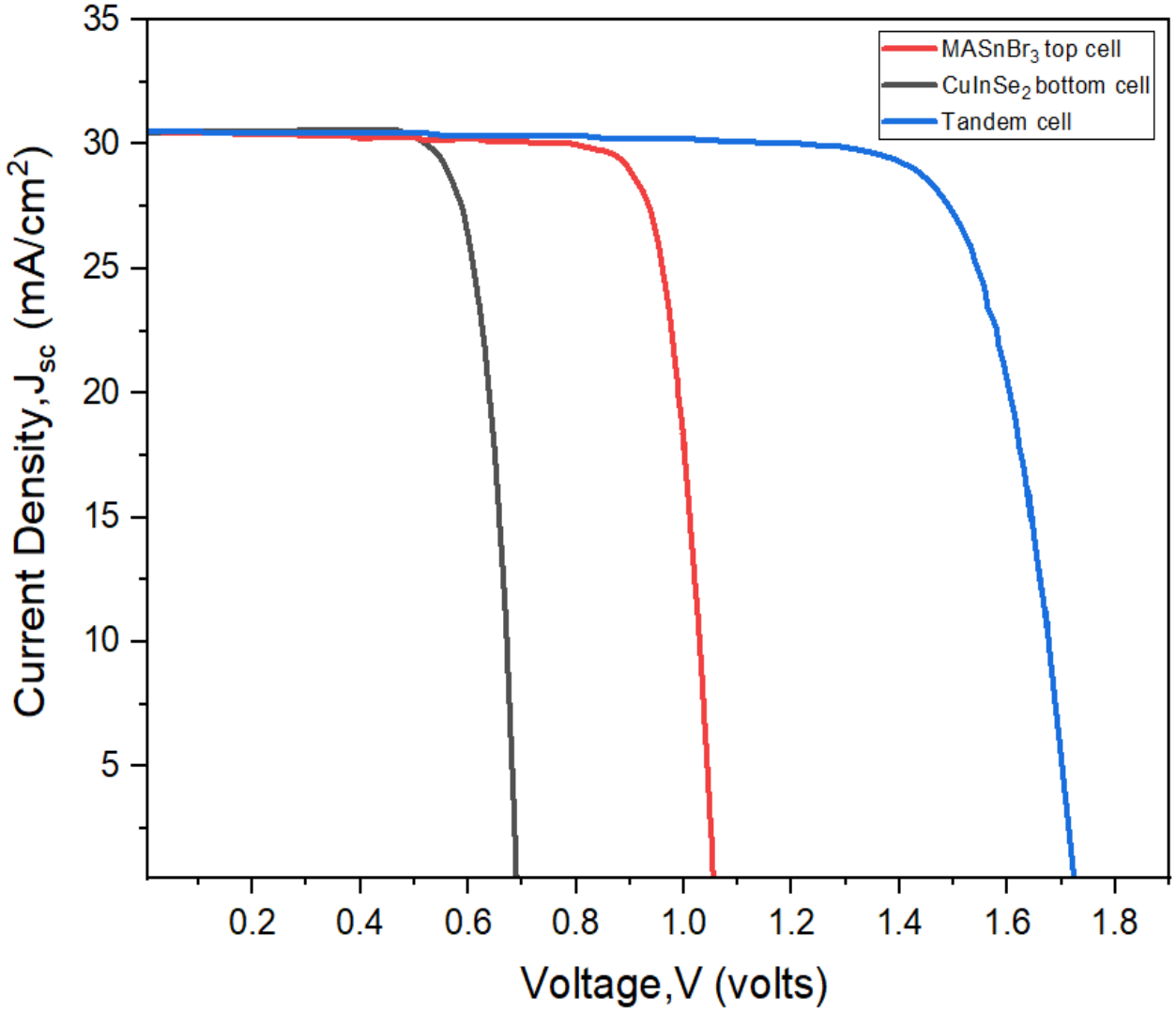

Figure 5-40 : JV curve of $MASnBr_3/CuInSe_2$ Tandem Cell

The JV curve relating to the $MASnBr_3/CuInSe_2$ tandem cell has been shown in figure 5-40. The JV curve exhibits a short-circuit current density (J_{sc}) of about 30.55 mA/cm^2 and open-circuit voltage (V_{oc}) of about 1.71 volts which is equal to the sum of open-circuit voltages of top cell and bottom cell. Fill factor and PCE of the tandem cell is 80.07% and 41.68%. Also, the current matching between the top, bottom and tandem cells are also shown in the figure.

5.6 Results and Analysis

5.6.1 Comparison between the designed solar cells performance

Table 5.9 : Comparative study between designed solar cell performance

Device Structures	V_{oc} (volts)	J_{sc} (mA/cm^2)	FF (%)	PCE (%)
$ITO/TiO_2/CH_3NH_3SnBr_3/Cu_2O/Au$	1.037	30.67	81.05	26.30
FTO/CdZnS/GeTe/Ni	0.55	30.57	80.96	26.70
Si(n) /Si(p) /Si(p+) /Au	0.71	30.76	80.65	25.85
$FTO/WS_2/CuInSe_2/MoTe_2/Ni$	0.68	30.58	82.34	30.13
$CH_3NH_3SnBr_3$ /Si	1.75	30.78	80.43	38.86
$CH_3NH_3SnBr_3$ /GeTe	1.58	30.63	80.95	39.20
$CH_3NH_3SnBr_3$ /$CuInSe_2$	1.71	30.55	80.07	41.68

Based on the comparison in the table 5.9, it is observed that $CH_3NH_3SnBr_3$ /$CuInSe_2$ tandem cell has the highest photo conversion efficiency out of them which is 41.68%. The tandem cell based on $CH_3NH_3SnBr_3$ /GeTe structure obtained second highest efficiency which is 39.20%. Finally, $CH_3NH_3SnBr_3$ /Si tandem cell has the lowest photo conversion efficiency which is 38.86%.

The efficiency achieved by the $CH_3NH_3SnBr_3$ /$CuInSe_2$ tandem cell is aided by the high open-circuit voltage of $CuInSe_2$ cell which in turn increased the overall open-circuit voltage of the tandem cell.

5.6.2 $MASnBr_3$ Cell Performance With and Without BSF Layer

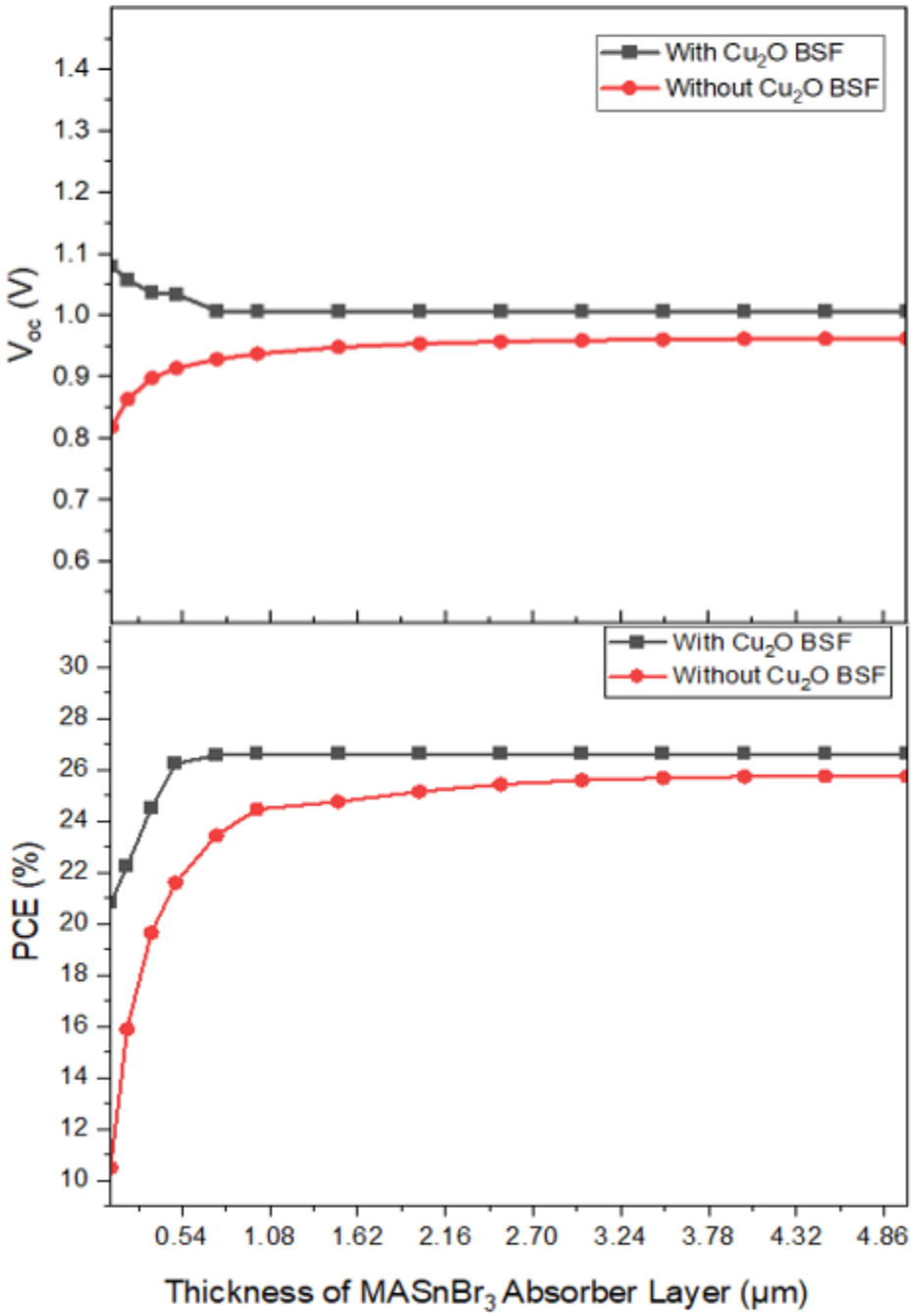

Figure 5-41 : V_{oc} and PCE variation with and without Cu_2O BSF layer

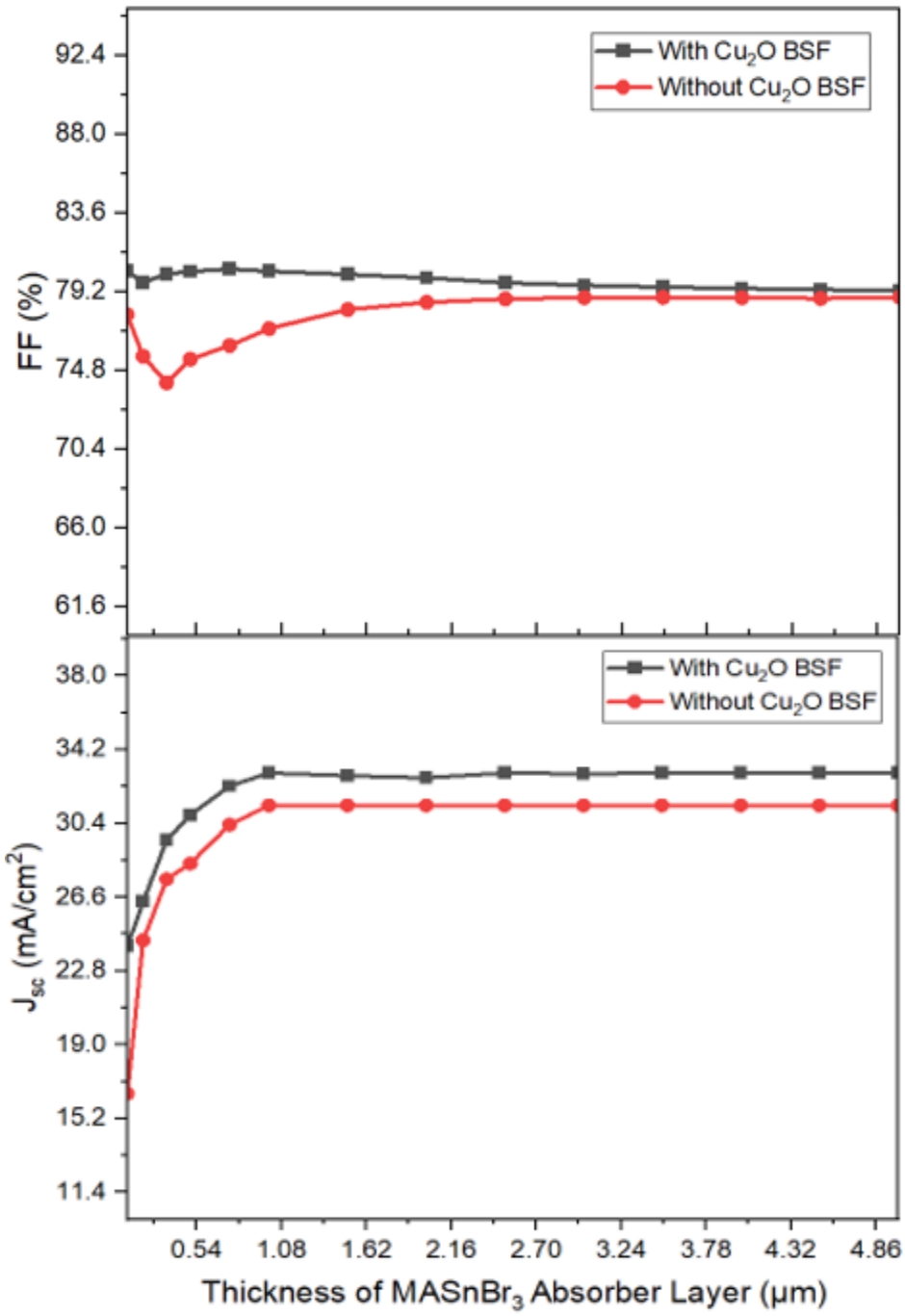

Figure 5-42 : FF and J_{sc} variation with and without Cu_2O BSF layer

The insertion of Cu_2O BSF layer in the top cell enhanced the device performance significantly.The BSF layer minimizes the recombination losses in the back surface which in turn improved the power conversion efficiency of the solar cell.

5.6.3 Comparison between thermal stability of the designed solar cells

5.6.3.1 Thermal Stability of $CH_3NH_3SnBr_3$ /Si Tandem Cell

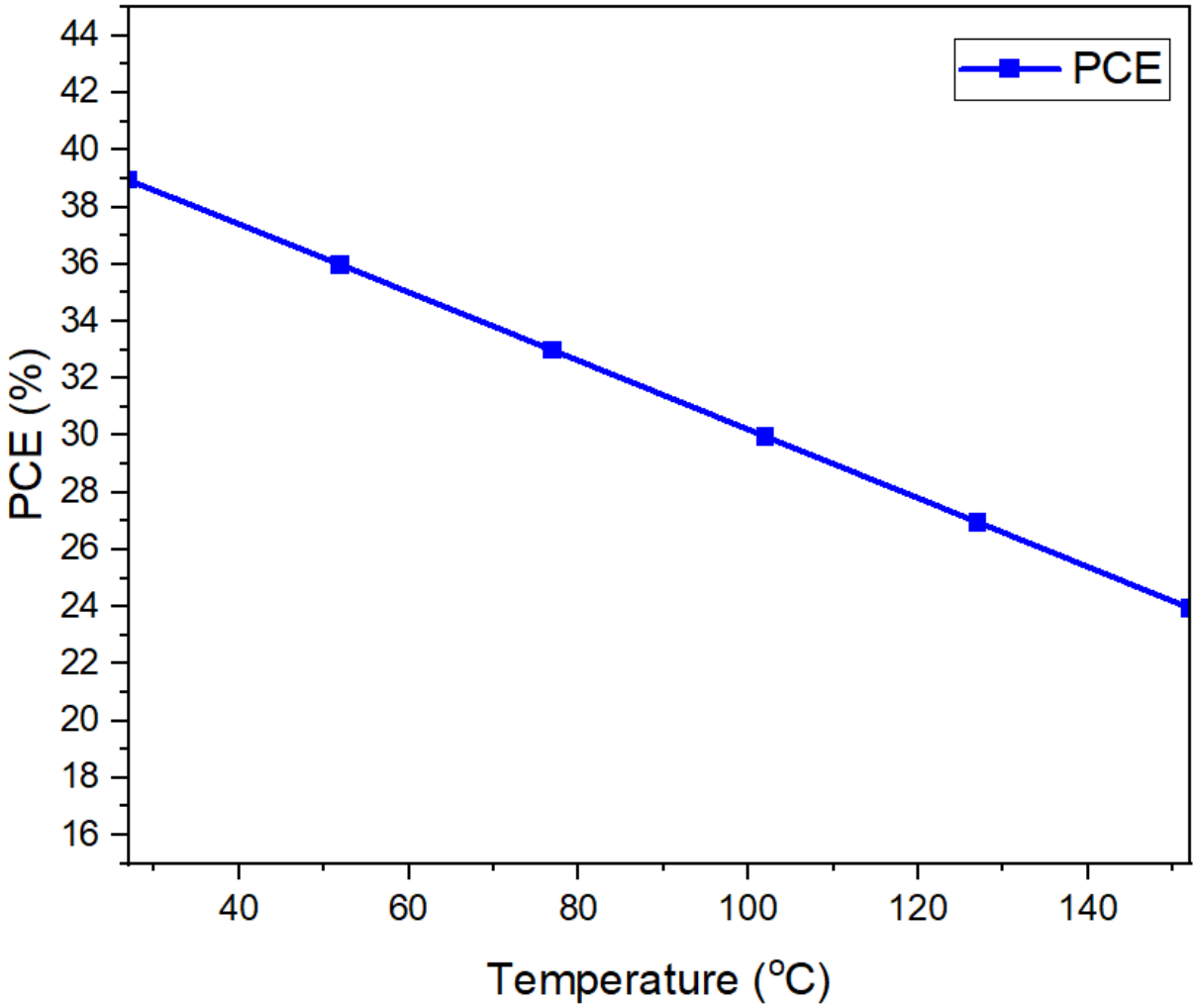

Figure 5-43 : Thermal Stability of $CH_3NH_3SnBr_3$ /Si tandem cell

Figure 5-43 dictates that PCE of the $CH_3NH_3SnBr_3$ /Si tandem cell went from 38.86% to 23.95% when temperature was varied from 27°C to 152°C. As a result, the temperature coefficient was calculated to be around -0.118% per °C.

5.6.3.2 Thermal Stability of $CH_3NH_3SnBr_3$ /GeTe Tandem Cell

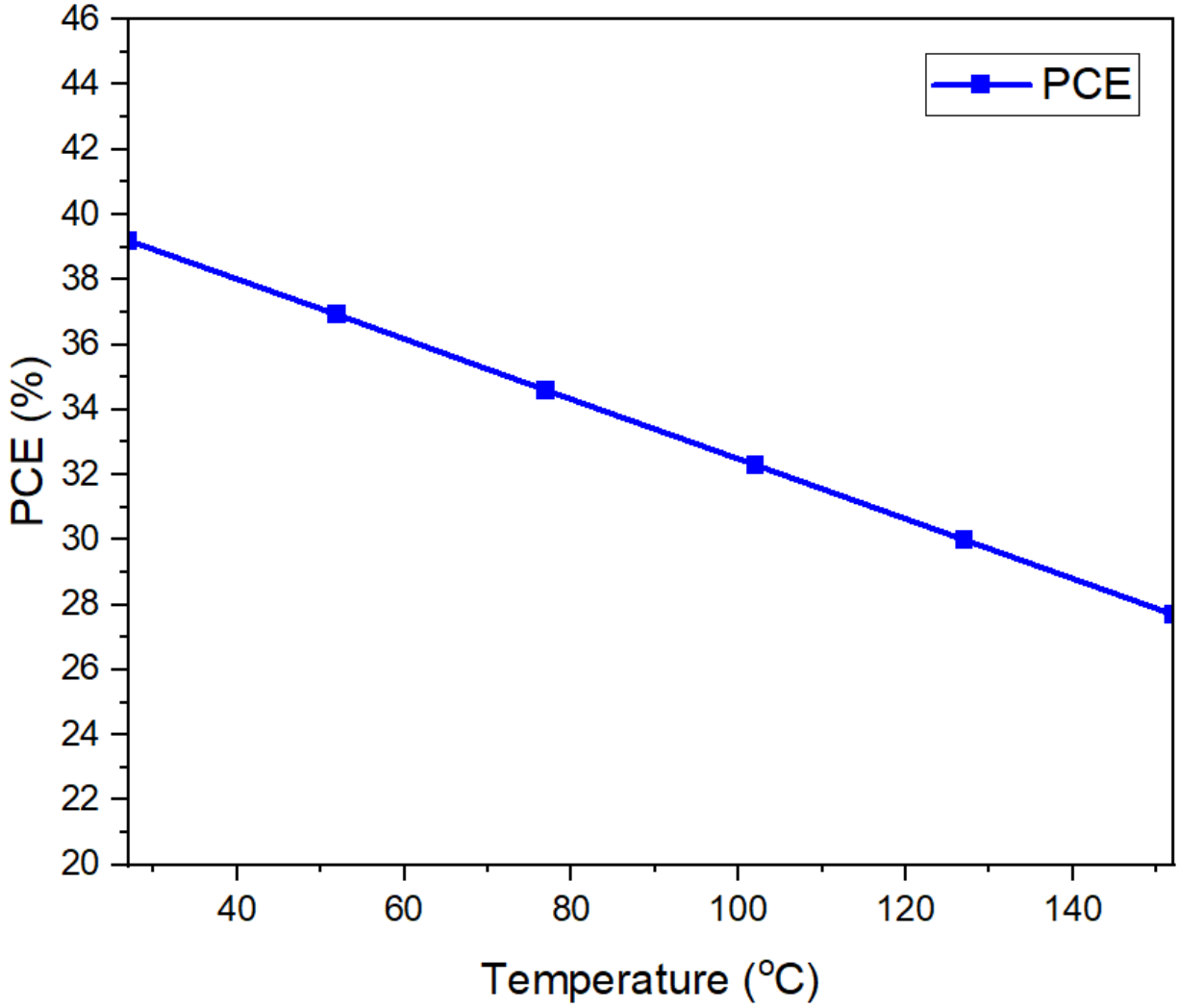

Figure 5-44 : Thermal Stability of $CH_3NH_3SnBr_3$ /GeTe tandem cell

Figure 5-44 dictates that PCE of the $CH_3NH_3SnBr_3$ /GeTe tandem cell went from 39.20% to 27.72% when temperature was varied from 27°C to 152°C. As a result, the temperature coefficient was calculated to be around -0.092% per °C.

5.6.3.3 Thermal Stability of $CH_3NH_3SnBr_3$ /$CuInSe_2$ Tandem Cell

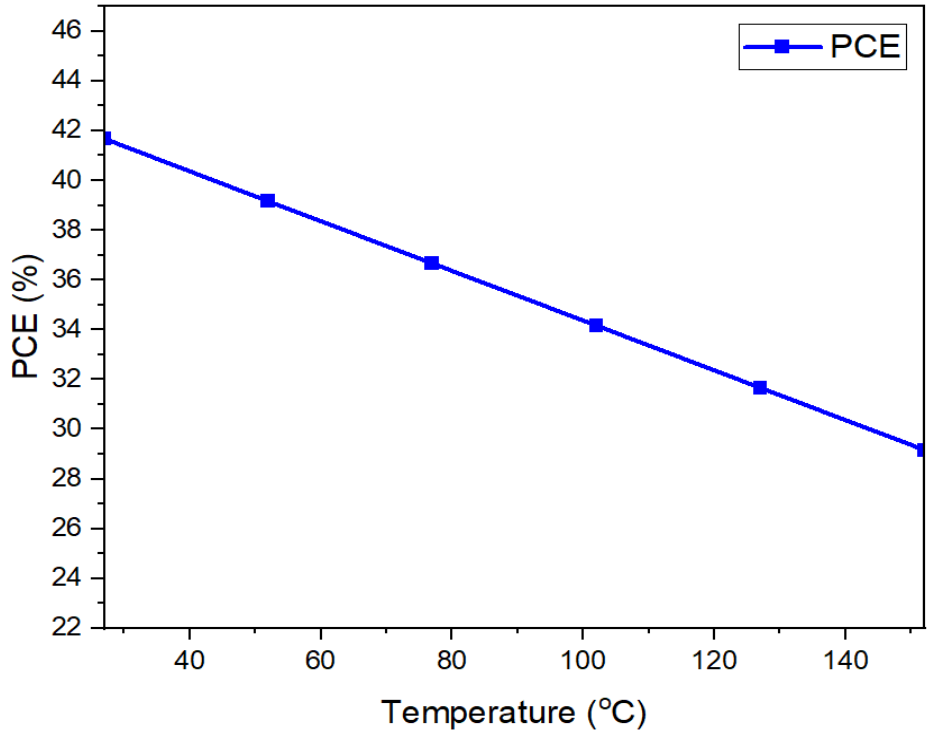

Figure 5-45 : Thermal Stability of $CH_3NH_3SnBr_3$ /$CuInSe_2$ tandem cell

Figure 5-45 dictates that PCE of the $CH_3NH_3SnBr_3$ /$CuInSe_2$ tandem cell went from 41.68% to 29.865% when temperature was varied from 27°C to 152°C. As a result, the temperature coefficient was calculated to be around -0.095% per °C.

Table 5.10 Summary of the Thermal Stability of the designed solar cells :

Tandem Structures	Efficiency at Room Temperature (27°C)	Temperature Coefficient (per °C)
$CH_3NH_3SnBr_3$ / Si tandem	38.86%	-0.118%
$CH_3NH_3SnBr_3$ / GeTe tandem	39.20%	-0.092%
$CH_3NH_3SnBr_3$ / $CuInSe_2$ tandem	41.68%	-0.095%

From the table 6.2, it can be observed $CH_3NH_3SnBr_3$ /$CuInSe_2$ tandem cell has the best efficiency at the room temperature and also has a moderately good temperature coefficient. Therefore, it is the best option indeed.

5.7 Comparison between this work and previously published works

Table 5.11 : Comparative Study between this work and previously published works :

Device Structures	**V_{oc} (volts)**	**J_{sc} (mA/cm^2)**	**FF (%)**	**PCE (%)**	**Ref.**
Glass-base / FTO / $Cd_{0.5}Zn_{0.5}S$ / $MASnI_3$ / $MASnBr_3$ / Au	0.96	32.48	76.40	23.86	[122]
ITO/ZnO/$MASnI_3$/ $CuSbS_2$/Ag	0.876	33.19	76.19	22.16	[123]
n-TiO_2/i- $MASnBr_3$ /p-NiO	0.80	31.88	84.89	21.66	[124]
ITO/ZnO/$MASnBr_3$/Spiro-OMeTAD/Au	1.01	32.42	75.67	25.02	[125]
$CH_3NH_3PbI_3$ / CIGS	1.81	20.49	81.90	30.50	[126]
$CH_3NH_3PbI_3$ / GeTe	1.747	25.88	79.40	35.90	[127]
$CH_3NH_3PbI_3$ / Si	2.11	20.95	79.45	35.30	[128]
$MAGeI_3$ / $FASnI_3$	2.62	14.69	79.80	30.86	[129]
$CH_3NH_3SnBr_3$ / Si	1.75	30.78	80.43	38.86	This work
$CH_3NH_3SnBr_3$ / GeTe	1.58	30.63	80.95	39.20	This work
$CH_3NH_3SnBr_3$ / $CuInSe_2$	1.71	30.55	80.07	41.68	This work

In table 5.11, we've compared our work with previously published works and the findings of previously published tandem solar cell studies are summarized. Comprehensive improvements in the device performances of the designed cells are shown.

CHAPTER 6 : CONCLUSION

6.1 Summary

In this work, we have designed a perovskite-based tandem solar cell using SCAPS 1D and optimized it to enhance its performance parameters. At first, we have designed the standalone top sub-cell consisting of ITO as TCO layer, TiO_2 as window layer, $MASnBr_3$ as absorber layer and Cu_2O as BSF layer. The ITO/TiO_2/$MASnBr_3$/Cu_2O/Au top cell showed a V_{oc} of 1.037 volts, J_{sc} of 30.67 mA/cm^2, FF of 81.05% and PCE of 26.30%. Then, the standalone bottom sub-cell was designed consisting of FTO as TCO layer, CdZnS as window layer, GeTe as absorber layer. The FTO/CdZnS/GeTe/Ni bottom cell showed a V_{oc} of 0.55 volts, J_{sc} of 30.57 mA/cm^2, FF of 80.96% and PCE of 28.43%. Furthermore, the standalone bottom sub-cell was designed consisting of c-Si(n), c-Si(p), c-Si(p+) layers. The c-Si(n)/c-Si(p)/c-Si(p+)/Au bottom cell showed a V_{oc} of 0.71 volts, J_{sc} of 30.76 mA/cm^2, FF of 80.63% and PCE of 25.85%. Finally, the standalone bottom sub-cell was designed consisting of FTO as TCO layer, WS_2 as window layer, $CuInSe_2$ as absorber layer and $MoTe_2$ as BSF layer. The FTO/WS_2/$CuInSe_2$/$MoTe_2$/Ni bottom cell showed a V_{oc} of 0.68 volts, J_{sc} of 30.58 mA/cm^2, FF of 82.34% and PCE of 30.13%. Our designed tandem structure consisting of $MASnBr_3$ based top cell and c-Si based bottom cell has shown a V_{oc} of 1.75 volts, J_{sc} of 30.78 mA/cm^2, FF of 80.43% and PCE of 38.86%. The configuration with $MASnBr_3$ based top cell and GeTe based bottom cell has shown a V_{oc} of 1.58 volts, J_{sc} of 30.63 mA/cm^2, FF of 80.95% and PCE of 39.20%. Finally, the $MASnBr_3$/$CuInSe_2$ tandem cell has shown a V_{oc} of 1.71 volts, J_{sc} of 30.55 mA/cm^2, FF of 80.07% and PCE of 41.68%. Therefore, our analysis provides a $MASnBr_3$ based tandem solar cell which exhibits an excellent efficiency of maximum 41.68% including eco-friendly, non-toxic and stability features.

6.2 Key Findings

1. TiO_2 as window layer : Titanium Dioxide was used as a window layer in our simulations which provided the desired outcome. The $MASnBr_3$ based top sub-cell including the TiO_2 window layer has shown an excellent PCE of 26.30%. It formed the required p-n junction associated with the top cell acted as the n-type layer. Without affecting the light absorption of the device, the window layer effectively lowered the surface recombination at the emitter surface.

2. Current matching properties : In this work, the top cell and bottom cells were designed separately and they were optimized to match the current between the top cell and bottom cell in the tandem configuration. As two sub-cells are connected in series, current matching between the top and bottom cell is always required to prevent the sub-cell with lower current from restricting the device's total current. The thickness of the absorber layer was optimized to adjust the current density of the cells to the desired level.

3. $CuInSe_2$ based bottom cell : The bottom sub-cell based on $CuInSe_2$ absorber layer exhibited the best performance characteristics with a high Photo-Conversion Efficiency (PCE) of 30.13%. The $CuInSe_2$ based bottom cell in conjunction with $MASnBr_3$ based top cell has shown a V_{oc} of 1.71 volts, J_{sc} of 30.55 mA/cm^2, FF of 80.07% and PCE of 41.68%. The highly efficient $MASnBr_3/CuInSe_2$ has also shown a moderately good temperature coefficient of -0.095%/per ^oC considering its performance parameters. Therefore, $CuInSe_2$ based bottom cell has a relatively better performance characteristics compared with the c-Si and GeTe based bottom cells. So, $CuInSe_2$ based cell is the most suitable bottom cell in this work.

4. Insertion of BSF layer in the perovskite top cell : The insertion of Cu_2O BSF layer in the perovskite based top cell enhanced the device performance significantly.The BSF layer minimizes the recombination losses in the back surface which in turn improved the parameters such as open-circuit voltage (V_{oc}), short-circuit current density (J_{sc}), fill factor and power conversion efficiency of the solar cell.

6.3 Limitations and Future Recommendations

In this work, we have optimized the cells by means of thickness, carrier density and defect density variations. Beside these methods, bandgap tuning can also be implemented to enhance the performance of the device. Also, the overall efficiency of the tandem solar cell can be boosted by designing multi-junction solar cells although the structure of the cell will get somewhat more complex. Furthermore, perovskite materials show instability and inherent weaknesses when they are exposed to moisture, O_2, UV light etc [153]. Additionally, the maximum experimental lifetime of a perovskite solar cell is approximately 1 year while Silicon solar cells can provide service almost up to 25 years [154].

To make the perovskite solar cells more usable and long-lasting, their stability and durability should be improved. The recommended methods to effectively extend the lifetime of perovskite solar cells are interface engineering, multi-junction structure, inorganic cations doped in a site of ABX_3 structure etc. As perovskite materials show instability issues whenever they are exposed to oxygen or moisture, To solve this problem, perovskite solar cells should be properly encapsulated and manufactured in a sealed box before being exposed to air.

References

[1] "What is Renewable Energy and the Sources of Renewable Energy - shah khan - Medium." Accessed: Mar. 25, 2024. [Online]. Available: https://medium.com/@shahkhan13115/what-is-renewable-energy-and-the-sources-of-renewable-energy-7cd21ad7ef2b

[2] "Summary of global expansion of renewable energies | en:former." Accessed: Mar. 25, 2024. [Online]. Available: https://www.en-former.com/en/summary-of-global-expansion-of-renewable-energies/

[3] "Renewable energy: the global transition, explained in 12 charts - Vox." Accessed: Mar. 25, 2024. [Online]. Available: https://www.vox.com/energy-and-environment/2019/6/18/18681591/renewable-energy-china-solar-pv-jobs

[4] "An overview of the hydropower production potential in Bangladesh to meet the energy requirements." Accessed: Mar. 25, 2024. [Online]. Available: https://www.eeer.org/journal/view.php?number=1237

[5] M. Abdullah-Al-Mahbub and A. R. M. T. Islam, "Current status of running renewable energy in Bangladesh and future prospect: A global comparison," *Heliyon*, vol. 9, no. 3. Elsevier Ltd, Mar. 01, 2023. doi: 10.1016/j.heliyon.2023.e14308.

[6] J. Heinimö and M. Junginger, "Production and trading of biomass for energy - An overview of the global status," 2009, doi: 10.1016/j.biombioe.2009.05.017.

[7] "Biomass Power Market Size, Growth, Trends, Report 2023-2030." Accessed: Mar. 25, 2024. [Online]. Available: https://www.precedenceresearch.com/biomass-power-market

[8] I. Malico, R. N. Pereira, A. C. Gonçalves, and A. M. O. Sousa, "Current status and future perspectives for energy production from solid biomass in the European industry," 2019, doi: 10.1016/j.rser.2019.06.022.

[9] "1: Wind energy status of world scenario | Download Scientific Diagram." Accessed: Mar. 25, 2024. [Online]. Available: https://www.researchgate.net/figure/Wind-energy-status-of-world-scenario_fig1_321194394

[10] "Global wind energy capacity growth. Data source: The Wind Power... | Download Scientific Diagram." Accessed: Mar. 25, 2024. [Online]. Available: https://www.researchgate.net/figure/Global-wind-energy-capacity-growth-Data-source-The-Wind-Power-Statistics-19_fig1_342995337

[11] "Wind Power Market Size, Share & Growth Report, 2021 - 2030." Accessed: Mar. 25, 2024. [Online]. Available: https://www.sphericalinsights.com/reports/wind-energy-market

[12] M. Fyk, V. Biletskyi, and M. Abbud, "Resource evaluation of geothermal power plant under the conditions of carboniferous deposits usage in the Dnipro-Donetsk depression," *E3S Web of Conferences*, vol. 60, p. 00006, May 2018, doi: 10.1051/e3sconf/20186000006.

[13] C. J. Cleveland, "Preface to the First Edition," *Dictionary of Energy*, p. 291, 2015, doi: 10.1016/b978-0-08-096811-7.50035-4.

[14] P. Amoatey, M. Chen, A. Al-Maktoumi, A. Izady, and M. S. Baawain, “A review of geothermal energy status and potentials in Middle-East countries,” *Arabian Journal of Geosciences 2021 14:4*, vol. 14, no. 4, pp. 1–19, Feb. 2021, doi: 10.1007/S12517-021-06648-9.

[15] “Solar energy | Definition, Uses, Advantages, & Facts | Britannica.” Accessed: Mar. 25, 2024. [Online]. Available: https://www.britannica.com/science/solar-energy

[16] “Solar Energy – Definition, Uses, Advantages, Facts | Fieldproxy Blog.” Accessed: Mar. 25, 2024. [Online]. Available: https://www.fieldproxy.com/blog/solar-energy-definition-uses-advantages-facts

[17] “Solar Energy Potential and Utilization | EARTH 104: Earth and the Environment (Development).” Accessed: Mar. 25, 2024. [Online]. Available: https://www.e-education.psu.edu/earth104/node/950

[18] “How does solar power work? | Solar energy explained | National Grid Group.” Accessed: Mar. 25, 2024. [Online]. Available: https://www.nationalgrid.com/stories/energy-explained/how-does-solar-power-work

[19] “How do solar panels work?. Solar panels, also known as… | by Brenda Rose | Medium.” Accessed: Mar. 25, 2024. [Online]. Available: https://medium.com/@Breadarose/how-do-solar-panels-work-bb3c63718ce

[20] A. S. Al-Ezzi and M. N. M. Ansari, “Photovoltaic Solar Cells: A Review,” *Applied System Innovation 2022, Vol. 5, Page 67*, vol. 5, no. 4, p. 67, Jul. 2022, doi: 10.3390/ASI5040067.

[21] “Uses of Solar Cells - Detailed List of Applications & Advantages with Videos.” Accessed: Mar. 25, 2024. [Online]. Available: https://byjus.com/chemistry/uses-of-solar-cell/

[22] “The scope for emerging solar cell technologies – pv magazine India.” Accessed: Mar. 25, 2024. [Online]. Available: https://www.pv-magazine-india.com/2024/01/25/the-scope-for-emerging-solar-cell-technologies/

[23] “Photovoltaic cell - Energy Education.” Accessed: Mar. 25, 2024. [Online]. Available: https://energyeducation.ca/encyclopedia/Photovoltaic_cell

[24] T. V. Torchynska, “III-V material solar cells for space application,” *Semiconductor Physics, Quantum Electronics and Optoelectronics*, vol. 5, no. 1, pp. 63–70, Mar. 2002, doi: 10.15407/SPQEO5.01.063.

[25] M. Gul, Y. Kotak, and T. Muneer, “Review on recent trend of solar photovoltaic technology,” *Energy Exploration and Exploitation*, vol. 34, no. 4, pp. 485–526, Jul. 2016, doi: 10.1177/0144598716650552.

[26] R. P. Smith, A. A.-C. Hwang, T. Beetz, and E. Helgren, “ Introduction to semiconductor processing: Fabrication and characterization of p-n junction silicon solar cells ,” *Am J Phys*, vol. 86, no. 10, pp. 740–746, Oct. 2018, doi: 10.1119/1.5046424.

[27] “Physics of Semiconductor Devices,” *Materials Today*, vol. 6, no. 1, p. 38, Jan. 2003, doi: 10.1016/S1369-7021(03)00132-9.

[28] A. Awasthi *et al.*, “Review on sun tracking technology in solar PV system,” *Energy Reports*, vol. 6, pp. 392–405, Nov. 2020, doi: 10.1016/J.EGYR.2020.02.004.

[29] R. W. Miles, K. M. Hynes, and I. Forbes, “Photovoltaic solar cells: An overview of state-of-the-art cell development and environmental issues,” *Progress in Crystal Growth and Characterization of Materials*, vol. 51, no. 1–3. Elsevier Ltd, pp. 1–42, 2005. doi: 10.1016/j.pcrysgrow.2005.10.002.

[30] M. B. Johnston and L. M. Herz, “Hybrid Perovskites for Photovoltaics: Charge-Carrier Recombination, Diffusion, and Radiative Efficiencies,” *Acc Chem Res*, vol. 49, no. 1, pp. 146–154, Jan. 2016, doi: 10.1021/ACS.ACCOUNTS.5B00411.

[31] “Solar Spectrum: Solar Radiation and Irradiance | Ossila.” Accessed: Mar. 27, 2024. [Online]. Available: https://www.ossila.com/pages/the-solar-spectrum

[32] “Concentrated Solar Power (CSP) Vs Photovoltaic (PV): An In-depth Comparison - SolarFeeds Magazine.” Accessed: Mar. 27, 2024. [Online]. Available: https://www.solarfeeds.com/mag/csp-and-pv-differences-comparison/

[33] R. A. Deshpande, “Advances in Solar Cell Technology: An Overview,” *Journal of Scientific Research*, vol. 65, no. 02, pp. 72–75, 2021, doi: 10.37398/JSR.2021.650214.

[34] N. Balaji, M. C. Raval, and S. Saravanan, “Review on Metallization in Crystalline Silicon Solar Cells,” *Solar Cells*, Mar. 2020, doi: 10.5772/INTECHOPEN.84820.

[35] “Thin-Film Solar Panels (2024 Guide).” Accessed: Mar. 25, 2024. [Online]. Available: https://www.ecowatch.com/solar/thin-film-solar-panels

[36] J. Yan and B. R. Saunders, “Third-generation solar cells: a review and comparison of polymer:fullerene, hybrid polymer and perovskite solar cells,” *RSC Adv*, vol. 4, no. 82, pp. 43286–43314, Sep. 2014, doi: 10.1039/C4RA07064J.

[37] M. A. Green, “Third generation photovoltaics: solar cells for 2020 and beyond,” *Physica E Low Dimens Syst Nanostruct*, vol. 14, no. 1–2, pp. 65–70, Apr. 2002, doi: 10.1016/S1386-9477(02)00361-2.

[38] “Single-junction solar cell definition - University Wafer.” Accessed: Apr. 02, 2024. [Online]. Available: https://www.universitywafer.com/single-junction-solar-cell.html

[39] B. M. Kayes *et al.*, “27.6% Conversion efficiency, a new record for single-junction solar cells under 1 sun illumination,” *Conference Record of the IEEE Photovoltaic Specialists Conference*, pp. 000004–000008, 2011, doi: 10.1109/PVSC.2011.6185831.

[40] “Tandem Solar Cells | The Solar Spark.” Accessed: Apr. 03, 2024. [Online]. Available: http://www.solarspark.chem.ed.ac.uk/science/solar-technology/tandem-solar-cells

[41] A. De Vos, “Detailed balance limit of the efficiency of tandem solar cells,” *J Phys D Appl Phys*, vol. 13, no. 5, pp. 839–846, 1980, doi: 10.1088/0022-3727/13/5/018.

[42] “NREL updates interactive chart of solar cell efficiency – pv magazine International.” Accessed: Apr. 03, 2024. [Online]. Available: https://www.pv-magazine.com/2022/11/21/nrel-updates-interactive-chart-of-solar-cell-efficiency/

[43] “An introduction to Perovskites | Perovskite-Info.” Accessed: Apr. 03, 2024. [Online]. Available: https://www.perovskite-info.com/introduction

[44] “Advent of alkali metal doping: a roadmap for the evolution of perovskite solar cells - Chemical Society Reviews (RSC Publishing).” Accessed: Apr. 03, 2024. [Online]. Available: https://pubs.rsc.org/en/content/articlelanding/2011/e0/d0cs01316a/unauth

[45] P. V. Kamat and C. M. Biegel, “Perovskite Stories from Around the World,” *ACS Energy Lett*, pp. 879–887, 2019, doi: 10.1021/ACSENERGYLETT.9B00512.

[46] “History and Evolution of Perovskites | Ossila.” Accessed: Apr. 03, 2024. [Online]. Available: https://www.ossila.com/pages/history-and-evolution-of-perovskites

[47] C. Motta, F. El-Mellouhi, S. Kais, N. Tabet, F. Alharbi, and S. Sanvito, “Revealing the role of organic cations in hybrid halide perovskite CH3 NH3PbI3,” *Nat Commun*, vol. 6, Apr. 2015, doi: 10.1038/NCOMMS8026.

[48] J. P. Correa Baena *et al.*, “Highly efficient planar perovskite solar cells through band alignment engineering,” *Energy Environ Sci*, vol. 8, no. 10, pp. 2928–2934, Oct. 2015, doi: 10.1039/C5EE02608C.

[49] D. Zhou, T. Zhou, Y. Tian, X. Zhu, and Y. Tu, “Perovskite-Based Solar Cells: Materials, Methods, and Future Perspectives,” *Journal of Nanomaterials*, vol. 2018. Hindawi Limited, 2018. doi: 10.1155/2018/8148072.

[50] F. Brivio, A. B. Walker, and A. Walsh, “Structural and electronic properties of hybrid perovskites for high-efficiency thin-film photovoltaics from first-principles,” *APL Mater*, vol. 1, no. 4, 2013, doi: 10.1063/1.4824147.

[51] Q. Xu, D. Yang, J. Lv, Y. Y. Sun, and L. Zhang, “Perovskite Solar Absorbers: Materials by Design,” *Small Methods*, vol. 2, no. 5, p. 1700316, May 2018, doi: 10.1002/SMTD.201700316.

[52] I. C. Smith, E. T. Hoke, D. Solis-Ibarra, M. D. Mcgehee, and H. I. Karunadasa, “A Layered Hybrid Perovskite Solar-Cell Absorber with Enhanced Moisture Stability**”, doi: 10.1002/anie.201406466.

[53] S. Mushtaq *et al.*, “Performance optimization of lead-free MASnBr3 based perovskite solar cells by SCAPS-1D device simulation,” *Solar Energy*, vol. 249, pp. 401–413, Jan. 2023, doi: 10.1016/j.solener.2022.11.050.

[54] P. V. Kamat, J. Bisquert, and J. Buriak, “Lead-free perovskite solar cells,” *ACS Energy Lett*, vol. 2, no. 4, pp. 904–905, Apr. 2017, doi: 10.1021/ACSENERGYLETT.7B00246.

[55] “Proposed Perovskite Structure CH3NH3SnBr3. | Download Scientific Diagram.” Accessed: Mar. 26, 2024. [Online]. Available: https://www.researchgate.net/figure/Proposed-Perovskite-Structure-CH3NH3SnBr3_fig1_351348545

[56] M. Shah Alam and O. Akter, “An Investigation of Several Factors Variation on the Performance of Snbr3 Based Perovskite Solar Cells with Different Electron and Hole Transport Layers An Investigation of Several Factors Variation on the Performance of SnBr 3 based Perovskite Solar Cells with Different Electron and Hole Transport Layers”, doi: 10.2139/ssrn.4318496.

[57] F. Chiarella *et al.*, “Combined experimental and theoretical investigation of optical, structural, and electronic properties of CH 3 NH 3 SnX 3 thin films "X = Cl, Br…”, doi: 10.1103/PhysRevB.77.045129.

[58] J. Sinopoli and C. Lamsal, “Electronic and optical properties of small clusters of methylammonium tin bromide (CH3NH3SnBr3),” *The European Physical Journal Special Topics 2024*, pp. 1–22, Feb. 2024, doi: 10.1140/EPJS/S11734-024-01113-6.

[59] J. Sinopoli and C. Lamsal, “Electronic and optical properties of small clusters of methylammonium tin bromide (CH3NH3SnBr3),” *The European Physical Journal Special Topics 2024*, pp. 1–22, Feb. 2024, doi: 10.1140/EPJS/S11734-024-01113-6.

[60] “Development of tin-based perovskite materials for solar cell applications: A minireview: Instrumentation Science & Technology: Vol 49, No 1.” Accessed: Apr. 04, 2024. [Online]. Available: https://www.tandfonline.com/doi/abs/10.1080/10739149.2020.1785891

[61] P. K. Patel, “Device simulation of highly efficient eco-friendly CH3NH3SnI3 perovskite solar cell,” *Scientific Reports 2021 11:1*, vol. 11, no. 1, pp. 1–11, Feb. 2021, doi: 10.1038/s41598-021-82817-w.

[62] Y. Q. Huang, J. Su, Q. F. Li, D. Wang, L. H. Xu, and Y. Bai, “Structure, optical and electrical properties of CH3NH3SnI3 single crystal,” *Physica B Condens Matter*, vol. 563, pp. 107–112, Jun. 2019, doi: 10.1016/J.PHYSB.2019.03.035.

[63] X. Bao *et al.*, “Ytterbium-doped fiber laser passively mode locked by evanescent field interaction with CH3NH3SnI3 perovskite saturable absorber,” *J Phys D Appl Phys*, vol. 51, no. 37, Aug. 2018, doi: 10.1088/1361-6463/AAD71D.

[64] I. O. A. Ali, D. P. Joubert, and M. S. H. Suleiman, “First-principles study of structural, mechanical, dynamical stability, electronic and optical properties of orthorhombic CH3NH3SnI3 under pressure,” *European Physical Journal B*, vol. 92, no. 9, Sep. 2019, doi: 10.1140/epjb/e2019-100101-1.

[65] R. Sabetvand, M. E. Ghazi, and M. Izadifard, “Studying temperature effects on electronic and optical properties of cubic CH3NH3SnI3 perovskite,” *J Comput Electron*, vol. 19, no. 1, pp. 70–79, Mar. 2020, doi: 10.1007/s10825-020-01443-3.

[66] F. Arif, M. Aamir, A. Shuja, M. Shahiduzzaman, and J. Akhtar, “Simulation and numerical modeling of high performance CH3NH3SnI3 solar cell with cadmium sulfide as electron transport layer by SCAPS-1D,” *Results in Optics*, vol. 14, Feb. 2024, doi: 10.1016/j.rio.2023.100595.

[67] A. Saeed *et al.*, “Design and Simulation of ETL-Free Perovskite/Si Tandem Cell With 33% Efficiency,” *WSEAS Transactions on Electronics*, vol. 13, pp. 137–141, 2022, doi: 10.37394/232017.2022.13.18.

[68] H. Li and W. Zhang, “Perovskite Tandem Solar Cells: From Fundamentals to Commercial Deployment,” *Chem Rev*, vol. 120, no. 18, pp. 9835–9950, Sep. 2020, doi: 10.1021/ACS.CHEMREV.9B00780/ASSET/IMAGES/MEDIUM/CR9B00780_0072.GIF.

[69] R. Lin *et al.*, “All-perovskite tandem solar cells with improved grain surface passivation,” *Nature*, vol. 603, no. 7899, pp. 73–78, Mar. 2022, doi: 10.1038/s41586-021-04372-8.

[70] M. M. Salah *et al.*, “High-Efficiency Electron Transport Layer-Free Perovskite/GeTe Tandem Solar Cell: Numerical Simulation,” *Crystals (Basel)*, vol. 12, no. 7, Jul. 2022, doi: 10.3390/cryst12070878.

[71] M. Gholipoor, N. Solhtalab, and M. H. Mohammadi, “High-performance parallel tandem MoTe2/perovskite solar cell based on reduced graphene oxide as hole transport layer,” *Sci Rep*, vol. 12, no. 1, Dec. 2022, doi: 10.1038/s41598-022-25015-6.

[72] S. Goutham Kumar, E. A. R, T. Surya Teja Reddy, P. C. R, and G. V Honnavar, “Performance Analysis and Optimization of Lead-Free Tin-Based MASnBr3 Tandem Perovskite Solar Cell Section A-Research paper PERFORMANCE ANALYSIS AND OPTIMIZATION OF LEAD-FREE TIN-BASED MASnBr3 TANDEM PEROVSKITE SOLAR CELL,” *Chem. Bull*, vol. 2023, no. 6, pp. 2814–2832, doi: 10.31838/ecb/2023.12.6.251.

[73] M. Mousa, F. Z. Amer, R. I. Mubarak, and A. Saeed, “Simulation of optimized high-current tandem solar-cells with efficiency beyond 41%,” *IEEE Access*, vol. 9, pp. 49724–49737, 2021, doi: 10.1109/ACCESS.2021.3069281.

[74] M. A. Green, et al., "Thin-film solar cells: review of materials, technologies, and commercial status," J. Mater. Sci.: Mater. Electron., vol. 29, no. 11, pp. 8581-8592, 2018.

[75] B. J. Stanbery, "Copper indium selenides and related materials for photovoltaic devices," Crit. Rev. Solid State Mater. Sci., vol. 27, no. 2, pp. 73-117, 2002.

[76] J. Y. Kim, et al., "Efficient perovskite solar cells fabricated via one-step deposition technique with anti-solvent engineering," J. Mater. Chem. A, vol. 3, pp. 9162-9165, 2015.

[77] A. Chirila, et al., "Highly efficient Cu(In,Ga)Se2 solar cells grown on flexible polymer films," Nat. Mater., vol. 10, pp. 857-861, 2011.

[78] H. Zhou, et al., "Interface engineering of highly efficient perovskite solar cells," Science, vol. 345, no. 6196, pp. 542-546, 2014.

[79] D. T. Moore, et al., "Crystallographic Orientation in Solution-Processed Hybrid Perovskite Thin Films: Implications for Optoelectronic Devices," J. Am. Chem. Soc., vol. 137, no. 6, pp. 2350-2358, 2015.

[80] J. P. Mailoa, et al., "A 2-terminal perovskite/silicon multijunction solar cell enabled by a silicon tunnel junction," Appl. Phys. Lett., vol. 106, no. 12, pp. 121105, 2015.

[81] Q. Chen, et al., "Planar heterojunction perovskite solar cells via vapor-assisted solution process," J. Am. Chem. Soc., vol. 136, no. 2, pp. 622-625, 2014.

[82] X. Lu, et al., "Improved Photovoltaic Performance of Perovskite Solar Cells with Chlorine Incorporated at the Grain Boundaries," ACS Appl. Mater. Interfaces, vol. 7, no. 16, pp. 7402-7411, 2015.

[83] H. J. Snaith, "Perovskites: the emergence of a new era for low-cost, high-efficiency solar cells," J. Phys. Chem. Lett., vol. 4, no. 21, pp. 3623-3630, 2013.

[84] Y. Rong, et al., "Critical kinetic control of non-stoichiometric intermediate phase transformation for efficient perovskite solar cells," Nat. Commun., vol. 8, pp. 14555, 2017.

[85] T. C. Sum, et al., "Nanoscale Perspectives on the Perovskite Solar Cells," J. Phys. Chem. Lett., vol. 6, no. 12, pp. 2418-2429, 2015.

[86] F. A. Castro-Mendez, et al., "Nanoscale Characterization of Thin Films and Nanomaterials for Photovoltaics," Adv. Energy Mater., vol. 8, no. 1, pp. 1702078, 2018.

[87] Kojima, et al., "Organometal halide perovskites as visible-light sensitizers for photovoltaic cells," J. Am. Chem. Soc., vol. 131, no. 17, pp. 6050-6051, 2009.

[88] N. A. Kadro, et al., "Solvent-Engineering and Postannealing of CH3NH3PbI3 Perovskite Films for Solar Cells," Adv. Energy Mater., vol. 5, no. 2, pp. 1401694, 2015.

[89] M. Liu, et al., "Efficient planar heterojunction perovskite solar cells by vapour deposition," Nature, vol. 501, no. 7467, pp. 395-398, 2013.

[90] K. K. Wong, et al., "Photophysical Dynamics of Hybrid Perovskite Thin Films and Solar Cells," Chem. Mater., vol. 29, no. 12, pp. 5416-5424, 2017.

[91] N. J. Jeon, et al., "Compositional engineering of perovskite materials for high-performance solar cells," Nature, vol. 517, no. 7535, pp. 476-480, 2015.

[92] S. G. Kim, et al., "High-efficiency, multi-junction solar cells with enhanced current collection and reduced recombination by silicon nanowire arrays," Nano Energy, vol. 53, pp. 598-606, 2018.

[93] Z. Liu, et al., "Fabrication and characterization of efficient perovskite solar cells based on solution-processed SnO2 electron selective layers," RSC Adv., vol. 5, pp. 28110-28115, 2015.

[94] L. Meng, et al., "Efficient and stable solution-processed planar perovskite solar cells via contact passivation," Science, vol. 361, no. 6407, pp. 1094-1098, 2018.

[95] C. Roldán-Carmona, et al., "High efficiency single-junction semitransparent perovskite solar cells," Energy Environ. Sci., vol. 7, no. 1, pp. 2968-2973, 2014.

[96] P. Wang, et al., "Stable and efficient perovskite solar cells with ultra-thin buffer layers," Nano Energy, vol. 64, pp. 103910, 2019.

[97] A. (Antonio) Luque and Steven. Hegedus, *Handbook of photovoltaic science and engineering*. Wiley, 2011.

[98] "Photovoltaic effect - Energy Education." Accessed: Mar. 30, 2024. [Online]. Available: https://energyeducation.ca/encyclopedia/Photovoltaic_effect

[99] P. Kamat and G. C. Schatz, "How to Make Your Next Paper Scientifically Effective," *J. Phys. Chem. Lett.*, vol. 4, no. 9, pp. 1578–1581, May 2013, doi: 10.1021/jz4006916.

[100] "Density of States - Engineering LibreTexts." Accessed: Mar. 30, 2024. [Online]. Available: https://eng.libretexts.org/Bookshelves/Materials_Science/Supplemental_Modules_(Materials_Science)/Electronic_Properties/Density_of_States

[101] "Fermi Function." Accessed: Mar. 30, 2024. [Online]. Available: https://www.acsu.buffalo.edu/~wie/applet/fermi/fermifunction/fermifunction.html

[102] “Fermi level and Fermi function.” Accessed: Mar. 30, 2024. [Online]. Available: http://hyperphysics.phy-astr.gsu.edu/hbase/Solids/Fermi.html

[103] “Energy Bands - Definition and Classification of Energy Bands | Band Theory.” Accessed: Mar. 30, 2024. [Online]. Available: https://byjus.com/physics/what-are-energy-bands/

[104] “Semiconductors - Types, Examples, Properties, Application and Uses.” Accessed: Mar. 30, 2024. [Online]. Available: https://byjus.com/jee/semiconductors/

[105] “How a Solar Cell Works - American Chemical Society.” Accessed: Mar. 30, 2024. [Online]. Available: https://www.acs.org/education/resources/highschool/chemmatters/past-issues/archive-2013-2014/how-a-solar-cell-works.html

[106] Y. Sun, W. Chen, and Z. Sun, “A mini review: Constructing perovskite p-n homojunction solar cells,” *Chinese Chemical Letters*, vol. 33, no. 4, pp. 1772–1778, Apr. 2022, doi: 10.1016/J.CCLET.2021.08.055.

[107] S. S. Perlman and D. L. Feucht, “p-n heterojunctions,” *Solid State Electron*, vol. 7, no. 12, pp. 911–923, Dec. 1964, doi: 10.1016/0038-1101(64)90070-X.

[108] H. Cotal *et al.*, “III-V multijunction solar cells for concentrating photovoltaics,” *Energy and Environmental Science*, vol. 2, no. 2. pp. 174–192, 2009. doi: 10.1039/b809257e.

[109] “High-Efficiency Multijunction Solar Cells.” [Online]. Available: www.mrs.org/bulletin

[110] N. Jain and M. K. Hudait, “III-V Multijunction Solar Cell Integration with Silicon: Present Status, Challenges and Future Outlook,” *Energy Harvesting and Systems*, vol. 1, no. 3, pp. 121–145, Dec. 2014, doi: 10.1515/EHS-2014-0012/MACHINEREADABLECITATION/RIS.

[111] “Approaching the Schottky–Mott limit in van der Waals metal–semiconductor junctions | Nature.” Accessed: Mar. 31, 2024. [Online]. Available: https://www.nature.com/articles/s41586-018-0129-8

[112] R. T. Tung, “The physics and chemistry of the Schottky barrier height,” *Appl. Phys. Rev.*, vol. 1, no. 1, p. 011304, 2014, doi: 10.1063/1.4858400.

[113] “Diode Equation | PVEducation.” Accessed: Mar. 31, 2024. [Online]. Available: https://www.pveducation.org/pvcdrom/pn-junctions/diode-equation

[114] I. Zarazua *et al.*, “Surface Recombination and Collection Efficiency in Perovskite Solar Cells from Impedance Analysis.”

[115] Fossum, “Physical operation of back-surface-field silicon solar cells,” *IEEE Trans Electron Devices*, vol. 24, 1977.

[116] “Optical Losses | PVEducation.” Accessed: Apr. 01, 2024. [Online]. Available: https://www.pveducation.org/pvcdrom/design-of-silicon-cells/optical-losses

[117] “Intrinsic Carrier Concentration | PVEducation.” Accessed: Apr. 01, 2024. [Online]. Available: https://www.pveducation.org/pvcdrom/pn-junctions/intrinsic-carrier-concentration

[118] "Equivalent Circuit of Solar Cell | Ossila." Accessed: Apr. 01, 2024. [Online]. Available: https://www.ossila.com/pages/equivalent-circuit-of-solar-cell

[119] L. Yue, B. Yan, M. Attridge, and Z. Wang, "Light absorption in perovskite solar cell: Fundamentals and plasmonic enhancement of infrared band absorption," *Solar Energy*, vol. 124, pp. 143–152, Feb. 2016, doi: 10.1016/J.SOLENER.2015.11.028.

[120] "Characteristics of a Solar Cell and Parameters of a Solar Cell | Electrical4U." Accessed: Apr. 02, 2024. [Online]. Available: https://www.electrical4u.com/characteristics-and-parameters-of-a-solar-cell/

[121] "Open-Circuit Voltage | PVEducation." Accessed: Apr. 02, 2024. [Online]. Available: https://www.pveducation.org/pvcdrom/solar-cell-operation/open-circuit-voltage

[122] "Fill Factor | PVEducation." Accessed: Apr. 02, 2024. [Online]. Available: https://www.pveducation.org/pvcdrom/solar-cell-operation/fill-factor

[123] "Efficiency of Solar Cells." Accessed: Apr. 02, 2024. [Online]. Available: https://sinovoltaics.com/learning-center/solar-cells/efficiency-of-solar-cells/

[124] H. Zhu, A. K. Kalkan, J. Hou, and S. J. Fonash, "Applications of AMPS-1D for solar cell simulation," in *AIP Conference Proceedings*, AIP, 1999, pp. 309–314. doi: 10.1063/1.57978.

[125] S. Assal, S. Yadir, H. Amiry, M. Sidki, and M. Benhmida, "Analysis of technological factors's influence on solar cell's performance by PC1D simulation," in *2014 International Renewable and Sustainable Energy Conference (IRSEC)*, IEEE, Oct. 2014, pp. 1–5. doi: 10.1109/IRSEC.2014.7059806.

[126] Y. Liu, Y. Sun, and A. Rockett, "A new simulation software of solar cells—wxAMPS," *Solar Energy Materials and Solar Cells*, vol. 98, pp. 124–128, Mar. 2012, doi: 10.1016/j.solmat.2011.10.010.

[127] S. S. Hussain *et al.*, "Numerical Modeling and Optimization of Lead-Free Hybrid Double Perovskite Solar Cell by Using SCAPS-1D," *Journal of Renewable Energy*, vol. 2021, pp. 1–12, Jul. 2021, doi: 10.1155/2021/6668687.

[128] J. Löckinger *et al.*, "TiO2 as intermediate buffer layer in Cu(In,Ga)Se2 solar cells," *Solar Energy Materials and Solar Cells*, vol. 174, pp. 397–404, Jan. 2018, doi: 10.1016/j.solmat.2017.09.030.

[129] E. I. Emon *et al.*, "A comprehensive photovoltaic study on tungsten disulfide (WS2) buffer layer based CdTe solar cell," *Heliyon*, vol. 9, no. 3, p. e14438, Mar. 2023, doi: 10.1016/j.heliyon.2023.e14438.

[130] C.-H. Lai, Z.-Y. Lee, S.-C. Lin, and Y.-H. Chuang, "Al-Doped ZnO Transparent Conducting Glass With an IGZO Buffer Layer for Dye-Sensitized Solar Cells," *IEEE J Photovolt*, vol. 10, no. 3, pp. 795–802, May 2020, doi: 10.1109/JPHOTOV.2020.2972264.

[131] V. Sivathanu, T. Rajalingam, and T. R. Lenka, "Modelling of CZTS/ZnS/AZO solar cell for efficiency enhancement," in *2018 3rd International Conference on Microwave and Photonics (ICMAP)*, IEEE, Feb. 2018, pp. 1–2. doi: 10.1109/ICMAP.2018.8354643.

[132] B. Sun, H. Chen, K. Yan, and X.-D. Feng, “Numerical investigation of the Cu2O solar cell with double electron transport layers and a hole transport layer,” *Opt Mater (Amst)*, vol. 131, p. 112642, Sep. 2022, doi: 10.1016/j.optmat.2022.112642.

[133] L. Nakka, Y. Cheng, A. G. Aberle, and F. Lin, “Analytical Review of Spiro-OMeTAD Hole Transport Materials: Paths Toward Stable and Efficient Perovskite Solar Cells,” *Advanced Energy and Sustainability Research*, vol. 3, no. 8, Aug. 2022, doi: 10.1002/aesr.202200045.

[134] M. Liang *et al.*, “Improving stability of organometallic-halide perovskite solar cells using exfoliation two-dimensional molybdenum chalcogenides,” *NPJ 2D Mater Appl*, vol. 4, no. 1, p. 40, Nov. 2020, doi: 10.1038/s41699-020-00173-1.

[135] D. Sharma, R. Mehra, and B. Raj, “Optimization of tin based perovskite solar cell employing CuSbS2 as HTL: A numerical simulation approach,” *Opt Mater (Amst)*, vol. 134, p. 113060, Dec. 2022, doi: 10.1016/j.optmat.2022.113060.

[136] H. B. Saim and D. S. Campbell, “Properties of indium-tin-oxide (ITO)/silicon heterojunction solar cells by thick-film techniques,” *Solar Energy Materials*, vol. 15, no. 4, pp. 249–260, May 1987, doi: 10.1016/0165-1633(87)90040-2.

[137] S. Mushtaq *et al.*, “Performance optimization of lead-free MASnBr3 based perovskite solar cells by SCAPS-1D device simulation,” *Solar Energy*, vol. 249, pp. 401–413, Jan. 2023, doi: 10.1016/j.solener.2022.11.050.

[138] M. N. Hasan, M. M. Habib, M. A. Matin, and N. Amin, “Modeling of high efficient perovskite-Si tandem solar cell,” in *2017 3rd International Conference on Electrical Information and Communication Technology (EICT)*, IEEE, Dec. 2017, pp. 1–5. doi: 10.1109/EICT.2017.8275213.

[139] F. Hazeghi and S. M. B. Ghorashi, “Simulation of perovskite solar cells by using CuSCN as an inorganic hole-transport material,” *Mater Res Express*, vol. 6, no. 9, p. 095527, Jul. 2019, doi: 10.1088/2053-1591/ab2f1b.

[140] X.-B. Xu, X.-Y. Wang, W.-P. Gu, S. Quan, and Z. Zhang, “Study on influences of CdZnS buffer layer on CdTe solar cells,” *Superlattices Microstruct*, vol. 109, pp. 463–469, Sep. 2017, doi: 10.1016/j.spmi.2017.05.033.

[141] M. M. Salah *et al.*, “High-Efficiency Electron Transport Layer-Free Perovskite/GeTe Tandem Solar Cell: Numerical Simulation,” *Crystals (Basel)*, vol. 12, no. 7, p. 878, Jun. 2022, doi: 10.3390/cryst12070878.

[142] N. H. Ke, P. T. K. Loan, D. A. Tuan, H. T. Dat, C. V. Tran, and L. V. T. Hung, “The characteristics of IGZO/ZnO/Cu2O:Na thin film solar cells fabricated by DC magnetron sputtering method,” *J Photochem Photobiol A Chem*, vol. 349, pp. 100–107, Dec. 2017, doi: 10.1016/j.jphotochem.2017.09.016.

[143] M. Ying, J. Wen, and Y. Zhao, “Numerical simulation of CuInSe2 solar cells using wxAMPS software,” *Chinese Journal of Physics*, vol. 76, pp. 24–34, Mar. 2022, doi: 10.1016/j.cjph.2021.12.020.

[144] N. Rahman *et al.*, “Assessing the performance of MoTe2 based solar cell with Cu2O hole transport layer through device simulation,” *Discov Mater*, vol. 3, no. 1, p. 25, Sep. 2023, doi: 10.1007/s43939-023-00061-7.

[145] Y. Gan *et al.*, “Numerical Investigation Energy Conversion Performance of Tin-Based Perovskite Solar Cells Using Cell Capacitance Simulator,” *Energies (Basel)*, vol. 13, no. 22, p. 5907, Nov. 2020, doi: 10.3390/en13225907.

[146] S. Bhattarai *et al.*, “Investigation of Carrier Transport Materials for Performance Assessment of Lead-Free Perovskite Solar Cells,” *IEEE Trans Electron Devices*, vol. 69, no. 6, pp. 3217–3224, Jun. 2022, doi: 10.1109/TED.2022.3165516.

[147] Md. Samiul Islam *et al.*, "Defect Study and Modelling of SnX3-Based Perovskite Solar Cells with SCAPS-1D," *Nanomaterials*, vol. 11, no. 5, p. 1218, May 2021, doi: 10.3390/nano11051218.

[148] Bala, N., & Mallik, S. K. (2024). Comparative Study of Lead-free Perovskite Materials MASnI3, MASnBr3 and MAGeI3 to Design, Simulate and Optimize Lead Free PSC. *Indian Journal of Pure & Applied Physics (IJPAP)*, *62*(4), 292-303.

[149] Shrivastav, N., Kashyap, S., Madan, J., Al-Mousoi, A. K., Mohammed, M. K., Hossain, M. K., ... & Ramanujam, J. (2023). Perovskite-CIGS monolithic tandem solar cells with 29.7% efficiency: a numerical study. *Energy & Fuels*, *37*(4), 3083-3090.

[150] Salah MM, Zekry A, Abouelatta M, Shaker A, Mousa M, Amer FZ, Mubarak RI, Saeed A. High-Efficiency Electron Transport Layer-Free Perovskite/GeTe Tandem Solar Cell: Numerical Simulation. *Crystals*. 2022; 12(7):878. https://doi.org/10.3390/cryst12070878.

[151] Pandey, R., Bhattarai, S., Sharma, K., Madan, J., Al-Mousoi, A. K., Mohammed, M. K., & Hossain, M. K. (2023). Halide composition engineered a non-toxic perovskite–silicon tandem solar cell with 30.7% conversion efficiency. *ACS Applied Electronic Materials*, *5*(10), 5303-5315.

[152] Mondol, N., Islam, K. S., Islam, M. R., & Das, S. K. (2024). Enhancing solar cell efficiency: Investigation of high-performance lead-based perovskite-on-silicon (PVK–Si) tandem solar cells through design and numerical analysis. *AIP Advances*, *14*(1).

[153] Duha, A. U., & Borunda, M. F. (2022). Optimization of a Pb-free all-perovskite tandem solar cell with 30.85% efficiency. *Optical Materials*, *123*, 111891.

[154] Chowdhury, T. A., Zafar, M. A. B., Islam, M. S. U., Shahinuzzaman, M., Islam, M. A., & Khandaker, M. U. (2023). Stability of perovskite solar cells: issues and prospects. *RSC advances*, *13*(3), 1787-1810.

Appendices

TiO_2

Wavelength (nm)	Absorption (1/cm)
305.0	1.497077e+05
310.0	1.476415e+05
315.0	1.455517e+05
320.0	1.434314e+05
325.0	1.412725e+05
330.0	1.390652e+05
335.0	1.367976e+05
340.0	1.344542e+05
345.0	1.320150e+05
350.0	1.294526e+05
360.0	1.237820e+05
370.0	1.167340e+05
380.0	1.030824e+05

ITO

Wavelength (nm)	Absorption (1/cm)
305.0	3.595902e+04
310.0	3.333024e+04
315.0	3.057027e+04
320.0	2.763493e+04
325.0	2.445596e+04
330.0	2.091690e+04
335.0	1.678490e+04
340.0	1.142502e+04

$MASnBr_3$

Wavelength (nm)	Absorption (1/cm)
305.0	1.458529e+05
310.0	1.441134e+05
315.0	1.424088e+05
320.0	1.407378e+05
325.0	1.390991e+05
330.0	1.374914e+05
335.0	1.359135e+05
340.0	1.343643e+05
345.0	1.328428e+05
350.0	1.313478e+05
360.0	1.284338e+05
370.0	1.256151e+05
380.0	1.228851e+05
390.0	1.202378e+05
400.0	1.176678e+05
410.0	1.151699e+05
420.0	1.127395e+05
430.0	1.103724e+05
440.0	1.080644e+05
450.0	1.058120e+05
460.0	1.036118e+05
470.0	1.014604e+05
480.0	7.968631e+04
490.0	7.756440e+04
500.0	7.547126e+04

$CuSbS_2$

Wavelength (nm)	Absorption (1/cm)
305.0	1.254233e+05
310.0	1.237578e+05
315.0	1.221235e+05
320.0	1.205191e+05
325.0	1.189435e+05
330.0	1.173954e+05
335.0	1.158738e+05
340.0	1.143775e+05
345.0	1.129057e+05
350.0	1.114573e+05
360.0	1.086272e+05
370.0	1.058806e+05
380.0	1.032110e+05
390.0	1.006129e+05
400.0	9.808103e+04
410.0	9.561044e+04
420.0	9.319661e+04
430.0	9.083534e+04
440.0	8.852267e+04
450.0	8.625486e+04
460.0	8.402841e+04
470.0	8.183995e+04

c-Si	
Wavelength (nm)	**Absorption** (1/cm)
305.0	1.617712e+05
310.0	1.599579e+05
315.0	1.581824e+05
320.0	1.564431e+05
325.0	1.547387e+05
330.0	1.530679e+05
335.0	1.514292e+05
340.0	1.498217e+05
345.0	1.482441e+05
350.0	1.466953e+05
360.0	1.436800e+05
370.0	1.407684e+05
380.0	1.379533e+05
390.0	1.352284e+05
400.0	1.325879e+05
410.0	1.300265e+05
420.0	1.275392e+05
430.0	1.251216e+05
440.0	1.227694e+05
450.0	1.204789e+05
460.0	1.182465e+05
470.0	1.160688e+05
480.0	1.139428e+05
490.0	1.118657e+05

GeTe	
Wavelength (nm)	**Absorption** (1/cm)
305.0	1.902599e+05
310.0	1.882915e+05
315.0	1.863658e+05
320.0	1.844811e+05
325.0	1.826358e+05
330.0	1.808285e+05
335.0	1.790576e+05
340.0	1.773220e+05
345.0	1.756202e+05
350.0	1.739511e+05
360.0	1.707064e+05
370.0	1.675793e+05
380.0	1.645620e+05
390.0	1.616474e+05
400.0	1.588289e+05
410.0	1.561007e+05
420.0	1.534574e+05
430.0	1.508938e+05
440.0	1.484055e+05
450.0	1.459882e+05
460.0	1.436379e+05
470.0	1.413510e+05
480.0	1.391241e+05
490.0	1.369541e+05
500.0	1.348380e+05
510.0	1.327732e+05

$CuInSe_2$	
Wavelength (nm)	**Absorption** (1/cm)
305.0	1.705618e+05
310.0	1.687034e+05
315.0	1.668842e+05
320.0	1.651028e+05
325.0	1.633576e+05
330.0	1.616474e+05
335.0	1.599707e+05
340.0	1.583263e+05
345.0	1.567131e+05
350.0	1.551300e+05
360.0	1.520495e+05
370.0	1.490769e+05
380.0	1.462051e+05
390.0	1.434274e+05
400.0	1.407378e+05
410.0	1.381309e+05
420.0	1.356014e+05
430.0	1.331449e+05
440.0	1.307570e+05
450.0	1.284338e+05
460.0	1.261715e+05
470.0	1.239668e+05
480.0	1.218166e+05